Forms and Rotational States of the Nuclei of Ecliptic Comets

A thesis submitted for the degree of
Doctor of Philosophy

by

Colin David Brodie Snodgrass, M Sci. (St. Andrews 2003)

Faculty of Engineering and Physical Sciences

Department of Physics and Astronomy
Queen's University Belfast
Belfast, Northern Ireland

September 2006

For my parents,
Liz and Jeremy Snodgrass

Acknowledgements

Firstly, I would like to thank Alan Fitzsimmons for supervising me in this work. He has taught me a great deal about observational astronomy in general and the minor bodies of the Solar System in particular, and has been a constant source of advice and constructive criticism in my research. I thank him for giving me the opportunity to do this work, and also for the opportunities for travel that have been part of this. A great deal of thanks must also go to Stephen Lowry for his help and advice, as an office mate, observer, drinking buddy and Patagonian adventurer. His expertise in cometary astronomy has been invaluable, and his reviewing of draft papers can only be described as very thorough!

I would also like to thank the other members of the ARC, past and present, who have made my time in Belfast an enjoyable one; from the 'humour' of the coffee room to the in depth academic discussions of the orange juice club. In particular, Shaun's almost constant presence in the common room bar, Pete's barbecuing (and St Patrick's day at his brother's in Sligo), Damien's soccer-ball watching and John's hospitality for Eurovision viewing have made for a fun time. Jonathon, Rachel and Tim were excelent companions on trips to the Mournes and expeditions to the bars of Belfast. I also thank Robert Ryans for his ungrudging and good humoured assistance with all computer matters.

Sean Denham has been a great flatmate for the last 3 years, as a constant source of Chicagoan wit and observation on the peculiarities of life in Belfast for us outsiders, and on the strangeness of the world in general. Furthermore, I thank my other friends from Selkirk and from St Andrews, now spread over the whole UK and beyond, for moral support and as great travelling companions or hosts on various trips. Here I must thank Al and Pete specifically for the regular use of their sofa, and their generosity with whisky. Those currently writing their own Ph.D theses, both from St Andrews and in the world wide graduate student community brought together by Ph.D comics online, have provided both support and distraction in equal measure, whenever either was required.

Finally, I thank my family; my parents for their continued support throughout my university career, and Keith for the comedy tales of his many adventures.

Abstract

In this thesis I present measurements of the physical properties of the nuclei of Jupiter Family comets (JFCs), based on time-series observations. These data were collected in four observing runs; two using the 3.6m NTT in Chile, and two using the 2.5m INT on the island of La Palma. From the time-series photometry rotation rates and elongations were measured, and from these constraints were placed on the bulk density and porosity of nuclei. Multi-filter imaging was performed to enable measurement of their surface colours. In addition, a large amount of 'snap-shot' imaging was performed during these observing runs, and taken with the time-series data is used to measure nuclei sizes.

These results are compared with other data from the literature to study the general properties of JFC nuclei. A size distribution is measured which is consistent with that predicted for a population of collisional fragments, while the distribution in rotation rates is found to be flat and non-collisional. The low minimum densities measured for all comets imply that the true bulk density of nuclei is low, and the porosity is high. These properties are shown to have similar values in the Kuiper Belt Object (KBO) population, which is the supposed parent population for JFCs. The surface colours of JFCs are shown to match the blue end of the KBO distribution, and can be derived from the observed KBO distribution under the assumption of a de-reddening function that preferentially depletes the reddest surfaces.

Contents

List of Tables

List of Figures

Publications

A list of publications resulting from work presented in this thesis is given below.

Refereed Publications

1. Snodgrass, C. D. B., Fitzsimmons, A., & Lowry, S. C.
   The nuclei of comets 7P/Pons-Winnecke, 14P/Wolf and 92P/Sanguin
   2005, A&A, **444**, 287–295

2. Meech, K., . . . Snodgrass, C. D. B., . . . et al.
   Deep Impact: Observations from a Worldwide Earth-Based Campaign
   2005, Science, **310**, 265–269

3. Snodgrass, C. D. B., Lowry, S. C., & Fitzsimmons, A.
   Photometry of cometary nuclei: Rotation rates, colours and a comparison with Kuiper Belt Objects
   2006, MNRAS, **373**, 1590-1602

Non-refereed Publications

1. Fitzsimmons, A., Snodgrass, C. D. B., & Hainaut, O.
   Comet P/2003 SQ_{215} (NEAT-Loneos)
   2004, IAUC 8274

2. Tubbiolo, A., Fitzsimmons, A., Lowry, S. C., Snodgrass, C. D. B., Tichy, M., & Ticha, J.
   Comet C/2005 E1 (Tubbiolo)
   2005, IAUC 8491

3. Snodgrass, C. D. B., Lowry, S. C., Fitzsimmons, A., Larson, S., & Skiff, B.
   Comet P/2005 JQ_5 (Catalina)
   2005, IAUC 8531

4. Snodgrass, C. D. B., Fitzsimmons, A., & Lowry, S. C.
   Physical properties of seven cometary nuclei
   2005, IAU Symposium No. 229: Asteroids, Comets, Meteors. Búzios, Rio de Janeiro, Brazil, 7–12 Aug.

5. Fitzsimmons, A., Snodgrass, C. D. B., Lowry, S. C., & Maui Deep Impact Workshop Participants Collaboration
   Optical and near-IR imaging of 9P/Tempel 1
   2005, Bulletin of the American Astronomical Society, **37**, 1569

6. McNaught, R. H., Fitzsimmons, A., Lowry, S. C., Snodgrass, C. D. B.
   Comet C/2006 HW_{51} (Siding Spring)
   2006, IAUC 8718

Chapter 1

Introduction - A brief history of comets

Here I review the subject of cometary physics by presenting a brief history of the study of comets, from superstition to the modern day. Major advances are highlighted, while results of consequence to this thesis and the current 'state of the art' are presented in more detail, although the intention is to provide a broad overview rather than a detailed chronicle of previous studies. More detailed accounts of the long and fascinating history of cometary astronomy are given by Brandt & Chapman (2004); Festou et al. (2004) and especially in the text by Yeomans (1991).

1.1 Early work

Comets have been known since pre-historic times; there are a few bright comets visible to the naked eye every decade, and such unexpected appearances in the sky would have been noticed by our earliest ancestors. Reports of comets appear in the earliest astronomical records, made in around 1000 BC by Chinese astronomers (Ho 1962). In pre-scientific times the appearances of bright comets were given supernatural explanations, and inspired both wonder and fear as signs from the gods or portents of great events; archaeologists suggest (with varying degrees of credibility) that the appearance of bright comets during ancient times could be responsible for a number of myths (McCafferty & Baillie 2005). It has also been suggested that the 'star of Bethlehem' was a comet, and the appearance of Halley's comet in 1066 is depicted in the Bayeux tapestry (fig. 1.1). Yet despite the long history of comet observations, it is normally the human cataclysms that accompanied the passage of the comet, and not any real information on the comets themselves, that are recorded in history. For many centuries research into comets was devoted entirely to their astrological implications; they nearly always foretold disaster.

At the time of the Renaissance, and the beginning of science as we know it in western Europe, comets still inspired wonder, if not fear, amongst the great thinkers of the age (comet apparitions still provoked panic in the general population, due to

Figure 1.1: The 1066 apparition of 1P/Halley coincided with the Norman invasion of England, and was thought to be a heavenly sign connected with these great events. Its appearance was recorded on the famous Bayeux Tapestry, showing the importance attached to the sighting of comets in pre-scientific times. The group of people towards the left see the comet (‘*istimirant stella’ = ‘they look at the star’*) which is depicted as the typical ‘hairy star’ with a tail, above the English King Harold II, who was killed at the battle of Hastings at around the time the comet was visible.

superstition that remained common even within the last century, and persists in some people to this day). It was at this time that the scientific study of comets could be said to have begun. While the heliocentric solar system theory of Copernicus was beginning to replace the ancient Greek view of a geocentric universe, the accepted theory on comets was still the Aristotlean view that they were atmospheric phenomena. Tycho Brahe was among the first to show that this was not the case, by means of very careful observations and measurement of the diurnal parallax of the comet of 1577, which he clearly showed to be beyond the Moon (Brahe 1578). It was not until the following century that the true orbital motions of comets were first described though, when Isaac Newton published a method for determining the orbital parameters of a parabolic comet orbit from a set of three observations using his theory of gravitation (Newton 1726). From this Edmond Halley was able to calculate the orbital parameters of a number of well observed comets (Halley 1705), and noted that the comets of 1531, 1607 and 1682 had similar orbits. This led him to make a confident prediction that these were one and the same comet, and that the comet would return in 1758. It did so, confirming not only the validity and great utility of Newton’s theory but also the astronomical nature of comets as solar

system objects with highly elliptical orbits.

This comet is the one now known as Halley's comet, and it is given the designation 1P - the first comet to be recorded at successive apparitions and be shown to be periodic. The modern numbering convention consists of either a P for periodic comets, a C for comets with approximately parabolic (i.e. very long period) orbits or a D for defunct (broken up or otherwise not recovered) comets. For comets with well known orbits, this letter is preceded with a sequential number based on when the orbit was confirmed; there are now 175 numbered comets. Comets are also identified by following the above letter with either their name, which is the name of their discoverer, or a designation of the form C/1995 O1, comprising the year of discovery, a letter which designates the half month in which the comet was discovered, and finally a number based on the order in which the comets were discovered during that half month (i.e. the example given – comet Hale-Bopp – was the first comet discovered during the later half of July 1995).

By the nineteenth century comets were recognised as astronomical phenomena; their appearances noted and their orbits around the Sun routinely measured. The return of comet Halley in 1835 inspired another advance, as telescopes had improved to the point where structure within the coma and tails were observable, and were described in detail (Bessel 1836a,b). The Bessel-Bredichin model described how an unknown force from the Sun pushed particles into straight (type I) and curved (type II) tails. The advent of spectroscopy revealed the presence of both neutral and ionised gasses in the coma and tails (Swings et al. 1943). Various models describing the physical nature of comets were proposed; the idea of a comet as a swarm of particles was popular, and Lyttleton (1948) proposed what is known as the 'sandbank' model. The current paradigm was proposed by Whipple in a series of papers in the 1950s (Whipple 1950, 1951, 1955), and explained many of the observed properties of comets. Once again comet Halley was instrumental in advancing our knowledge, when spacecraft missions to the comet in the 1980s showed the Whipple model to be a good representation of its morphology. More recent works have updated and modified the Whipple model,

although these improvements do not radically alter the basic theory.

1.2 Comet morphology - nucleus models

Whipple's 'icey-conglomerate' or 'dirty snowball' model addressed a number of observed cometary properties: The bright comae of comets were known to be of considerable size ($\sim 10^5$ km) from direct observation and knowledge of the distance of comets, and showed structure within them (jets and fans). It was known to be tenuous as stars were observed through it, yet it clearly contained solid particles as meteor showers had been associated with cometary orbits. Comets had to possess some solid core, as they could survive a close pass to the Sun, yet this nucleus had to be smaller than 100 km in diameter as neither the Great Comet of 1882 nor Halley's Comet in 1910 were seen when they transited the Sun (Brandt & Chapman 2004). In addition to fitting these requirements, the great triumph of the Whipple model is that it explains the observed non-gravitational motion of comets first noted in 2P/Encke (and originally attributed to the comet's passage through some sort of resisting medium – Encke 1836). This force causes alteration of comet orbits, changing the date of perihelion by up to a few days from the time expected from orbit calculations accounting only for gravity (including perturbations due to the planets).

The Whipple model is based on a very small (a few km in diameter) solid nucleus made up primarily of water ice, and also containing other volatile ices (NH_3, CH_4, CO_2 and C_2N_2) and rock particles of sizes $10^{-6} - 10^{-1}$ m. When the comet approaches the Sun, incident Solar radiation heats these ices and causes sublimation. The resultant gasses, and dust particles carried with them, form the coma. This sublimation is restricted to certain areas on the daylight side of the nucleus (the fraction of sublimating area varying depending on how active the comet is), and thus material is released in jets from these areas. These produce the jets and fans observed in the coma at larger scales, and also act like rockets; the reaction force on the nucleus from the expelled material

Figure 1.2: A bright comet (Hale-Bopp), showing the characteristic coma and tails (ion tail – blue, dust tail – white) seen when comets approach the Sun. The solid central nucleus is too small to see on this scale, and even in images of the central part of the coma is obscured as light reflected from the nucleus is swamped by the reflected flux from the coma.

changes the comet's motion and provides the sought after non-gravitational acceleration. As ice is a poor conductor of heat, only the surface layers would experience heating and lose material through sublimation, explaining how comets could survive multiple perihelion passages.

The existence of various volatile species was postulated to explain the presence of gasses such as C_2, CN and CO^+ identified in spectra of cometary comae and tails. Their parent molecules are thought to be trapped within a matrix of less volatile H_2O ice, either at a crystalline level in the form of clathrate hydrates (Delsemme & Miller 1970), or within pores in amorphous water ice (Bar-Nun et al. 1985), which is why it is the sublimation rate of H_2O that controls the activity level of comets. The level of activity observed can be generalised by solving the energy balance equation (Cowan & A'Hearn 1979). This states that the energy received from the Sun must equal the energy

radiated back into space plus the energy used to vaporise the ices and any heat passed into the interior. Assuming the conduction term to be negligible, and that radiation and vaporisation take place over the sunlit hemisphere of the comet;

$$F_0(1-A_0)\frac{\pi r_{\rm N}^2}{R_{\rm h}^2} = 2\pi r_{\rm N}^2(1-A_1)\sigma\overline{T}^4 + Q(T)L(T) \tag{1.1}$$

where F_0 is the solar flux at Earth, A_0 and A_1 are the albedos at visual and infrared wavelengths, $r_{\rm N}$ is the nuclear radius and $R_{\rm h}$ is the heliocentric distance. $\overline{T}$ is the average temperature, σ the Stefan-Boltsman constant, $L(T)$ the latent heat of vaporisation and $Q(T)$ is the total vaporisation rate. For the most abundant volatile species, H_2O, the vaporisation rate is negligible at $R_{\rm h} > 3$ AU, and rises steeply when closer to the Sun. So, generally, comets are likely to be 'inactive' beyond 3 AU, although this depends on the intrinsic activity of the comet; C/1995 O1 Hale-Bopp has been observed to be active at $R_{\rm h} \geq 13$ AU (Hainaut 2001). This is of course a simplified picture of cometary activity, but sufficient for the purposes of this thesis. Prialnik et al. (2004) give a detailed review on modelling the process of sublimation from the nucleus.

Once sublimated into the coma, gas and dust are further altered by sunlight. Photochemistry is responsible for converting the parent molecules thought to exist in the nucleus into the various daughter molecules seen in spectra (Swings et al. 1943; see Rodgers et al. 2004 for a modern review). Incident UV radiation ionises gas to produce charged particles, which are then accelerated away from the Sun by the solar wind to produce the ion tail (the straight tail seen when a comet is highly active, previously called a type I tail). Radiation pressure also acts to push particles away from the comet to produce the dust tail, which is seen to curve (type II tail) due to the trajectories followed by particles ejected from the nucleus at different times.

The essential theory of a small nucleus of ice and rock, producing coma through sublimation and thereby tails, remains the currently favoured theory, and has largely been confirmed by space-craft missions to comets (see section 1.5). However there have been a number of variations proposed concerning the structure of the nucleus.

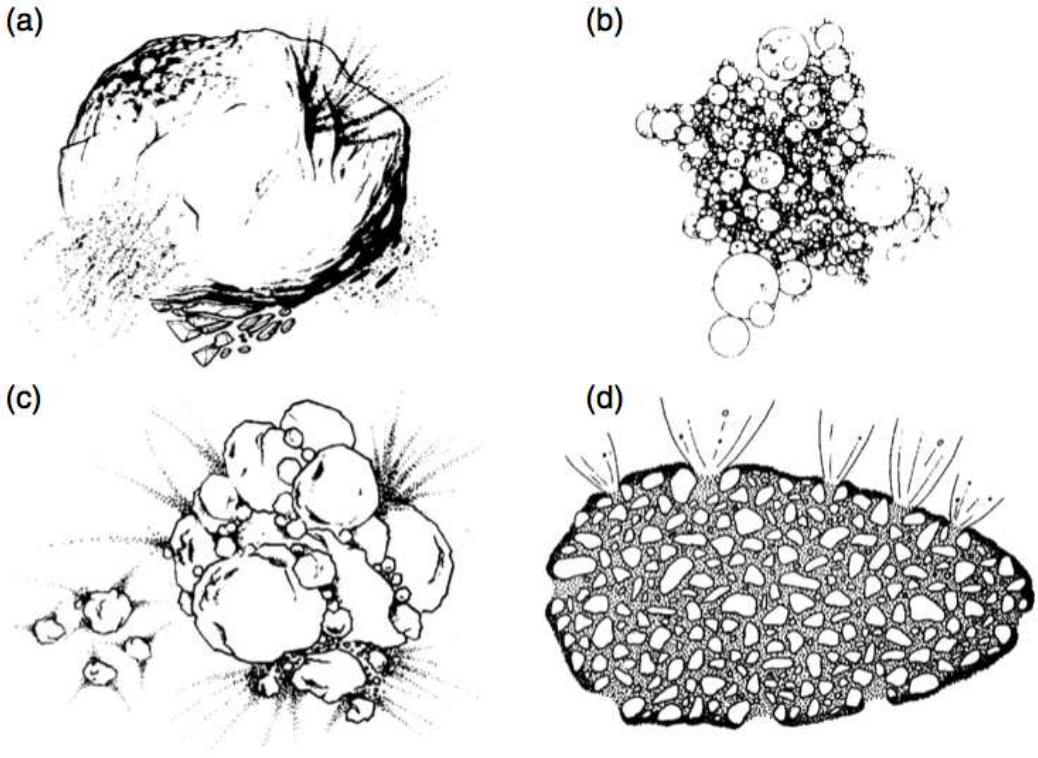

Figure 1.3: Artists' impressions of four different models of comet nuclei. (a) Whipple's icy-conglomerate, (b) Donn et al.'s fractal aggregate, (c) Weissman's primordial rubble pile, (d) Gombosi and Houpis' icy-glue model. Taken from Weissman et al. (2004).

Whipple's original model was of a solid, coherent snow-ball with considerable material strength, enabling it to survive close perihelion passages and periods of activity from the surface. Subsequent authors have postulated considerably weaker bodies, held together by self gravity and with very little tensile strength. Figure 1.3, reproduced from Weissman et al. (2004), shows four nucleus models; the Whipple snow-ball, two 'rubble-pile' models, and the theory of Gombosi & Houpis (1986) of 'icy-glue' holding the nucleus together. Rubble-piles are loosely bound aggregates of rock held together by self gravity, forming a body which is solid, but has very little strength. This description was first proposed for asteroids in the 1970s, as nearly all main belt asteroids could be expected to have had non-catastrophic collisions over their lifetime (Chapman et al. 1978). It is now accepted that most asteroids over $\sim$ 100 m in radius are rubble-piles, and have either been fractured or completely disrupted and reformed by collisions [as discussed by a number of authors in the Asteroids III book (Bottke et al. 2002)]. Images returned by the recent *Hayabusa* probe appear to show that its target, Near Earth

Asteroid Itokawa, is indeed a rubble-pile (Fujiwara et al. 2006). Rubble-pile structure was suggested as a model for cometary nuclei by two groups in the 1980s. Donn et al. (1985) came to this conclusion through considering the way that small icy grains would accrete in such a way to produce self-similar structures at larger and larger scales, producing a fractal type, loosely bound, 'fluffy aggregate' (fig. 1.3 (b)). Weissman (1986) approached the problem by considering the mass of a typical nucleus and noting that there is not enough gravitational potential to heat the interior, and that therefore the primordial fragments would not have melted and combined to form a single body (fig. 1.3 (c)). The 'icy-glue' model suggests that larger boulders are held together by a glue of volatile ices (Gombosi & Houpis 1986), although this theory has difficulty explaining the observed lack of strength seen in comets (see below).

The currently favoured model is that of a rubble-pile, although the idea that nuclei are formed from unaltered primordial solar nebula material has been challenged by the likelihood that comets have undergone collisions (Weissman et al. 2004). Although dependant on the source region for the class of comets under consideration (see next section), calculations of the collisional time-scale for nuclei show that they must have undergone significant collisions over the age of the Solar System (Stern 1995, 1996).

There is considerable observational evidence in support of the rubble-pile hypothesis, the greatest of these being that comets are effectively strengthless. The question of whether or not comets are actually strengthless, or have strength at a very weak level, is still of considerable interest. Comets are seen to split, either under the gravitational influence of the Sun or planets or spontaneously with no obvious cause (Boehnhardt 2004). The splitting of comets indicates that they can not have considerable strength; the split comet which is best understood is D/1993 F2 (Shoemaker-Levy 9), which was torn apart when it passed within the Roche limit of Jupiter in 1992, forming a long line of 20 fragments which subsequently collided with the planet. Modelling of this event by Asphaug & Benz (1996) showed that the material strength of the nucleus must be less than 6.5 Pa, which is very weak. For comparison, snow and soils have strengths in

the range 1 - 10^2 kPa, concrete $\sim$ 1 MPa, marble $\sim$ 10 MPa and common metals in the range $10^2 - 10^3$ MPa; cometary material clearly has a very low strength indeed.

This lack of strength is important as it means that nuclei must be held together by self gravitation, which is dependant on the mass (or equally, the density) of the nucleus. This means that constraints on the mass, density and internal structure of the nucleus can be determined using ground based techniques, which are described in chapter 3.

1.3 Flavours of comets - taxonomy and source regions

During the early to mid-20th century it became clear that there were different classes of comet. The first distinction was based purely on historical grounds: Division of comets into short period (with orbital period $P \leq 200$ years) and long period ($P > 200$ years) was based on the fact that astronomers had been reliably measuring orbits for approximately 200 years, so objects which returned in a time less than that could have been seen before. Short period comets were subsequently split into two groups, the Jupiter family comets (JFCs) with $P < 20$ years whose orbits are governed by the planet Jupiter, and the Halley type (named after the ubiquitous 1P/Halley) with longer periods ($20 \leq P \leq 200$ years).

Subsequently this taxonomy has been modified to have a basis in the orbital dynamics of the comets; JFC orbits are generally prograde, approximately confined to the ecliptic plane, with inclinations $i \leq 40^\circ$. Halley type and long period comets have (to a good approximation) randomly inclined orbits. Levison (1996) formalises the distinction between Ecliptic and Nearly Isotropic Comets (NICs) based on the Tisserand parameter T_J, which remains approximately constant for any given comet, even after perturbations due to Jupiter. The Tisserand parameter with respect to Jupiter is given by;

$$T_J = \frac{a_J}{a} + 2\sqrt{\frac{a(1-e^2)}{a_J}}\cos(i) \tag{1.2}$$

where e is the eccentricity of the orbit, a the semi-major axis and a_J the semi-major axis of Jupiter's orbit ($a_J \approx 5.2$ AU). As it is based on the orbital elements, the Tisserand parameter uses dynamical properties to differentiate between groups of comets. Those comets with $T_J < 2$ are designated NIC; with $T_J > 2$ are Ecliptic. Halley type and long period comets are NICs, while JFCs are Ecliptic. Strictly, JFCs fall into the range $2 \leq T_J \leq 3$, while comets with $T_J > 3$ do not approach Jupiter; they orbit either entirely within (*e.g.* 2P/Encke) or beyond (the Centaurs – see below) Jupiter's orbit.

At around the same time as Whipple was proposing his physical model of a comet nucleus to explain non-gravitational acceleration and the solar wind was being postulated to explain comet tails that a third great theoretical advance was presented. Oort (1950) calculated the original (*i.e.* before planetary perturbations) orbits of long period comets, and deduced that there must exist a reservoir of comets between 20,000 and 200,000 AU from the Sun, from which comets would be perturbed inwards by the passage of nearby stars. More recent works have slightly modified this theory, with the addition of interstellar clouds and the galactic tide as perturbers, and the analysis of many more comets (Marsden et al. 1978), but the presence of the Oort Cloud is well accepted. Indeed, the Oort cloud solves a significant problem in cometary astronomy in that it identifies a source for comets. The median dynamical lifetime of comets in the inner solar system is 3×10^5 years (Duncan et al. 2004), due to interactions with the planets causing the comet to collide with a planet or be ejected from the system. Also, the activity of comets causes significant mass loss with each perihelion passage, meaning that a 1 km radius comet will be destroyed in a few hundred orbits, depending on its perihelion distance (Wallis & Wickramasinghe 1985). Therefore a source of comets to replenish those lost or destroyed is required to maintain the observed flux of comets. The Oort cloud provides this source, but how did this cloud form? Simulations of the formation of the solar system show that comets which originally formed through the accretion of ices in the giant planet region are scattered by the planets into Oort cloud orbits (see Dones et al. 2004).

The Oort cloud is now well accepted as the source of long period comets, and its predicted spherical shape (orbits randomised in inclination by interactions with passing stars) explains the approximately random distribution of inclinations of LP comet orbits. However, the Oort cloud theory had significant problems explaining why the majority of short period comets (the JFCs) had low inclinations. Attempts were made to explain their orbits in terms of them being captured into low inclination, short period, orbits by interactions with the planets (primarily Jupiter), but these did not reproduce the observed distribution. It was suggested, first in a relatively unnoticed work by Edgeworth (1949) and then independently in the better known paper by Kuiper (1951), that a belt of comets confined roughly to the ecliptic plane and orbiting beyond Neptune (between 30 and 50 AU) could provide the source for Ecliptic Comets. Dynamical calculations (Fernández 1980) showed that this was a far more efficient source than the capture of high inclination comets, and attempts were made to discover objects in this belt (now generally known as the Kuiper Belt, but also as the Edgeworth-Kuiper Belt in belated recognition of the Irishman's work). The first Kuiper Belt Object (KBO) was discovered in 1992 (1992 QB1 - Jewitt & Luu 1993), and was quickly followed by further discoveries (Williams et al. 1993). There are now 990 KBOs known (as of May 2006), including objects of similar size to (in the case of 2003 UB_{313} larger than) Pluto, calling into question Pluto's planetary status. The belt is thought to have $\sim 7 \times 10^4$ objects larger than 100 km in diameter within it (Trujillo et al. 2001), and perhaps $\sim 10^8$ larger than 1 km (Bernstein et al. 2004). It is now generally accepted that it is the source of the Ecliptic comets; they are perturbed inwards by Neptune and then fall under Jupiter's influence to be brought into the inner Solar System as JFCs. The current scheme is complicated slightly further as KBOs are split into various populations depending on their dynamics, such as the classical and scattered disk objects, and objects which fall into mean motion resonances with Neptune, *e.g.* the Plutinos (so named as Pluto is one of them) which fall into the 3:2 resonance (Morbidelli & Brown 2004). The scattered disk is made up of objects which have encountered Neptune and been pushed into higher eccentricity orbits, and is now thought to be the element of the

Kuiper Belt which supplies the JFC population (Duncan et al. 2004). A further dynamical class of objects are the Centaurs, which are objects which orbit between Saturn and Neptune, and are thought to be the intermediary stage which KBOs pass through on their way to becoming JFCs (Duncan et al. 2004).

The Kuiper Belt, as originally envisaged, was a remnant of the formation of the Solar System; the KBOs were the left over lumps of rock and ice that never formed into a planet due to the low surface density of material that far out in the accretion disk around the young Sun. By studying KBOs, and therefore by studying the nuclei of JFCs, which come from the Kuiper Belt, the properties of the planet forming disk can be deduced. Comets provide an advantage in that they visit the inner Solar System and are therefore easier to study, especially at the small end of the size distribution, although they cannot be thought of as entirely pristine remnants due to alteration of their surface layers by activity. It is now realised that KBOs are also non-primordial, and will have undergone some processing over the age of the Solar System. Firstly, it was realised that the collisional time scale in the classical Kuiper Belt means that the vast majority of objects will have undergone a number of collisions (Stern 1995, 1996). This means that all but the largest are likely to be fractured or entirely fragmented, and this process also provides an energy source for melting of volatiles or other geophysical and chemical processing of the primordial material. The size distribution of KBOs will also be affected: collisional populations have distinctive size distributions (Davis et al. 2002). The second way in which KBOs will have been modified from their original state is chemical or physical alteration of the exposed surface layers, which should manifest itself in changes to the observed optical characteristics such as colour and albedo. So called 'space weathering' is caused by the impact of energetic particles and photons, which cause sputtering or chemical reactions with surface organic molecules. The effect of this is to build up an outer layer of very dark, red, material (Johnson et al. 1987). Therefore JFC nuclei start out not as pristine remnants of the formation of the Solar System, but come from a reddened, collisional[1] population. They remain

[1] If the JFCs come from the Scattered disk, not the classical Kuiper Belt, then their collisional history

the least altered bodies from that time, and an important current area of study is to assess the amount of alteration bodies undergo in the Kuiper Belt, and the nature and quantity of further alterations due to activity once these bodies become comets. This thesis tackles the latter issue in chapter 6.

Finally, recent work suggests that a further population of comets exists, the Main Belt Comets (MBCs), which have asteroid-like orbits (low inclination and eccentricity, $T_J > 3$) within the main asteroid belt between Mars and Jupiter. As these objects tend to have very low activity they are generally first identified as asteroids. The first of these objects to be observed to show cometary activity was 133P/Elst-Pizarro, which had originally been identified and numbered as asteroid 7968 Elst-Pizarro but has been observed to show sporadic weak activity (Hsieh et al. 2004; Toth 2006). This object was for some time regarded as either a strange JFC or an unusual asteroid, and a unique oddity, however early this year the discovery of further similar objects was announced, and it now appears that there is a population of comets within the asteroid belt (Hsieh & Jewitt 2006). If 133P is typical of the MBCs then this population may well have different physical properties to other comets, as it is an outlier in trends presented in this thesis for JFCs (see later chapters).

1.4 Earth based observations of nuclei

While the theory of cometary nuclei was being developed they remained invisible to observers, as a nucleus only a few kilometres in diameter is too small to identify within the bright coma of an active comet, unless it is observed at very high spatial resolution. There are three techniques by which this difficulty can be overcome at optical wavelengths. First, the nucleus can be seen within the coma by employing space-craft to image the comet from very close range. The successes of various space-craft missions

will be different; in fact they may well have escaped major collisions over the age of the Solar System (Rickman 2004). Whether or not the parent population of JFCs is collisionally relaxed is an important issue which is discussed in chapter 6.

are described in section 1.5.

A second method relies not on going to the comet, but waiting for the comet to come to us. By taking advantage of very close passes of comets to the Earth, and very high resolution imaging using the *Hubble Space Telescope*, the signal from the nucleus can be separated from the surrounding coma (*e.g.* Lamy et al. 1999). This method relies on the fact that the high resolution means that the central pixel will be dominated by the nucleus, and a coma model can be calculated to exactly match the profile and then be subtracted to leave a nuclear image. This method can only be applied to a limited number of comets, due to the rarity of close passes of comets to the Earth, but has been applied to a handful of comets.

The third method, which is employed in this thesis, is to image comets when effectively inactive at large distance. As described above, for a primarily water ice nucleus equation 1.1 gives a dramatic increase in activity (sublimation) when the comet is at heliocentric distances of $R_{\rm h} \leq 3$ AU. This is found to be a reasonable rule of thumb for deciding when a comet is likely to be active, although the distance at which the onset of activity occurs does vary between comets. Therefore comets are targeted when at $R_{\rm h} \geq 3$ AU in the hope of detecting the nucleus, although in a number of cases activity is seen at large heliocentric distance (see chapter 5). This method is difficult due to the small size and very low albedos of nuclei (see chapter 3), which makes them very faint targets at large distances.

The first goal of observations of bare nuclei was to measure their intrinsic brightness and therefore size. There have been a number of programmes of snap-shot photometry of nuclei, these surveys being led by Lowry et al. (Lowry et al. 2003; Lowry & Weissman 2003; Lowry & Fitzsimmons 2005), Licandro et al. (2000b) and Meech et al. (2004). In addition there is a catalogue of nucleus sizes from Tancredi et al. (2000), who follow a different approach; they collect all brightness estimates made by both amateurs and professionals for each comet (mostly taken while active) and from the heliocentric light-curve derive a 'nuclear' magnitude. The light-curves are noisy (even by Tancredi

et al.'s own reckoning, the vast majority fall into the lowest quality categories) and the estimates are therefore very approximate; these radii cannot be regarded as reliable unless independently confirmed by observations of the inactive nucleus. Around a third of numbered JFCs have had their radii measured by snap-shot surveys; results from the above surveys and other sources have been compiled by Lamy et al. (2004). This compilation gives reliable radius measurements for 64 ecliptic comets and 11 NICs, and limits on the sizes of many others that have been either observed when active, or have not been detected at large $R_{\rm h}$.

Measuring radii for a large sample of nuclei allows calculation of the size distribution. The number of comets with radii greater than $r_{\rm N}$ can be approximated by a power law:

$$N(>r_{\rm N}) \propto r_{\rm N}^{-q} \tag{1.3}$$

The size distribution is an important marker of the history of nuclei; if the population are collisional fragments of larger bodies then they should have a distribution with $q = 2.5$ (Dohnanyi 1969). Recent work on the size distributions of asteroids suggests that this is a simplified picture and the size distribution can have 'bumps' within it (Davis et al. 2002); theoretical work by O'Brien & Greenberg (2003) gives a wavy distribution with an average $q = 2.04$ over the size range observed in comets. For comets the theory is complicated by mass loss, and observational data is incomplete at small radii due to the difficulties in detecting these objects, but a number of attempts to measure the distribution have been made. Reliable estimates fall in the region $1.6 \leq q \leq 1.9$ (Lowry et al. 2003; Lamy et al. 2004), implying either a non-collisional parent population or significant modification of the size distribution by cometary activity; this topic is discussed in more detail and an updated measurement is presented in section 6.1 in chapter 6.

In addition to measuring the size of nuclei from their brightnesses, Earth based observations also allow study of their surface composition through studying how their reflectance varies at different wavelengths. The most complete compositional infor-

mation comes from spectroscopy, which is regularly used in observations of active comets to study the gasses present in the coma or tails. However, it has been seldom used in studies of nuclei due to the technical difficulties this presents: Spectroscopy works by splitting the light from the target into multiple wavelengths, and therefore requires relatively bright targets to give sufficient signal-to-noise at each wavelength. Distant inactive nuclei are very faint targets. The few nuclei spectra available are featureless and rise at a fairly constant gradient towards longer wavelengths (Luu 1993). Lower resolution spectral information can be obtained through multi-colour photometry, where the brightness of the nucleus is measured through a number of broad-band filters and the difference in reflectance between these bands gives the colour of the nucleus. As the observed cometary spectra are featureless no information is lost by performing broad-band photometry instead of spectroscopy, and photometry is considerably easier to perform on faint objects. In cometary studies the brightness is typically measured between the V (effective wavelength $\lambda_{\rm eff} = 5448$ Å) and R ($\lambda_{\rm eff} = 6407$ Å) bands; the average $(V-R)$ colour found for JFC nuclei is ~ 0.45, somewhat redder than the Solar $(V-R)_{\odot} = 0.35$ (Holmberg et al. 2006). This colour gives a very rough description of the spectra over the VR wavelength range; no detail is available, but the spectral gradient S' can be found from

$$(V-R)_{\rm N} = (V-R)_{\odot} + 2.5\log\left[\frac{2+S'\Delta\lambda}{2-S'\Delta\lambda}\right] \tag{1.4}$$

where $\Delta\lambda = 959$ Å is the difference between the effective wavelengths of the V and R bands. S' approximates the shape of the spectra by describing it as a linear increase (or decrease) of the reflectance over the wavelength range considered; it has units of percent per 1000 Å. Jewitt (2002) gives a mean value of $S' = 8.3 \pm 2.8$ % kÅ^{-1} for cometary nuclei. Further information on the rough shape of the spectra can be obtained by measurement of the nucleus brightness in more band-passes; plotting $(V-R)$ against $(B-V)$ or $(V-R)$ against $(R-I)$ has been a successful technique in identifying different compositional types in asteroids, as different shaped spectra occupy different

regions on such plots (Tholen 1984). In this thesis V-, R- and I-band ($\lambda_{\rm eff} = 7980$ Å) photometry is presented to allow measurement of $(V-R)$ and $(R-I)$ colours (see section 6.4 of chapter 6).

Over the last decade the direct study of JFCs' supposed parent bodies, KBOs, using Earth-based telescopes has begun. The observed objects are large ($r \gtrsim 100$ km) by cometary standards, as only large objects can be detected at distances $R_{\rm h} \geq 30$ AU. The size distribution of KBOs is steeper, with $q \approx 3.2$ (Lamy et al. 2004), although this is for a different size range due to the lack of observed small KBOs and non-existence of 100 km scale JFCs. The surface colours of KBOs exhibit a very wide distribution, but are typically very red, with a mean $(V-R)$ of 0.60 from the data in the catalogues of Jewitt & Luu (2001) and Peixinho et al. (2004). The mean spectral gradient for KBOs is $S' = 22.9 \pm 1.7$ (Jewitt 2002). The range in colour may be at least partially related to orbital parameters: objects with perihelia beyond 40 AU appear to be redder, and possibly there is a lack of bluer objects at lower inclinations (McBride et al. 2003). Such direct measurements of the JFC parent population allow direct comparison and investigation of the effects of the process of evolution into, and activity of, JFCs (see chapter 6).

1.5 Space-craft missions to nuclei

This thesis presents a large quantity of ground based observations; in this section I outline some of the advances made by space-craft that help in understanding and interpretation of these data. Sending space-craft to comets provides by far the richest source of information on these bodies, and a variety of instruments on various missions have probed the nucleus, coma and tails of active comets. While the detail they provide dwarfs that which can be obtained from the most detailed Earth based observations, only a handful of comets can ever be visited by such missions due to their expense and complexity. Therefore a synergy of the detail of space missions and the general proper-

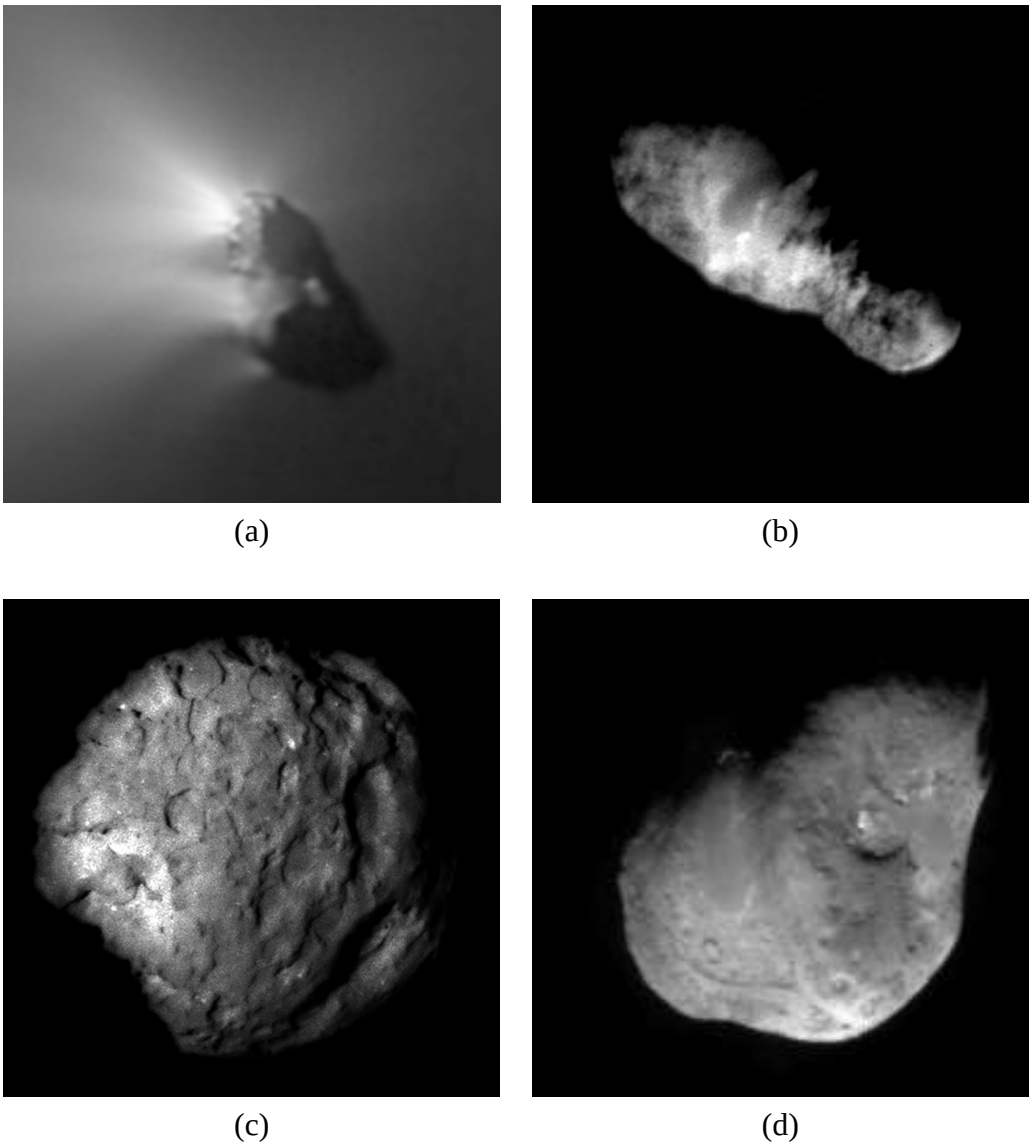

(a) (b)

(c) (d)

Figure 1.4: Nucleus images from space-craft: (a) 1P/Halley imaged by *Giotto*, (b) 19P/Borrelly imaged by *Deep Space 1*, (c) 81P/Wild 2 imaged by *Stardust* and (d) 9P/Tempel 1 imaged by *Deep Impact*.

ties observed for large numbers of comets measured from Earth is required to gain the most complete understanding possible. Figure 1.4 shows images of nuclei obtained by these missions.

Each new space-craft mission has revolutionised our understanding of comets, but none more so than the 'Armada' that met 1P/Halley on its last pass through the inner solar system in 1986. As has been noted through-out this introduction, apparitions of Halley's comet always mark an advance in our understanding. This was the first pass of this most famous comet during the space age, and the Russian, European and Japanese

space agencies all sent probes. NASA did not send a probe directly, although it participated in the *International Cometary Explorer* mission, which measured the effects of Halley's magnetic field from 28 million km away on the Sun-ward side, having previously passed 21P/Giacobini-Zinner at 8000 km. The Japanese probes *Sakegaki* and *Suisei* also passed to the Sun-ward side of the comet within its magnetic influence but beyond the inner coma; they were not designed to study the nucleus (Hirao & Itoh 1987).

The first images of the nucleus of a comet were returned by the Russian *VEGA* and European *Giotto* missions at comet 1P/Halley during 1986 (Sagdeev et al. 1986; Keller et al. 1986). These confirmed Whipple's 'dirty snow-ball' model, and also showed that Halley's nucleus is small ($r_{\rm N} = 5.5$ km), dark (albedo 0.04 - 0.08) and elongated (axial-ratio $a/b \approx 2$). There was some debate on the nucleus' rotation despite the wealth of information from the probes and the extensive ground based observations that complemented them (the *International Halley Watch*); it is now generally thought that the nucleus is in an excited rotational state (Samarasinha et al. 2004). At its closest pass of ~ 600 km, *Giotto* had a resolution of ~ 40 m per pixel, and was able to discern structure such as hills and craters, and identify discrete active areas correlated with the sources of jets (fig. 1.4 (a)).

Recently, a number of further missions have returned images of cometary nuclei, including the first images of a JFC nucleus taken by the *Deep Space 1* (*DS1*) probe at 19P/Borrelly (Soderblom et al. 2002). *DS1* was primarily a NASA technology testing mission, trying out a new ion drive propulsion system. It passed within ~ 2000 km of the nucleus and achieved a pixel scale of ~ 50 m pix^{-1}, showing surface details (fig. 1.4 (b)). This nucleus was also found to be highly elongated, showing an excellent agreement with Earth based results obtained by Lamy et al. (1998b) using the *Hubble Space Telescope*, with various surface features including areas which appeared to be smoothed and raised mesas. Again, a very low albedo ($p_V = 0.029$) was measured. The nuclei of the Oort cloud comet Halley and the JFC Borrelly were noted to be

remarkably similar.

The *Stardust* mission to 81P/Wild 2 was designed primarily to capture dust particles from the coma and return them to Earth for laboratory analysis, but also carried a camera (Brownlee et al. 2004). The craft safely returned its samples; the results are eagerly awaited and will cast new light on the composition and structure of the coma grains and therefore the nucleus itself. The images returned were the most detailed yet obtained of a nucleus (fig. 1.4 (c)), and showed considerable differences from 1P and 19P. 81P is seen to be less elongated, and has a surface covered in large crater like formations, demonstrating that there is significant diversity within the JFC population.

The most recent comet mission was *Deep Impact* at 9P/Tempel 1, which actually made contact with the nucleus, in spectacular fashion (A'Hearn et al. 2005). This mission was designed to probe the interior of a JFC nucleus by producing a fresh crater and studying the ejecta from it. This was achieved using a two part space-craft made up of a mother-ship with instruments to image the nucleus (fig. 1.4 (d)) and an impactor which collided with the nucleus. In addition, a very large ground based effort followed the effects of the impact – primarily an expanding ejecta cloud (Meech et al. 2005). The impactor also had its own camera, which in the seconds before the impact returned very high resolution images from exceptionally close range. Both craft returned images which contain interesting surface features, including flat areas with bright edges and what appear to be craters. The mission was able to make measurements of the mass and volume of the nucleus, leading to a density measurement of 0.4 g cm^{-3} (Richardson & Melosh 2006), and an implied highly porous internal structure.

The only comet mission currently funded and in flight is the *Rosetta* mission, which is on its way to 67P/Churyumov-Gerasimenko (Schwehm & Schulz 1998). This ESA mission will provide another major leap in the understanding of JFCs, as it will enter orbit around the nucleus and follow the comet as it enters the inner solar system and becomes active. The satellite will map the nucleus in detail and also land a probe on the surface, and carry out various experiments to investigate the internal structure.

1.6 Layout of this thesis

This thesis presents results from ground based time-series photometry on JFC nuclei. Chapter 2 describes the telescopes and instruments used in this work, and the data reduction procedures followed to obtain accurate calibrated photometry of the nuclei. The methods employed to gain such physical properties as size, shape and bulk density of the nuclei from this photometric data are described in chapter 3, while the results for individual comets are presented in chapters 4 and 5. The implications for the ensemble properties of the JFC population, such as size and spin rate distributions, and a comparison with the general properties of other minor bodies, are discussed in chapter 6. Finally, some interesting future directions for this work are suggested in chapter 7.

The reduction, analysis and interpretation of the data presented in this thesis is my own work. I performed the observations with the assistance of Prof. Alan Fitzsimmons or Dr. Stephen Lowry on three of the four runs, while the fourth data set was collected for me by Dr. Lowry (see table 2.1). In the reduction and analysis I used a variety of software; the most important were standard IRAF reduction and photometry routines, scripts I wrote to further automate the reduction using IRAF, and periodicity analysis software which I also wrote myself.

Chapter 2

Instrumentation and data reduction

The data on which this thesis is based were collected over five observing runs using three different telescopes, which are summarised in table 2.1. This chapter describes the telescopes and instruments used, the observing strategies followed and the conditions during each run. It then describes the techniques applied to calibrate this photometry and obtain reduced magnitudes and colours.

2.1 New Technology Telescope

The 3.58m New Technology Telescope (NTT) was used twice in observing comets for this thesis, between the 20th and 22nd of January 2004, and on the nights of the 5th to 7th March 2005. During the earlier run the first two nights were photometric and the third was lost entirely due to high humidity. Three comets were observed at distances of $4.5 \leq R_{\rm h} \leq 5.5$ AU: 7P/Pons-Winnecke, 14P/Wolf and 92P/Sanguin, and

Table 2.1: Summary of all observing runs on which this thesis is based.

Date	Telescope[a]	Nights[b]	Observers[c]	Summary
Jan 2004	NTT	3	CDBS & AF	2 photometric nights, 1 lost to high humidity, light-curves on 3 comets.
Mar 2005	NTT	3	CDBS & SCL	1.5 photometric nights, 1.5 lost to high humidity, light-curves on 4 comets, snap-shots on 4.
Jul 2005	INT	7×0.5	SCL	7 photometric half nights, light-curves on 3 comets and snap-shots on 7.
Feb/Mar 2006	INT	4	CDBS & AF	1 photometric night, 1 non-photometric, 2 lost to blizzard, light-curves on 2 comets, snap-shots on 12.
May 2006	FTN	1 hr	CDBS	Follow up on 1 comet, photometric.

[a]NTT - New Technology Telescope, La Silla (ESO), Chile; INT - Isaac Newton Telescope, Roque de Los Muchachos (ING), La Palma; FTN - Faulkes Telescope North, Haleakala, Hawaii

[b]Amount of time allocated, in nights unless stated

[c]CDBS - C.D.B. Snodgrass; AF - A. Fitzsimmons; SCL - S.C. Lowry

time-series CCD imaging was obtained for each. On the second run the latter half of the 1st night and the third night were lost to poor weather, but conditions were photometric during the remaining time. The comets targeted were at heliocentric distances between 3 and 7 AU; snap-shot observations were obtained on four comets (43P/Wolf-Harrington, 44P/Reinmuth 2, 103P/Hartley 2 and 104P/Kowal 2) and time-series data was acquired on another four (17P/Holmes, 36P/Whipple, 47P/Ashbrook-Jackson and 137P/Shoemaker-Levy 2).

The NTT is an altitude-azimuth telescope of Richey-Chretien design, originally built to test novel technologies including active optics and the characteristic angular enclosure for the Very Large Telescope (VLT). It is situated at the European Southern Observatory (ESO)'s La Silla site on the southern edge of the Atacama desert in Chile. The NTT has instruments mounted at both of its f/11 Naysmith foci. The data presented in this thesis was obtained by CCD imaging performed using the red arm of EMMI (ESO Multi-Mode Instrument). The EMMI red arm contains a mosaic of 2 MIT/LL 2048×4096 CCDs, and was used in 2×2 binning mode to give a pixel scale of 0.332 arcsec per pixel. The effective field of view is 9.1×9.9 arcmin^2. The images were taken primarily through the Bessell *R* band filter, with at least one set of images taken through the Bessell *V* and *I* filters each night for each comet to allow measurement of colour indices.

All images were taken with the telescope tracking at the sidereal rate, with exposure times chosen so that the apparent motion of the comet would be less than 0.5″, and would thus remain within the seeing disk. This allowed accurate measurement of the stellar-background point spread function (PSF), and highly accurate differential photometry. The $FWHM$ of the stellar-background PSF was typically $\sim 1''$ in all NTT data. The *VRI*-filter exposure times therefore varied between comets, depending on their apparent motion on the sky, but were of order 100 seconds (see table 4.1 for a full log of observations). Each comet was observed in blocks of exposures lasting $\sim$ 20 minutes, cycling between each of the comets that were visible at any given point in

the night. This procedure gave good temporal coverage without losing too much time slewing the telescope between targets.

The EMMI red arm camera reads out through four individual amplifiers (two per CCD chip) to improve read out times. At the time of the first run (January 2004) the telescope pipeline software stored the data in a multi-extensions fits-format file with 4 extensions, one per amplifier. The telescope pointing centre falls to the left of the centre of CCD 1. The telescope was positioned to keep the comets and the comparison field stars on this half of the chip throughout the run to minimise the reduction workload; the appropriate extension of the original .fits file was copied into a single extension file before processing. By the time of the second NTT run (March 2005) the ESO software produced only dual extension files (*i.e.* 1 extension per chip).

The reduction was performed using standard IRAF tasks (Tody 1986, 1993). Bias-subtraction was performed utilising the prescan strip of CCD 1. Twilight sky exposures were acquired during the evening and morning, and these were combined to produce a flat-field image for each filter for each night. Comparison of evening and morning flats revealed a slight change in illumination of the focal plane, giving a variation of $\sim 1\%$ in the overall field illumination from one side of the image to the other. This effect had been noted (Hainaut 2003) in images taken with the SuSI (Superb Seeing Imager) instrument, which is mounted at the opposite Naysmith focus to EMMI, and was attributed to scattered light from the Naysmith mirror baffle, which varies with rotator angle. As this is due to the telescope and not the instrument, I assume that this is also the cause of the illumination differences in the EMMI images. It was found that averaging both morning and evening flats for each filter cancelled this effect out, as the rotator angle was $\sim 180^{\circ}$ different between morning and evening. With prior knowledge of this issue on the second run, it was countered by taking sets of flats at a number of opposing rotator angles, which when averaged corrected the problem. Note that this problem is due to scattered off-axis light from the bright twilight sky; it does not affect the astronomical data as the scattered light is entirely negligible once the sky

is dark.

2.2 Isaac Newton Telescope

The 2.5m Isaac Newton Telescope (INT) [part of the Isaac Newton Group (ING) of telescopes at the Roque de Los Muchachos observatory on the island of La Palma] was also used on two occasions to obtain light-curves of cometary nuclei. The first was in July 2005, on seven nights (July 1st - 7th) around the time of the *Deep Impact* mission's encounter with 9P/Tempel 1. The telescope was being used to follow the evolution of the dust coma and tails of this comet before and after the impact (Lowry et al. 2005), but was available during the later half of each night after 9P had set. All seven nights were photometric; time-series data was collected on three comets [40P/Vaisala 1, 94P/Russell 4 and P/2004 H2 (Larsen)] and snap-shot observations were made of 7 others. The telescope was used again between the 27th of February and the 2nd of March 2006, during which the first two nights were lost due to severe winter weather. The third night was clear but non-photometric, while the 4th was photometric with periods of excellent seeing (the $FWHM$ of the image PSF varied between 0.8 and $2.7''$, with a median of $1.1''$). Time series observations of comets 36P/Whipple and 121P/Shoemaker-Holt 2 were obtained, and snap-shots were taken of 12 other objects.

The imager on the INT is the Wide Field Camera (WFC) which is mounted at the primary focus. The WFC is a mosaic of four thinned EEV 2048×4096 pixel CCDs, which has a pixel scale of $0.33''$ per pixel and a total field of view of $34'$ on a side. The wide field nature of the camera is not necessary to this work, and as with the NTT only one element of the multi-extension fits file is used to minimise the reduction workload. In the 2006 data this mostly corresponds to the central CCD 4, while the comets were centred on CCD 3 in the 2005 data as the telescope pointing had been offset to make use of the full width of the WFC mosaic in observing 9P's tails. Even the single CCD has a field of view of 11.5×23 arcmin^2, which gives the advantage

of having a constant set of comparison stars over two nights for all but the fastest moving comets, allowing light-curves to be fully differential with no uncertainties from night to night calibration (see section 2.4). Also, by a fortuitous coincidence, comets 44P/Reinmuth 2 and 47P/Ashbrook-Jackson were close together on the sky during the February/March 2006 run, and the wide field of the WFC allowed both to be observed simultaneously giving 'two for the price of one'. 44P fell on CCD 1 and 47P fell on CCD 2.

The same observing strategy was followed as for the NTT observations, cycling between targets with ∼20 minute blocks of observations, with exposure times chosen to keep the comet motion below $0.5''$. For the third night of the February/March 2006 run (the first night of actual observations) the seeing was poor (median PSF $FWHM \approx 2''$), so exposure times were doubled, keeping the motion at $1''$, while increasing the signal-to-noise (S/N) to counter the decrease due to the poor seeing. Again occasional V- and i'-band frames were taken between r'-band frames to measure the comet colours; the filters used were the Harris V and Sloan r' and i'. The Sloan filters have the advantage of having sharp cut-on and -offs with little overlap in sensitivity at wavelengths between the bands, although further reduction steps are required as the i'-band has significant fringing which had to be subtracted from the data manually for each frame, as pipelines or automated routines failed to measure the fringe brightness correctly. The basic reduction was carried out using IRAF routines in the same way as for the NTT data for the 2006 run, with the pre-scan region of the appropriate CCD used for bias subtraction and twilight sky flats used for flat fielding. It was only possible to obtain twilight flats on the 4th night, when both morning and evening flats were taken, so the average night 4 flat field was used for both nights. The 2005 data was reduced (along with the 9P data taken during the run) using the Wide Field Survey (WFS) pipeline[1]; inspection of data from each run showed that both reduction methods gave equally good results.

[1] `http://www.ast.cam.ac.uk/~wfcsur/`

2.3 Faulkes Telescope North

The Faulkes Telescope project consists of two identical 2.0m robotic telescopes, of Alt-Az design, the North (FTN) on the mountain of Haleakala on Maui, Hawaii, and the South (FTS) at Siding Springs, Australia. The telescopes can be operated in two different modes; fully robotic off-line mode, or under direct control of observers in remote on-line mode. The Faulkes Telescope Project primarily exists to provide access to large telescopes for schools use, who use the on-line interface to control the telescopes in real time, but it is also used by a number of research groups who take advantage of the robotic nature of the telescopes for either automated surveys (*e.g.* microlensing searches for extrasolar planets[2]), fast response (*e.g.* Gamma Ray Burst follow up), or flexible scheduling of regular short observing sessions (*e.g.* Near Earth Asteroid tracking[3]).

I used approximately 1 hour of time on the 31st of May 2006 to perform follow up observations on comet 121P/Shoemaker-Holt 2, which INT observations had shown to be brighter than expected and showing evidence of having only recently ceased out-gassing (see chapter 5), to search for any sign of continuing activity. The comet was imaged in the Bessell *R*-band using the DillCam CCD imager, which has a single 2048×2048 pixel CCD with a pixel scale of 0.278 arcsec per pixel in the default 2×2 binning mode, giving a 4.6×4.6 arcmin^2 field of view. Frames were also taken of the comet through the Bessell *V*-band, and of standard stars through both bands, to allow for photometric calibration. The comet appeared fainter than expected, although subsequent calibration showed that the comet magnitude matched the predicted value, and that the low S/N ratio in individual images was due to a loss of sensitivity. This appears to be due to deterioration of the telescope mirror surface; analysis of standard star calibrations performed by the United Kingdom Astrometry and Photometry Programme (UKAPP) showed a continuing decrease in the FTN *R*-band zero-point over ∼

[2] `http://star-www.st-and.ac.uk/~kdh1/ustaps.html`
[3] `http://star.pst.qub.ac.uk/~ukapp/index.html`

18 months (Fitzsimmons, private communication 2006). While the ease of scheduling short periods of time for such 'quick look' follow up observations is a major advantage of the robotic FTN, this loss of sensitivity beyond $m_R \approx 20$ meant that the usefulness of the FTN data to search for continuing faint activity around 121P was limited, and this telescope was not used for other faint comets.

2.4 Photometry

Photometry was performed on the comets using custom written semi-automated routines which measure the brightness of the comet and a number of comparison stars in each frame to give a differential light-curve, obtain calibrated magnitudes and colours, and perform some of the activity level analysis that is described in the next chapter. Here I describe the methods by which these routines determine accurate photometry.

Differential photometry provides a precise measurement of how the brightness of the comet varies with time by comparing it to the brightness of nearby field stars, which can be assumed to have constant intrinsic brightness. This assumption is checked by plotting the brightness of each comparison star against time, and rejecting any which are seen to vary relative to the others. The difference in brightness between the stars and the comet will then only be affected by intrinsic variations in the light from the comet, as all other effects (such as variable absorption by thin clouds) should affect both the stars and comet equally and therefore cancel out.

The routines first use the two IRAF packages DIGIPHOT and APPHOT (Davis 1999) to perform photometry within circular apertures centred on the comet position and on the stars. The aperture radii were set equal to the $FWHM$ of the stellar PSF, which has previously been found to be the optimum for maximising S/N (Howell 1989). Choosing aperture radii as a function of stellar PSF also counters the problem of variations in measured brightness with changing seeing, which is encountered when using small fixed apertures (Licandro et al. 2000a). In addition, photometry of the field

stars used to measure the differential magnitudes, and of standard stars from the Landolt (1992) catalogue, was performed using an aperture of diameter $10''$. The smaller aperture was used for differential photometry between the comets and field stars, while the larger diameter was used for photometric calibration and was that used by Landolt.

The calibrated magnitude of an object in a given waveband m_λ is related to its instrumental magnitude m'_λ by the following equations, for the $\lambda = V, R, I$ bands used to study the comets:

$$m_V = m'_V - ZP_V - k_V X_V - k'_V(V-R) \quad (2.1)$$

$$m_R = m'_R - ZP_R - k_R X_R - k'_R(V-R) \quad (2.2)$$

$$m_I = m'_I - ZP_I - k_I X_I - k'_I(R-I) \quad (2.3)$$

where ZP is the zero point, k is the extinction, X is the airmass, k' is the colour term and $(V-R)$ and $(R-I)$ are the object colours [the differences between m_λ in the V and R bands, and the R and I bands respectively]. Using the IRAF package PHOTCAL, Landolt's tables of m_V and colours and the measured m'_λ for the same standard stars, these equations were solved to give the zero-point, extinction coefficient[4] and colour term for each filter for each photometric night (these are listed in table 2.2). For a given instrument and filter combination k' should be constant; inspection of table 2.2 shows that the measured values for each telescope were constant within the uncertainties on each. These calibration constants were then used to calculate the magnitudes of the field stars in each frame; taking the mean of these values gave a very accurate measurement of the brightness of the comparison stars, $\overline{m_R(s)} \pm \sigma_R(s)$. Adding this value to each of the differential comet magnitudes gave accurate calibrated comet magnitudes. As the magnitude of the stars should not vary over the course of the night, the error $\sigma_R(s)$ is simply the standard deviation on this average. This is normally small compared with

[4]Both the 2004 NTT and 2005 INT runs had relatively few standard star observations, so the extinction coefficient was measured using bright field stars which were observed at a range of airmasses. Using this value for k and the limited standard star observations allowed the equations to be solved for ZP and k'.

the formal errors on each magnitude, which include uncertainties in the values of ZP_R, k_R and k'_R; this method reduces the formal uncertainty on the comet photometry by including all calibration uncertainty within $\sigma_R(s)$ instead of direct calibration of each point, which would have to include the errors on each term.

There is also a colour term involved in the transformation from differential to calibrated magnitudes, due to the difference in colour between the stars and the comet. The full calibrated comet magnitude is given by

$$m_R(c) = \left[m'_R(c) - m'_R(s)\right] + \overline{m_R(s)} + k'_R\delta(V-R) \tag{2.4}$$

where the term in brackets is the differential instrumental magnitude, and $\delta(V-R)$ is the difference in $(V-R)$ colour between the star and the comet. When k'_R is low (as with the NTT observations with $|k'_R| \lesssim 0.06$ during both runs) and the comparison stars and the comet have similar colours, the final term is negligible. Care was taken to select comparison stars with colours in the range expected for cometary nuclei to minimise any uncertainties in this colour term, although experimentation found this method of obtaining calibrated photometry to be robust and independent of which comparison stars were chosen. In the INT data, with Sloan r' and i' filters, the colour terms are significant for even slight differences between star and comet colours. As can be seen, the dependance on the comet colour in the calibrated magnitude causes the determination of both the magnitude and the colours to be an iterative process. A direct calibration of the comet photometry was used to provide a first estimate of its colour (with large error bars), and therefore calibrated magnitudes and from those a revised $(V-R)$ colour. This method typically found a stable solution within three or four iterations.

For most of the comets which were only observed in snap-shots, only R- or r'-band frames were taken. In these cases the colours of the stars and of the comet were unknown, and the colour contribution to m_R could not be calculated. For those comets which were bright and had short sequences of observations, the above calibration method was used, and it was assumed that the star and comet colours were close

enough to give $\delta(V-R)=0$. As most stars in any given field were likely to be late type main sequence stars (Christian et al. 2006) their colours would generally be close to Solar, and therefore similar to typical nuclei colours, this assumption is justified. This was also found to be the case observationally in those fields that were observed through multiple filters. For some snap-shot comets there were either few frames, or a combination of all frames was required to detect the comet, in which case the brightness of the comet was measured in the combined frame and calibrated directly using equation 2.2 and assuming a typical nuclear colour of $(V-R)$ = 0.45 (see chapter 6). Although these assumptions obviously introduce some uncertainty into the value of m_R measured in snap-shots, these were generally short observations of faint nuclei, and this uncertainty does not contribute significantly to the total error bars on the photometry.

During the INT run in February/March 2006 the 3rd night was non-photometric; inspection of the instrumental magnitudes of bright stars showed some variation due to thin cloud. However, as stated above the wide field of view of the WFC meant that the target comets were in approximately the same star field on the 4th night, which was photometric, so differential magnitudes from the 3rd night were simply calibrated from the colours and magnitudes of the stars on the 4th.

It is important to note that while the calibration onto standard magnitude scales is necessary for comets in different star fields, and to allow calculation of absolute magnitudes and colours for the objects, searching for periodicity can be done just as well using differential light-curves. Where possible the differential light-curve is preferred as it contains no sources of error beyond the photometric measurement uncertainties, allowing optimum measurement of the relative variation of brightness with time. The next chapter describes the techniques used to derive physical properties of cometary nuclei from this photometry.

Table 2.2: The calibration constants (Zero-point *ZP*, extinction *k* and colour term k') for each photometric night.

Date	'scope	Filt.[a]	ZP[b]	k	k'
20/01/2004	NTT	V	-0.940 ± 0.032	0.137 ± 0.019	-0.003 ± 0.026
		R	-1.052 ± 0.010	0.091 ± 0.001	-0.024 ± 0.020
		I	-0.616 ± 0.044	0.049 ± 0.025	0.060 ± 0.042
21/01/2004	NTT	V	-0.936 ± 0.066	0.144 ± 0.039	0.013 ± 0.039
		R	-1.047 ± 0.027	0.071 ± 0.003	0.061 ± 0.047
		I	-0.616 ± 0.044	0.023 ± 0.040	0.219 ± 0.135
05/03/2005	NTT	V	-0.929 ± 0.022	0.158 ± 0.012	-0.029 ± 0.019
		R	-1.042 ± 0.031	0.098 ± 0.016	-0.059 ± 0.024
		I	-0.601 ± 0.037	0.064 ± 0.019	-0.056 ± 0.027
06/03/2005	NTT	V	-0.917 ± 0.015	0.150 ± 0.011	-0.062 ± 0.013
		R	-1.024 ± 0.015	0.075 ± 0.010	-0.061 ± 0.009
		I	-0.587 ± 0.014	0.057 ± 0.009	-0.059 ± 0.010
01/07/2005	INT	V	0.202 ± 0.026	0.147 ± 0.018	0.007 ± 0.011
		r'	0.314 ± 0.040	0.083 ± 0.022	0.295 ± 0.042
		i'	0.897 ± 0.024	0.027 ± 0.014	0.232 ± 0.028
02/07/2005	INT	V	0.251 ± 0.028	0.146 ± 0.005	-0.008 ± 0.065
		r'	0.332 ± 0.008	0.106 ± 0.004	0.404 ± 0.030
		i'	1.030 ± 0.068	0.059 ± 0.003	0.259 ± 0.249
03/07/2005	INT	V	0.206 ± 0.011	0.156 ± 0.005	-0.004 ± 0.025
		r'	0.259 ± 0.011	0.132 ± 0.005	0.284 ± 0.037
		i'	0.987 ± 0.007	0.076 ± 0.004	0.178 ± 0.021
04/07/2005	INT	V	0.260 ± 0.012	0.145 ± 0.007	-0.083 ± 0.028
		r'	0.326 ± 0.005	0.099 ± 0.005	0.247 ± 0.016
		i'	1.017 ± 0.007	0.046 ± 0.005	0.207 ± 0.019
05/07/2005	INT	V	0.239 ± 0.008	0.143 ± 0.006	0.001 ± 0.020
		r'	0.295 ± 0.004	0.132 ± 0.005	0.259 ± 0.011
		i'	0.987 ± 0.007	0.083 ± 0.005	0.264 ± 0.019
06/07/2005	INT	V	0.214 ± 0.011	0.127 ± 0.005	0.063 ± 0.022
		r'	0.305 ± 0.005	0.094 ± 0.003	0.300 ± 0.018
		i'	1.053 ± 0.042	0.025 ± 0.003	0.143 ± 0.131
07/07/2005	INT	V	0.245 ± 0.008	0.125 ± 0.005	-0.024 ± 0.017
		r'	0.308 ± 0.024	0.094 ± 0.004	0.218 ± 0.074
		i'	0.984 ± 0.014	0.067 ± 0.003	0.192 ± 0.046
02/03/2006	INT	V	0.113 ± 0.056	0.210 ± 0.041	-0.038 ± 0.030
		r'	0.262 ± 0.020	0.114 ± 0.015	0.244 ± 0.013
		i'	0.868 ± 0.026	0.093 ± 0.019	0.187 ± 0.019
31/05/2006	FTN	V	1.736 ± 0.017	0.119 ± 0.012	0.069 ± 0.009
		R	1.837 ± 0.052	0.086 ± 0.040	0.093 ± 0.031

[a]The filters used varied; the terms given convert instrumental magntiudes through the given filter onto the standard Landolt *VRI* system.

[b]Zero points are relative to the default IRAF *ZP* of 25, which is included in the instrumental magnitudes.

Chapter 3

Methodology

This chapter gives detailed descriptions of the methods used to obtain such physical parameters as size, shape and spin rate of nuclei from photometric data. I also describe how the level of any faint activity is quantified, and discuss how the shape and spin rate can be used to constrain the internal structure of the nuclei by inferring properties such as bulk density and porosity.

3.1 Deep imaging search for activity

The first issue that must be considered when observing supposedly inactive nuclei at large heliocentric distance is to confirm that they are indeed inactive. To do this very deep images of the comet are produced, in which any faint coma will be visible. A further check is then carried out by plotting a surface brightness profile, as even apparently inactive comets can have unresolved residual coma.

A combined image is produced by first combining all *R*-band images to calculate the median image for the data, giving a deep image of the background star field without the comet or cosmic rays. For slow moving comets it is frequently necessary to produce this background image using only alternate frames or less, to ensure that the comet has moved sufficiently to be entirely removed from it. A scaled version of this image is then subtracted from each individual *R*-band frame, removing fixed objects and the background sky. Each subtracted frame is then shifted to centre on the comet, and these are combined using a median filter to remove cosmic rays and leave only the comet.

The brightness profile of the comet measured in this combined image is compared with the point spread function (PSF) of the image to search for any unresolved activity. A completely inactive comet nucleus, with a radius of a few km at distances of a number of AU, will be unresolved even using the largest telescopes, and therefore should appear as a point source and the profile will match the image PSF entirely. The image PSF is obtained from the profile of a bright star measured in the deep star field (background) image. The stars in each individual frame give a measurement of the PSF

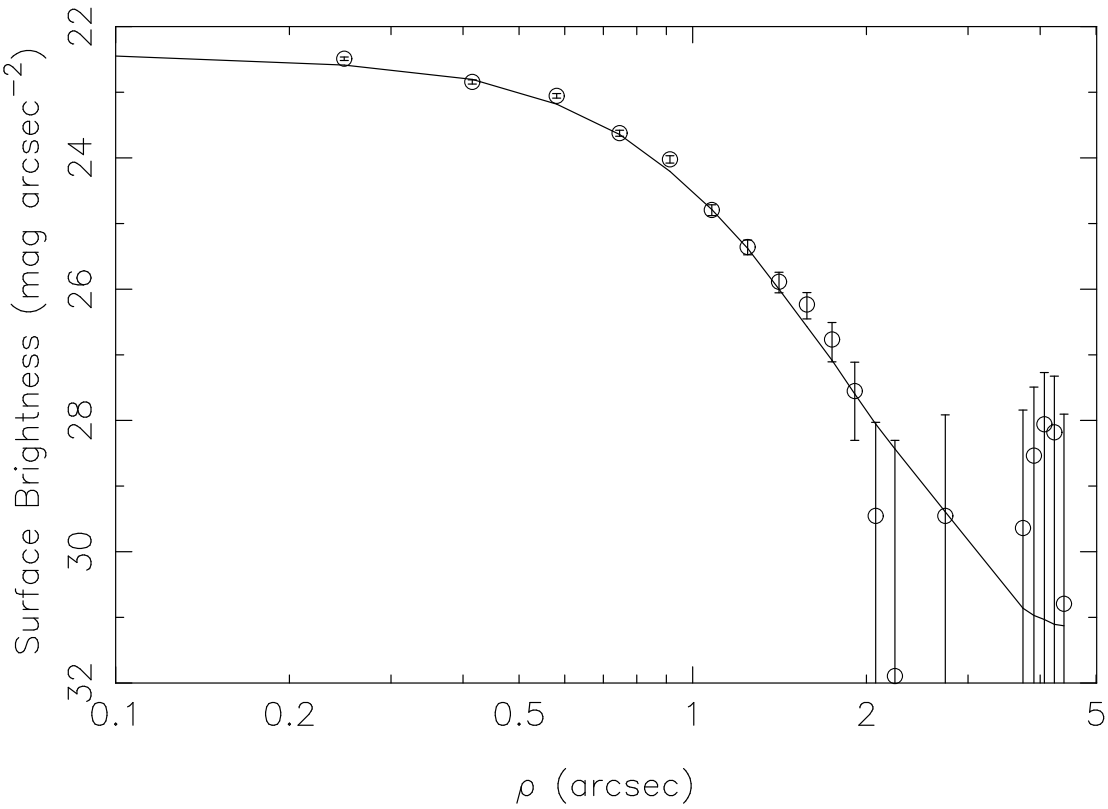

Figure 3.1: Surface brightness profile (SBP) of 7P/Pons-Winnecke, as an example: Here the surface brightness in mag. arcsec^{-2} is plotted as a function of radius ρ from the centre of the comet in arcsec. The profile is indistinguishable from the scaled stellar PSF (the solid line), implying that the comet is a point-source, and therefore inactive. At a surface brightness of $\Sigma \approx 30$ the flux is only a few counts per arcsec^2, even in combined images giving long exposures with 2-4m class telescopes.

at that time; by measuring the PSF in the combined image all seeing variations and any errors associated with shifting the images to a common centre are included. Theoretically, any remaining difference between the comet and the stellar PSF is therefore due to the comet being a non-point source (*i.e.* showing faint activity), although in practice there is often a slight broadening of the comet profile due to errors in shifting of frames to comet centred co-ordinates. This is minimised by using the measured comet centre to calculate the shifts between images for long sequences, instead of the predicted motion from ephemerides, as the motion of the comet on the sky is likely to be non-linear over the course of a night. The example shown in fig. 3.1 (of 7P/Pons-Winnecke) is indistinguishable from the scaled stellar profile, and therefore the PSF, and means that this comet was effectively inactive at the time of observation.

To put quantitative limits on any unresolved coma, I measure the surface brightness Σ_c at a large distance ρ (arcsec) from the centre of the comet image. I set $\rho = 5''$ as at this radius any coma present should dominate the observed flux. The measured $FWHM$ of the combined comet image is typically $\sim 1''$, given the seeing conditions at the time of the observations (see chapter 2). The integrated coma magnitude m_c measured within this aperture can be compared with the calibrated total magnitude m_R, as an aperture of $\rho = 5''$ is to calibrate the field stars, therefore including an implicit aperture correction in the comet magnitude. For a steady state coma, the surface brightness is inversely proportional to ρ, and m_c is given by (Jewitt & Danielson 1984):

$$m_c(\rho) = \Sigma_c(\rho) - 2.5\log(2\pi\rho^2). \tag{3.1}$$

The fraction of the flux f which could then be due to any unresolved coma can then be limited to being $f \leq 10^{0.4(m_R - m_c)}$. When this is less than $\sim 10\%$ the nucleus can be assumed to be effectively inactive, as any coma can only contribute at a level below the typical errors on the comet photometry in individual frames.

3.2 Absolute magnitude and nucleus size

The observed magnitude of a cometary nucleus is given by

$$m_R = m_R(1,1,0) + 5\log(R_{\rm h}\Delta) + \beta\alpha, \tag{3.2}$$

where $m_R(1,1,0)$ is the 'absolute' magnitude of the nucleus as it would be measured at a hypothetical point with heliocentric ($R_{\rm h}$) and geocentric (Δ) distances of 1 AU and a phase angle $\alpha = 0^\circ$. For well studied asteroids, the phase function is described using the H-G system, which includes the 'opposition surge' that causes an increase in brightness at low phase angles ($\alpha \leq 2^\circ$) and a non-linear response at large α. Such phase functions take a large number of observations over a full range of phase angles, and such data

simply do not exist for cometary nuclei. It is therefore necessary to assume the simple model of a linear phase function, which is justified as none of the observations are at very large phase angle and few are at very low phase angle, so the nuclei were generally in the linear phase function regime. With observations over short time-frames (typically only two nights in each run) at approximately constant α, the phase coefficient β cannot be independently measured. I therefore take the commonly assumed value of $\beta = 0.035$ mag. deg^{-1} (Lowry & Fitzsimmons 2001). For most of the comets studied the variation in the last two terms was found to be negligible over the observing run; for example for 7P the difference in m_R due to these terms between the first and last frame was found to be $\delta m_R = 0.008$ mag, considerably smaller than the uncertainty on the individual measurements. As the conversion to absolute magnitudes is therefore unnecessary, I use apparent magnitudes to produce a light curve. The exceptions are those comets which were observed over 4–7 nights during the July 2005 INT run, which had $\delta m \approx 0.04$ mag, and were consequently reduced to absolute magnitudes.

The average radius of the nucleus $r_{\rm N}$ (m) is given by (Russell 1916)

$$p_R r_{\rm N}^2 = 2.238 \times 10^{22} R_h^2 \Delta^2 10^{0.4(m_\odot - m_R + \beta\alpha)} \tag{3.3}$$

or, in terms of the absolute magnitude,

$$p_R r_{\rm N}^2 = 2.238 \times 10^{22} 10^{0.4(m_\odot - m_R(1,1,0))} \tag{3.4}$$

where p_R is the geometric albedo and $m_\odot = -27.09$ is the apparent magnitude of the Sun[1], both in the *R*-band. The other terms are as defined above.

The geometric albedo is defined as the amount of light reflected by a surface at zero phase angle compared with a 'perfect' reflecting surface at a given wavelength. It can be measured for resolved objects as the disk integrated brightness and the true surface area of the disk can be measured, but this applies only to those comets which have been

[1]From the Solar $m_V = -26.74$ and $(V-R)_\odot = 0.35$ (Holmberg et al. 2006)

visited by space-craft. The albedo can be measured from Earth by measuring the brightness of the nuclei at both visual and thermal (infrared) wavelengths simultaneously and by balancing the incoming and outgoing energy (Lebofsky & Spencer 1989):

$$\frac{\pi r_{\mathrm{N}}^2(1-A)S_0}{R_{\mathrm{h}}^2} = \eta\varepsilon\sigma r_{\mathrm{N}}^2 \int_{-\frac{\pi}{2}}^{\frac{\pi}{2}} \int_{-\frac{\pi}{2}}^{\frac{\pi}{2}} T^4(\theta,\psi)\cos\theta \mathrm{d}\psi \mathrm{d}\theta \tag{3.5}$$

where S_0 is the solar flux at 1 AU, ε is the thermal emissivity, η is the beaming parameter, which scales the thermal emission to account for its angular distribution, and T is the temperature of a point [latitude and longitude (θ, ψ), where (0,0) is the sub-solar point] on the surface of the nucleus. A is the Bond albedo, which is the product of the geometric albedo and the phase integral q, which is given by

$$q = 2\int \Phi(\alpha)\sin\alpha \mathrm{d}\alpha. \tag{3.6}$$

where $\Phi(\alpha)$ is the phase function. Strictly, A in equation 3.5 is the bolometric Bond albedo (*i.e.* the Bond albedo integrated over all wavelengths) however for fairly grey bodies such as most Solar System minor bodies the albedo varies little with wavelength and $p_R \approx p_V \approx p_{\mathrm{bol}}$. Nuclei are not grey but slightly red, with a spectral gradient of ~ 10 % per 1000 Å. However this gives a variation in reflectance over the whole visual range that is less than the uncertainty on the few measured albedo values, and consequently the albedo is generally assumed to be approximately constant with wavelength for the purposes of measuring radii.

The critical modelled parameter is the temperature map $T(\theta,\psi)$. There are two common models to describe the thermal state of the nucleus; the Standard Thermal Model (STM) and the Isothermal Latitude Model (ILM). STM describes a body which is not rotating, and therefore temperature is at a maximum at the sub-solar point and decreases with distance from it over the sunlit hemisphere, with $T = 0$ over the permanently dark side. ILM describes a fast-rotating body (or one with high thermal inertia) in which there is no change in temperature between the day and night sides and the tem-

perature depends on distance from the equator. Results from the *Deep Impact* mission show that the STM gives an excellent description of the nucleus of 9P; it is rotating, so this implies that it has very low thermal inertia (A'Hearn et al. 2005).

The geometric albedo of cometary nuclei has previously been found to be very low (Lamy et al. 2004), with a mean value around $p_R = 0.04$. This value is used for the comets studied in this thesis, for which the albedos have not been measured. The uncertainties on the nuclear radii given in this thesis are based purely on the uncertainty in the photometry, and do not take into account any uncertainties in the values of either p_R or β, which at $\sim 50\%$ (Lamy et al. 2004) entirely dominate the size measurement in the case of precise photometry.

3.3 Period finding

I use a version of the method of Lomb (1976) to search for periodicities in the brightness variations of the comet. I fit a first-order Fourier model:

$$m_R(t) = C + A\cos\omega t + B\sin\omega t \tag{3.7}$$

to the data for a range of frequencies ω, finding the optimum coefficients A, B and C for each and calculating the reduced χ^2 for each to produce a periodogram (fig. 3.2 shows the periodogram for 14P/Wolf as an example). The reduced χ^2 is χ^2/ν, where ν is the number of degrees of freedom of the model, given by $\nu = (N-3)$ where N is the number of data points, and χ^2 is the usual badness-of-fit parameter:

$$\chi^2 = \sum_{i=1}^{N} \left(\frac{X_i - \mu_i}{\sigma_i} \right)^2 \tag{3.8}$$

This compares each data point X_i to the model value μ_i at that point, where σ_i is the error on each X_i. A good fit to the data, where the scatter of residuals is a gaussian with 1σ variance, gives $\chi^2/\nu = 1 \pm \sqrt{2/\nu}$. Larger values of χ^2/ν imply that the model is less

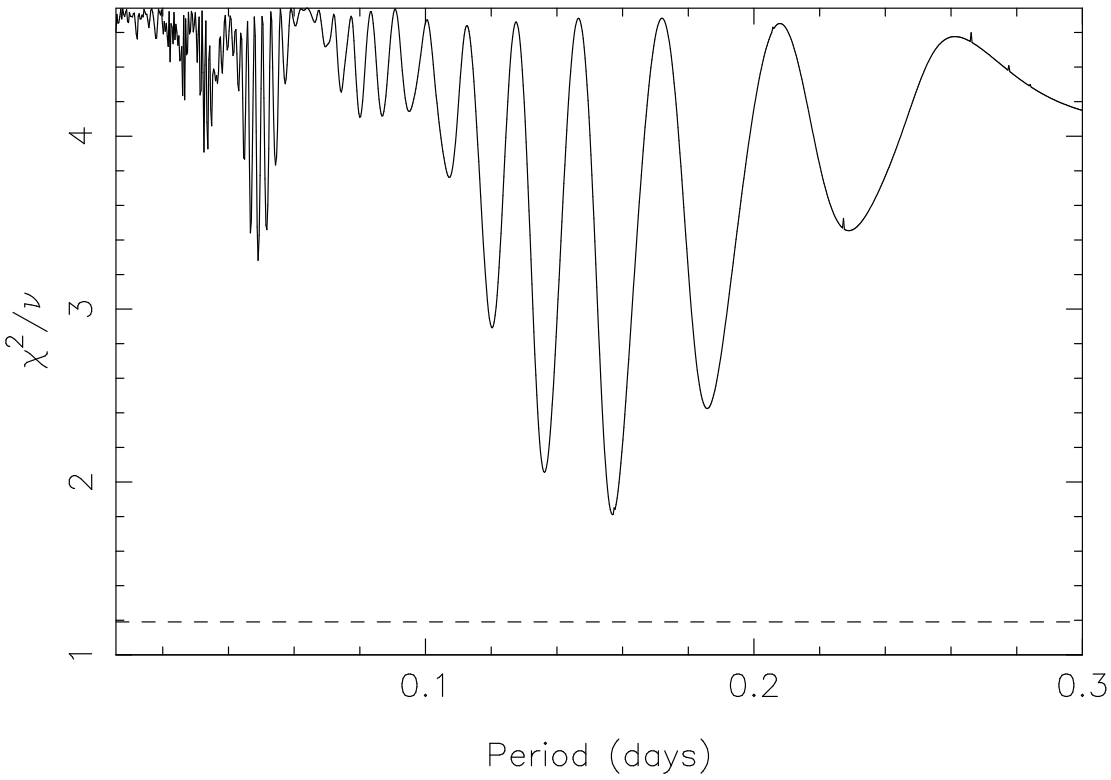

Figure 3.2: Periodogram showing reduced χ^2 against period. The horizontal line shows the expected value of χ^2/ν for 1σ residuals. The example here is for 14P/Wolf.

than optimal, while lower values imply that the error bars have been over-estimated.

Assuming that the variation in brightness is due to the nucleus being a rotating non-spherical body, the rotation period $P_{\rm rot}$ is twice the fitted period $P_{\rm fitted}$. This produces the expected double peaked light-curve. The shape of some of the light-curves presented in chapter 5 (*e.g.* 14P/Wolf) suggest that a higher order fit, with two minima of different depths, may give a better model to the data. This would suggest a departure from a simple tri-axial ellipsoid, as this sort of light-curve would be produced by a rotating body with, for example, a pear-like shape. To look for higher order fits, and evaluate the more complex shape models that would reproduce them, requires a very well sampled light-curve. This has been done for a number of asteroids (Kaasalainen et al. 2002) which are bright and have short rotation periods, lending themselves to precise high cadence time-series photometry with dedicated observations using smaller aperture telescopes. The data presented in this thesis was obtained with the aim of measuring the rotation periods of a large number of comets, therefore the observations cycled over a number of

targets and do not provide the complete phase coverage required for such an analysis. Higher order variations in the comet data were investigated by fitting a more general model

$$m_R(t) = C + \sum_{l=1}^{M} A_l \cos l\omega t + B_l \sin l\omega t \tag{3.9}$$

but this generally did not produce an improved χ^2/ν for M = 2 or higher orders. With relatively sparse data it would have been difficult to justify a choice of a higher order fit without a significant improvement in reduced χ^2. This more general model has $\nu = N - (2M+1)$, taking into account the inclusion of more model parameters. For $M = 1$ this reduces to the simple first order equation.

I also test the null hypothesis that there is no periodic variation by fitting a $M = 0$ constant brightness model, and compare the reduced χ^2 with the best fit periodic models. This also gives a good measurement of the mean magnitude for calculating the radius of the equivalent spherical nucleus, which is the r_N quoted in the presented results. However nearly all of the comets studied with time-series photometry had significant variation; the null hypothesis was formally rejected and the nuclei were found to be rotating elongated bodies, for which the effective radius is only an approximation.

3.4 Nucleus shape and density

3.4.1 Elongation

I assume that the brightness variations are due to the changing observed cross-section of a rotating elongated nucleus. This is a fair assumption, as those nuclei which have resolved images observed during comet fly-bys by spacecraft have been observed to be non-spherical (see section 1.5 of chapter 1). However, there is another plausible explanation for periodic photometric variation; that instead of changing cross-section of a non-spherical nucleus the brightness variations are caused by albedo variations across the surface of a spherical body (for example, a bright spot on one side of the

nucleus). This provides one motivation for performing multi-colour observations of the nuclei, as the broad-band colour variations with rotation would imply changes in the hemispherically averaged surface properties of the nucleus, and therefore likely albedo variations. The colours measured at different phases were consistent for each of the comets presented in this thesis, supporting the assumption that the brightness variations observed were shape induced.

I model the nucleus as the simplest non-spherical shape, a tri-axial ellipsoid with semi-axes a, b and c where $a > b$ and $b = c$. The axial-ratio a/b is related to the peak-to-trough range in magnitude Δm by

$$\frac{a}{b} \geq 10^{0.4\Delta m}, \tag{3.10}$$

following the usual method of converting a difference in magnitudes into ratio of fluxes. As the reflected flux is directly proportional to the area, this gives the axial-ratio, as the maximum cross-sectional area of such an ellipsoid (πab) divided by the minimum area (πb^2) gives a/b. This gives a lower limit on a/b as it is only the axial-ratio projected onto the plane of the sky, and the orientation of the rotation axis is unknown. The axial-ratio gives only a very simplified description of shape; it does not contain enough information to adequately describe an irregularly shaped nucleus.

The mean radius of the equivalent spherical nucleus and the minimum axial-ratio can be taken together to give dimensions for the ellipsoidal nucleus. The measured $r_{\rm N}$ is taken from the mean magnitude, *i.e.* the magnitude half way between the minimum and maximum, and corresponds to the flux reflected by a cross-sectional area half way between the maximum and minimum areas above, given by

$$\pi\left(b^2 + \frac{ab - b^2}{2}\right) \tag{3.11}$$

Substituting in $a = \frac{a}{b}.b$, simplifying, and setting this equal to the cross-sectional area

of the equivalent sphere gives:

$$\pi b^2 \left[\tfrac{1}{2}\left(1+\tfrac{a}{b}\right)\right] = \pi r_{\rm N}^2 \tag{3.12}$$

$$\therefore \quad b = r_{\rm N}/\sqrt{\tfrac{1}{2}\left(1+\tfrac{a}{b}\right)} \tag{3.13}$$

and a is found using the above substitution. Again these are only limits on the true dimensions as the projected axial-ratio gives only the minimum true axial-ratio, and the shape of the nucleus is likely to be more complex than a simple ellipsoid.

Figure 3.3 shows the rotation periods and projected axial-ratios for all JFCs published by other investigators that have reliable measurements of these properties. It also shows the limits on bulk density that can be found using a/b and $P_{\rm rot}$ (see next section).

The fastest rotating comet in fig. 3.3 is 133P/Elst-Pizarro. This object is thought to be an asteroid-comet transition object; it was first found and numbered as asteroid 7968, and has an asteroid-like orbit, but has subsequently been found to have a dust trail along its orbit, and shows sporadic activity (Hsieh et al. 2004; Toth 2006). It has been classed as a JFC, but this and similar objects have recently been shown to be from a dynamically and possibly compositionally distinct population (Hsieh & Jewitt 2006), hence I disregard it when discussing the global properties of the JFC population.

3.4.2 Bulk density

Various methods exist to measure the bulk density of Solar System bodies. Clearly the most reliable method is direct measurement where both the volume and mass of the body are known, but this applies only to resolved bodies whose gravitational effect on moons or other bodies can be measured; *i.e.* the major planets. Visits by space-craft present an opportunity to measure the density of minor bodies as they obtain resolved images and allow measurement of the mass of the body due to the deflection of the space-craft it causes. The change in velocity of the space-craft ΔV is related to the

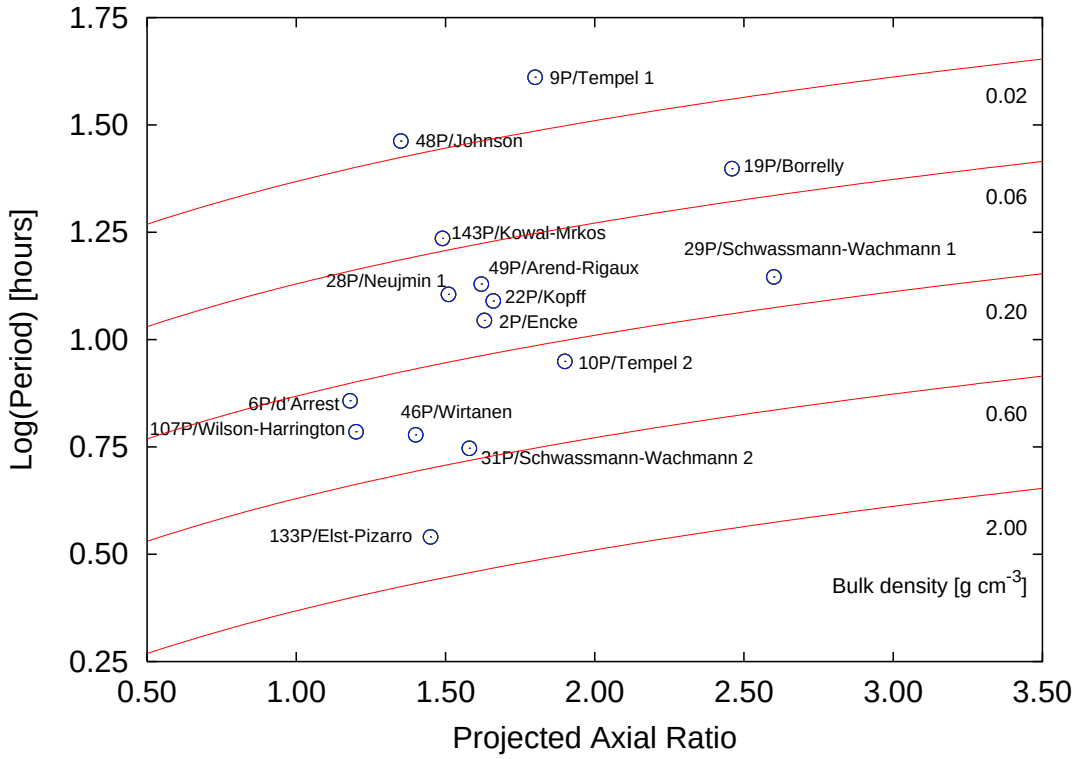

Figure 3.3: Rotation period against projected axial-ratio, for all JFC nuclei with light-curves observed prior to the work presented in this thesis. The lines show lower limits on density, from equation 3.29, of 0.02, 0.06, 0.20, 0.60 and 2.00 g cm^{-3}. Data from: 2P/Encke: Fernández et al. 2005; 6P/d'Arrest: Lowry & Weissman 2003; 9P/Tempel 1: A'Hearn et al. 2005; 10P/Tempel 2: A'Hearn et al. 1989; 19P/Borrelly: Lamy et al. 1998b; 22P/Kopff: Lowry & Weissman 2003; 28P/Neujmin 1: Delahodde et al. 2001; 29P/Schwassmann-Wachmann 1: Meech et al. 1993; 31P/Schwassmann-Wachmann 2: Luu & Jewitt 1992; 46P/Wirtanen: Boehnhardt et al. 2002; 48P/Johnson: Jewitt & Sheppard 2004; 49P/Arend-Rigaux: Millis et al. 1988; 107P/Wilson-Harrington: Osip et al. 1995; 133P/Elst-Pizarro: Hsieh et al. 2004; 143P/Kowal-Mrkos: Jewitt et al. 2003.

mass of the body M by

$$\Delta V = \frac{2GM}{rV_\infty} \tag{3.14}$$

where G is the gravitational constant, r is the distance between the object and the spacecraft at closest approach and V_∞ is the relative velocity between them at infinity. Unfortunately this method has yet to be applied directly to cometary nuclei, as the ΔV on comet flyby space-craft has been below the level measurable by tracking stations (Weissman et al. 2004). The unambiguous mass measurement of comet 67P/Churyumov-Gerasimenko will be one of the interesting results from the *Rosetta* mission; its presumed low value also presents a significant challenge for the mission

controllers trying to place the satellite in orbit around the nucleus.

Where there are not resolved images of bodies, the volume must be assumed based on sizes and approximate shapes obtained from photometry as described above. The mass can be found remotely by one of a number of techniques. Larger bodies can have their mass determined by measuring the gravitational perturbation that they cause to other bodies. However, the mass of cometary nuclei is too small to cause such perturbations. A large number of minor bodies have been found to be binaries or multiple systems; in such systems the motions around the system barycentre can be used to determine the mass. In asteroids approximately 15% of the near Earth population are binaries or multiple systems (Merline et al. 2002; Pravec et al. 2006); for KBOs the observed binary fraction is $\sim 2\%$, with a higher fraction for close binaries than for systems with widely spaced components (Kern & Elliot 2006). Recently Noll et al. (2006) reported the first discovery of a binary Centaur, (42355) 2002 CR46. As yet, however, there have been no clear detections of satellites to cometary nuclei. A theoretical companion has been invoked to explain outbursts on 17P/Holmes (Whipple 1984, 1999) but this is speculative and requires that the companion was destroyed in a collision producing the second outburst. There are two suggested detections of companions; one orbiting within the coma of the bright comet Hale-Bopp (Sekanina 1997), the other around 26P/Grigg-Skjellerup (McBride et al. 1997). There is some debate as to the reality of the Hale-Bopp companion (see Lamy et al. 2004), while the second case suffers from the common problem of determining whether fragments from nuclei are actually gravitationally bound (*i.e.* satellites).

Comets frequently split (Boehnhardt 2004), although fragments are seen to follow their own orbits around the Sun having escaped from their mutual gravitational influence. This can be used to put very approximate limits on the density $D_{\rm N}$ of (assumed spherical) nuclei, as the separation velocity $v_{\rm sep}$ of the fragments must exceed the es-

cape velocity $v_{\rm esc}$ of the nucleus:

$$v_{\rm sep} \geq v_{\rm esc} = \sqrt{\frac{2GM}{r}} = r\sqrt{\frac{8\pi G}{3} D_{\rm N}}. \tag{3.15}$$

For a typical nucleus with a radius of 1 km, this means that

$$D_{\rm N} \leq 1.79 v_{\rm sep}^2, \tag{3.16}$$

where the density is expressed in g cm^{-3}. Boehnhardt (2004) gives separation velocities from modelling of split comets, mostly by Sekanina and co-workers. For the mean observed separation velocity for short period comets, 2.7 m s^{-1}, this gives the very weak constraint of $D_{\rm N} \leq 13$ g cm^{-3}. The smallest separation velocity reported by Boehnhardt (2004) for short-period comets is $v_{\rm sep} \approx 0.3$ m s^{-1}, implying a low density of $D_{\rm N} \leq 0.16$ g cm^{-3}. This method of limiting densities is however inherently approximate and dependant on the models of the dynamics of the comet fragments, which generally experience significant non-gravitational acceleration as the fragmentation exposes fresh ice which sublimates in the sunlight.

Such non-gravitational accelerations can however be used to directly estimate the mass of single nuclei, using a technique developed by Rickman (1986, 1989). The rocket like effect of asymmetric out-gassing from the nucleus produces a net acceleration on the nucleus, which causes the observed change in orbital period ΔP from the expected Newtonian orbit. The non-gravitational acceleration is quantified by the vector **j**, which can be split into 3 orthogonal components: j_r in the radial (Sun–comet) direction, j_t in the transverse direction and j_n in the direction normal to the orbital plane. These forces are connected with ΔP by

$$\Delta P = \frac{6\pi\sqrt{1-e^2}}{n^2} \left(\frac{e}{a(1-e^2)} \int_0^P j_r \sin\theta {\rm d}t + \int_0^P \frac{j_t}{R_{\rm h}} {\rm d}t \right), \tag{3.17}$$

where n is the mean motion, a the semi-major axis, e the eccentricity and θ the true

anomaly. The mass M of the comet can then be determined by equating

$$M\mathbf{j} = -Qm\mathbf{u}, \tag{3.18}$$

where Q is the gas production rate, m the average molecular mass and $\mathbf{u}$ the outflow velocity. By modelling $Q(t)$ to match the heliocentric light-curve (*i.e.* assuming that brightness changes are directly related to changes in gas production rate) equations 3.17 and 3.18 can be used to solve for the nucleus mass. This has been carried out for a number of comets, and gives densities in the range ~ 0.01 – 1.0 g cm^{-3} (Sosa & Fernández 2005), although with large error bars due to the large number of assumptions that have to go into such a model-dependant approach. Recently Davidsson & Gutiérrez (2004, 2005, 2006) improved the basic approach to include a full thermo-physical nucleus model, with discrete active areas, to reproduce the observed gas production curve. This method is again model dependant and is also complicated and computationally intensive, and requires very detailed observational constraints to fulfil its potential (their results for 19P/Borrelly are based in part on results from the *Deep Space 1* fly-by).

The final method for constraining the density of minor bodies, and the one used here for nuclei, is based on the rotational properties. It is assumed that nuclei have negligible tensile strength, as evidenced by the break up of D/Shoemaker-Levy 9 under the gravitational influence of Jupiter (Asphaug & Benz 1996) and results from the *Deep Impact* mission to 9P/Tempel 1 (A'Hearn et al. 2005); see also Weissman et al. (2004). Therefore a lower limit on the density can be found by balancing self gravity with centrifugal force. I use the approximation given by Pravec & Harris (2000);

$$D_{\mathrm{N}} \geq \frac{10.9}{P_{\mathrm{rot}}^2}\frac{a}{b} \tag{3.19}$$

where P_{rot} is in hours. This equation provides an acceptable approximation to the more complex solution found by integrating over the volume of an ellipsoid. Following Richardson et al. (2005), this is given by balancing the centripetal acceleration at the

end of the long axis

$$(2\pi/P_{\rm rot})^2 a \tag{3.20}$$

with the gravitational acceleration at this point, given by integrating over the volume of an ellipsoid of uniform density $D_{\rm N}$. Expressing the volume integral in cylindrical coordinates (r,ϕ,z), the force balance equation for a particle at the end of the long axis $(z=+a)$ is given by

$$\left(\frac{2\pi}{P_{\rm rot}}\right)^2 a = GD_{\rm N}\int_{-a}^{a}\int_{0}^{b\sqrt{1-z^2/a^2}}\int_{0}^{2\pi}\frac{r(z-a)}{[(z-a)^2+r^2]^{3/2}}{\rm d}\varphi{\rm d}r{\rm d}z \tag{3.21}$$

where G is the gravitational constant. The symmetry of the ellipsoid means that the integral over φ simply gives a factor of 2π on the right hand side of this equation, while the integral over r is

$$\int_{0}^{b\sqrt{1-z^2/a^2}}\frac{r(z-a)}{[(z-a)^2+r^2]^{3/2}}{\rm d}r = \left[\frac{-(z-a)}{\sqrt{(z-a)^2+r^2}}\right]_0^{b\sqrt{1-z^2/a^2}} \tag{3.22}$$

$$= -\frac{z-a}{\sqrt{(z-a)^2+b^2(1-z^2/a^2)}}+1 \tag{3.23}$$

Substituting back into equation 3.21 gives

$$\left(\frac{2\pi}{P_{\rm rot}}\right)^2 a = 2\pi GD_{\rm N}\left(2a-\int_{-a}^{a}\frac{z-a}{\sqrt{(z-a)^2+b^2(1-z^2/a^2)}}{\rm d}z\right) \tag{3.24}$$

Using a symbolic integrator[2] and then applying the boundary conditions $z=\pm a$, the integral is found to be

$$\frac{a^2}{(a^2-b^2)^{3/2}}\left[b^2\ln\frac{-2ab^2}{\sqrt{a^2-b^2}}-b^2\ln\left(2a\left\{2a-\frac{2a^2-b^2}{\sqrt{a^2-b^2}}\right\}\right)-2a\sqrt{a^2-b^2}\right] \tag{3.25}$$

The logarithmic terms combine to give

$$-b^2\ln\frac{2a\sqrt{a^2-b^2}-2a^2+b^2}{-b^2} \tag{3.26}$$

[2] `http://integrals.wolfram.com`

Using q to denote the inverse of the axial-ratio (*i.e.* $q = b/a$) and substituting qa for b throughout, followed by cancelling out a, reduces equation 3.24 to

$$\left(\frac{2\pi}{P_{\rm rot}}\right)^2 = -2\pi G D_{\rm N} q^2 \frac{2\sqrt{1-q^2} + \ln -\frac{-2+q^2+2\sqrt{1-q^2}}{q^2}}{(1-q^2)^{3/2}} \tag{3.27}$$

Using the definition of $e \equiv \sqrt{1-(\frac{b}{a})^2} = \sqrt{1-q^2}$ gives

$$\left(\frac{2\pi}{P_{\rm rot}}\right)^2 = 2\pi G D_{\rm N}(e^2-1)\frac{2e + \ln\frac{-e^2+2e-1}{e^2-1}}{e^3} \tag{3.28}$$

taking the constants to the left hand side, simplifying the logarithm term by dividing both numerator and denominator by $(e-1)$, and taking the square root of both sides to give the equation in terms of $P_{\rm rot}$ instead of $P_{\rm rot}^2$ gives (Richardson et al. 2005)

$$\frac{1}{P_{\rm rot}}\sqrt{\frac{2\pi}{G D_{\rm N}}} = \frac{1}{e^{3/2}}\sqrt{(e^2-1)\left(2e + \ln\frac{1-e}{1+e}\right)} \tag{3.29}$$

The derivation of this expression is also given by a slightly different route using energy of the system by Harris (2002, appendix). Equation 3.29 is entirely equivalent to the commonly used expression given by Luu & Jewitt (1992), who use the symbol f for the inverse axial-ratio given by q above, and quote the gravitational acceleration in the form of equation 3.27, but without combining the logarithm terms.

Instead of calculating the density required by a given shape, an alternative approach is to start with the bulk properties and calculate the shape which the body would take under equilibrium conditions. There is a long history of these studies for fluid bodies, starting with Newton and progressing through the works of Maclaurin and Jacobi, who showed that there are discrete solutions and certain axial-ratios that rotating fluid bodies must assume. This subject is covered in detail by Chandrasekhar (1969). Note that the fluid solutions (the Jacobi ellipsoids) do not allow the simple model of a rotating ellipsoid with semi-axes $a \geq b = c$, except in the special case of a non-rotating sphere. However, I do not believe that the nuclei can be described as equilibrium fluid bod-

ies; almost all Solar System minor bodies with known densities and dimensions have non-Jacobian shapes. Holsapple (2001, 2004) shows that the solid bodies of the Solar System cannot be approximated as fluids, and goes on to describe the equilibrium states for solid bodies. The limits on shape for cohesionless rubble-piles found by Holsapple are complicated, and depend on the angle of friction ϕ, but reduce to the special case of fluid behaviour for $\phi = 0^\circ$. The upper bound found at the other extreme ($\phi = 90^\circ$) gives the same a/b–$P_{\rm rot}$ relation as equation 3.29, for ellipsoids with $a \geq b = c$ (Richardson et al. 2005). As both approaches give the same result under the most general assumptions (I make no assumption about likely values of ϕ for comets), I can be confident that equation 3.29 (and therefore its useful approximation, equation 3.19) gives a good description of the required minimum density for a rotating nucleus.

It is important to note that this method only gives the *minimum* bulk density of the nucleus, for two reasons. Firstly, equation 3.19 is dependent on the axial-ratio, and the amplitude of the light-curve only gives us the minimum a/b as the orientation of the rotation pole is not known. Secondly, the density is found by balancing the forces at the point where the nucleus would only just hold itself together gravitationally. However, there is no reason why the comet must be rotating this fast, and therefore this is only a minimum rotation period. The lower limits on $D_{\rm N}$ can however be used to assess the true bulk density of nuclei by studying a large number of comets; both the axis orientation and the rotation rate are expected to be randomly distributed, so over a large enough sample minimum densities will be found up to and including the true density. The limiting case, where a nucleus spinning very close to its critical rate and is observed equator on, will give a 'minimum' bulk density through equation 3.19 that approximately equals its true density. Many comets will be observed to have minimum densities below this density, but none will be seen to have minimum densities above it, assuming that JFC nuclei have similar densities. Therefore a cut-off in minimum densities will be observed, which will correspond to the true bulk density of the population. This is observed in asteroids, where the cut-off is at ~ 3 g cm^{-3} (Pravec et al. 2002). The data in this thesis, when combined with previous research, presents evidence for

such a cut-off for ecliptic comets.

3.5 Density related characteristics

With a measure of the bulk density of a nucleus, constraints can be placed on its porosity and composition. The porosity Ψ is the fraction of void space within the total volume of the nucleus. There are two sorts of porosity, micro-porosity Ψ_μ and macro-porosity Ψ_M. Micro-porosity refers to space within particles; high micro-porosity is suggested in models of cometary nuclei formed from 'fluffy' particles (Donn et al. 1985) where these spaces can be thought of as pores. Macro-porosity is due to spaces between large particles, and is high in rubble-piles consisting of large irregular boulders which would not fit closely together. The total porosity of a body is the sum of these two types, and is linked to the bulk density by

$$\Psi = 1 - \frac{D_\mathrm{N}}{D_\mathrm{g}} \tag{3.30}$$

where D_g is the grain density, or density of individual particles. This is an expression for Ψ_M where D_g is the bulk density of micro-porous particles, but where the structure of the particles is unknown and the density of the underlying materials is used it gives the total porosity. When I refer to Ψ without a subscript, or porosity generally, I will be referring to total porosity.

For asteroids D_g and Ψ_μ can be assessed by studying meteorites corresponding to asteroids of different spectral classes; the review by Britt et al. (2002) gives the following results. Grain densities depend on the composition, but fall in the range $2.3 \lesssim D_\mathrm{g} \lesssim 3.8$ g cm^{-3} (carbonaceous chrondites - ordinary chrondites). The micro-porosity of meteorites varies between $6\% \lesssim \Psi_\mu \lesssim 16\%$. Considering asteroids with known densities to be composed of the same materials gives porosities between 0 and 70%, with average values of $\sim 30\%$ (S-type) and $\sim 40\%$ (C-type). Hence there is evidence that more volatile bodies have higher porosities, which is important when it comes to studying cometary nuclei.

Davidsson (1999) gives an expression for tensile strength T (Pa) in terms of densities

$$T = 6.1 \times 10^{-12} \left(\frac{D_{\rm N} \beta}{D_{\rm g} r_{\rm g}^2} \right) \tag{3.31}$$

where $r_{\rm g}$ is the mean grain radius and β is the number of contact points with other grains, per grain. In terms of porosity, this gives

$$T = 6.1 \times 10^{-12} (1 - \Psi) \frac{\beta}{r_{\rm g}^2} \tag{3.32}$$

showing that strength decreases with increasing porosity. Davidsson (1999) assumes 'realistic' values for comets of $r_{\rm g} = 1.5 \times 10^{-5}$ cm, $\beta = 5$ and $D_{\rm g} = 1.54$ g cm^{-3} (although see below regarding nucleus grain density), which give the simple relation

$$T = 0.88 D_{\rm N} \tag{3.33}$$

Davidsson (1999) then uses tensile and shear strengths to define three regions of $P_{\rm rot}$-$r_{\rm N}$ space for a given density; the allowed region where objects are stable against rotational break up, the damaged region where shear forces will have fractured bodies, but they are still held together by gravitation, and finally the forbidden region where objects would be spun apart. This method allows testing of the assumption of effectively zero strength used to place limits on density above: Equation 3.33 gives a strength two orders of magnitude greater than that found by Asphaug & Benz (1996) for Comet Shoemaker-Levy 9 during its break-up around Jupiter, but three orders of magnitude below the strength of solid water ice (Davidsson 1999). Toth & Lisse (2006) showed that for likely values of $D_{\rm N}$ in the range found by the methods in section 3.4.2 all short period comets fall into the allowed region, even for very low densities/high porosities/low strengths (see chapter 6), while the presence of the long period comet Hale-Bopp in the damaged region is postulated as an explanation of its very high activity levels.

In comets the grain density is not well known, as the 'grains' are not of uniform composition; comets contain both rocky dust and also various volatile ices, and $D_{\rm g}$ is

the average of the grain density of all the components. There have been attempts to measure $D_{\rm g}$ and Ψ_μ for 'comet particles' (interplanetary dust particles - IDPs) which are captured by high flying aircraft as they enter earth's atmosphere; these are found to have low densities and considerable micro-porosity. The IDPs lack volatiles, and it is suggested that in the nucleus volatiles would fill some of the porous voids (Weissman et al. 2004). The chief problems with using this method to study cometary grains is the uncertainty over whether or not they are of cometary origin, and the processing which they will have undergone in ejection from the nucleus, transport to the Earth and entry into the atmosphere. Greenberg (1998) gives a value of $D_{\rm g} \approx 1.65$ g cm^{-3} for average cometary material, from dust models. The *Stardust* mission will shed considerable light onto this subject by bringing back particles captured from the coma of comet 81P/Wild 2 for laboratory analysis.

Chapter 4

Results from snap-shot imaging

4.1 Overview of observations

This chapter and the following one present the photometric data and derived physical properties of each of the comets observed. The goal of each observing run was to gather time-series photometric data on a number of JFCs, and targets were selected with this in mind. To be sure of being able to detect the nucleus at sufficient signal-to-noise (S/N), targets with good previous absolute magnitude estimates were taken from the compilation by Lamy et al. (2004) and predicted apparent magnitudes at the time of observation were calculated using equation 3.2. The position and projected rate of motion of the comet were generated using the NASA/JPL *HORIZONS* software[1], allowing calculation of the visibility and maximum exposure time (for $0.5''$ motion). This exposure time, taken with the predicted magnitude, allowed theoretical S/N levels to be calculated using appropriate web-forms[2]. Experience over the course of the observing runs showed that a predicted $S/N \approx 20$ would give a bright enough target to measure a reliable light-curve, although the predicted magnitudes and S/N levels were often found to give only a very approximate estimate of the brightness observed. Further target selection criteria were that the comet was at airmass ≤ 2 for a number of hours per night to give good light-curve coverage and that it was at $R_{\rm h} > 3$ AU, to maximise the likelihood of it being inactive.

In addition to these time-series targets, a list of 'snap-shot' targets was prepared for each observing run. This consisted of comets at large $R_{\rm h}$ with unknown or poorly constrained radii. The purpose of this list was two-fold: Firstly, it provided back up targets if the weather prevented time-series observations (*i.e.* if only one night was observable then there would be insufficient time to measure useful light-curves, but a large number of snap-shots could be obtained and sizes measured for comets with previously unknown radii). Secondly, on some occasions comets with unknown radii were otherwise very favourable targets for time-series observation, and an initial snap-

[1] `http://ssd.jpl.nasa.gov/horizons.cgi`
[2] `http://www.eso.org/observing/etc/`, `http://www.ing.iac.es/~crb/signal.html`

shot observation might show them to be worth following (as happened with P/2004 H2).

At the telescopes these carefully made plans of course became only guidelines, as weather or unexpected brightness, faintness or activity of the comets made sure that it was necessary to alter which targets were followed: some time-series targets were abandoned after initial snap-shots, while some snap-shot targets became the subject of extended observations. A full log of the comet observations carried out is given in table 4.1. This chapter describes the comets with snap-shot observations, while the comets with time-series observations each have their own section in chapter 5.

Table 4.1: Log of all observations.

Comet	UT Date	'scope	R_h[a] [AU]	Δ [AU]	α [deg.]	$N_{exp}\times$ Filter[b]	t_{exp} [s]	App[c]
7P	20/01/04	NTT	4.69^I	4.30	11.6	$28\times R$, $2\times V$, $2\times I$	120	S
	21/01/04	NTT	4.69^I	4.32	11.6	$14\times R$, $2\times V$, $2\times I$	120	S
8P[d]	01/07/05	INT	7.42^I	6.76	6.3	$13\times r'$	95	S
14P	20/01/04	NTT	5.51^O	4.96	8.9	$29\times R$, V, I	220	S
	21/01/04	NTT	5.51^O	4.95	8.8	$29\times R$, V, I	220	S
17P	05/03/05	NTT	4.66^I	3.93	9.0	$14\times R$, $2\times V$, $2\times I$	100	S
	06/03/05	NTT	4.66^I	3.91	8.9	$25\times R$, $3\times V$, $3\times I$	100	S
36P	05/03/05	NTT	4.08^O	3.39	11.0	$5\times R$, V, I	200	S*
	06/03/05	NTT	4.08^O	3.41	11.2	$17\times R$, V, I	200	S*
	01/03/06	INT	4.78^O	3.79	1.0	$63\times r'$, $10\times V$, $10\times i'$	150	S
	02/03/06	INT	4.78^O	3.79	1.0	$55\times r'$, $5\times V$, $5\times i'$	75	S

Continued on next page...

[a]Superscripts I and O refer to whether the comet is inbound (pre-perihelion) or outbound (post-perihelion). The variations in R_h, Δ and α over the course of any one night were smaller than the significance quoted here.

[b]The number of exposures N_{exp} in each filter in the final data set: frames rejected during reduction/analysis are not counted.

[c]Appearance given as S – Stellar, A – Active, or N – Not detected. F is used to denote comets detected, but at too faint a level to determine whether or not activity was present: these are assumed to be inactive. S* indicates that faint activity was later detected despite a stellar appearance.

[d]Note that 8P/Tuttle is not an ecliptic comet, but a NIC with a short period; it has an inclination of $\sim 55^\circ$ and $T_J = 1.6$. The radius obtained from this snap-shot is presented, but is not included in the analysis of the ensemble properties of ecliptic comets in chapter 6.

Table 4.1: continued.

Comet	UT Date	'scope	R_h[a] [AU]	Δ [AU]	α [deg.]	$N_{exp}\times$ Filter[b]	t_{exp} [s]	App[c]
40P	01/07/05	INT	4.57^O	3.68	7.0	$8\times r'$	85	S*
	02/07/05	INT	4.57^O	3.68	6.8	$15\times r', V, i'$	85	S*
	03/07/05	INT	4.58^O	3.68	6.6	$7\times r', V, i'$	85	S*
	04/07/05	INT	4.58^O	3.68	6.4	$20\times r', V, i'$	85	S*
	05/07/05	INT	4.59^O	3.67	6.2	$17\times r', V, i'$	85	S*
	06/07/05	INT	4.59^O	3.67	6.0	$20\times r', 2\times V, 2\times i'$	85	S*
	07/07/05	INT	4.60^O	3.67	5.7	$18\times r', 2\times V, 2\times i'$	85	S*
43P	05/03/05	NTT	3.30^O	2.61	13.9	$4\times R$	100	A
44P	06/03/05	NTT	5.17^I	4.21	3.0	$2\times R$	80	S
	01/03/06	INT	4.51^I	3.84	10.1	$2\times r'$	300	F
	02/03/06	INT	4.50^I	3.83	10.0	$3\times r', 3\times V, 3\times i'$	170	S
47P	05/03/05	NTT	5.42^I	4.48	3.5	$19\times R, 2\times V, 2\times I$	85	S
	06/03/05	NTT	5.42^I	4.47	3.2	$34\times R, 2\times V, 2\times I$	85	S
	01/03/06	INT	5.11^I	4.45	8.9	$2\times r'$	300	S*
	02/03/06	INT	5.11^I	4.43	8.8	$3\times r', 3\times V, 3\times i'$	170	S*
56P	01/03/06	INT	3.83^O	3.14	11.8	$3\times r', 2\times V$	520	A
	02/03/06	INT	3.83^O	3.15	12.0	$5\times r', V, i'$	260	A
70P	01/07/05	INT	4.84^I	4.26	10.6	$6\times r'$	295	F
72P	02/03/06	INT	3.28^O	2.35	7.1	$5\times r'$	50	N
75P	02/07/05	INT	4.95^I	3.94	1.7	$3\times r'$	75	N
78P	02/03/06	INT	3.84^O	2.86	1.8	$3\times r'$	60	A
92P	20/01/04	NTT	4.46^O	3.58	6.3	$63\times R, 3\times V, 3\times I$	75	S
	21/01/04	NTT	4.46^O	3.59	6.4	$49\times R, 3\times V, 3\times I$	75	S

Continued on next page...

Table 4.1: continued.

Comet	UT Date	'scope	R_h[a] [AU]	Δ [AU]	α [deg.]	$N_{exp}\times$ Filter[b]	t_{exp} [s]	App[c]
94P	04/07/05	INT	4.14^O	3.19	5.6	$14\times r'$, V, i'	75	S*
	05/07/05	INT	4.14^O	3.18	5.3	$20\times r'$, $3\times V$, $2\times i'$	75	S*
	06/07/05	INT	4.14^O	3.18	5.1	$26\times r'$, $2\times V$, $2\times i'$	75	S*
	07/07/05	INT	4.15^O	3.18	4.9	$23\times r'$, $2\times V$, $2\times i'$	75	S*
103P	06/03/05	NTT	3.24^O	2.28	5.0	$3\times R$	45	A
	01/03/06	INT	5.03^O	4.30	8.3	$2\times r'$, V, i'	200	A
	02/03/06	INT	5.03^O	4.29	8.1	r', V, i'	110	A
104P	05/03/05	NTT	3.06^O	2.31	13.8	$2\times R$	80	N
114P	04/07/05	INT	3.75^I	2.95	10.9	$8\times r'$	90	S
120P	02/03/06	INT	3.89^O	3.05	8.8	$5\times r'$	115	F
121P	01/03/06	INT	3.92^O	3.43	13.5	$4\times r'$, V, i'	400	S
	02/03/06	INT	3.93^O	3.42	13.4	$18\times r'$, V, i'	215	S
	31/05/06	FTN	4.18^O	3.34	8.6	$14\times R$, $3\times V$	60	S
131P	02/03/06	INT	3.48^O	2.65	10.1	$3\times r'$, $3\times V$	105	S
135P	02/03/06	INT	3.55^I	2.65	7.5	$5\times r'$	80	N
137P	06/03/05	NTT	6.95^I	6.17	5.3	$22\times R$, $2\times V$, $2\times I$	140	S
160P	02/03/06	INT	3.98^O	3.41	12.5	$3\times r'$	140	F
A1[e]	02/07/05	INT	5.52^I	4.71	6.9	$8\times r'$	135	S
BZ8[e,f]	02/03/06	INT	2.32^I	1.35	7.1	$15\times r'$, $3\times V$, $3\times i'$	10	S

Continued on next page...

[e]The abbreviated designations used in the text are used here for these un-numbered comets:
A1 – P/1995 A1, BZ8 – 2006 BZ8, H2 – P/2004 H2, H3 – P/2004 H3, T1 – P/2004 T1, X2 – P/2001 X2.

[f]2006 BZ8 was observed to search for activity in this newly discovered object, which has a comet-like ($T_J = -1$) orbit. None was found, and BZ8 is officially a Centaur. The results on this object are given in this chapter, but are not included in the discussion on ecliptic comets in chapter 6.

Table 4.1: continued.

Comet	UT Date	'scope	R_h[a] [AU]	Δ [AU]	α [deg.]	$N_{exp}\times$ Filter[b]	t_{exp} [s]	App[c]
H2[e]	01/07/05	INT	3.70^O	3.06	13.6	$14\times r'$	210	S*
	02/07/05	INT	3.70^O	3.06	13.4	$19\times r', V, i'$	210	S*
	03/07/05	INT	3.71^O	3.05	13.3	$14\times r', V, i'$	210	S*
	04/07/05	INT	3.71^O	3.04	13.1	$16\times r', 2\times V, i'$	210	S*
	05/07/05	INT	3.71^O	3.03	12.9	$14\times r', 4\times V, 2\times i'$	210	S*
	06/07/05	INT	3.72^O	3.02	12.7	$10\times r', 6\times V, 3\times i'$	210	S*
	07/07/05	INT	3.72^O	3.02	12.6	$11\times r', 4\times V, 2\times i'$	210	S*
H3[e]	05/07/05	INT	3.71^O	2.97	12.0	$6\times r'$	90	F
T1[e]	02/03/06	INT	3.82^O	2.86	3.9	$5\times r'$	60	N
X2[e]	02/07/05	INT	5.02^I	4.02	2.4	$2\times r'$	80	N

'Snap-shot' images of all potential target comets were obtained, to ascertain their suitability for time-series photometry. For comets which were not selected as primary targets, the goal was to obtain measurements or limits on the brightness and activity level of the nuclei. These results are summarised in table 4.3. There are three possible outcomes from imaging of comets; the comet is either undetected, unresolved or active. Undetected comets are either simply too faint to see, in which case upper limits on the size are found, or confused with background sources, in which case very little information can be obtained. Unresolved comets are detected and appear as point sources, and may be interpreted as being bare nuclei, depending on evaluation of the contamination by dust comae. Active comets have resolvable coma in individual images; the information obtainable on the nucleus from these data are limited. The snap-shot data presented here is divided into three sections according to these appearance categories.

4.2 Undetected comets

4.2.1 72P/Denning-Fujikawa

72P/Denning-Fujikawa was a back-up target for the 2006 INT run, as its radius was unknown. Five r'-band exposures were taken, giving a total exposure time of 250 seconds, but the comet was not detected, even in a combined image. Historically, this comet has proved elusive: It was first discovered in October 1881, but lost until a chance recovery during a close pass to the Earth in 1978, which was linked to the earlier comet despite it being unobserved during any of the 10 intervening apparitions.[3] Subsequent attempts to recover the comet during its 1987, 1996 and 2005 apparitions have failed; the non-detection reported here continues this trend. Lamy et al. (2004) quote an unpublished radius estimate from the updated catalogue of Tancredi et al. of 0.8 km, but caution that there is no way to assess the accuracy of this result. It is far from clear what data their estimate is based on, considering the lack of reported observations; it must be regarded as unreliable, even by the standards of the Tancredi et al. (2000) catalogue. If it were true, then this radius implies a predicted $m_R = 22.4$ at the time of the INT run, which should have been just detectable.

There are three likely interpretations of this non-detection; firstly, the orbit could be incorrect, and in fact Denning in 1881 and Fujikawa in 1978 discovered two different comets. Assuming that this is not the case, the alternative explanations are that the comet has ceased to exist (*i.e.* broken up) since 1978, or that it is a very small nucleus that exhibits little out-gassing near perihelion, and has consequently escaped detection despite numerous attempts. If the comet exists, and was in the predicted position, then the fact that no object was observed to $m_R \geq 22.2$ implies an absolute magnitude for this comet of $m_R(1,1,0) \geq 17.6$ and therefore $r_{\rm N} \leq 0.88$ km (3σ limits).

[3]Historical information on observations of the previous apparitions of this comet, and of others in this thesis, is taken from Gary Kronk's Cometography (`http://cometography.com/`). Dates of last observation and orbital parameters are also sourced from the Minor Planets Center (MPC – `http://cfa-www.harvard.edu/iau/mpc.html`) and the JPL small bodies database (`http://ssd.jpl.nasa.gov/sbdb.cgi`)

4.2.2 75P/Kohoutek and P/2001 X2 (Scotti)

Both 75P/Kohoutek and P/2001 X2 (Scotti) [hereafter abbreviated to X2] were observed during the 2005 INT run at right ascension 18 h - 19 h and declination $\sim$ -20°, which unfortunately placed them in the galactic plane [galactic co-ordinates $(l,b) \approx$ (10,0) - (20,-10)]. This meant that both were observed against a dense star field, making identification of the comets difficult. For X2 this was exacerbated by the loss of one of the frames taken due to a malfunction in the CCD camera, leaving only two r'-band frames. It proved impossible to identify either comet, even with the aid of astrometric predictions of their precise positions within these fields. As there is a high likelihood of the comet being blended with one of the stars within the predicted area it is also impossible to constrain the brightness of the comets other than to say that they must be considerably fainter than the field stars, but this does not put meaningful limits on the radius as for any sensible size the comet would fit this constraint: for 75P the stars in the search area have magnitudes in the range $m_R \approx 14.5 - 20.5$, while the comet is expected to have $m_R \geq 22.8$ based on a limit of $r_{\rm N} \leq 1.6$ km (Lowry et al. 2003)[4], from a non-detection in 1999.

4.2.3 104P/Kowal 2

Lowry et al. (2003) have also previously observed 104P/Kowal 2 when inactive at a heliocentric distance of 3.9 AU, in snap-shot data acquired with the 1.0m Jacobus Kapteyn Telescope (JKT) on La Palma in June 1999. They obtained a radius measurement of 1.1$\pm$0.5 km, again assuming an albedo of 0.04, which allowed prediction of an apparent nuclear magnitude of 21.8 at the time of the 2005 NTT observations, making this a primary target. However, this comet was not immediately detected in initial snap-shot

[4]Note that the R-band magnitude of the Sun used by Lowry et al. (1999, 2003) and Lowry & Fitzsimmons (2001, 2005), $m_\odot = -27.26$, was found to be incorrect. The difference between this and the true value of $m_\odot = -27.09$ means that while the magnitudes measured in these works are accurate, the true radii are $10^{0.2(-27.09+27.26)} = 8\%$ larger. The radius quoted for 75P, and for all others quoted in this thesis from this group of papers, have been corrected to account for this.

observations and removed from the time-series target list. Upon subsequent processing in Belfast it became clear that the comet was undetectable even in images combining both *R*-band frames. The comet has a well known orbit, having been observed during four apparitions since its discovery in 1979 and most recently in February 2004, and an astrometric fit allowed calculation of the precise position of the comet at the time of observation. There was no object detected to $m_R \geq 23.3$ within the expected area. Using equation 3.2 this gives a 3σ limiting magnitude of $m_R(1,1,0) \geq 18.53$, while equation 3.3 gives a 3σ upper limit on the radius of the nucleus of 0.56 km, assuming $p_R = 0.04$.

This limit is in agreement with the previous measurement, although at the small end of the expected size. Comets are known to spontaneously disrupt (Boehnhardt 2004); break-up of this nucleus during its perihelion passage in May 2004 would also explain the non-detection. With this in mind I searched for any other observations of 104P since the last reported to the Minor Planets Centre in February 2004, and discovered[5] that Reach et al. observed the comet with the *Spitzer* infra-red space telescope at almost the same time as the NTT observations. The comet was detected in the *Spitzer* data (W. Reach, private communication, 2006), so it has not broken up and therefore the non-detection gives a true upper limit on the size for the assumed albedo.

By assuming that this limit corresponds to observing the nucleus at a light-curve minima (*i.e.* when it shows the smallest projected area) and that Lowry et al. (2003) observed it near maximum brightness, then a crude estimate of the shape of the nucleus can be obtained. The axial-ratio a/b is equal to the ratio of the projected areas, and therefore the ratio of the squares of the effective radii, so in this case

$$\frac{a}{b} = \frac{r_{\rm N}^2(max)}{r_{\rm N}^2(min)} = \frac{1.12^2}{0.56^2} \approx 4.0 \tag{4.1}$$

However, the large error bars on the measured radii render such a calculation virtually

[5] A Google search found the 104P observations on Yan Fernandez's useful page of the *Spitzer* logs for Solar System objects - `http://www.physics.ucf.edu/~yfernandez/sss.html`

meaningless and I still regard the shape of 104P as unknown.

4.2.4 135P/Shoemaker-Levy 8

135P/Shoemaker-Levy 8 was discovered in April 1992, and has an orbital period of 7.5 years. It was seen during its 1998/9 apparition, with the last reported observations from Japan in June 1999, and was inbound at $R_{\rm h}$ = 3.6 AU at the beginning of March 2006, on its way to perihelion at 2.7 AU in May 2007. It was observed on the 2006 INT run as a secondary target of unknown size, and was undetected in any of the five 80 second r'-band exposures or in a combined frame. There is no object at the position given by an astrometric fit to $m_R \geq 22.7$, giving a 3σ limit to the absolute magnitude of $m_R(1,1,0) \geq 17.59$ and therefore a radius of $r_{\rm N} \leq 0.87$ km.

4.2.5 P/2004 T1 (LINEAR-NEAT)

P/2004 T1 (LINEAR-NEAT) [hereafter T1] was discovered in September 2004 before passing through perihelion at 1.7 AU in November 2004. It was last observed outbound in March 2005, and was still outbound at 3.8 AU during February/March 2006. No further information has been recorded on this comet. 5×60 second r'-band exposures were taken, but the comet was not detected. An astrometric fit allowed measurement of a limiting magnitude of $m_R \geq 24.4$, implying $m_R(1,1,0) \geq 19.1$ and $r_{\rm N} \leq 0.43$ km, again placing 3σ lower and upper bounds on these quantities.

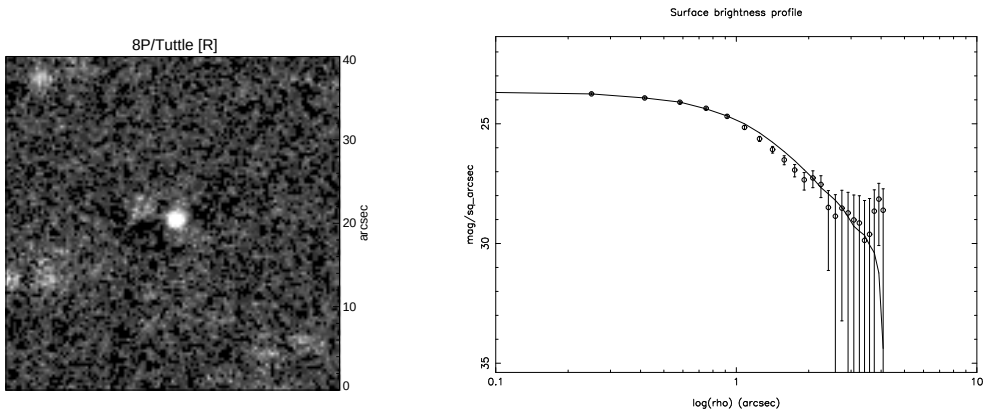

(a) (b)

Figure 4.1: Image (a) showing 8P on the 1st of July 2005, which appears to be stellar. Here the background is largely removed, despite the star field being very crowded. The faint residual star flux near to the comet is the cause of the slight rise at the end of the profile (b). For the most part the comet (points) and scaled stellar (solid line) profiles are in excellent agreement, implying that the comet is inactive.

4.3 Unresolved comets

4.3.1 8P/Tuttle

The results from the snap-shot observations of 8P/Tuttle obtained during the July 2005 INT run are presented here, although they are not included in the analysis of the ensemble properties of ecliptic comets. 8P is an unusual comet; by the 'classical' definition, it is a JFC, as it has an orbital period less than 20 years ($P = 13.5$ yr), however on dynamical grounds it is a NIC, as it has $T_J = 1.6$, and has a Halley-like high inclination ($i = 55°$) orbit. It therefore is likely to be an Oort cloud comet which has been captured into a shorter period orbit by interactions with the planets. It is also known to have a reasonably large (r_N = 7.8 km) nucleus, from snap-shot observations by Licandro et al. (2000b), and was therefore predicted to be a bright target suitable for time-series observation at R_h = 7.4 AU with the INT, providing an opportunity to add to the very few data on the rotational properties of Oort cloud comets. However, upon observation the target field was seen to be far too crowded for time-series observation, and attempts to observe the comet during this run were abandoned after only a short series of 13 r'-band frames. It was possible to separate the comet from background sources

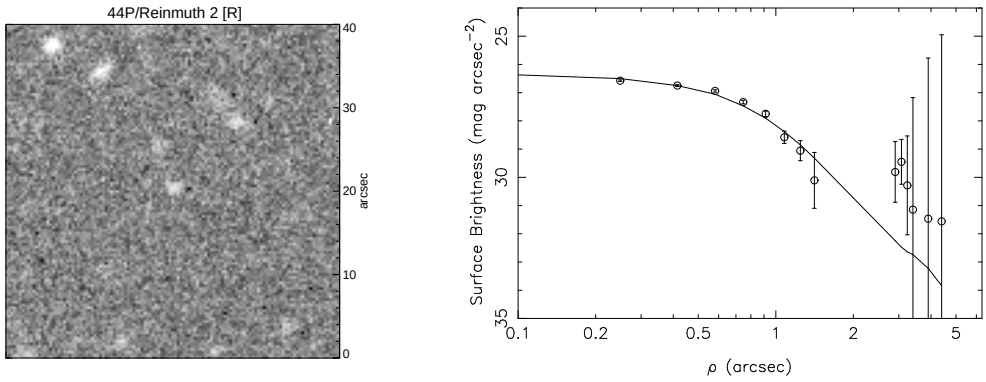

(a) (b)

Figure 4.2: Image (a) showing 44P on 6/3/05, made up of 2×80 second exposures. The comet, in the centre of the frame, is faint but appears to be inactive, as is shown by the surface brightness profile (b). Beyond 2.5″ sky noise dominates the profile, however the comet and scaled stellar profiles are indistinguishable in the inner part, implying that the comet was indeed inactive.

in the majority of frames; the average $m_R = 21.61 \pm 0.03$ is taken over the 9 of these frames over which the magnitude of the comet was $\sim$ constant, with a brightening in the remaining 4 being attributed to proximity to a background star. Equation 3.2 allows conversion of this magnitude to an absolute $m_R(1,1,0) = 12.88$, corresponding to a radius of 7.58 ± 0.12 km, in excellent agreement with the value of Licandro et al. (2000b). The combined image from these data show a star-like appearance (fig. 4.1); although the surface brightness profile is affected at $\sim 5''$ by the proximity of background sources, it shows an inactive nucleus within the inner part. Avoiding the stellar contamination, equation 3.1 gives $m_c(4.3'') = 25.1$, and therefore a negligible coma flux contribution of $\leq 4 \pm 8\%$.

4.3.2 44P/Reinmuth 2

44P/Reinmuth 2 was expected to have m_R = 22.8 at the time of the 2005 NTT observations, and was therefore a secondary target. Only one frame was taken of this comet on the first night of observations before high humidity brought an end to observations, making it impossible to distinguish the comet from faint background stars. Two more frames were acquired on 44P on the second night.

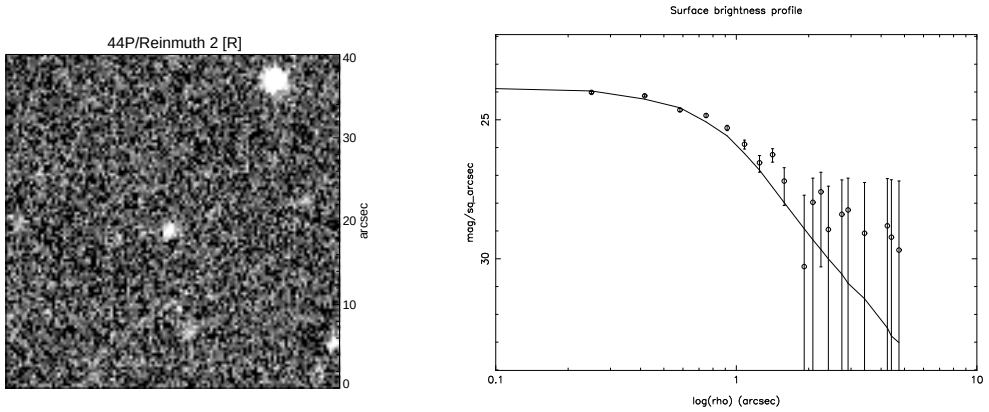

(a) (b)

Figure 4.3: Image of 44P taken during the 2006 INT run, made up of 3×170 second exposures taken on the 2nd of March. The profile is slightly suggestive of faint activity, as the comet points are generally higher than the scaled stellar line, but the profiles are consistent within the error bars.

The comet appears faint but stellar in each of these frames, and in a combined frame (fig. 4.2 (a)). To put limits on any unresolved coma, I measured the surface brightness profile (fig. 4.2 (b)), which appears stellar within the inner 2.5″, but is dominated beyond that by sky noise. The limit on any coma within this radius is $m_c(2.5) \geq 26.9$, corresponding to at most 2% of the total flux from the comet. This comet was therefore inactive at the time of observation, as expected at $R_{\rm h}$ = 5.2 AU.

The nuclear magnitude was measured to be m_R = 22.62±0.12, corresponding to $r_{\rm N}$ = 1.96±0.11 km. This measurement is consistent with the upper limit of $r_{\rm N} \leq 3.2$ km found by Lowry et al. (2003). It is slightly larger than the value of 1.61 km quoted by Lamy et al. (2004), but is in agreement assuming that the nucleus is slightly elongated. Such a range in magnitudes is consistent with a nucleus with $r_{\rm N}$ = 1.79 and a minimum axial ratio of a/b = 1.5, which is typical of the values determined for JFC nuclei (see chapter 6).

44P was observed again during the 2006 INT run, when a total of 5 r'-band images were taken over the course of the two nights. The comet was detected on both nights, although was very faint in poor seeing on the first. The comet's magnitude was constant, within the error bars on each point, over the two nights at $m_R = 22.49 \pm 0.06$, and apparently inactive (fig. 4.3). The profile is consistent with the background PSF, within

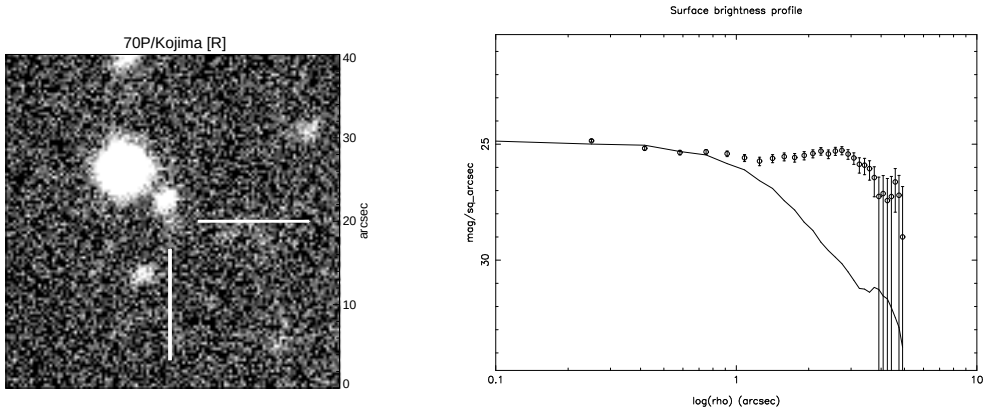

(a) (b)

Figure 4.4: Image showing 70P taken on the 1st July 2005., The comet is in the centre of the frame and very faint (marked by cross hairs here). This is a single 295 s r'-band frame; in subsequent frames the comet moved towards the two stars and was not separable from them. The profile shows the effect of the nearby star; no sensible constraints on the activity level of this comet can be made.

the error bars on each point, and equation 3.1 gives $m_c \geq 23.26$, or $\leq 50 \pm 72\%$ of the flux. The absolute magnitude was measured to be $m_R(1,1,0) = 15.95$, implying $r_{\rm N} = 1.84 \pm 0.05$ km, which is consistent with the NTT measurement and within the range discussed above. Colours of $(V-R) = 0.31 \pm 0.09$ and $(R-I) = 0.42 \pm 0.13$ were measured.

4.3.3 70P/Kojima

Lamy et al. (2004) quote measurements for 70P/Kojima from their own unpublished work, from a 'partial rotational light-curve'. No indication is given of the quantity of data involved, however the limited available time on HST means that 'full' light-curves from these authors can contain less than 10 photometric data points (*e.g.* Lamy et al. 1998a). Accordingly, their results ($r_{\rm N}$ = 1.86 km, $a/b \geq 1.1$ and $P_{\rm rot} \geq 22$ hours) are treated with caution, although the radius measurement can be taken at face value if regarded as a snap-shot. Based on this radius, the comet had a predicted $m_R = 22.9$ at the time of the 2005 INT observing run. Despite the long integration times (295 s) possible due to the slow apparent motion of the comet, it was not detected in individual

images at the telescope, and this target was abandoned after 6 frames. Upon subsequent processing, and with the aid of an astrometric prediction of the precise position of the comet (whose orbit is well known despite a 0.15 AU close encounter with Jupiter in 1996), the comet was found near the expected position. Its identification at the telescope had been hampered by the faintness of the target and its proximity to a bright field star; only in the first frame was it sufficiently separated from the star to allow photometry (fig. 4.4). Even in this first frame a small amount of flux from the star may have been present within the aperture centred on the nucleus; the following results should be treated with due caution, and the radius is more properly considered to be an upper limit. Discussion on the shape based on this radius assumes that it is unaffected by star light, and is therefore approximate. The measured comet magnitude is $m_R = 22.53 \pm 0.15$, which corresponds to $m_R(1,1,0) = 15.59$ and $r_N \leq 2.18 \pm 0.15$ km. Taken with the radius measurement from Lamy et al., this implies $a/b \geq 1.4$, which is typical for JFCs. This is larger than Lamy et al.'s value, but even if they did observe the full range in magnitudes in their partial light-curve then a change of viewing angle could increase the range observed at a different epoch: light-curves only give a *minimum* a/b when the orientation of the rotation axis is unknown. Assuming that any stellar flux contamination in this measurement was negligible and taking it with the measurement of Lamy et al.[6], an average $r_N = 2.0 \pm 0.2$ seems a reasonable value to assume for the size of 70P.

4.3.4 114P/Wiseman-Skiff

114P/Wiseman-Skiff was discovered in January 1987, and has since been observed at each pass through the inner solar system on its 6.7 year orbit. It was observed with the INT in July 2005 when inbound at 3.75 AU, and was detected but at too faint a level to produce a reliable light-curve. The combined image of all 8 frames taken is

[6]While even a partial time-series should provide a more accurate measurement of r_N than a single snap-shot, the Lamy et al. data on 70P remains unpublished and therefore cannot be scrutinised.

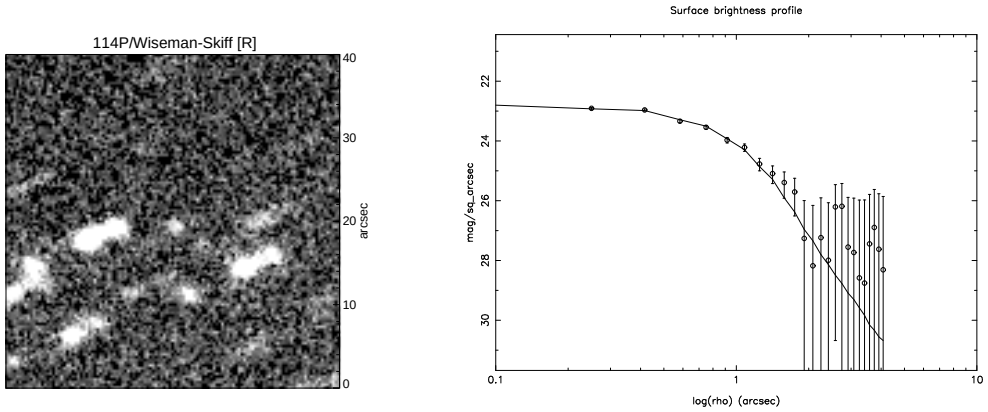

(a) (b)

Figure 4.5: Image showing 114P on 4/7/05, which can be seen as the faint star-like source in the centre of the frame, which is a sum of 8× 90 s r'-band frames. The background stars are trailed in this image as it has been corrected for the comet's motion; with only 8 frames it was not possible to construct a good background image to subtract the stars. The profile is inactive in the inner part, although dominated by sky noise and the star trails in the outer section.

shown in fig. 4.5 (a), along with the profile (fig. 4.5 (b)) which shows that the comet appeared inactive. The profile was only measurable to $\rho = 4''$, but gives $m_c = 24.45$ and therefore a limit on the coma contribution of $\leq 25 \pm 41\%$, with the large error bars due to the noisy profile in the outer part. The measured $m_R = 22.95 \pm 0.11$ gives $m_R(1,1,0) = 17.34$ and $r_{\rm N} = 0.97 \pm 0.05$ km. This agrees with the assessment that the nucleus is a relatively small one from Lamy et al. (2004), who again quote their own unpublished result of $r_{\rm N} = 0.78 \pm 0.04$, based on an HST snap-shot when the comet was at $R_{\rm h}$ = 1.6 AU and presumably active. Again assuming that these two snap-shots were taken at opposing light-curve extrema, then the minimum required axial-ratio is $a/b \geq 1.5$, and the average effective radius is $r_{\rm N}$ = 0.89 km.

4.3.5 120P/Mueller 1

Although not detectable in individual images, 120P/Mueller 1 was found in a co-added image of all the data shifted to account for its predicted motion (fig. 4.6). A cosmic ray hit near the comet's predicted position meant that the third frame is not included in this summed image; it is made up of the remaining 4× 115 s r'-band frames. The comet

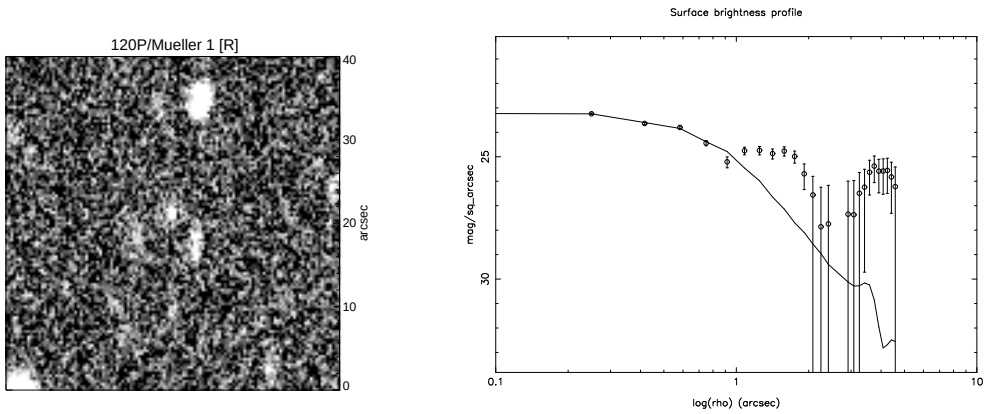

(a) (b)

Figure 4.6: Image showing 120P, taken on 2/3/06, which is seen to be very faint, but distinguishable from the trailed stars in this combination of 4 r'-band frames. The star trails give two additional peaks in the profile at larger ρ, although the inner $1''$ implies a bare nucleus.

had $m_R = 23.52 \pm 0.13$ in the combined image. This gives $m_R(1,1,0) = 17.84$ and $r_{\rm N} = 0.77 \pm 0.05$ km. The surface brightness profile for this comet matches the stellar PSF within the inner arcsecond, although beyond this there are two further peaks due to the nearby trails of background stars, making the formal limit of $m_c \geq 23.1$ meaningless. The $FWHM$ of the stellar PSF in the background image is $\sim 1''$, so the flux from the comet was measured within the star-like part of the comet image (an aperture correction was applied to give the flux within $5''$). I therefore assume that this measurement is of the radius of the bare nucleus, and can be compared with the previous measurement of Lowry et al. (1999). They measured $r_{\rm N} = 1.7 \pm 0.2$ with a snap-shot of a star-like nucleus at $R_{\rm h}$ = 3.1 AU, which at approximately twice the radius measured here is a large discrepancy; such disparate measurements would require $a/b = 4.7$ to be explained purely by the shape of the nucleus, which is rather high. It is possible that there was either a non-zero coma contribution in Lowry et al.'s $R_{\rm h}$ = 3.1 AU measurement which was not present here at 3.9 AU, or that the comet has a steeper than normal phase function / opposition surge (Lowry et al.'s observations were taken at $\alpha = 2.9^\circ$). The unknown colour of the nucleus could also contribute, but only at a level similar to the uncertainty on m_R: If 120P has a very red nucleus the difference in colour term between Lowry et al.'s R-band and my r'-band measurements could cause the m_R presented here to be up to a tenth of a magnitude too faint. It is likely that some com-

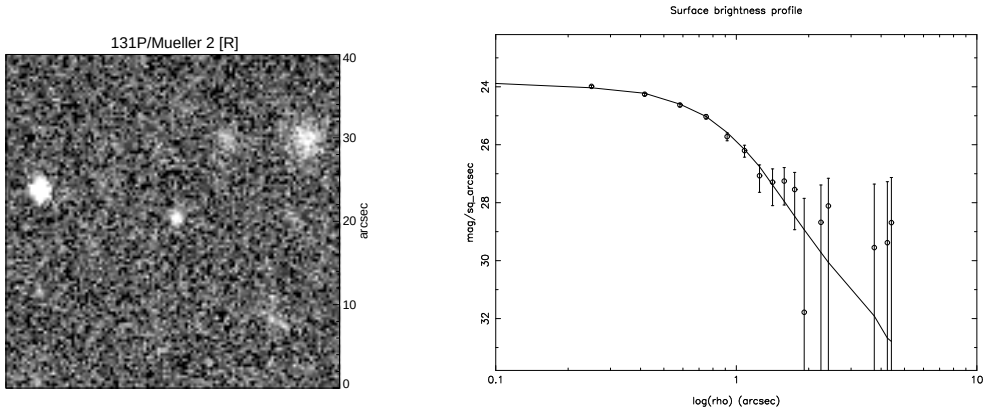

(a) (b)

Figure 4.7: Image showing 131P as a faint but star-like source in a combination of 3 frames taken on 2/3/06. The profile is in agreement with the image PSF within the error bars, implying that the comet was inactive.

bination of these factors, combined with a more modest elongation of the nucleus, is required to explain the differences between these measurements.

4.3.6 131P/Mueller 2

131P/Mueller 2 was outbound at 3.5 AU when observed with the INT in 2006. No prior information was available on this comet, and a snap-shot was attempted to constrain its size. Three r'-band frames were taken, and the comet was found and observed to have a faint, star-like appearance (fig. 4.7). The large error bars on the surface brightness at large ρ make the coma limit of $m_c \geq 23.1$ ($\leq 68 \pm 94\%$ of the total flux) almost meaningless, but the profile appears star-like and the comet can be assumed to have been inactive. The average magnitude was $m_R = 22.77 \pm 0.09$, corresponding to an absolute magnitude of $m_R(1,1,0) = 17.59$, and therefore a radius of $r_{\rm N} = 0.87 \pm 0.04$ km. In addition, three V-band frames were taken, allowing measurement of the colour of the nucleus. A value of $(V-R) = 0.45 \pm 0.12$ was obtained, which falls in the centre of the observed JFC distribution (see section 6.4 of chapter 6).

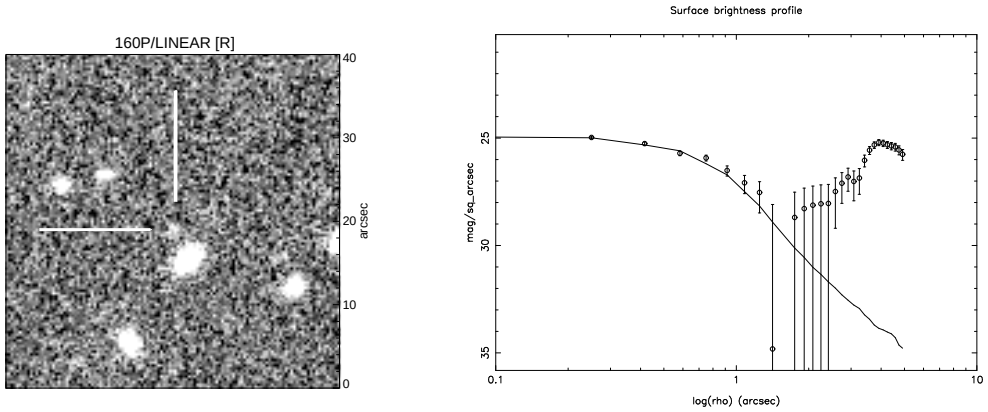

(a) (b)

Figure 4.8: Image showing 160P, which was detected at a very faint level, even in this combined image of three 140 s r'-band frames taken on 2/3/06. The profile appears stellar in the inner part, but is confused with a background galaxy in the outer part.

4.3.7 160P/LINEAR

Observations of 160P/LINEAR from the INT during 2006 detected the comet when outbound at ~ 4 AU. The comet appeared as a very faint but apparently inactive object in 3×140 s r'-band exposures (fig. 4.8). The presence of a nearby galaxy prevents measurement of limits on any coma, with $m_c(5'') = 22.6$. The inner part of the profile is a good match for the background PSF; measuring the surface brightness at $1.3''$ gives $m_c \geq 28.0$, $\leq 1.9 \pm 5.8\%$ of the total flux. The measured value of $m_R = 23.69 \pm 0.18$ implies $m_R(1,1,0) = 17.58$ and $r_{\rm N} = 0.87 \pm 0.07$ km.

4.3.8 P/1995 A1 (Jedicke)

P/1995 A1 (Jedicke) [hereafter A1] had only been previously observed at one apparition, when it was discovered in January 1995, already outbound after passing through perihelion in 1993. It was observed through to January 1996, and consequently has a well calculated orbit with a period of 14.3 years. An attempt to detect the return of this comet was made in July 2005 with the INT, although the comet was still at $R_{\rm h}$ = 5.5 AU. A faint object was discovered near the nominal position, an average $m_R = 22.63 \pm 0.07$ was measured. Measured in a combination of all 8 r'-band frames (fig. 4.9), the comet's

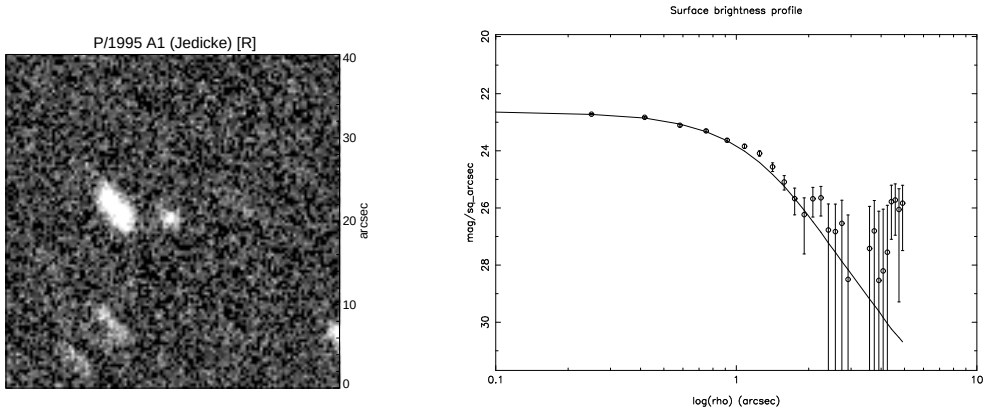

(a) (b)

Figure 4.9: Image showing P/1995 A1, which was recovered on 2/7/05 returning to the inner solar system 10 years after it was last observed. The orbit is accurate, as the predicted motions allowed the 8 frames to be combined to give a star-like comet image (with trailed background stars). The profile matches the PSF, even in the outer noisy part, except at $\rho \approx 5''$ where flux from the nearby star trail raises the measured surface brightness.

surface brightness profile appeared stellar in the inner region, although was dominated by sky noise beyond $2''$, which is taken to show that it was inactive, as would be expected with the comet still beyond Jupiter's orbit. This implies a radius for the nucleus of A1 of $r_{\rm N} = 2.48 \pm 0.08$, and an absolute magnitude of $m_R(1,1,0) = 15.31$.

4.3.9 P/2004 H3 (Larsen)

P/2004 H3 (Larsen) [hereafter H3] is also a recently discovered comet, and was only at its second opposition when observed with the INT in July 2005, having been discovered the previous April. It was at $R_{\rm h}$ = 3.7 AU, outbound, and was only just recovered in a frame combining all six 90 s r'-band exposures (fig. 4.10 (a)). The measured magnitude, in the combined frame, was $m_R = 24.30 \pm 0.21$, implying that the nucleus of H3 is small, with $m_R(1,1,0) = 18.67$ and a corresponding radius of $r_{\rm N} = 0.53 \pm 0.05$ km. A profile is just measurable (fig. 4.10 (b)), but only within $3''$, and is very noisy. Formally, the coma magnitude from equation 3.1 is $m_c \geq 24.6$, implying a flux contribution of $\lesssim 80\%$, although the error on this is also $\sim 80\%$, making it of limited value. The profile matches the stellar PSF at all radii, within the error bars.

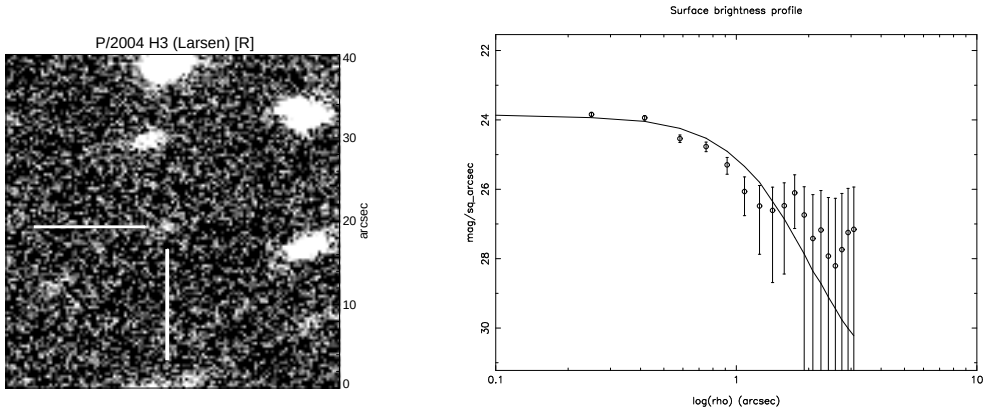

(a) (b)

Figure 4.10: Combined image of 6 r'-band frames on P/2004 H3 taken on the 5th of July 2005, in which the comet is just detectable as a very faint point source among the trailed stars. The profile is noisy due to the extreme faintness of the comet, but is consistent with an inactive nucleus.

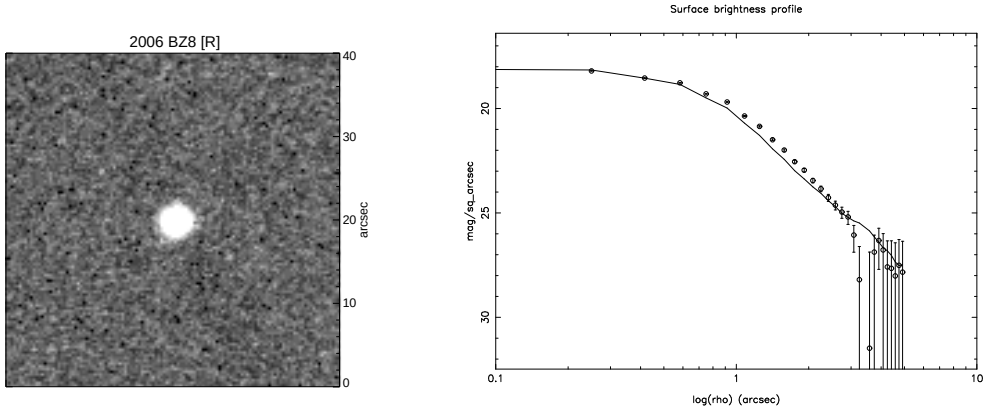

(a) (b)

Figure 4.11: Image showing the Centaur 2006 BZ8 (on 2/3/06), which was bright in individual 10 s exposures, and is clearly stellar in this combination of all 15 r'-band exposures. The profile confirms this.

4.3.10 2006 BZ8

Observations of 2006 BZ8 [hereafter BZ8] were carried out to search for activity around this newly discovered object. Such observations are frequently carried out using 2-4m class telescopes, either when a few minutes are available during a run (as was the case for BZ8, which was observed during the 2006 INT run) or through the UKAPP project[7]. The goal of such observations is to demonstrate the cometary nature of suspect objects which have been discovered and identified as asteroids by large surveys, by

[7] `http://star.pst.qub.ac.uk/~ukapp/index.html`

searching for any faint coma. Suspected comets are primarily identified by their orbits; highly elliptical or inclined orbits are 'cometary', any object with $T_J \ll 3$ is a good candidate. Snap-shots of such candidates have shown a number of them to be comets (*e.g.* Fitzsimmons et al. 2004; Snodgrass et al. 2005c; Lowry et al. 2006).

BZ8 was regarded as being almost certainly a comet, with $T_J = -1.0$. No activity was observed though, and the object was bright ($m_R = 16.858 \pm 0.003$) and stellar (fig. 4.11). A surface brightness profile entirely matched the combined frame PSF, and equation 3.1 gave a limit on any coma at $m_c \geq 21.67$, or $\leq 1.2 \pm 1.2\%$ of the flux. BZ8 is officially a Centaur[8], as it has an orbital semi-major axis of $a = 9.7$ AU, however it seems likely that it is from the Oort cloud due to its Tisserand parameter and high inclination ($i = 165°$). The absolute magnitude of BZ8 was measured to be $m_R(1,1,0) = 14.14$, corresponding to $r_N = 4.22 \pm 0.02$ km, and its colours were found to be $(V-R) = 0.62 \pm 0.01$ and $(R-I) = 0.36 \pm 0.01$. These results are not included in the discussion on the ensemble properties of JFCs in chapter 6.

4.4 Active comets

4.4.1 43P/Wolf-Harrington

43P/Wolf-Harrington was visibly active in snap-shot frames (fig. 4.12), and was immediately rejected as an unsuitable target for nucleus photometry. Upper limits on the size of the nucleus can be obtained for active comets, as the flux from the nucleus cannot be larger than the total flux measured. For 43P, the total brightness within an aperture of radius 5″ is m_R = 20.53±0.03, which gives an upper limit on the radius of $r_N \leq 2.42$ km.

The level of activity of a comet can be quantified using the quantity $Af\rho$ (A'Hearn et al. 1984), which is roughly proportional to the dust production rate of the comet,

[8] Objects with $5.5 \leq a \leq 30.1$ AU are designated Centaurs.

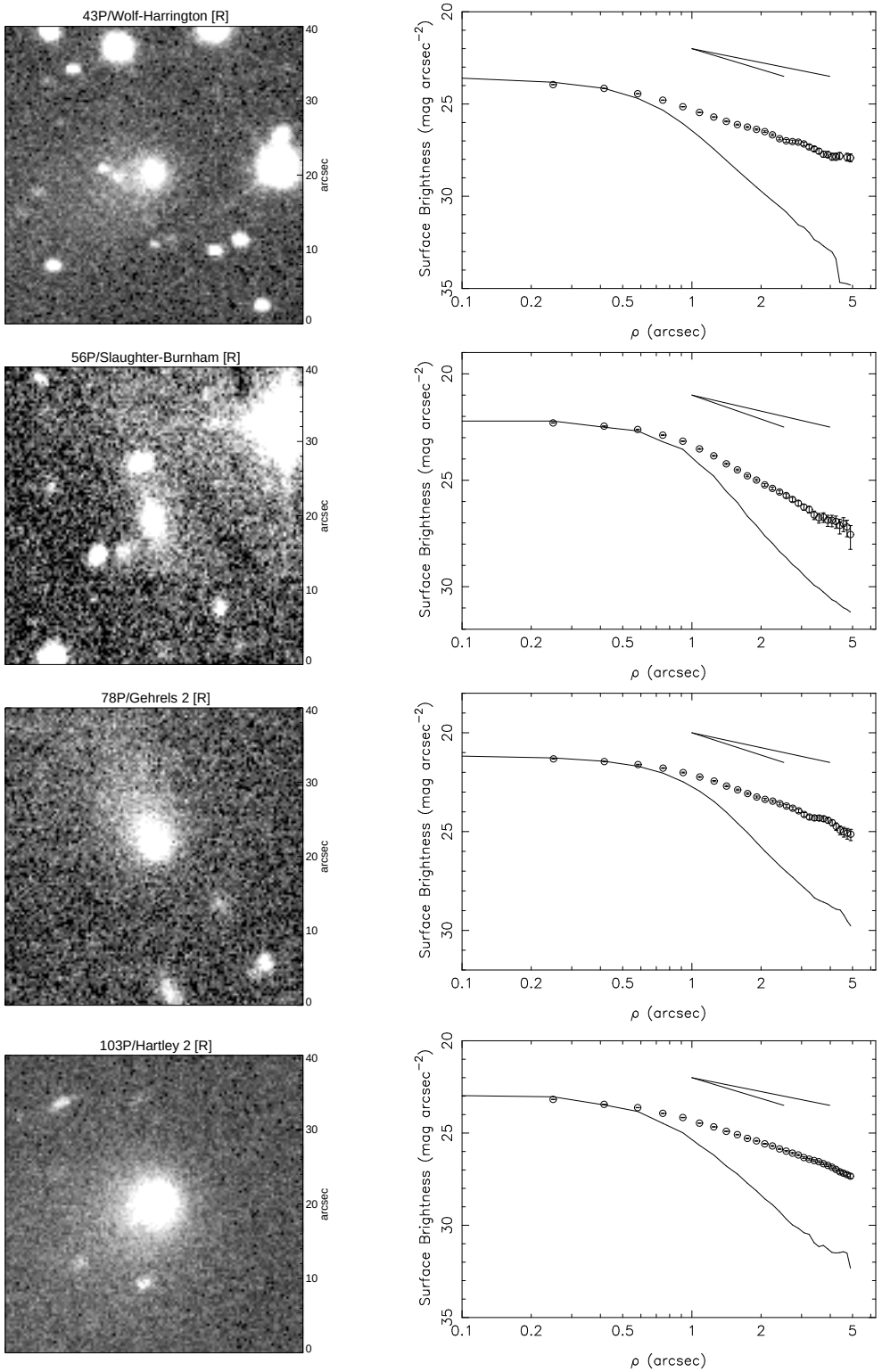

Figure 4.12: Images and surface brightness profiles for 43P, 56P, 78P and 103P (from the 2005 NTT data). The comets are visibly active. The solid diagonal lines in the top right corner of each profile show gradients of -1 and -1.5, from two theoretical models of steady state coma; the comets all have profiles with gradients ~ -1.5.

assuming steady state production. It is the product of the geometric albedo A, the radius of the photometric aperture at the comet ρ, and the filling factor f, which is the total scattering cross-section of the grains within this aperture. This quantity is calculated by

$$Af\rho[\mathrm{cm}] = \frac{(2\Delta R_\mathrm{h})^2 F_\mathrm{comet}}{\rho F_\odot}, \tag{4.2}$$

where R_h is in AU, but Δ and ρ are in cm. F_comet and $F_\odot$ are the fluxes measured at the Earth from the comet and from the Sun respectively. Expressed in this fashion, $Af\rho$ is theoretically independent of the chosen aperture, again assuming a steady state coma. For such a coma the gradient of the surface brightness profile should equal -1. For a steady state coma affected by radiation pressure on the grains the gradient should be -1.5 (Jewitt & Meech 1987); it can be seen from fig. 4.12 that the gradient of 43P's profile is ~ -1.5, meaning that the measure of $Af\rho$ is not strictly independent of ρ in this case. $Af\rho$ remains a useful measure of activity, although the chosen ρ must be noted. I take an aperture of radius $5''$, which corresponds to ρ = 9400 km for 43P, and gives $Af\rho$ = 206 $\pm$ 2 cm. This is a large value, showing high activity levels well beyond the canonical 3 AU 'cut-off' for H_2O sublimation. This comet's perihelion distance jumped from q = 2.5 to 1.5 during 1936 after a close encounter with Jupiter, and has had a considerable change in its non-gravitational acceleration (interpreted as being due to a change in the active areas of the nucleus surface: see Szutowicz 2000); it is possible that the major change in its orbit is connected to the high activity level observed.

This activity level has frustrated previous efforts to obtain a definitive measurement of the radius of the nucleus; although there have been a number of published snapshot observations of 43P, it has mostly been observed when active, even at distances beyond 4 AU (table 4.2). The upper limits obtained when the comet was active are all *below* the radii determined by Lowry et al. (1999, 2003) from images in which the comet appeared inactive. There are two possible explanations for this discrepancy; firstly, that the range in reported magnitudes is due to elongation of the comet, in which

case the full range of Δm = 0.97 mag. from the peer-reviewed literature (Lowry et al. 1999; Licandro et al. 2000b; Lowry et al. 2003; Lowry & Fitzsimmons 2005) gives a minimum axial ratio of $a/b \geq 10^{0.4\Delta m} = 2.4$. The alternative explanation is that the apparently stellar observations contained significant unresolved coma. This would be quite possible, as both were obtained with the 1.0m JKT, and surface brightness profiles and equation 3.1 reveal that $m_c \approx m_R$ in both cases, suggesting that unresolved coma could have contributed over 90% of the flux in each of these observations.

Lowry & Fitzsimmons (2005) argue for the first scenario, as Lowry et al.'s images were taken at larger $R_{\rm h}$, the two values of $r_{\rm N}$ obtained are consistent with each other and $a/b \geq 2.4$ falls within the observed range for nuclei, albeit at the high end of the distribution (see chapter 6). However, the additional limit below 2.5 km from the 2005 NTT data pushes the weight of probability towards the second explanation. Furthermore, including Hainaut et al.'s 1996 result of $m_V(1,1,0) \geq 16.4$ (MPC 27955, quoted in Licandro et al. 2000b) and using $(V-R) = 0.15 \pm 0.08$ (Lowry & Fitzsimmons 2005)[9] to convert to the *R*-band, the first scenario requires Δm = 1.82, and therefore $a/b \geq 5.3$, which is unrealistically large. Even taking the 3σ upper limit on the colour of $(V-R)$ = 0.39 gives $r_{\rm N} \leq 1.8$ km and $a/b \geq 4.3$. I therefore conclude that there was significant flux from unresolved coma present in Lowry et al.'s observations, and that 43P definitely has $r_{\rm N} \leq 2.4$ km, and possibly $r_{\rm N} \leq 1.8$ km. Tancredi et al. (2000) estimate $r_{\rm N}$ = 1.8 km from a heliocentric light-curve which shows evidence of activity out to $\sim$ 4 AU.

[9]Note that $(V-R)$ = 0.15 is a very blue colour compared to the values found for nuclei, however this is the coma colour. Two effects can produce a blue coma; the presence of gaseous emissions in the *V*-band increasing the apparent brightness in that filter, or dominance of sub-micron grains in the dust coma scattering bluer wavelengths. Where $(V-R)$ and $(R-I)$ are known one effect may be chosen over the other (*e.g.* the case of 103P/Hartley 2 discussed in section 4.4.4), as the presence of gas does not have a large effect on $(R-I)$. However, Lowry & Fitzsimmons only measured $(V-R)$, so either effect could be present.

Table 4.2: Reported observations of 43P/Wolf-Harrington

Date	$R_{\rm h}$[a]	Δ	α	m_R	m_c	$m_R(1,1,0)$[b]	$r_{\rm N}$[b]	App.[c]	Ref.
	[AU]	[AU]	[deg.]				[km]		
04/02/1992	3.04^O	2.69	18.6	20.45 ± 0.13[d]	-	$\geq$15.24	$\leq$2.57	A	Licandro et al. 2000
24/08/1995	4.87^I	4.26	10.1	21.40 ± 0.50	$\geq$21.48	14.46	3.67	S	Lowry et al. 1999
June 1996	3.9^I	-	-	-	-	≥ 16.25[e]	$\leq$1.61	A	Hainaut et al. 1996
13/06/1999	4.46^O	3.66	9.0	20.81 ± 0.14	$\geq$20.35	14.43	3.72	S	Lowry et al. 2003
12/07/2002	4.43^I	3.45	3.8	21.45 ± 0.06	-	$\geq$15.40	$\leq$2.38	A	Lowry & Fitzsimmons 2005
05/03/2005	3.30^O	2.61	13.9	20.53 ± 0.03	-	$\geq$15.37	$\leq$2.42	A	this work

[a] Superscripts I and O refer to whether the comet is inbound (pre-perihelion) or outbound (post-perihelion).
[b] Recalculated here using $m_\odot$=-27.09, p_R=0.04 and β=0.035, for consistency.
[c] Appearance is given as either A – active, or S – stellar.
[d] From reported $m_V = 20.6 \pm 0.1$, using $(V-R) = 0.15 \pm 0.08$ from Lowry & Fitzsimmons 2005
[e] From reported $m_V(1,1,0) \geq 16.4$, using $(V-R) = 0.15 \pm 0.08$ from Lowry & Fitzsimmons 2005

4.4.2 56P/Slaughter-Burnham

56P/Slaughter-Burnham was discovered in 1958, and has previously been found to have $r_{\rm N}$ = 1.56 km (Meech et al. 2004). This led to a predicted nuclear magnitude of $m_R = 22.1$ at the time of the 2006 INT observations, and the comet was well placed for time-series observations at the beginning of the night. On the first night the comet appeared anomalously bright in poor seeing, and activity was suspected. Three r'- and two V-band images were taken before moving on to other targets. On the second night conditions were photometric and the seeing vastly improved, and the comet appeared active even in initial frames in which it was blended with a field star. Further frames were taken once it had moved away from the star (fig. 4.12), which confirmed that the comet was indeed active at $R_{\rm h}$ = 3.8 AU (outbound) and allowed measurement of the colours. A total of 5×260 s r'-band frames were taken on the second night, along with one frame each in V and i'. The mean magnitude, measured on the second night when the comet was well separated from background sources, was $m_R = 20.73 \pm 0.04$, implying $m_R(1,1,0) \geq 14.90$ and $r_{\rm N} \leq 3.00$ km, in broad agreement with the measurement by Meech et al. (2004). The colours of the comet were measured to be $(V-R) = 0.51 \pm 0.05$ and $(R-I) = 0.35 \pm 0.08$, which fall in the observed range for nuclei, although it should be noted that these colours represent the colours of the coma, as the comet was active. These colours are similar to other measurements of the broad-band colours of dust comae (Lowry et al. 1999, 2003), and also appear to be in agreement with the trend of cometary dust to have more neutral (less red) colours at longer wavelengths, which is interpreted as showing that the dominant grains are larger than 1 μm in size (Jewitt & Meech 1986). It cannot be assumed that the coma has the same colour as the surface of the nucleus for highly active comets; even if the dust component is of similar composition, there is likely to be gas present also, especially in the V-band. The flux within an aperture of $\rho = 5''(\equiv 11400$ km at the comet) gives $Af\rho = 22.3 \pm 0.3$ cm.

4.4.3 78P/Gehrels 2

Three r'-band frames were taken of 78P/Gehrels 2 during the 2006 INT run, which showed the comet to be clearly active when outbound at $R_{\rm h}$ = 3.8 AU (fig. 4.12). This is not overly surprising, as Lamy et al. (2004) suggest that this comet exhibits activity at least out to $R_{\rm h}$ = 3.5 AU due to the large scatter in the heliocentric light-curve of Tancredi et al. (2000) at this distance. Lowry & Weissman (2003) measured a radius of $r_{\rm N} = 1.54 \pm 0.12$ km from a snap-shot taken when the comet was at $R_{\rm h}$ = 5.5 AU; the upper limit obtained here of $r_{\rm N} \leq 4.21$ km, from $m_R = 19.42 \pm 0.01$ and $m_R(1,1,0) \geq 14.16$, is consistent with this. The activity level, measured within $\rho = 5''(\equiv 10400$ km), was found to be $Af\rho = 18.2 \pm 0.2$ cm.

4.4.4 103P/Hartley 2

103P/Hartley 2 was observed twice during the preparation of this thesis, and was visibly active each time. During the 2005 NTT run the brightness within an aperture of radius $5''$ was m_R = 18.72±0.02, implying $r_{\rm N} \leq 4.13$ km. Within ρ = 8200 km the activity level was quantified as $Af\rho$ = 196 ± 1 cm. Such high activity is unsurprising as the comet was outbound at only 3.2 AU, and it has been observed active at 4.6 AU (Lowry et al. 2003). The radius limit is in agreement with other limits of $\leq$ 5.3 km (Licandro et al. 2000b), $\leq$ 6.4 km (Lowry & Fitzsimmons 2001) and $\leq$ 6.3 km (Lowry et al. 2003), although it has been reported that the radius is much smaller than these limits; Groussin et al. (2004) give a radius of 0.71 ± 0.13 km from *Infrared Space Observatory* observations of the comet when it was active at $R_{\rm h}$ = 1.2 AU in February 1998. These authors also show that for such a small nucleus to produce the high levels of activity observed (from H_2O gas production rates), the required active area must reach 100% at perihelion, at odds with the general trend for active areas to make up only a small fraction of the nuclear surface (A'Hearn et al. 1995).

103P was observed again during the 2006 INT run, despite a strong suspicion that it may still be active at R_h = 5.0 AU, as this comet is a possible target for the *Deep Impact* extended mission[10]. The comet was detected in two r'-band frames taken on the first night, and was clearly active. Single V and i' frames were taken on the first night, and one frame in each of $Vr'i'$ was taken on the second night, to allow calibration onto the standard Landolt magnitude scale. The measured $m_R = 21.00 \pm 0.05$ implies another radius upper limit of $r_N \leq 4.45$, while the flux within $\rho = 15600$ km gives $Af\rho = 47.2 \pm 0.7$ cm. The comet has colours of $(V-R) = 0.16 \pm 0.09$ and $(R-I) = 0.35 \pm 0.08$. The rather blue $(V-R)$ measurement could reflect the presence of significant flux from gas emissions within the V-band, such as the C_2 bands at 5165 and 5635 Å, while the $(R-I)$ colour is similar to that found for nuclei and dust comae.

[10]The proposed *Deep Impact* extended mission (*DIXI*) is to fly the surviving *Deep Impact* mother-ship, which still has working instruments including two colour cameras, onto another nucleus. The space-craft can reach one of two possible comets with its current orbit and remaining fuel, 85P/Boethin or 103P. The primary target, 85P, has not been seen since 1986, and has had close encounters with Jupiter since then, leaving its orbit based on 45 observations at two apparitions, and poorly constrained. An effort is underway to recover the comet to improve the orbit and to provide a size measurement, but the search area is large. 103P therefore remains a potential target for *DIXI*, making further physical studies and precise astrometry useful to this mission.

Table 4.3: Derived values and limits on radii and activity from snap-shot photometry.

Comet	m_R	m_c[a]	$m_R(1,1,0)$	r_N [km]	$Af\rho$ [cm][b]
UNDETECTED					
72P	≥ 22.2[c]	-	≥ 17.6[c]	≤ 0.88[d]	≤ 0.45[d]
75P	-	-	-	-	-
104P	$\geq$23.3[c]	-	$\geq$18.5[c]	$\leq$0.56[d]	$\leq$5.9[d]
135P	≥ 22.7[c]	-	≥ 17.6[c]	≤ 0.87[d]	≤ 0.88[d]
X2	-	-	-	-	-
T1	≥ 24.4[c]	-	≥ 19.1[c]	≤ 0.43[d]	≤ 0.57[d]
UNRESOLVED					
8P	21.61±0.03	$\geq$25.1 (4.3″)	12.88±0.03	7.58±0.12	-
44P[e]	22.62±0.12	$\geq$26.9 (2.5″)	15.83±0.12	1.96±0.11	$\leq$40.4[d]
44P[f]	22.49±0.06	$\geq$23.3	15.95±0.06	1.84±0.05	$\leq$1.7[d]
70P	22.53±0.15	$\geq$23.9	15.59±0.16	2.18±0.15	$\leq$23.7[d]
114P	22.95±0.11	$\geq$24.5 (4.0″)	17.34±0.11	0.97±0.05	$\leq$0.24[d]
120P	23.52±0.13	$\geq$23.1	17.84±0.13	0.77±0.05	$\leq$2.9[d]
131P	22.77±0.10	$\geq$23.1	17.49±0.10	0.87±0.04	$\leq$0.50[d]
160P	23.69±0.18	$\geq$28.0 (1.3″)	17.58±0.18	0.87±0.07	$\leq$4.7[d]
A1	22.63±0.07	$\geq$22.1	15.31±0.07	2.48±0.08	$\leq$5.7[d]
H3	24.19±0.21	$\geq$24.6 (3.0″)	18.55±0.21	0.56±0.06	$\leq$0.69[d]
BZ8	16.88±0.01	$\geq$21.7	14.16±0.01	4.22±0.02	$\leq$41.4[d]
ACTIVE					
43P	20.53±0.03	-	$\geq$15.37	$\leq$2.42	206±2
56P	20.73±0.04	-	$\geq$14.90	$\leq$3.00	22.2±0.3
78P	19.42±0.01	-	$\geq$14.16	$\leq$4.21	18.2±0.2
103P[e]	18.72±0.02	-	$\geq$14.21	$\leq$4.13	196±1
103P[f]	21.00±0.05	-	$\geq$14.04	$\leq$4.45	47.2±0.7

[a]Coma magnitude within $\rho = 5''$ (unless stated otherwise) measured using equation 3.1.
[b]$Af\rho$ measured through an aperture of radius 5″.
[c]3σ limiting magnitudes.
[d]3σ upper limits.
[e]Results from 2005 NTT observations.
[f]Results from 2006 INT observations.

Chapter 5

Results from time-series observations

This chapter presents the results for each comet with time-series data. The observed sequences vary in length, between ~ 20 measurements over a few hours on a single night for 137P/Shoemaker-Levy 2 to over 100 individual data points over a full week for 40P/Väisälä 1. The following sections describe the results for each comet found through application of the techniques described in chapter 3. The results are summarised in table 5.1 at the end of the chapter.

5.1 7P/Pons-Winnecke

7P/Pons-Winnecke appears stellar in each of the 42 individual *R*-band images. A combined image (fig. 5.1 (a)) was produced using the technique described in section 3.1 to remove fixed objects, cosmic rays and the background sky. The image of 7P produced using the 28×120 s *R*-band exposures taken on the first night of the 2004 NTT run is equivalent to a single 56 minute exposure. The brightness profile of the comet measured in this combined image is shown in fig. 5.1 (b). It is indistinguishable from the image PSF obtained from the profile of a bright star measured in the deep star field image.

Limits on any unresolved coma are found using equation 3.1; the surface brightness of the coma at $\rho = 5''$ was measured to be $\Sigma_c(5) \geq 30.8$ mag. arcsec^{-2}, giving $m_c(5) \geq 25.3$. The integrated magnitude of the comet was found to be $m_R = 22.465 \pm 0.016$, meaning that any unresolved coma contributes $\leq 10^{0.4(m_R - m_c)} = 7 \pm 16\%$ of the flux from 7P. The nucleus was effectively inactive during these observations.

For 7P the difference in m_R due to the change in R_h, Δ and phase angle between the first and last frame was found to be $\delta m_R = 0.008$ mag, considerably smaller than the uncertainty on the individual measurements. As the conversion to absolute magnitudes is therefore unnecessary, apparent magnitudes are used to produce a light-curve.

The null hypothesis is that there is no periodic variation; a $M = 0$ constant bright-

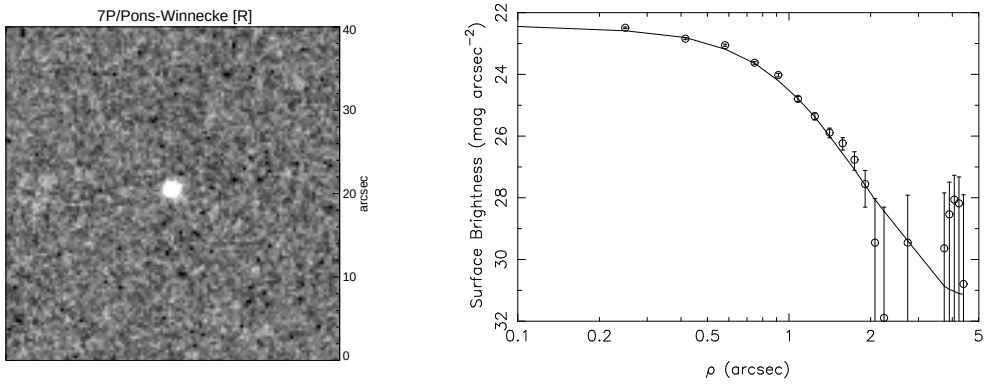

(a) (b)

Figure 5.1: (a) Co-added image of 7P from 28 frames taken on the January 20th 2004. Each frame had an exposure time of 120s, giving this combined frame an equivalent exposure time of 56 min. The shift-and-add procedure used to produce this image was designed in such a way to remove cosmic rays, field stars and the background sky, leaving only the comet. (b) Surface brightness profile of 7P. The profile is indistinguishable from the scaled stellar PSF, implying that the comet is a point source, and therefore inactive.

ness model gives $\chi^2/\nu = 2.22 \approx 5.5\sigma$. I can therefore reject the null hypothesis at a 5σ level and be confident that there is a real variation in the brightness of the comet. Fitting a first-order Fourier model to the data for a range of periods produces the periodogram shown in fig. 5.2. There are 4 minima which fall close to the horizontal line marking $\chi^2/\nu = 1 + \sqrt{2/\nu} = 1.23$ in the periodogram. The first, at ~ 1 hour, can be ignored as it is due to the data sampling period. The second grouping, with the strongest minimum at $P_{\rm fitted} = 0.165 \pm 0.006$ days $= 3.95 \pm 0.15$ hours, produce acceptable light-curves. With only two nights data, I cannot differentiate between the 3 minima; the central minimum is fractionally lower, and statistically acceptable with $\chi^2/\nu = 1.22 < 1.23$, but the others are close to this ($\chi^2/\nu = 1.23$ and 1.25) and all 3 produce equally acceptable light-curves, as determined by visual inspection of the phased data. I therefore quote the best-fit period to be $P_{\rm fitted} = 3.95 \pm ^{0.80}_{0.54}$ hours, where the uncertainty covers the acceptable periods either side of the most probable period in fig. 5.2. Assuming that the variation in brightness is due to the nucleus being a rotating non-spherical body, the rotation period $P_{\rm rot}$ is twice the fitted period $P_{\rm fitted}$. This gives $P_{\rm rot} = 7.9\ ^{+1.6}_{-1.1}$ hours and the expected double-peaked light-curve (fig. 5.3). More data may constrain the period further; it is likely that it would have been possible to choose between the three pos-

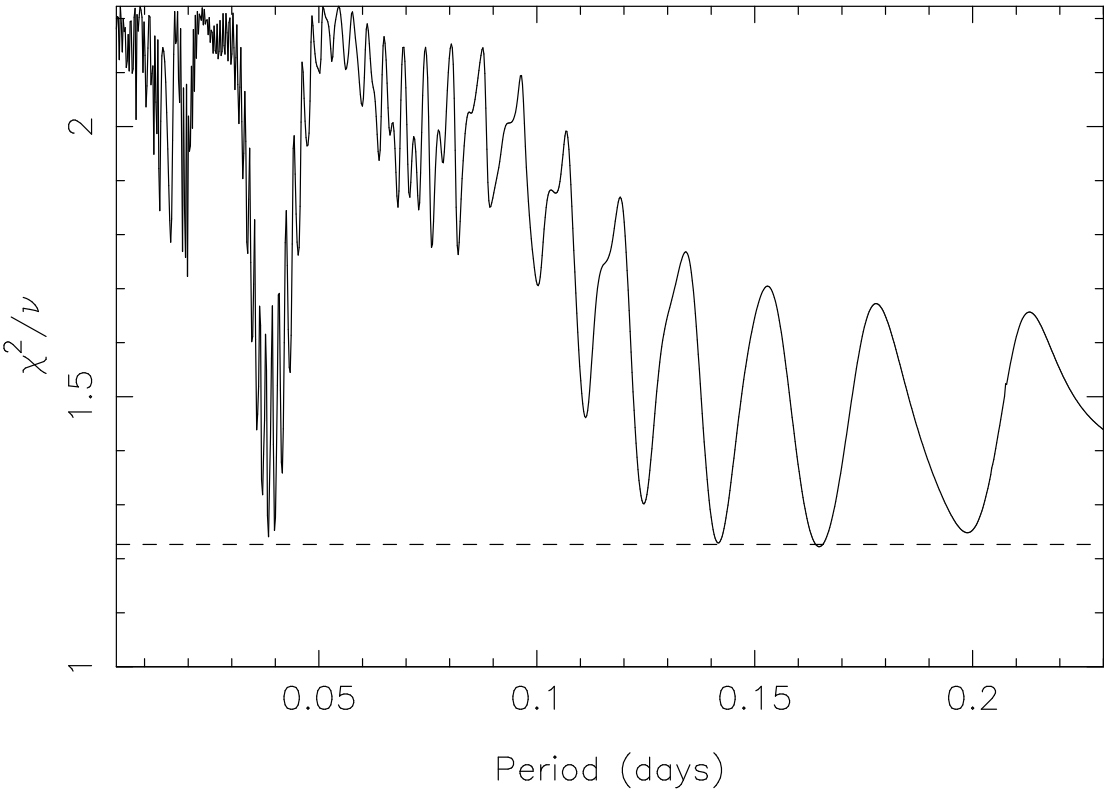

Figure 5.2: Periodogram for 7P, showing reduced χ^2 against period. The horizontal line shows the expected value of χ^2/ν for 1σ residuals. There are a number of periods which give minima close to this line. The first can be rejected, and is due to the sampling period, but the group around $P_{\rm fitted} \sim 0.16$ days all produce acceptable light-curves. The data do not allow choice of one of these periods as the 'correct' value, so I take $P_{\rm rot} = 7.9\ ^{+1.6}_{-1.1}$ hours, from the period with the deepest minima, but with the uncertainty encompassing the full range of acceptable periods. Beyond the range of periods shown the periodogram again rises and is undefined at a number of longer periods where the fitting routines diverge. There are no further realistic solutions: the plotted range is restricted to that shown to show the detail at short periods.

sibilities had the third night of the run been clear. As can be seen in fig. 5.3 there is some scatter around the average magnitude measured in each block, meaning that the fit is really based on 6 'points' at these average values. The points in each block are consistent with the averages for each though, so these average values are well determined. Although the resultant period determination is uncertain, the constraint placed on the rotation period by this result is sufficient to allow comparison of the spin-rate of 7P with those measured for other nuclei, which is the main aim of this work. Fitting a higher order model to the data did not produce an improved χ^2/ν for $M = 2$ or higher orders; with such sparse data it would have been difficult to justify a choice of a higher

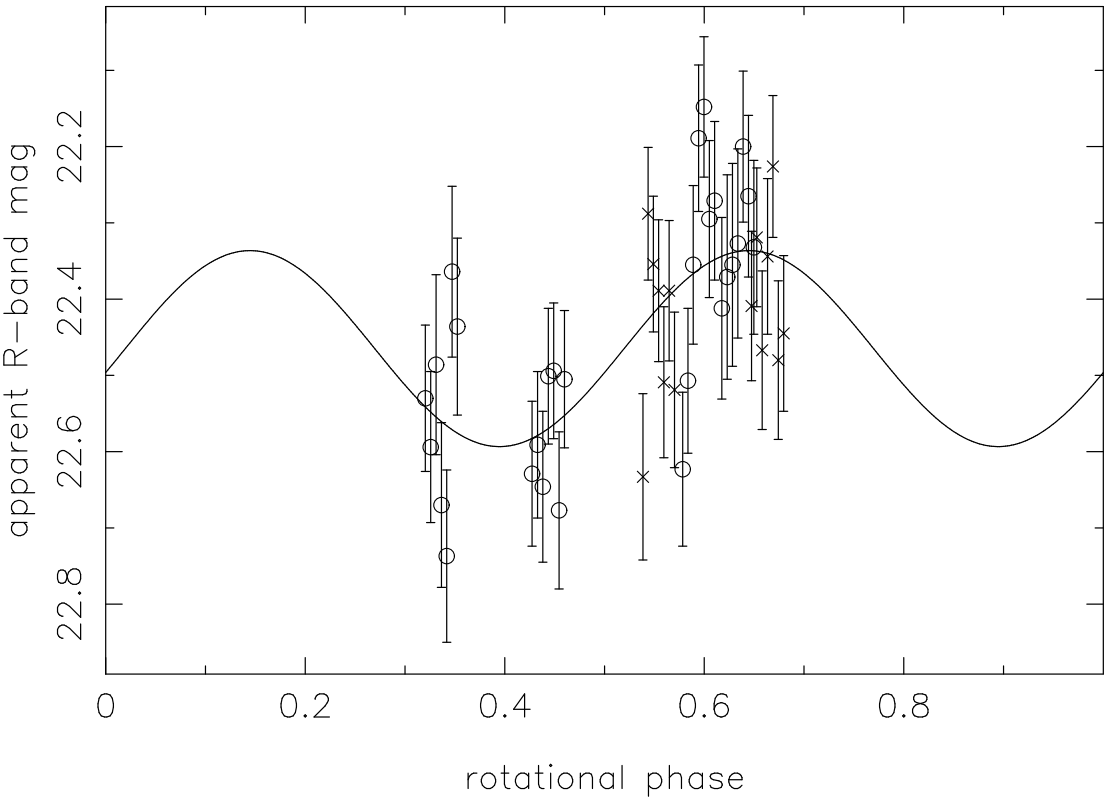

Figure 5.3: Folded light-curve for 7P, period = 7.89 hours. This was the strongest periodicity found, however the period could also be 5.8 or 9.5 hours. Data from the first night is plotted as circles, and from the second night as crosses.

order fit without a significant improvement in reduced χ^2.

The peak-to-trough range in brightness of the nucleus $\Delta m = 0.30 \pm 0.05$ mag. Assuming that the brightness variations are due to the changing observed cross-section of a rotating elongated nucleus, this gives a lower limit on the axial-ratio (using equation 3.10) of $a/b \geq 1.3 \pm 0.1$ for 7P.

The mean measured apparent magnitude gives $m_R(1,1,0) = 15.532$ and therefore $r_{\rm N} = 2.24 \pm 0.02$ km. This mean radius gives us the size of the equivalent spherical nucleus; taking into account an ellipsoidal model with $a/b = 1.3$ gives dimensions of the nucleus of $a \times b = 2.75 \times 2.08$ km. These results are consistent at a 3σ level with the result found by Lowry & Fitzsimmons (2001), who measured a radius of $r_{\rm N} = 2.7 \pm 0.1$ km, assuming that their snap-shot observation was taken at a light-curve maximum, which in the model above would be equivalent to $r_{\rm N}$ = 2.4 km.[1]

[1]Note that the equivalent $r_{\rm N}$ observed at maximum light for a model ellipsoid with semi-axes $a \geq$

One set of observations were taken each night through V and I filters in addition to the time-series photometry in the R-band. Interpolation between R-band measurements was used to find the apparent m_R at the time of the V and I-band observations, and thus measure the colour indices $(V-R)$ and $(R-I)$. For 7P, $(V-R) = 0.40 \pm 0.05$ and $(R-I) = 0.41 \pm 0.06$, both of which are slightly redder than the Sun and in the expected range for cometary nuclei (see chapter 6).

5.2 14P/Wolf

The same procedures were followed for 14P/Wolf, which was also observed during the 2004 NTT run. A co-added R-band image of the 29 individual frames taken on each night appears stellar (fig. 5.4 (a)), with an effective exposure time of 106 minutes. For 14P the average coma surface brightness from the two nights was found to be $\Sigma_c(5) \geq$ 31.0 mag. arcsec^{-2} (fig. 5.4 (b)). Using equation 3.1 and the integrated magnitude of the comet $m_R = 22.281 \pm 0.007$, this gives a limit on the flux from the coma of $\leq 5 \pm 10\%$ of the observed flux of 14P. Again the nucleus is therefore assumed to be inactive.

Figure 5.5 shows the first order periodogram for 14P. Although there are no periods with the expected $\chi^2/\nu < 1.19$, there is a strong minimum at $P_{\text{fitted}} \approx 0.16$ days which corresponds to a 4.3σ fit. The null hypothesis, that the brightness of the comet is constant and the variations are due entirely to observational errors, is rejected at a 19σ confidence level. There is clearly a periodic brightness variation, as can be seen in fig. 5.6, which shows the photometric data folded onto twice the strongest period, assuming a double-peaked rotational light-curve. This gives $P_{\text{rot}} = 7.53 \pm 0.10$ hours. The reason why the minimum χ^2/ν is not ~ 1 is that the fitted function used to describe the periodicity is a sinusoid, but this is only an approximation to the light-curve shape.

$b = c$ is not equal to the longest dimension a, but is found by equating the area cross sectional areas $\pi r_{\text{N}}^2 = \pi ab$. The effective radius of the equivalent sphere at minimum light is equal to the semi-minor axis, $r_{\text{N}} = b$.

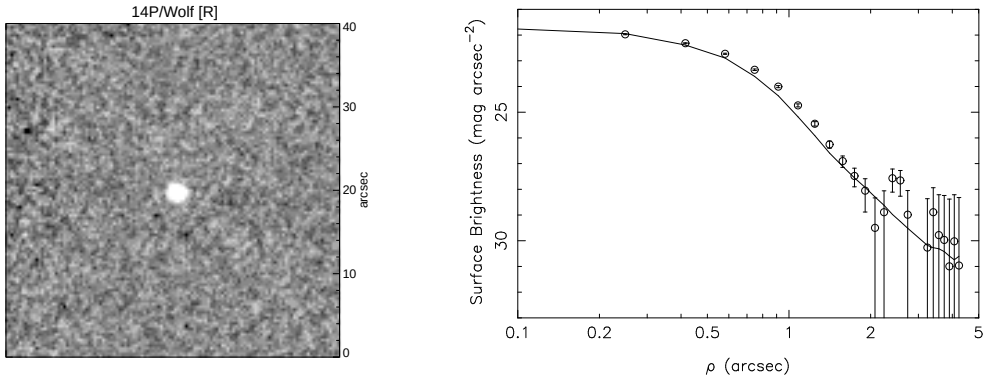

(a) (b)

Figure 5.4: Co-added image (a) of all 29 frames taken of 14P on the January 20th 2004. Each frame had an exposure time of 220s, giving this combined frame an equivalent exposure time of 1.77 hr. 14P appears stellar; the surface brightness profile (b) and calculated limits on the coma brightness of $\leq 5\%$ on the flux show that it was most likely inactive at the time of observation.

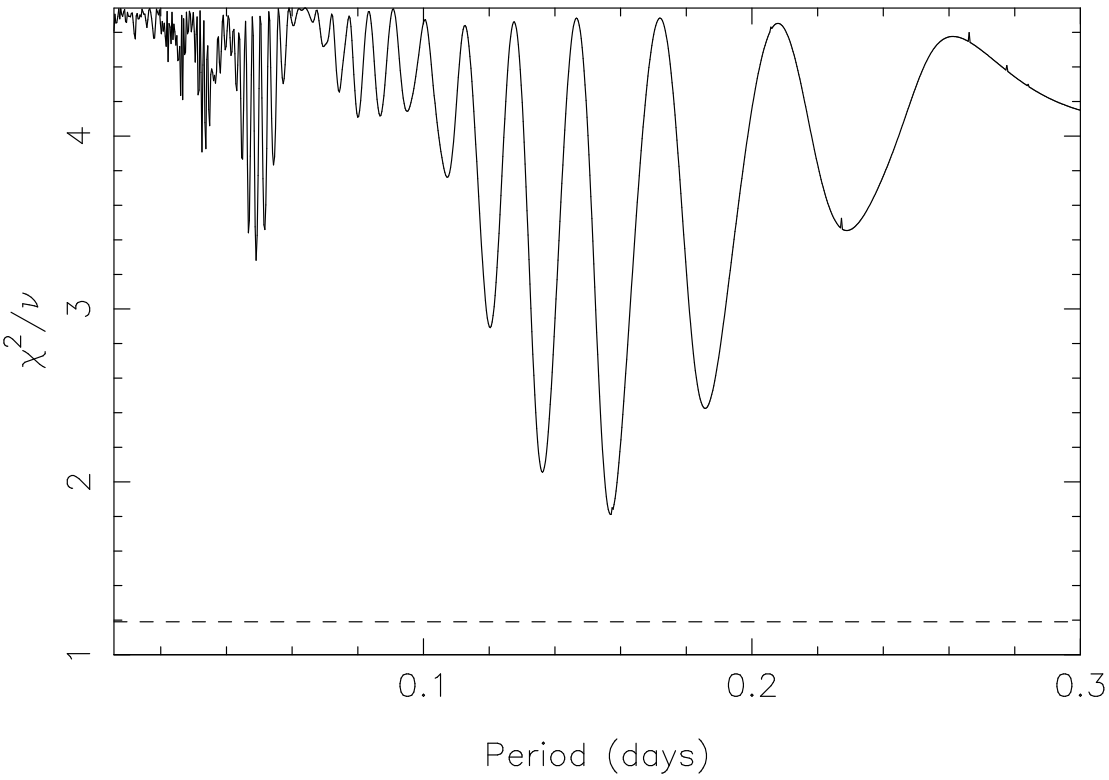

Figure 5.5: Same as fig. 5.2, for 14P. The strongest period found is at $P_{\rm fitted} = 3.72 \pm 0.05$ hours, corresponding to rotation period of $P_{\rm rot} = 7.53 \pm 0.10$ hours.

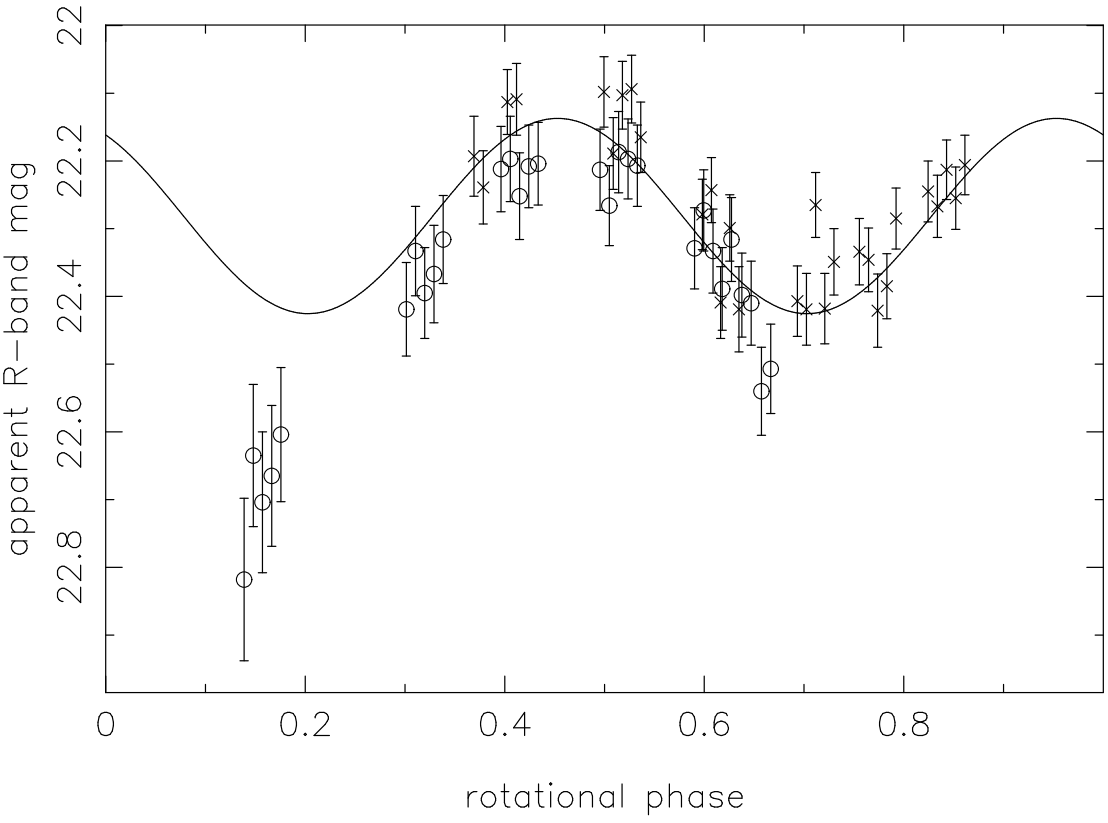

Figure 5.6: Folded light-curve for 14P, period = 7.53 hours.

The shape of the light-curve in fig. 5.6 suggests that a higher order fit, with two minima of different depths, may give a better model to this data. This suggests a departure from a simple tri-axial ellipsoid. The strongest minimum in a second order fit periodogram is at the same period, giving a slightly saw tooth shaped model light-curve and a marginal reduction in χ^2/ν, but this still gives light-curve minima with equal depths. A group of minima around $P_{\rm rot} = 7.5$ hours produce asymmetric light-curves, however they do not give a formal improvement on the fit as they do not lower χ^2/ν relative to the 1st order fit.

The observed data (table A.2) has a range in magnitudes $\Delta m = 0.55 \pm 0.05$ mag., which, using equation 3.10, allows description of 14P as a tri-axial ellipsoid with axial ratio $a/b \geq 1.7 \pm 0.1$. However the axial ratio gives only a very simplified description of shape; it does not contain enough information to adequately describe an irregularly shaped nucleus.

The mean apparent magnitude of 14P gives a mean effective radius of $r_{\rm N} = 3.15 \pm$

0.01 km, again assuming an albedo of 4%. This implies dimensions of the nucleus of $a \times b = 4.5 \times 2.7$ km. This is larger than the snap-shot radius found by Lowry et al. (2003) of $r_N = 2.51 \pm 0.13$ km, but consistent at a 2σ level with the observed shape induced light-curve. Considering the lack of observed coma, contamination by dust is unlikely. Alternately, it can be assumed that Lowry et al. measured the light-curve at a minimum, but due to different viewing geometry at that time the projected cross-sectional area was lower than at the minima observed in this work (*i.e.* they observed the nucleus when the orientation of the rotation pole was closer to $\theta = 90^\circ$ from the line of sight, and saw the nucleus closer to 'narrow end on'). If this were the case, then they would have observed a larger a/b, had they performed time-series observations at that time, than the minimum value found here. Taking the well measured effective r_N above (which would not be altered by observing a time-series at different θ), and setting $b = 2.51$ on the assumption that Lowry et al.'s r_N is the radius of the minimum cross-sectional area (*i.e.* b), gives $a/b = 2.2$ by rearranging equation 3.13. This is slightly larger than the observed average elongation of other comets, although quite reasonable considering measurements are of the minimum a/b. While considering this as a possibility, I choose to quote the minimum axial-ratio as the value found from the light-curve data alone ($a/b \geq 1.7$) rather than taking a single snap-shot as proof of greater elongation.

Colour indices of $(V-R) = 0.57 \pm 0.07$ and $(R-I) = 0.51 \pm 0.06$ were measured for 14P, placing it towards the red end of the observed range in colours for JFCs. This is in sharp contrast with the colours measured by Lowry et al. (2003), which at $(V-R) = 0.02 \pm 0.22$ and $(R-I) = 0.25 \pm 0.35$ made 14P the bluest cometary nucleus, and considerably bluer than the Sun, although the large error bars on their result do overlap with the one presented here at a 2σ level. The large uncertainties are due to the poor atmospheric conditions experienced at the time of observation by this earlier work. The new data provide a much more reliable measurement of the nucleus surface colour, and I believe that the change is due to improved measurement, not any physical change in the comet during the 4.5 years (including a perihelion passage in November 2000)

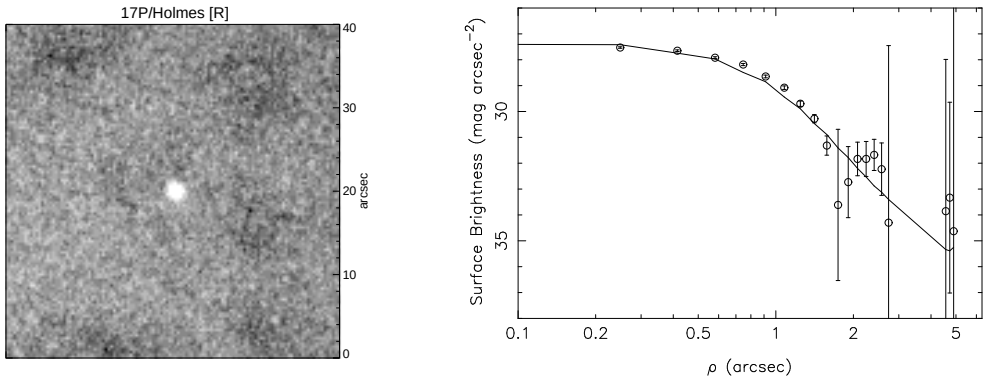

(a) (b)

Figure 5.7: Image showing 17P, made up of 25×100 second exposures taken on the second night. The comet appears to be inactive, which is confirmed by the close match of the comet and stellar profiles.

between the observations.

5.3 17P/Holmes

17P/Holmes appears to have been inactive at the time of observation. Figure 5.7 (a) shows a combined image showing only the comet, and is made up of all 25 *R*-band exposures taken on the second night of the 2005 NTT run, giving an effective exposure of 2500 seconds = 42 minutes. A surface brightness profile (fig. 5.7 (b)) shows no sign of activity, and equation 3.1 puts a limit on any unresolved coma at $m_c \geq 24.6$, or $\leq 14 \pm 29$ % of the total flux.

The photometric data is given in table A.3. The null hypothesis (that there is no periodic variation, and all scatter is due to noise around the mean magnitude) is only rejected at the 2σ level. Figure 5.8 shows the periodogram for 17P, with χ^2/ν against period in days. There are a total of 39 data points in the *R*-band, so $\sqrt{2/\nu} = \sqrt{2/(39-3)} = 0.236$. There are clearly a number of solutions within the dotted lines marking $\chi^2/\nu = 1 \pm 0.236$. With only 1.5 nights of data it is impossible to choose between the possible periods. Those marked 'A' in fig. 5.8 can be rejected as they are at periods between half and 1.5 hours, and are due to the various aliases created by observing the comet in blocks with temporal separation of that order. Figure 5.9 shows

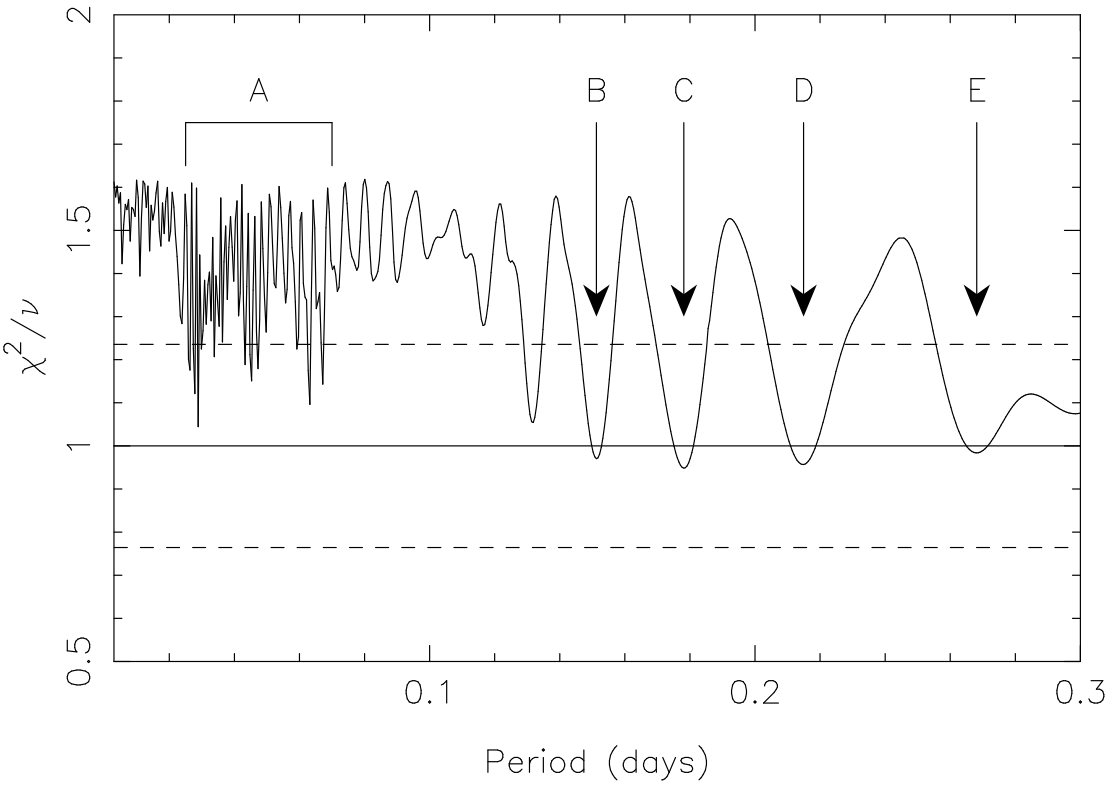

Figure 5.8: Periodogram for 17P. There are many statistically acceptable minima: those marked 'A' are at periods between 30 and 90 minutes and are due to the data sampling frequency. The data folded onto the periods with each of the four strongest minima are shown in fig. 5.9.

the data folded onto the rotation periods corresponding to each of the four periods with $\chi^2/\nu \approx 1$ (marked B–E), and note that they each produce a visually acceptable light-curve. The four minima are found at $P_{\rm fitted}$ = 3.6 (B), 4.3 (C), 5.2 (D) and 6.4 (E) hours, and correspond to rotation periods of $P_{\rm rot}$ = 7.2, 8.6, 10.3 and 12.8 hours.

While the period remains uncertain, it can be seen that 17P was observed at a light-curve minimum on the first night, and at around maxima on the second (fig. 5.9 plots the data from night 1 as open circles and the night 2 data as crosses). Unfortunately there is a gap in the data on the second night, due to the comet passing in front of a star, which appears to have coincided with the minimum between these maxima, assuming that one of the above periods is correct. The calibration of the data from the two different nights is accurate; repeating the method with different comparison stars produced no significant difference in the calibrated magnitudes. The uncertainty on the night-to-night calibration is much smaller than the error bars on individual points. Therefore the

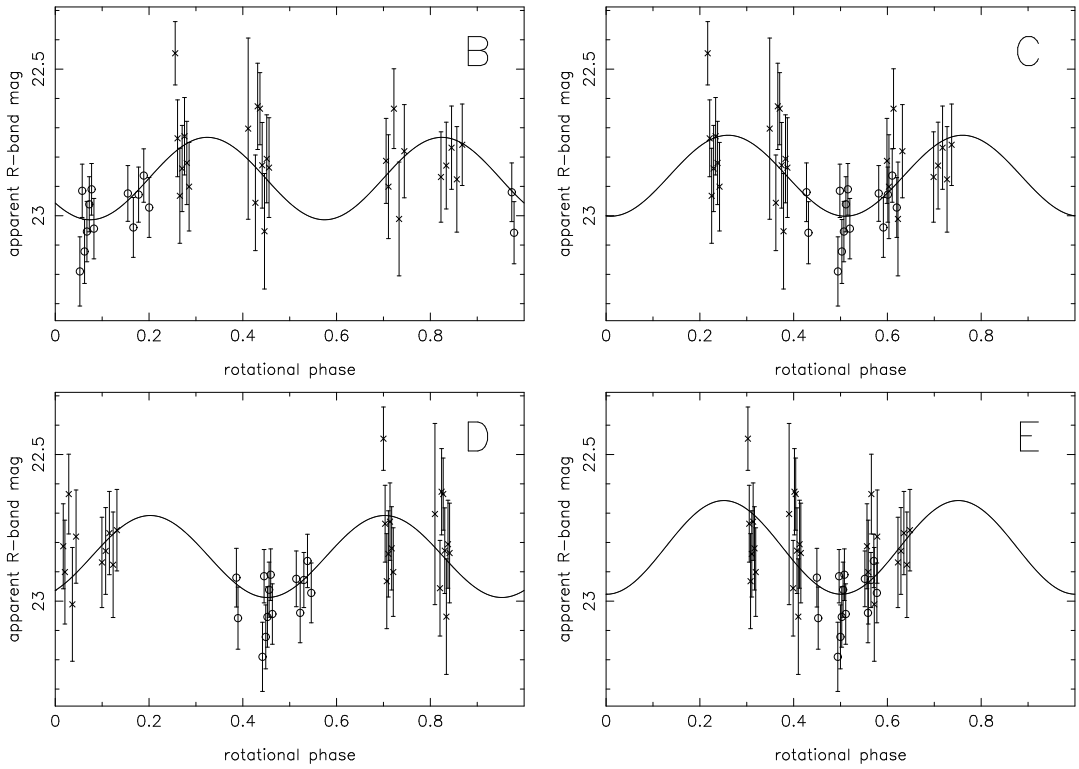

Figure 5.9: 17P photometric data folded onto each of the four strongest periods found in the periodogram (fig. 5.8). These have $P_{\rm rot}$ = 7.2 (B), 8.6 (C), 10.3 (D) and 12.8 (E) hours. The 1.5 nights of data acquired on this comet are insufficient to choose one of these periods over the others.

full range of the light-curve was observed, and from Δm = 0.3 mag. a lower limit on the elongation of the nucleus of $a/b \geq 1.3$ is inferred.

The mean apparent magnitude of 17P was measured to be $m_R = 22.86 \pm 0.02$. Using equation 3.3, this gives an effective radius of $r_{\rm N} = 1.61 \pm 0.01$ km for the equivalent spherical body. Taking $a/b = 1.3$, this corresponds to dimensions of the nucleus of $a \times b = 2.0 \times 1.5$ km. This is in excellent agreement with the $r_{\rm N}$ = 1.71 km measurement from a snap-shot observation acquired by Lamy et al. (2000) using the HST.

Measuring the elongation from the range of the light-curve requires that the variations are in fact due to changes in the projected surface area of the comet, and not due to large scale changes in albedo. For 17P one colour block, containing 2×100s V and I-band frames in the sequence *RVRIRVRIR*, was taken on the first night and two blocks on the second. The colours measured were consistent within the uncertainties on each, supporting the assumption that variations are due to the shape of the nucleus, and give

mean colours of $(V-R) = 0.41 \pm 0.07$ and $(R-I) = 0.44 \pm 0.08$.

5.4 36P/Whipple

36P/Whipple was observed twice during this work; over 1.5 nights during the March 2005 NTT run, and over a further two nights a year later with the INT. The reason for returning to the same comet was that, as with the others observed during the shortened NTT run, its rotation period was not confirmed at the first attempt. What made 36P particularly interesting however was the fact that the rotation period suggested by the first data set was very short, at around 3.5 hours. Such a period implied a minimum density considerably higher than any other previously observed nucleus; equation 3.19 gave a minimum density required for gravitational cohesion of 1.2 g cm^{-3}, greater than that of water ice. This preliminary result was presented at the 2005 ACM conference (Snodgrass et al. 2005a), and attracted some interest (*e.g.* Toth & Lisse 2006), although it was realised at the time that further data would be required before publishing such a result. Here I first describe the results from the NTT run, before presenting those from the 2006 INT run and discussing the interpretation of both data sets.

5.4.1 NTT data: March 2005

36P was at $R_{\rm h}$ = 4.1 AU and moving at a relatively slow rate on the sky, allowing 200s exposures to be taken while still tracking at the sidereal rate without distorting the comet image. The comet was found to be bright ($m_R = 21.37 \pm 0.02$) and appeared stellar in each individual frame. A combined image (fig. 5.10) also appears fairly stellar, but there is a slight extension towards the East (right in fig. 5.10 (a)) and a surface brightness profile (fig. 5.10 (b)) shows clear signs of coma. Equation 3.1 gives a coma magnitude of $m_c \geq 22.4$, which corresponds to 40 $\pm$ 23% of the total flux being due to steady state coma. The flux within an aperture of $\rho = 5'' \equiv 12000$ km gives $Af\rho =$

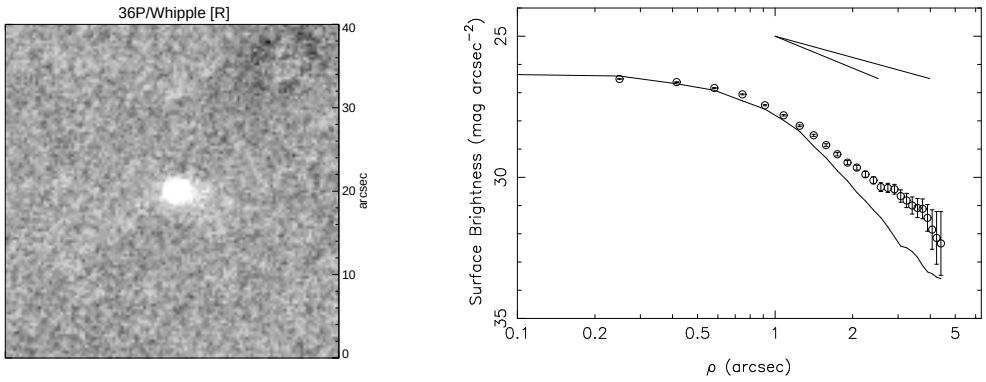

(a) (b)

Figure 5.10: Image showing 36P, made up of 17×200 second exposures taken on the 6th March 2005. There is some possible activity in the image, which appears to be confirmed by the active profile, where a clear difference between the comet and background PSF is visible.

20.2 ± 0.3, which is more properly considered an upper limit since the slope of the profile is steeper than the $m = -1.5$ limit for a steady state coma. Such activity at $R_h > 4$ AU is surprising for a comet that has never been seen to show any large amount of activity.

It is clear that the total flux is still dominated by the flux from the nucleus, as obvious variations can be seen in the brightness of the comet in table A.4 and in fig. 5.13, which shows the varying brightness in the original data folded onto a period of 3.5 hours. This period corresponds to twice the fitted period of 0.074 days given by the strongest minimum in the periodogram (fig. 5.11); a minimum of $\chi^2/\nu = 0.55$, which is actually below the expected value, but within 2σ of the expected $\chi^2/\nu = 1$. The null hypothesis of constant brightness is rejected at a 6σ level, implying that the variations are real.

The unknown contribution to the flux from the coma causes uncertainty in both the average magnitude of the comet and the amplitude of the light-curve variation. Assuming a steady state coma, its contribution is modelled as a constant flux level, which is then subtracted from the data to leave the variation due to the nucleus. A constant coma contribution acts to raise the overall brightness, and to reduce the amplitude of the observed variation, as it will contribute relatively more when the nucleus cross section is at a minimum than at maximum. Taking the measured coma contribution from the sur-

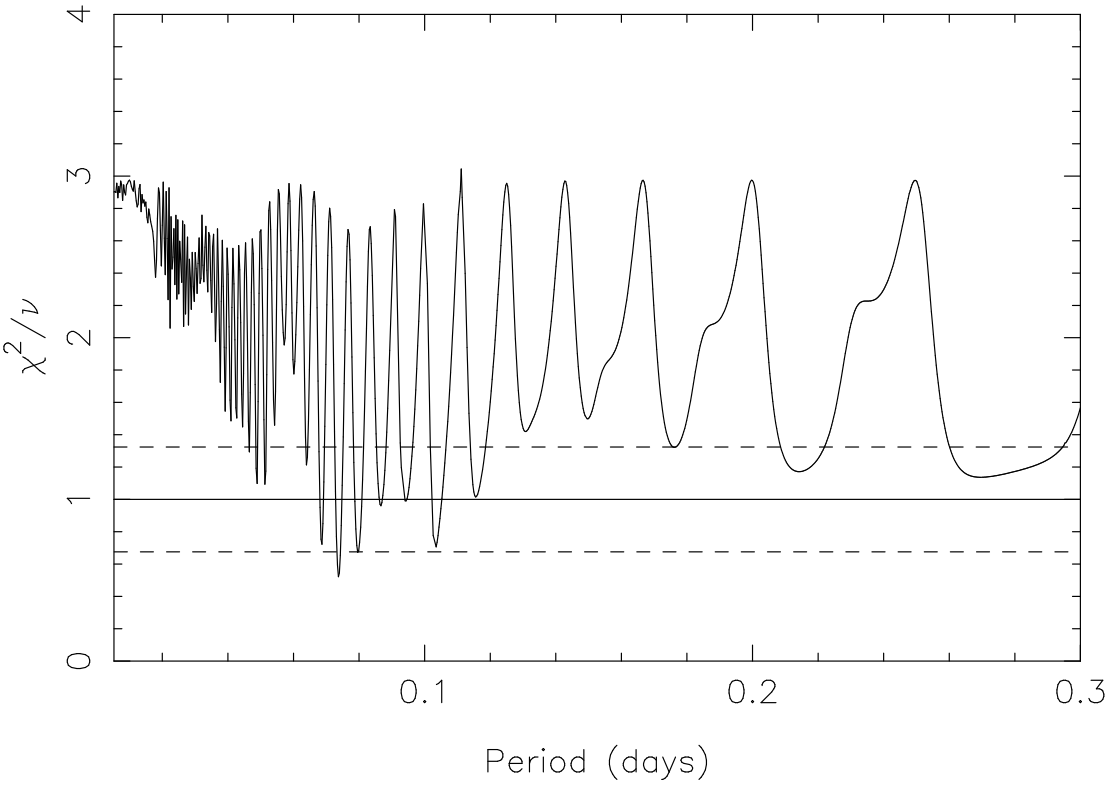

Figure 5.11: Periodogram for 36P, using the total observed brightness of the comet.

face brightness profile (40% of the average total flux), and removing this from the data, gives approximate 'nuclear' magnitudes. Figures 5.12 and 5.13 show the periodogram and folded light-curve for these data. The rotation period found does not change; the presence or lack of coma at this level does not affect the measurement of this value. It can clearly be seen that the amplitude of the light-curve is greatly increased from Δm = 0.4 mag to Δm = 0.65 mag, and that this increase in the size of variation relative to the size of the error bars on individual data points increases the χ^2/ν. There are no longer any minima within $\chi^2/\nu = 1 \pm \sqrt{2/\nu}$; the strongest minimum in the coma subtracted periodogram has χ^2/ν = 1.8, corresponding to 2.3σ. The mean magnitude is increased by removing a coma component; the original data has $m_R = 21.37$, removing 40% of this flux gives $m_R = 21.94$. These values are all calculated taking the value of 40% to be fixed; in reality the 23% uncertainty on the flux contribution leads to large error bars on any coma subtracted photometry.

The sizes and shapes implied by the two light-curves are different. The original data give a radius for the equivalent sphere of 2.5 km, and an axial ratio of $a/b \geq 1.4$, and

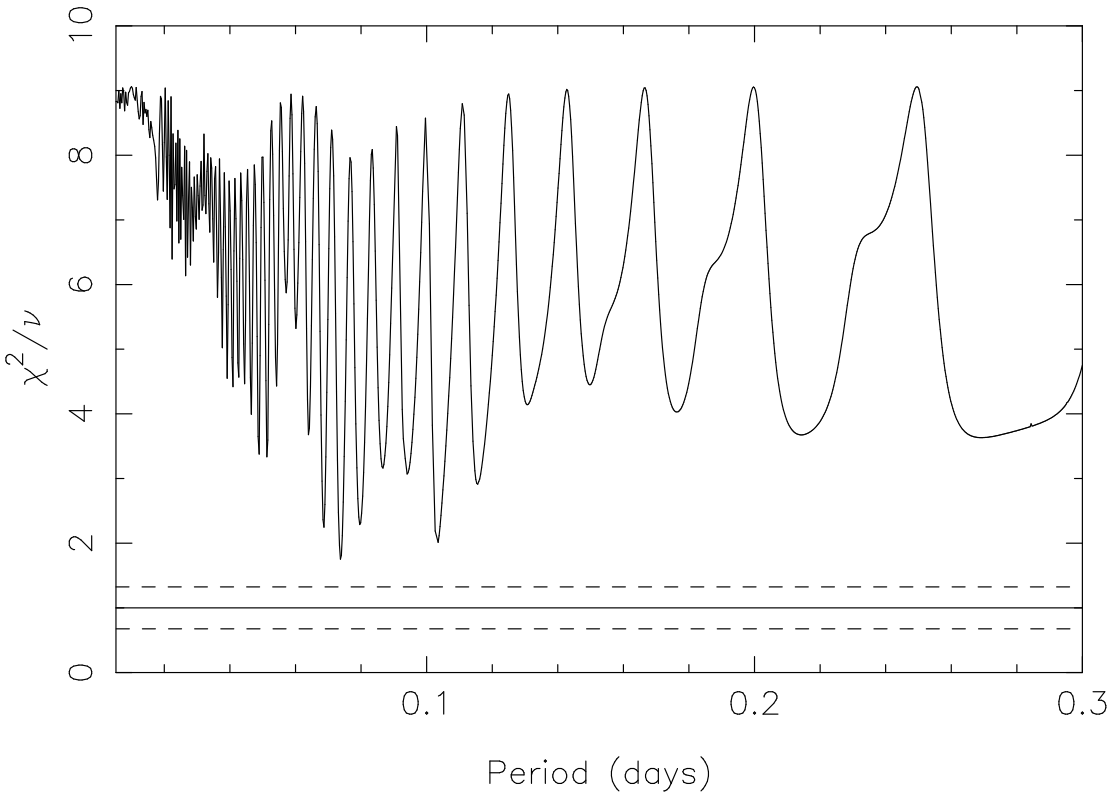

Figure 5.12: Periodogram for 36P, from data with a constant flux level due to the coma removed.

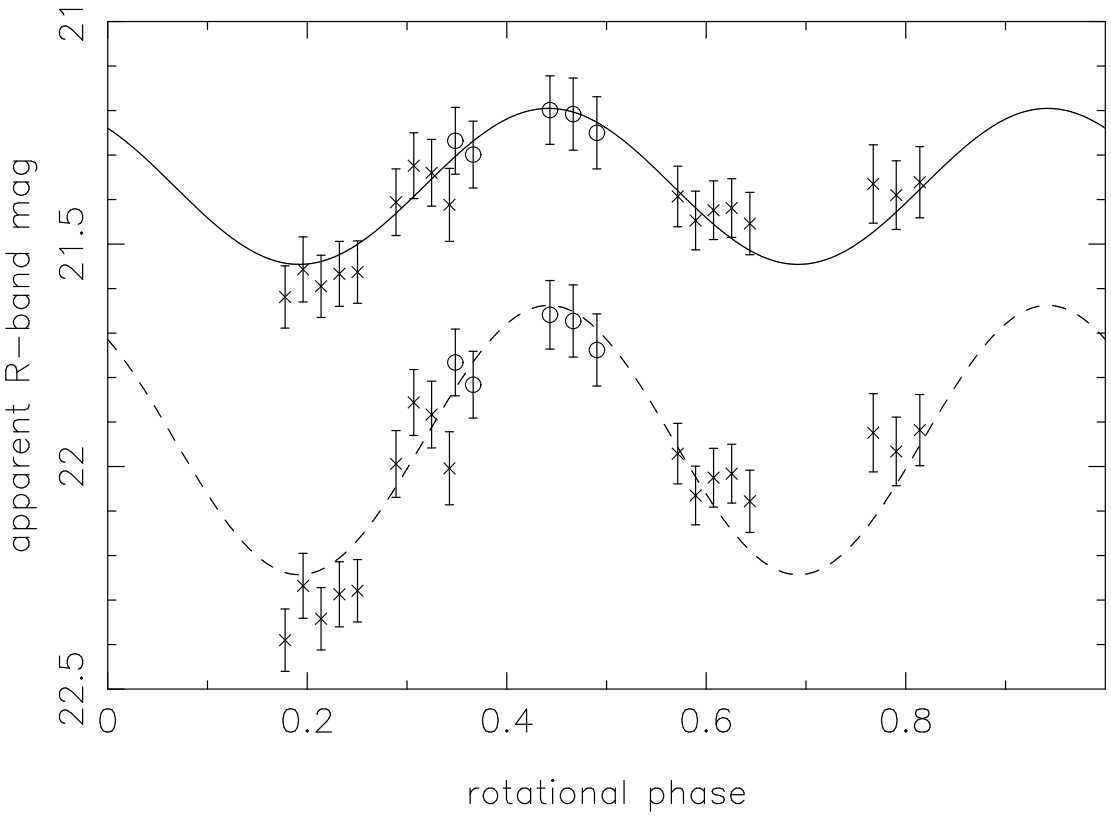

Figure 5.13: 36P photometric data folded onto a 3.5 hour rotation period. The lower data set, with the dashed line drawn through it, are the data with a constant coma flux equivalent to m_c = 22.4 removed from them.

therefore nuclear dimensions of $a \times b = 3.3 \times 2.3$ km. The coma subtracted model gives a smaller, more elongated body, with $r_N = 1.9$ km, $a/b \geq 1.8$ and thus $a \times b = 3.1 \times 1.6$ km. The first solution matches the value of $r_N = 2.5 \pm 0.2$ km found by Lowry & Weissman (2003), who obtained a snap-shot of 36P when it was inbound at 4.4 AU in May 2001. The second solution is also consistent with this considering the uncertainties on the coma fraction.

Figure 5.13 shows that the faint coma detected does not prevent measurement of a rotation period, and that this period is independent of any corrections to the photometry applied to correct for coma. It is the determined period which is of greatest interest for this object; at 3.5 hours, these data show 36P to be the fastest rotating comet known. This implies that it has a surprisingly dense nucleus, under the assumption that it is essentially strengthless, or that this nucleus has tensile strength not seen in others. Either of these present a challenge to the general picture of nuclei that is beginning to be built up; that they are weak and very low density bodies. The required density for a strengthless body rotating at a 3.5 hr period depends on its elongation, and therefore for 36P depends on whether or not a coma model is subtracted. Equation 3.19 gives minimum bulk densities for 36P of 1.2 g cm^{-3} for the original data (with $a/b \geq 1.4$) and 1.6 g cm^{-3} for the coma subtracted version. Clearly the density is greater than water ice, for any level of coma, and over twice that derived for any other nucleus.

Colours were also measured for 36P, and were found to be consistent across both nights with average values of $(V-R) = 0.46 \pm 0.05$ and $(R-I) = 0.52 \pm 0.04$. These colours are entirely typical of JFC nuclei and fall near the centre of the observed distribution. It must be remembered that some fraction of this colour will be due to dust grains in the detected coma, although it is plausible to assume that they share similar optical properties with the nucleus.

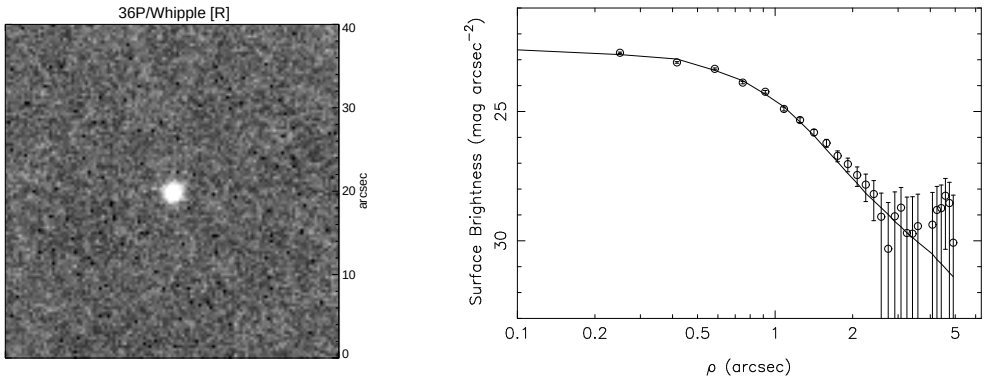

(a) (b)

Figure 5.14: Image showing 36P, made up of 55×75 second exposures taken on the 2nd March 2006 with the INT, and the corresponding profile. The comet is clearly inactive.

5.4.2 INT data: March 2006

With this potentially interesting result in mind, 36P was the primary target of the 2006 INT run. After the first two nights were lost to poor weather, 36P was intensively monitored on the third to ensure unambiguous detection of a 3.5 hour period. A total of 63 r'-band images were taken over ~ 5.5 hours, meaning that any short period would give almost complete phase coverage. As this night was non-photometric, and to search for longer periods, a considerable amount of data was also gathered on 36P on the fourth night, with 55 r'-band frames taken over almost 7 hours. A combination of these data and a surface brightness profile of the resultant image (fig. 5.14) show that the comet was effectively a bare nucleus; a year later and 0.7 AU further from the Sun the faint activity seen in the NTT data had clearly ceased. The formal coma limit measured within $\rho = 5''$ is $m_c \geq 23.31$, or $\leq 20\%$ of the flux, however this is probably an over-estimate due to the slight rise in the outer part of the profile due to residual sky noise (note that the profile is entirely consistent with the stellar PSF within the error bars); in the inner part the profile is clearly inactive and measuring the brightness within $\rho = 3.33''$ gives $m_c \geq 24.51$ and limits on the flux from the coma at $\leq 7 \pm 6\%$.

Although more distant during the INT run than in the NTT run, 36P was closer to opposition, and consequently of similar apparent magnitude: $m_R = 21.570 \pm 0.008$.

Assuming the standard linear phase law with $\beta = 0.035$ mag. deg^{-1} gives $m_R(1,1,0) = 15.247$ for the bare nucleus; comparison with the non-coma subtracted value from the NTT run, $m_R(1,1,0) = 15.272$, allows calculation of the fraction of flux from the nucleus during that run by:

$$f_{\rm N} = 10^{0.4(m_R - m_{\rm N})} = 10^{0.4(m_R(1,1,0)_{\rm NTT} - m_R(1,1,0)_{\rm INT})} = 102\% \qquad (5.1)$$

Clearly this cannot be true: the bare nucleus should be fainter than the active one, and the fraction of flux due to the nucleus should be $\sim 60\%$ if the measurement of 40% coma contamination is correct. The discrepancy is probably due to an incorrect phase law. Taking both of the measurements (NTT at $\alpha = 11.1^\circ$, INT at $\alpha = 1.0^\circ$), together with the snap-shot by Lowry & Weissman (2003) taken at $\alpha = 7.3^\circ$, allows calculation of an approximate phase co-efficient. Taking the original NTT result (*i.e.* assuming that the coma contamination was actually zero; the condition which would give the nucleus flux as 100% from equation 5.1) gives a minimum value of $\beta = 0.037 \pm 0.002$ mag. deg^{-1}, which provides an excellent fit to the three points and is close to the canonical cometary value. If any coma contribution is removed from the NTT data then the phase function slope becomes steeper; for the results quoted above with 40% of the flux removed, the best fit gives $\beta = 0.094$ mag. deg^{-1}. This is probably unrealistic, as the previous largest reported value of this parameter is $\beta = 0.06$ for 2P/Encke (Fernández et al. 2000), and would require the nucleus of 36P to have exceptional phase darkening, with a very rough surface. Also, this slope does not provide as good a fit to the point from Lowry & Weissman, despite the relatively large error bars on this point (the fit is dominated by the two time-series results due to their much smaller uncertainties), although it falls within the expected range if the error bars on this point are expanded to take in the full range from the light-curves, on the basis that the rotational phase at the time of the snap-shot was unknown.

The full range of the INT data is $\Delta m = 0.7 \pm 0.1$ mag, larger than that measured in the NTT data but similar to the range observed in the coma-corrected data. It implies

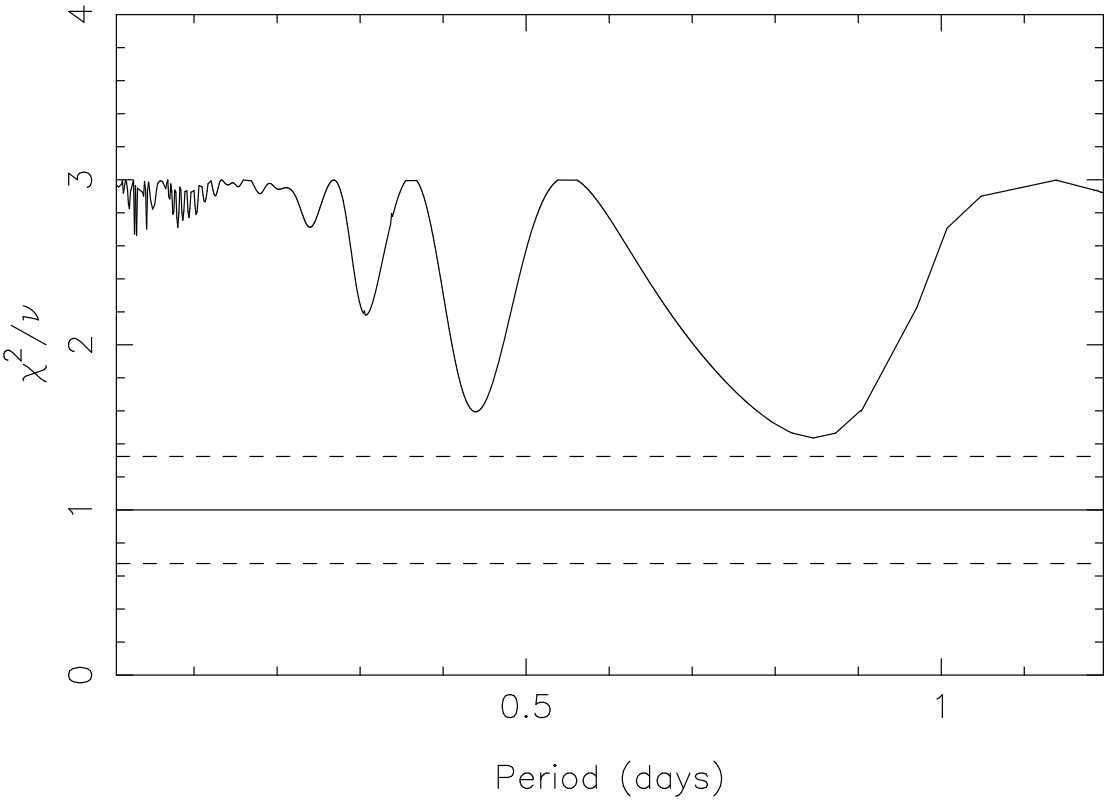

Figure 5.15: Periodogram for 36P from INT data.

$a/b \geq 1.9$. The size of the nucleus is measured by extrapolating the above phase laws back to $\alpha = 0^\circ$, giving $m_R(1,1,0) = 15.244 \pm 0.007$ for $\beta = 0.037$ and $m_R(1,1,0) = 15.189 \pm 0.007$ for $\beta = 0.094$ mag. deg^{-1}. These correspond to radii of $r_\mathrm{N} = 2.55 \pm 0.01$ and $r_\mathrm{N} = 2.62 \pm 0.01$ km; the constraint of an accurate measurement of m_R when inactive and near to opposition with the INT greatly reduces the uncertainty on the radius due to both coma contamination and uncertain phase function. The radius of 36P is taken to be $r_\mathrm{N} = 2.55 \pm 0.01$ km, which when taken with $a/b = 1.9$ implies dimensions of $a \times b = 4.0 \times 2.1$ km.

The periodogram for the INT data is shown in fig. 5.15, which shows that the fit to the fluctuations in the brightness is dominated by a long period variation. This periodicity search is based on differential magnitudes, since the large field of view of the WFC meant that the same stars could be used for comparison on both nights, meaning that no uncertainty is added due to calibration onto a standard scale. The data folded onto the best period, at $P_\mathrm{rot} = 40.6$ hours, is shown in fig. 5.16. Such a long period

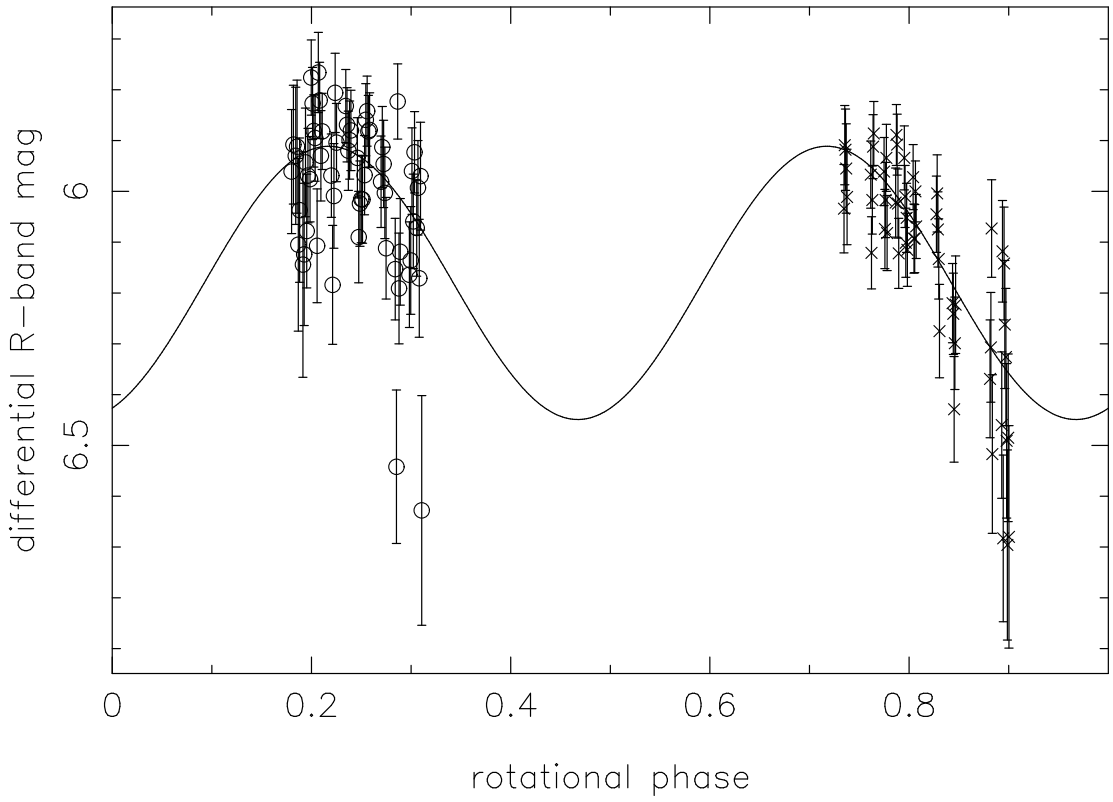

Figure 5.16: 36P differential photometric data folded onto an 40.6 hour rotation period.

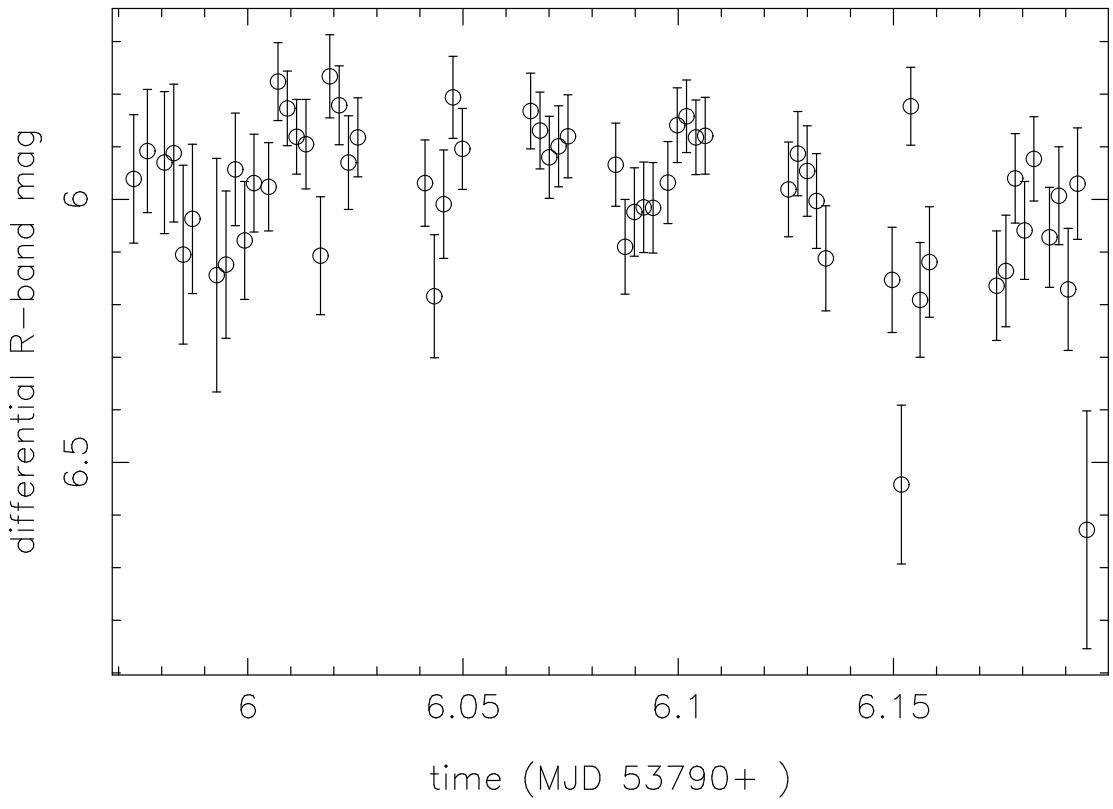

Figure 5.17: 36P differential photometric data taken on the 1st March 2006.

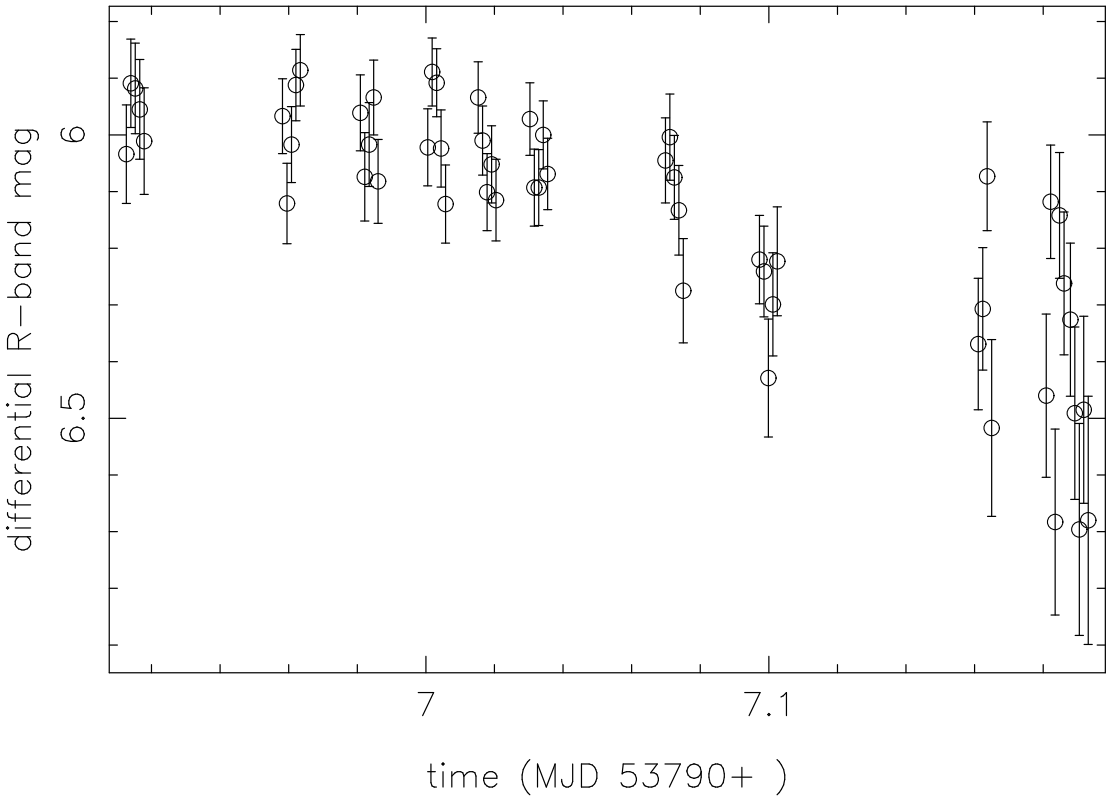

Figure 5.18: 36P differential photometric data taken on the 2nd March 2006.

could not have been detected in the shorter and sparser data set obtained with the NTT, but there remains the question of where the 3.5 hour period came from, and whether it has any basis in reality. It is clear from fig. 5.11 that there are many statistically acceptable periods in the NTT data; due to the few data points many periods can be found which have sufficiently low χ^2/ν. The NTT data can be folded onto a 40.6 hour period to give a visually acceptable light-curve, however this could be said of a large number of periods given the sparse data. Of more interest is whether or not any short period variation exists in the INT data. The unfolded data from each of the INT nights are shown in fig. 5.17 and fig. 5.18, which show hints of shorter period variation. It is possible that the 3.5 hour period and these short variations are part of a non-symmetric light-curve with a longer period. The relatively noisy INT data does not allow a definite conclusion that the 40.6 hour period is correct, nor entirely rule out a short period. The longer period is taken for the rotation period of 36P elsewhere in this thesis as it does not require that the nucleus is far denser than other nuclei, however further data is required to confirm the true rotational period of this comet.

A large number of colour frames were taken within the time-series on 36P, giving good phase coverage for the fitted (long) period. Using the calibrated magnitudes of stars from the fourth (photometric) night gave the colours from differential magnitudes involving the same stars on the non-photometric night. All individual colours are consistent with means of $(V-R) = 0.48 \pm 0.03$ and $(R-I) = 0.62 \pm 0.02$, within the error bars on individual points. These colours are a reasonable match with the values measured using the NTT; a weighted average of both sets gives $(V-R) = 0.47 \pm 0.02$ and $(R-I) = 0.60 \pm 0.02$.

5.5 40P/Väisälä 1

40P/Väisälä 1 was observed over 7 nights during the 2005 INT run, despite not having a good previous size estimate, as it was found in an initial snap-shot. This comet has never been observed to be particularly bright, and was not detected on the only previous attempt to observe its nucleus (Lowry et al. 1999). It was faint in each of the INT frames, with a mean $m_R = 22.08 \pm 0.02$, and also in a combined image equivalent to a 28 minute exposure (fig. 5.19). The surface brightness profile shows that the comet was weakly active at $R_{\rm h}$ = 4.6 AU. The coma contribution, assuming steady state, was measured to be $m_c \geq 22.22$ within $5''$, and therefore up to $\sim 95\%$ of the flux, but the irregular shape of the profile implies that the steady state assumption may not be valid in this case.

With observations over 7 nights, changes in the relative positions of the Earth and the comet meant that there was a non-negligible change in observing geometry. The change in apparent magnitude due to variations in $R_{\rm h}$, Δ and α between the first and last frames is $\delta m_R \approx 0.04$ mag., which although small compared with the uncertainty on individual points (typically ~ 0.2 mag.) is considerable when compared to the error on the average magnitude. The photometry was therefore reduced to the appropriate $m_R(1,1,0)$ using the precise position of the comet at the time of each observation,

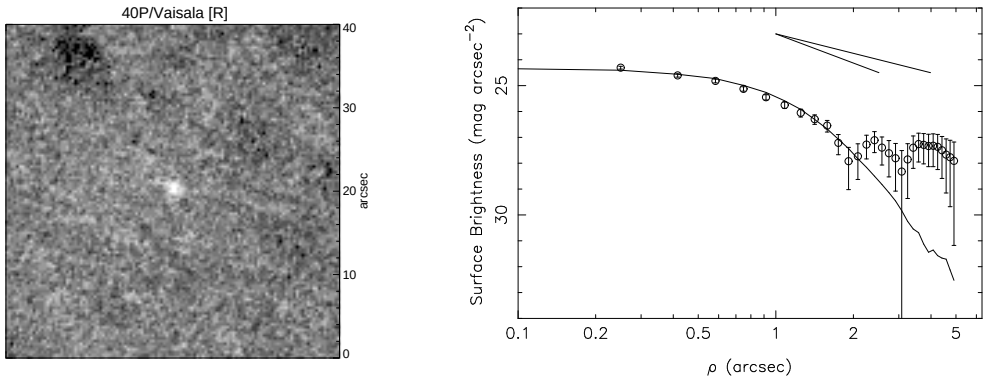

(a) (b)

Figure 5.19: Image showing 40P, made up of 20×85 second exposures taken on the 6th night of the 2005 INT run. The profile implies that the comet was active.

which was generated using *HORIZONS* in batch mode, with the Julian Date of each observation from the image headers taken as input. The phase function is assumed to be linear with $\beta = 0.035$ mag. deg^{-1}, as the range in phase angle over 7 nights is not large enough to independently measure β for 40P. The mean $m_R(1,1,0) = 15.72$ gives an upper limit to the radius of $r_{\rm N} \leq 2.05 \pm 0.02$ km, assuming a 4% albedo. This is a stronger constraint than the previous upper limit of $r_{\rm N} \leq 3.6$ km from Lowry et al. (1999), who did not detect the comet when it was at $R_{\rm h}$ = 6.01 AU, outbound, in 1995. If the coma contamination is considerable, as suggested above, then the true radius of the nucleus could be considerably smaller than this.

The absolute magnitude variations were searched for periodicities, but none were found which were convincing. The strongest minimum in the periodogram (fig. 5.20) corresponds to $P_{\rm fitted} = 15.3$ hours, and therefore a long rotation period of 30.6 hours, but does not give a visually acceptable light-curve at either of these periods. Periodogram searches were also carried out on short subsets of the data, using fully differential light-curves for each pair of nights, during which the comet's motion was small enough to give common comparison stars. Shorter periods in these data are neither particularly convincing in the subsets, due to sparse data, nor good fits to the full data set. Although there is a large range in observed magnitudes ($\Delta m \approx 1.4 \pm 0.3$ mag), this appears to be due to variations in the dust coma, and is not due to the nucleus, again implying that in this case the coma completely dominates.

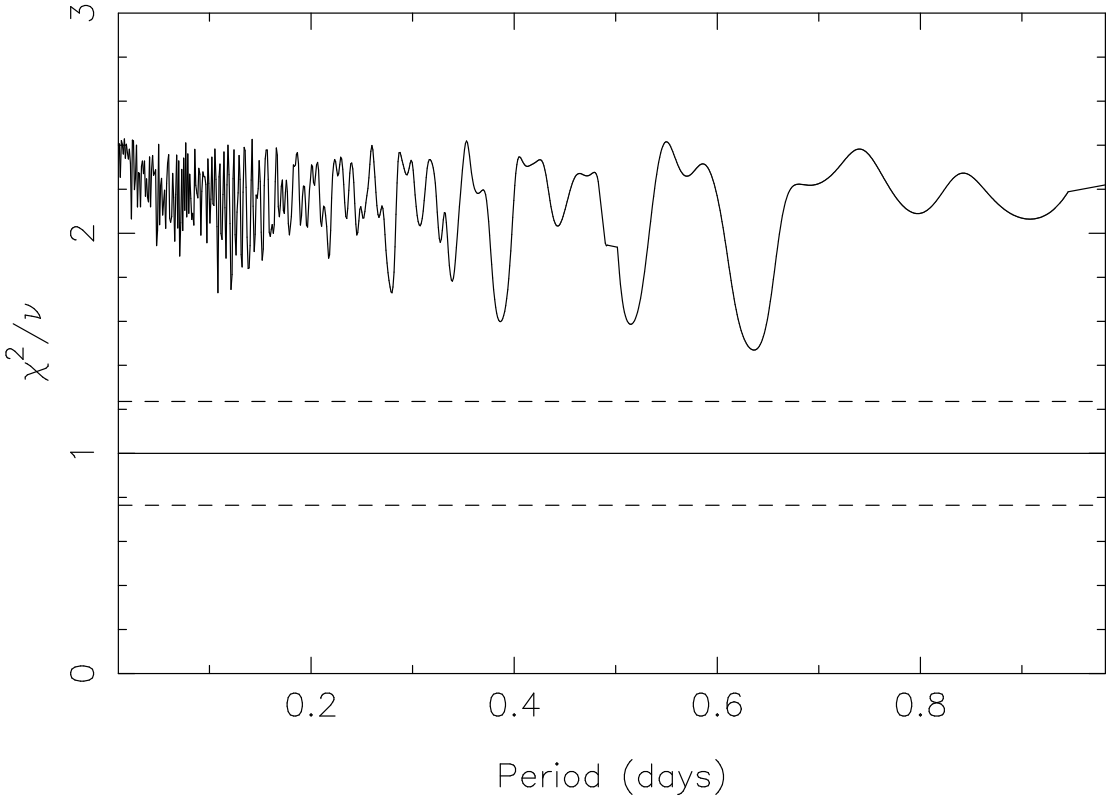

Figure 5.20: Periodogram for 40P.

The colours of the comet were measured each night apart from the first, when only r'-band images were taken of all objects to allow more snap-shots to be performed and more potential targets identified. At large distance from the Sun the coma should be dominated by dust, with very little gas present; the colours measured for the comet are therefore assumed to be approximately the same as the colours of the nucleus, as the dust should have similar optical properties to the nucleus. On the fourth night the colour block was unfortunately taken when the comet was coincident with a background star, and the remaining colour measurements have large uncertainties due to the comet being very faint, but are consistent with means of $(V-R) = 0.37 \pm 0.10$ and $(R-I) = 0.65 \pm 0.11$.

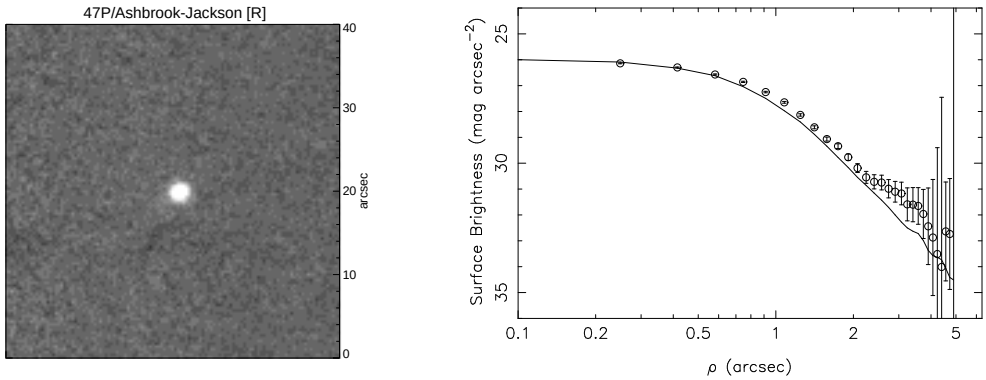

(a) (b)

Figure 5.21: Image showing 47P, made up of 34×85 second exposures taken on the second night of the 2005 NTT run. The stellar profile matches the comet, implying that the comet was inactive.

5.6 47P/Ashbrook-Jackson

47P/Ashbrook-Jackson was visible throughout the entire 2005 NTT run and consequently was well monitored, with a total of 53 *R*-band exposures of 85 seconds each (table A.6). The comet appeared bright and stellar in each; a combination of all of the frames (equivalent to a 48 minute exposure) taken on the second night is shown in fig. 5.21 (a). A surface brightness profile (fig. 5.21 (b)) shows that the comet has negligible coma, with a scaled stellar profile matching the comet down to surface brightness $\Sigma > 30$ mag arcsec^{-2}. Equation 3.1 puts limits on any unresolved coma at $m_c \geq 27.4$, implying that activity is entirely negligible and can contribute no more than $0.5 \pm 2.1\%$ of the total flux.

There are four statistically acceptable minima in the periodogram for 47P, which are marked A–D in fig. 5.22. Period 'C' ($P_{\rm rot} = 21.6$ hrs) is marginally the strongest minima, but the data do not allow differentiation between these periods. Light-curves showing the data folded onto each of these are shown in fig. 5.23. In this figure it can clearly be seen that over the course of the second night a definite maximum was observed, and the approach to a maximum appears to have been observed on the first night, which puts strong constraints on the rotation period. Note that the probable periods of $11.2 \pm 0.3, 15.5 \pm 0.5, 21.6 \pm 1.0$ and $44.0^{+1.0}_{-2.9}$ hours have relatively small error

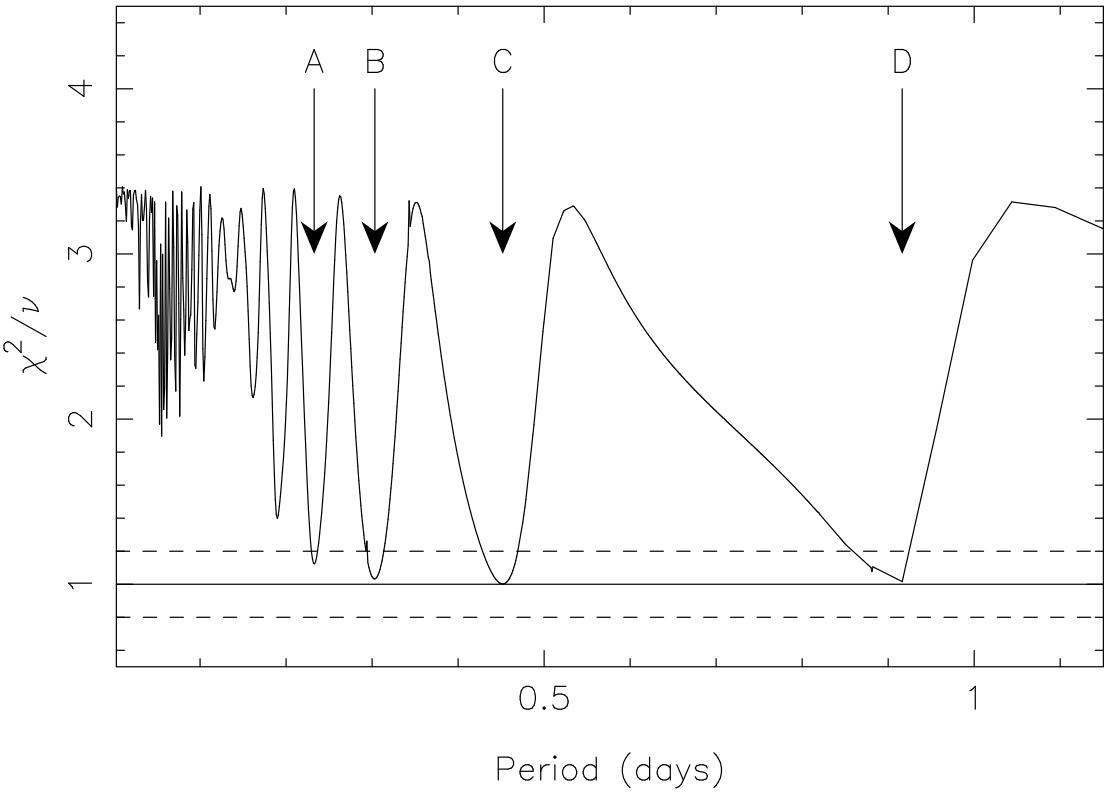

Figure 5.22: Periodogram for 47P. There are four statistically acceptable minima: the data folded onto the periods with each of these minima are shown in fig. 5.23.

bars, but do not give a unique solution. These periods are clearly aliases of each other at $\sim 1, 3/2, 2$ and 4×11 hours, yet it is not possible to select one as the correct period. The rotation period cannot be longer than 44 hours (period 'D'), as this period requires that alternate maxima of a double peaked light-curve were observed on the 2 nights; the remaining solutions imply that there were other maxima unobserved between these events. There is an unpublished partial light-curve on 47P acquired by Lamy et al. using the HST, which puts a lower limit on the rotation period at 44.5 hours. If this is correct, it would suggest that period 'D' is the real one, and that the shape of the body is irregular: The 'best-fit' sinusoid drawn through the data to guide the eye in fig. 5.23(D) does not represent the data well. The range in magnitudes from the data is Δm = 0.45, giving $a/b \geq 1.5$, which is typical of JFC nuclei.

The mean magnitude of 47P's nucleus was measured to be $m_R = 21.680 \pm 0.007$, which gives $m_R(1,1,0) = 14.638$ and a radius of 3.37 $\pm$ 0.01 km, assuming an albedo of 4%. Taken with the elongation implied by the full range in the data, $a/b \geq 1.5$,

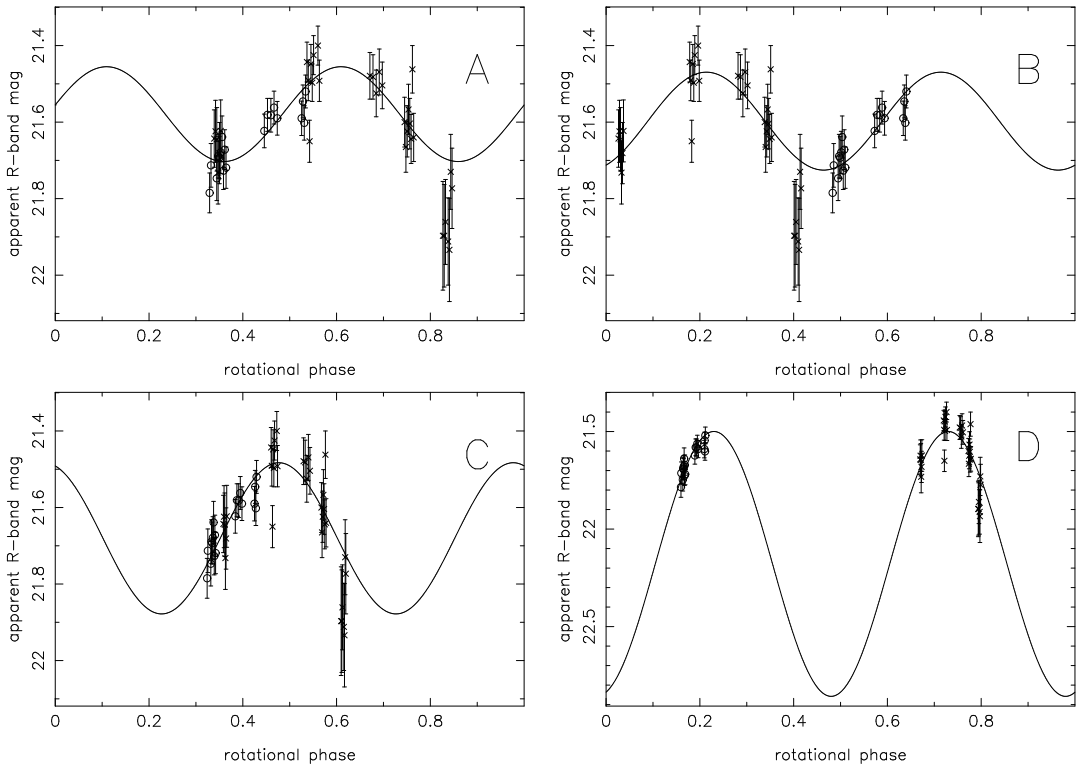

Figure 5.23: 47P photometric data folded onto each of the four strongest periods found in the periodogram (fig. 5.22). These have $P_{\rm rot}$ = 11.2 (A), 15.5 (B), 21.6 (C) and 44.0 (D) hours. The 1.5 nights of data acquired on this comet are insufficient to choose one of these periods over the others.

dimensions of the nucleus of $a \times b = 4.6 \times 3.0$ km are suggested, for what is most likely an overly simple model of the nucleus. This is in reasonable agreement with the radius measurements of 2.8 km (Lamy et al. 2004), 3.1 km (Licandro et al. 2000b) [assuming that these authors observed the nucleus near light-curve minimum] and the limit of $r_{\rm N} \leq$ 6.6 km found by Lowry et al. (2003). The colours measured were $(V-R) = 0.45 \pm 0.03$ and $(R-I) = 0.38 \pm 0.03$.

47P was observed again during the 2006 INT run, one year later when the comet was 0.3 AU closer to the Sun, at $R_{\rm h}$ = 5.1 AU. A total of 5 r'-band exposures totalling 18.5 minutes were taken over the two nights. Upon processing these data, 47P was found to be faintly active at the time of the INT run, despite still being beyond 5 AU, with a faint tail visible to the West of the comet (fig. 5.24). The activity is clearly weak: The profile measured in good ($\sim 1''$) seeing on the last night matches the stellar PSF within the inner part, where the nucleus appears to dominate the flux. The activity level can

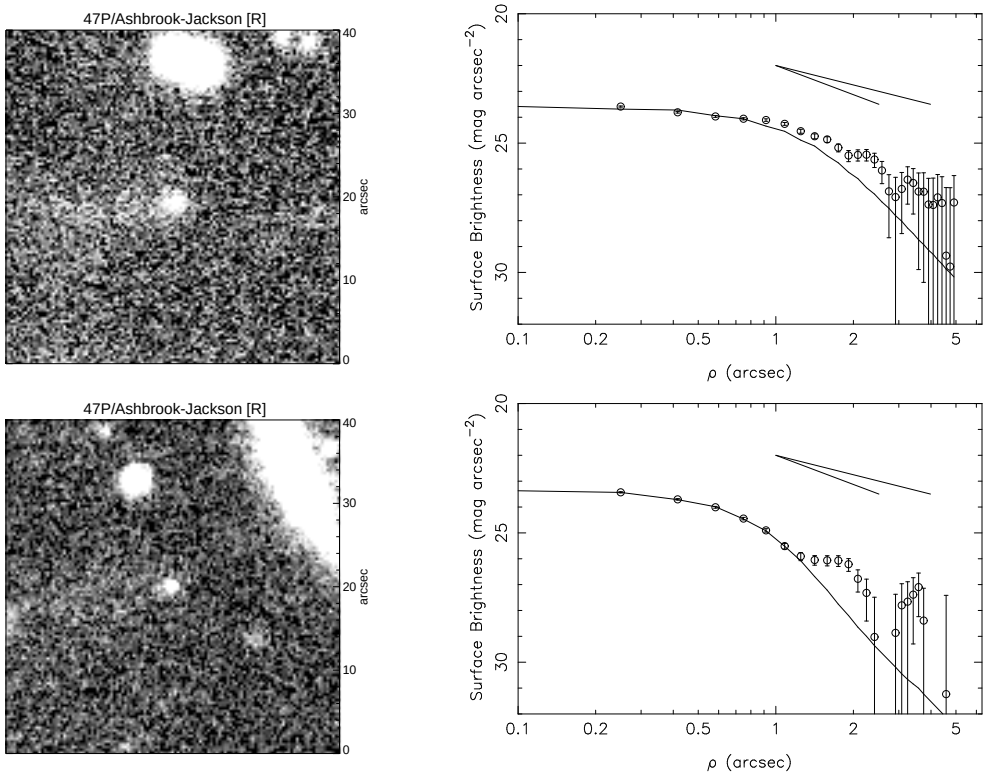

Figure 5.24: Images of 47P taken during the INT run. There is a faint tail visible to the West (left in these images) of the comet, which is clearer in the night 3 data (top). The profile shows activity. In the night 4 data (bottom), the tail is less obvious, as the total exposure time is less.

be quantified as $Af\rho = 3-11$ cm, with the lower number being measured on the latter night. The average magnitude over the two nights is $m_R = 22.01 \pm 0.04$, with a total variation similar to that observed in the light-curves above, of $\Delta m = 0.4$ mag. These imply $m_R(1,1,0) \geq 14.93$ and $r_N \leq 2.96 \pm 0.05$ km, with $a/b \geq 1.4$, slightly fainter than the NTT results despite the weak coma, possibly due to a steeper phase function than $\beta = 0.035$ mag. deg^{-1}. Taking both the NTT and INT results, and those of Licandro et al. (2000b) and Lamy et al.[2], allowed calculation of a rough phase function (fig. 5.25). A best fit straight line gives a steep phase function of $\beta = 0.083 \pm 0.006$ mag. deg^{-1}, implying a true $m_R(1,1,0) = 14.477 \pm 0.007$ and consequently $r_N = 3.63 \pm 0.01$ km.

[2]In this case taking the r_N =2.8 km quoted by Lamy et al. (2004) and calculating the nuclear magnitude at the time of their *HST* observations. The uncertainty on this radius is not reported: The error bar on this point is set equal to that on INT data (0.04 mag.) for the purposes of weighting the best fit. This does lead to some uncertainty on the phase function; if the error bar is instead set equal to that from the extended NTT observations (0.007 mag.) then the corresponding increase in weight on the point gives $\beta = 0.076$ mag. deg^{-1}.

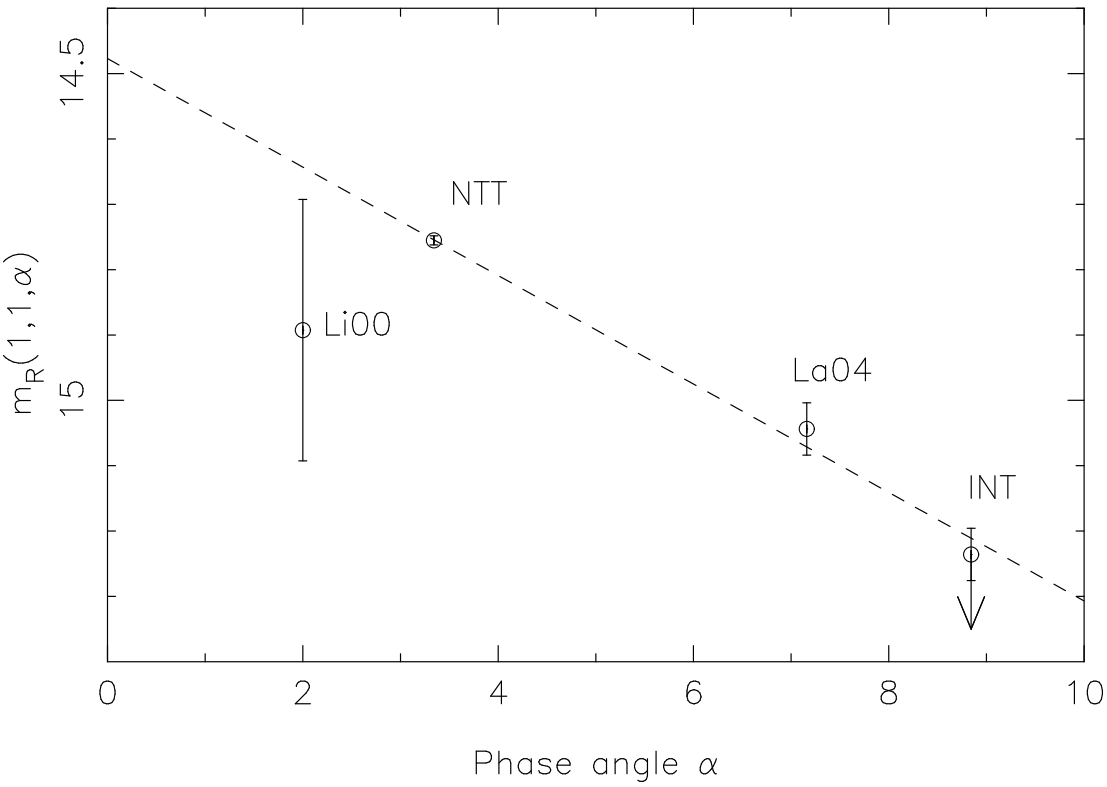

Figure 5.25: 47P mean magnitudes from both NTT and INT data and from the literature reduced to $R_h = \Delta = 1$ AU and plotted as a function of phase angle α. There is a good fit through the time-series data giving a linear phase law with $\beta = 0.083$. Labels give the sources of each point; Li00: Licandro et al. 2000b; La04: Lamy et al. 2004. The faint activity seen in the INT data means that it provides a lower limit on $m_R(1,1,\alpha)$, although the coma clearly contributes little flux as making this point any fainter would mean an even steeper phase function and a poor fit.

The fit to the three time-series measurements[3] is excellent, while the snap-shot from Licandro et al. also agrees with this fit if it is assumed that it was taken near a light-curve minimum. Therefore I regard this as a reasonable determination of the phase function of 47P, despite the fact that it is unusually steep.

Colours were measured of $(V-R) = 0.29 \pm 0.06$ and $(R-I) = 0.79 \pm 0.07$. These are unusual when compared to typical nuclei colours, and show a large change from those measured with the NTT and Licandro et al.'s $(V-R) = 0.4 \pm 0.3$. The activity is weak and most likely dust dominated, so does not explain such a large discrepancy.

[3]Here I regard the 5 points over 2 nights from the INT data as a 'time-series' as it exhibited a similar variation to the others and thus gave an average magnitude relatively free of rotational phase effects. There are too few data in this set to put any statistically meaningful constraint on the rotation period, although coincidentally the best fit period to the data is $\sim$21 hours, similar to one of the possible periods from the NTT data.

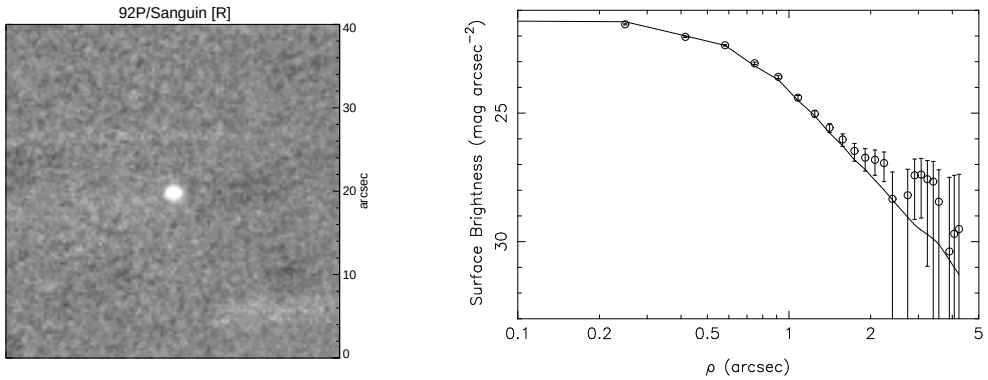

(a) (b)

Figure 5.26: Co-added image of all 63 frames taken of 92P on January 20th, 2004. Each frame had an exposure time of 75s, giving this combined frame an equivalent exposure time of 1.31 hr. Again, the profile and 8% coma upper limit imply that the comet was inactive at the time of observation.

There are two possible explanations: Firstly, the discrepant colours could be due to the measured *R*-band magnitude being too faint, which would decrease $(V-R)$ and increase $(R-I)$ relative to their true values. A second explanation for the discrepancy of the $(R-I)$ measurement is residual fringing in the i'-band which could not be removed. This is unlikely to have such a large effect, and does not explain the low $(V-R)$ colour, so I favour the first explanation. The relatively large uncertanties on these colours mean that a weighted mean of all colour data for 47P (including that of Licandro et al.) gives values closer to the NTT results: $(V-R) = 0.42 \pm 0.02$, $(R-I) = 0.44 \pm 0.03$.

5.7 92P/Sanguin

92P/Sanguin appears stellar in both individual and co-added images (fig. 5.26 (a)), and a surface brightness profile (fig. 5.26 (b)) shows that it was inactive at the time of observation in January 2004. Again, I calculate limits on any unresolved coma by measuring $\Sigma_c(5) \geq 30.1$ mag. arcsec^{-2}. This corresponds to a coma magnitude of $m_c \geq 24.6$, equivalent to $\leq 9 \pm 18\%$ of the average flux from the comet, which was found to have an integrated magnitude of $m_R = 21.938 \pm 0.007$.

Table A.9 gives the measured apparent *R*-band magnitudes for 92P. The null hy-

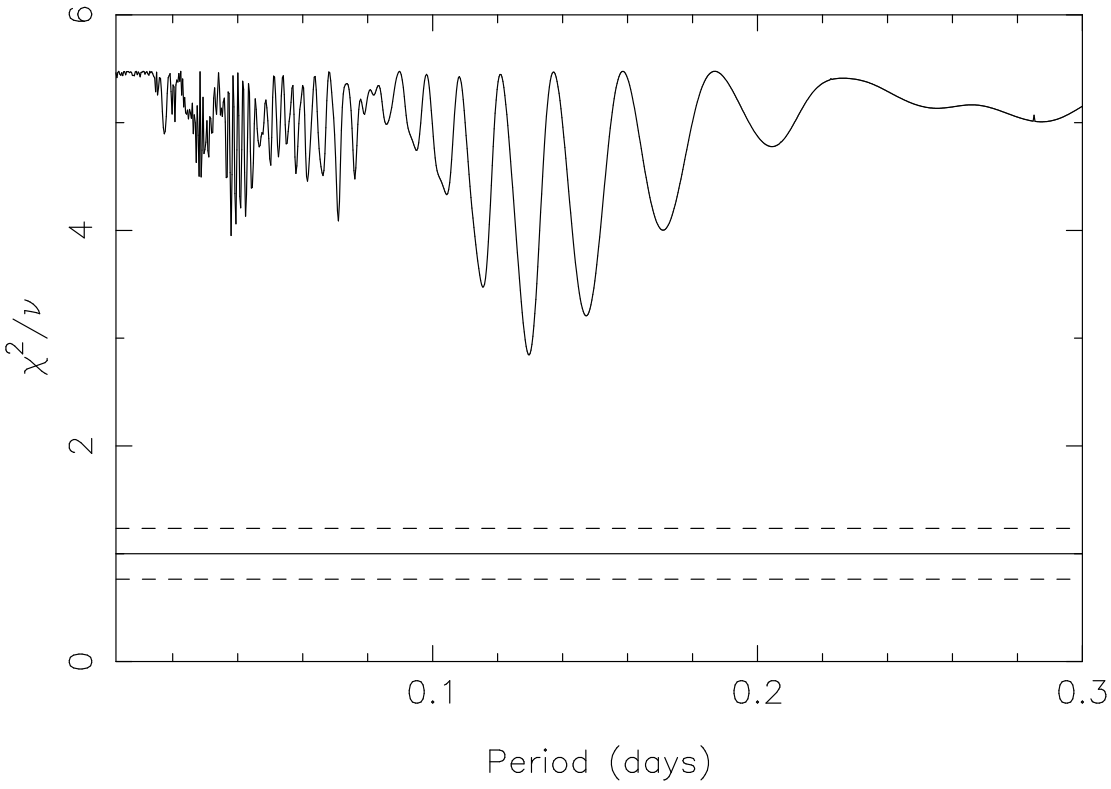

Figure 5.27: Periodogram for 92P. The strongest period found is at $P_{\text{fitted}} = 3.11 \pm 0.03$ hours, corresponding to rotation period of $P_{\text{rot}} = 6.22 \pm 0.05$ hours.

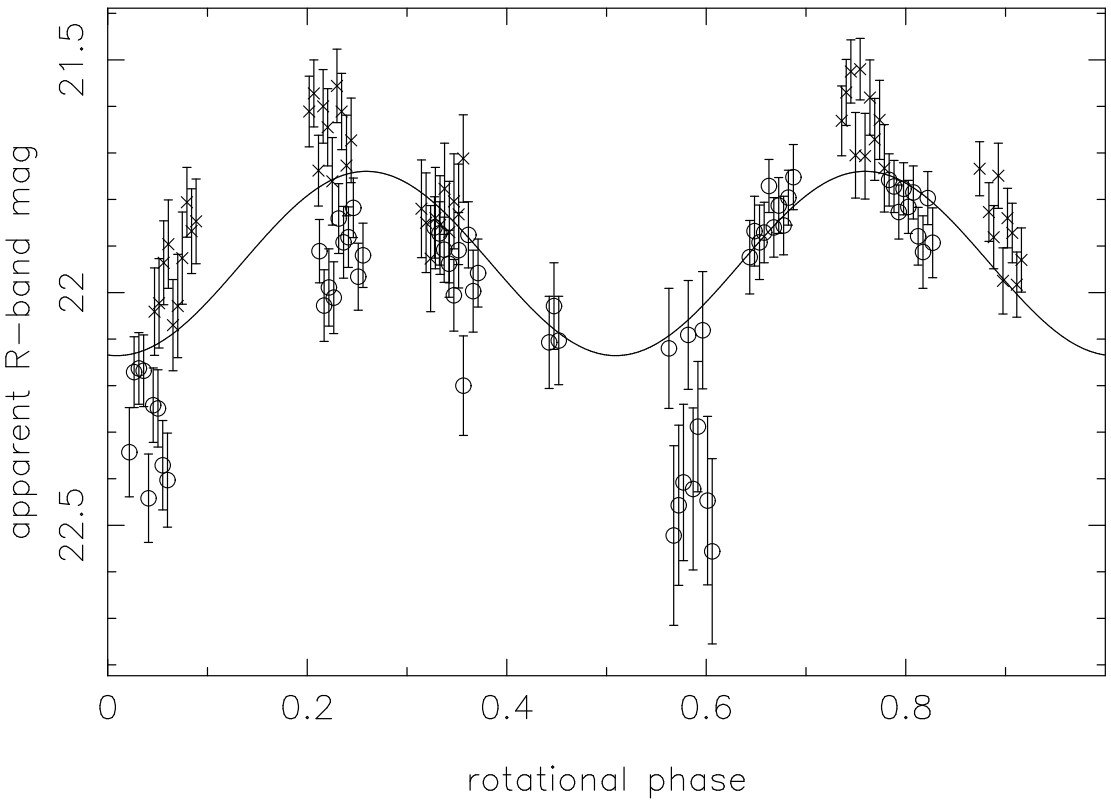

Figure 5.28: Folded light-curve for 92P, period = 6.22 hours.

pothesis (constant brightness) is rejected at a 39σ confidence level. The periodogram for 92P (fig. 5.27) shows a clear minimum at 0.13 days, corresponding to a rotation period at $P_{\rm rot} = 2 \times P_{\rm fitted} = 6.22 \pm 0.05$ hours. This minima has $\chi^2/\nu = 2.85 \approx 14\sigma$; again not very close to the theoretical $\chi^2/\nu = 1$ but acceptable for the best fit sinusoid to a real light-curve which is non-sinusoidal. The brightness variations are clearly real; the light-curve, folded onto the best-fit rotation period, is shown in fig. 5.28. Second order or higher fits to the data do not formally improve upon the fit; the data which suggest to the eye a deeper second minimum, and therefore a higher order fit, may be an artefact of the larger scatter of points at lower S/N at lower intrinsic brightness. The fit can be slightly improved by introducing a shift of ~ 0.2 mag between the 2 nights, which could be attributed to the fact that relatively few comparison stars were available for this comet and those chosen had non-optimal colours. However, the relative shift can not be determined with sufficient accuracy to justify changing the photometry, and such a shift does not have a significant effect on the measured physical properties of the nucleus.

The data give $\Delta m = 0.60 \pm 0.05$ mag., corresponding to an axial ratio of $a/b \geq 1.7 \pm 0.1$. The mean magnitude is $m_R = 21.938 \pm 0.007$. Once again, equation 3.3 gives a radius of the equivalent spherical body of $r_{\rm N} = 2.07 \pm 0.01$ km. This gives the nucleus of 92P projected dimensions of $a \times b = 3.1 \times 1.8$ km.

The radius of 92P has previously been measured to be $r_{\rm N} = 1.84 \pm 0.07$ km (Lowry & Weissman 2003) and $r_{\rm N} = 1.18 \pm 0.20$ km from Meech et al. (2004), calculating $r_{\rm N}$ in this case from their result $m_R = 26.451 \pm 0.364$ using the position of the comet at the time of observation ($R_{\rm h}$ = 8.57 AU, Δ = 8.43 AU, α = 6.6°), $p_R = 0.04$ and $\beta = 0.035$ mag. deg^{-1} for consistency with the other results presented here. The first of these produces results consistent with the NTT data, from a snap-shot taken at similar heliocentric distance ($R_{\rm h} \approx 4.5$ AU). The second result gives a lower radius, but is consistent at a 3σ level with my measurements if I assume that this snap-shot was taken at a minimum in the rotational light-curve. Alternatively, following the logic

described in section 5.2 for 14P, Meech et al.'s snap-shot could have been taken at a deeper minimum than observed here due to differences in observational geometry. If this were so, and assuming that their radius then gives the semi-minor axis $b =$ 1.18 km while the true effective radius is 2.07 km, then an axial-ratio of $a/b = 5.2$ is required. This does not seem to be be plausible, and an alternative explanation for the discrepancy is needed. A different phase law suggests itself, but is rejected as all three observations were at similar α and a measurement of β cannot be made, let alone be used to explain the difference in measured sizes. The possibility that there is some faint coma associated with the comet at $R_{\rm h} \sim 4.5$ AU that does not exist at 8.6 AU would account for the increase in brightness. However, fig. 5.26 shows an inactive comet, and equation 3.1 puts strong limits on any coma at $\leq 8\%$ of the flux. Finally, the colour indices of 92P are measured to be $(V-R) = 0.54 \pm 0.04$ and $(R-I) = 0.54 \pm 0.04$.

5.8 94P/Russell 4

94P/Russell 4 was observed over 4 nights in July 2005 using the INT. It became a time-series target following detection at suitable S/N in a speculative snap-shot observation, as it had no previous size measurement other than an estimate of $r_{\rm N}$ = 1.9 km by Tancredi et al. (2000). A total of 83 r'-band frames were taken, and in addition at least one colour block on each night. The combined image (from all but 2 of the 26 frames taken on the 6th of July; the 2 not included were slightly trailed due to the telescope shifting during the exposures) and corresponding profile show that the comet was possibly active at the time of observation, when it was at $R_{\rm h}$ = 4.1 AU, outbound (fig. 5.29). The profile shows some signs of faint activity beyond $2''$ from the nucleus, although this may be due to residual flux in the combined image from particularly bright nearby stars. The calculated coma contribution within $5''$ is $m_c \geq 21.25$, or $\leq 77 \pm 30\%$; measured before the peak from possible stellar contamination the contribution is $m_c(3'') \geq 22.06$, or $\leq 37 \pm 15\%$.

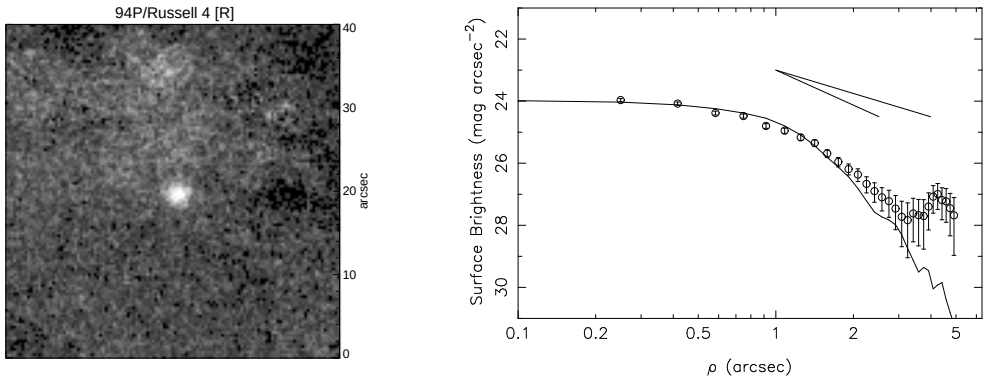

(a) (b)

Figure 5.29: Co-added image of 24 frames taken of 94P on July 6th, 2005. Each frame had an exposure time of 75s, giving this combined frame an equivalent exposure time of ∼30 minutes. The profile implies that the comet was weakly active at the time of observation, although the rise at the end may be due to residual star light.

The mean magnitude of 94P was measured to be $m_R = 20.974 \pm 0.015$; as with other comets observed during this run the individual magnitudes were converted to absolute magnitudes due to the $\delta m_R \approx 0.03$ mag. difference over the four nights, primarily due to the changing phase angle. The weak activity means that this only gives limits on the absolute magnitude and radius; these were measured to be $m_R(1,1,0) \geq 15.187$ and $r_{\rm N} \leq 2.62 \pm 0.02$ km.

The motion of this comet was such that it was not possible to use common stars to produce multi-night differential light-curves, but since it was reasonably bright and exhibited a large amplitude variation the increase in size of the error bars due to calibration onto the Landolt scale was not significant. The null hypothesis of constant brightness is rejected at a 50σ level. The periodogram for 94P is shown in fig. 5.30; the strongest minimum is at $P_{\rm fitted} = 16.7 \pm 0.4$, corresponding to a rotation period of $P_{\rm rot} = 33.4 \pm 0.8$ hours. Although this minimum only has $\chi^2/\nu = 193/79 = 2.45 \equiv 9\sigma$, and the data folded onto this period displays considerable scatter (fig. 5.31), it is clear that there is variation in the brightness of the comet.

The full range observed in the data is $\Delta m = 1.6 \pm 0.2$ mag., implying $a/b \geq 4.4$. This is a very extreme elongation, well in excess of any other measured nucleus, and exceeded by only a very few asteroids. The fact that there are large ranges in observed

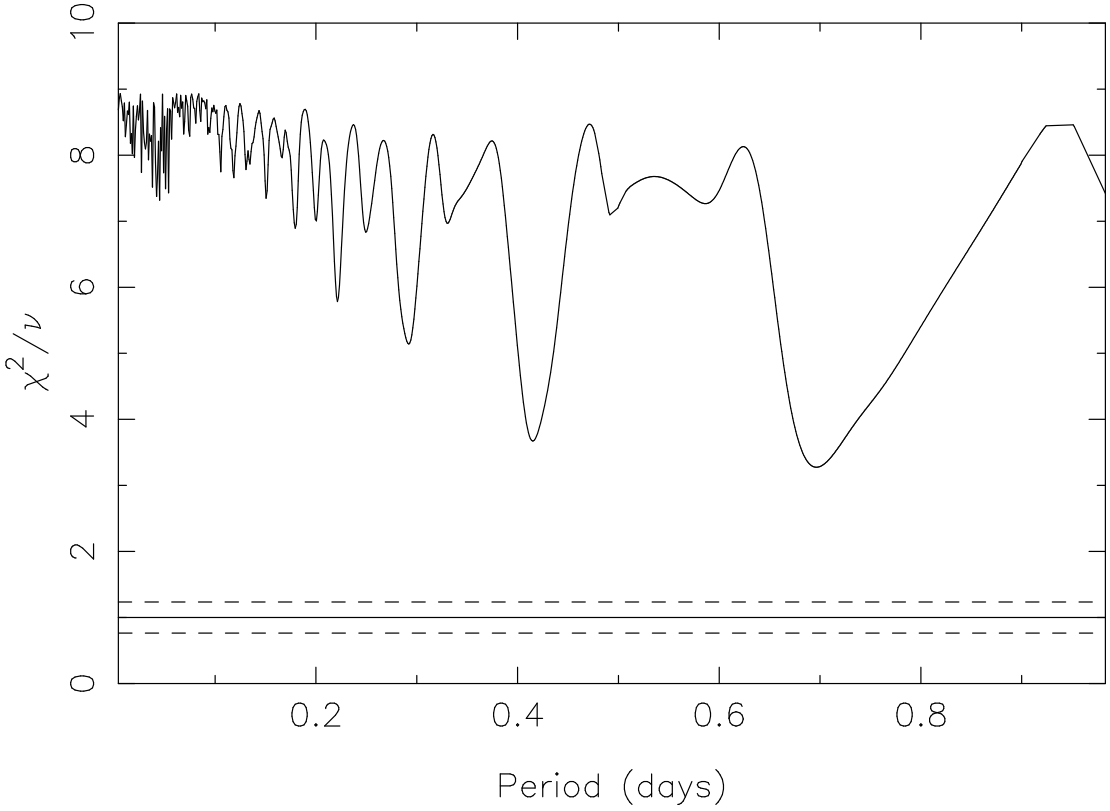

Figure 5.30: Same as fig. 5.2 for 94P.

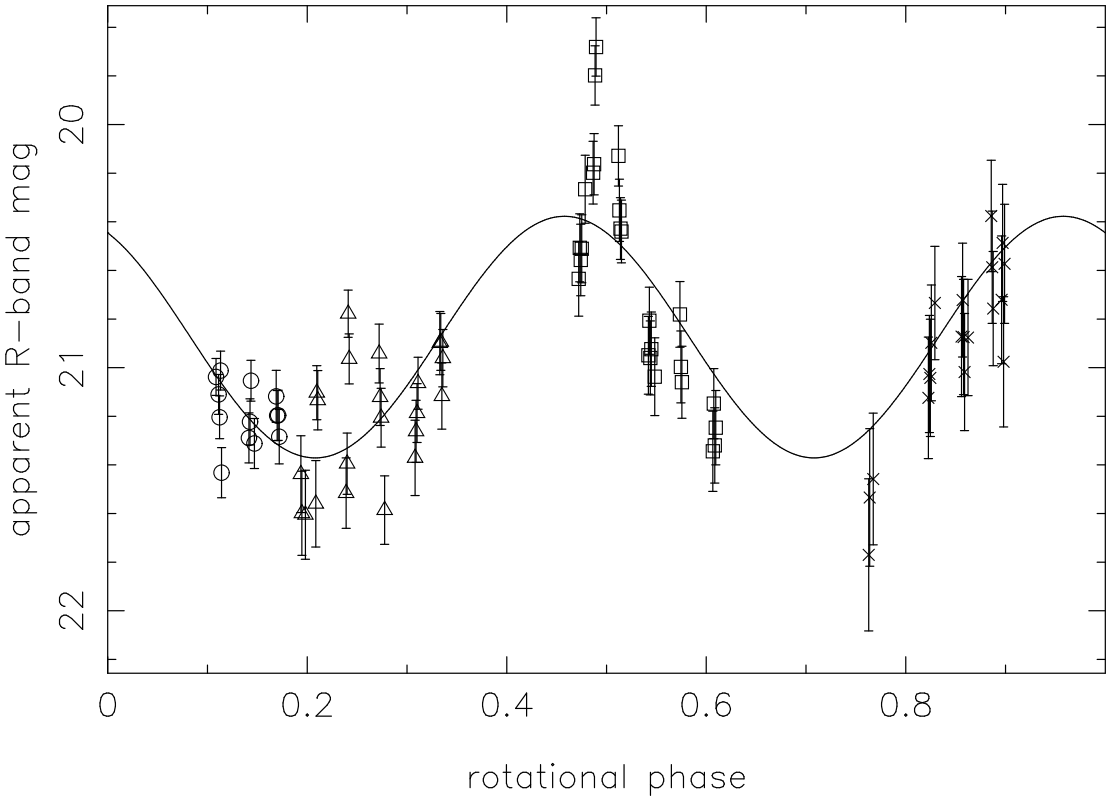

Figure 5.31: Folded light-curve for 94P, period = 33.4 hours. Data from separate nights are plotted with different symbols (circle - night 1; cross - 2; square - 3; triangle - 4): the variation in brightness is considerable even during single nights.

brightness on individual nights and that this comet was bright, but a reasonable periodic light-curve cannot be found in four nights of data strongly implies that these variations are not due to the nucleus but due to the coma. Sharp changes in the brightness due to changing quantities of dust within the photometric aperture could be caused by outbursts.

An alternative explanation is that the range in m_R is due to the nucleus, but variations in albedo across its surface instead of changing cross-sectional area, which would be revealed by periodicities in the colour indices. There are some variations in the measured colours of the comet, although the individual measurements are normally distributed around the mean values of $(V-R) = 0.62 \pm 0.05$ and $(R-I) = 0.44 \pm 0.06$, with the exception of one measurement made when the comet was relatively close to a bright star. The variations do not appear to be correlated with either of the above periods, nor can the r'-band data be fit to periodicities found in the $(R-I)$ sequence. Changes in surface colour do not seem to be the cause of the large amplitude variations seen in the light-curve; I conclude that outbursts changing the amount of observed coma are responsible for the photometric variations.

The $(V-R)$ measurement places 94P towards the red end of the distribution of JFC colours. Following the theory that cometary nuclei become less red with time and activity following insertion from the Kuiper Belt, this would imply that this is a 'young' nucleus. It was only discovered in 1984 after a close (0.6 AU) encounter with Jupiter in 1975 inserted it into its current 6.6 year orbit, however a more thorough dynamical study would be required to test whether or not there are any grounds for speculation about the age of the comet.

5.9 121P/Shoemaker-Holt 2

121P/Shoemaker-Holt 2 was predicted to have $m_R = 22.18$ during the 2006 INT run, based on a radius of $r_{\rm N} = 1.75 \pm 0.63$ km from a snap-shot observation in June 1999 by

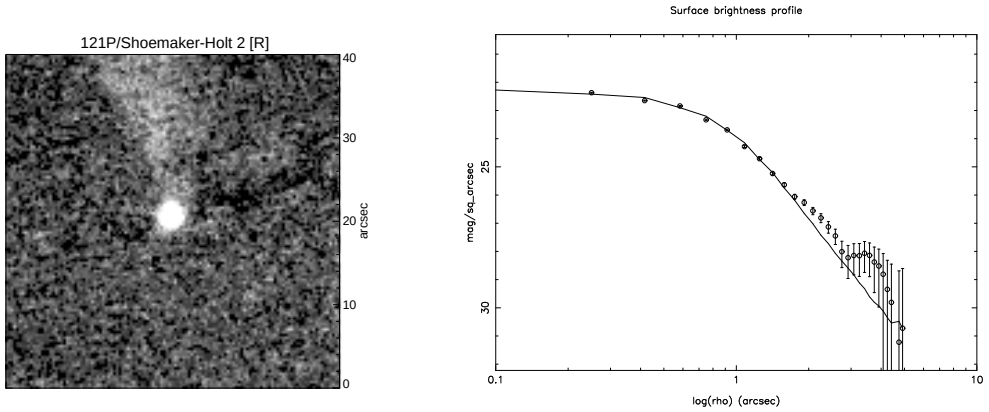

(a) (b)

Figure 5.32: Co-added image of 121P. The nucleus appears star-like, and the profile implies that the comet was inactive at the time of observation, yet there is a tail visible $\sim$ West [upwards in (a)] of the nucleus (highlighted in fig. 5.33).

Lowry et al. (2003). The comet was brighter than expected, but a combined image and surface brightness profile showed the comet to be inactive (fig. 5.32), with a calculated coma contribution within $5''$ of $m_c \geq 24.95$, or $\leq 2 \pm 4\%$ of the total flux. The nucleus profile appears to be a good match to the image PSF, implying that it is a point source and therefore inactive. However, inspection of the co-added frame revealed a dust feature in the plane of the comet's orbit. Originally suspected to be a dust *trail* of remnant dust particles along the orbit due to the apparent inactivity of the comet, it is clear from fig. 5.33 (in which colours are used to highlight faint features, and the orbit of the comet projected onto the sky is over-plotted) that the feature is a *tail*, as it is not entirely in the orbital plane and spreads around the anti-solar direction. This means that there are two contradictory measurements; the stellar nucleus profile implies that there is no coma, and there is clearly none resolvable, yet there is a tail, which implies that the comet is quite highly active. A tempting interpretation is that the observations happened to catch the comet just after it 'turned off', or shortly after an outburst from an otherwise inactive comet, meaning that there is no near nucleus coma, but the material in the tail has not yet dispersed.

Assuming that the nucleus was inactive, the measured $m_R = 20.775 \pm 0.006$ implies $m_R(1,1,0) = 14.660$ and $r_{\rm N} = 3.35 \pm 0.01$ km. This is considerably larger than the $r_{\rm N} = 1.75 \pm 0.63$ result found by Lowry et al. (2003), even considering the large error bar on

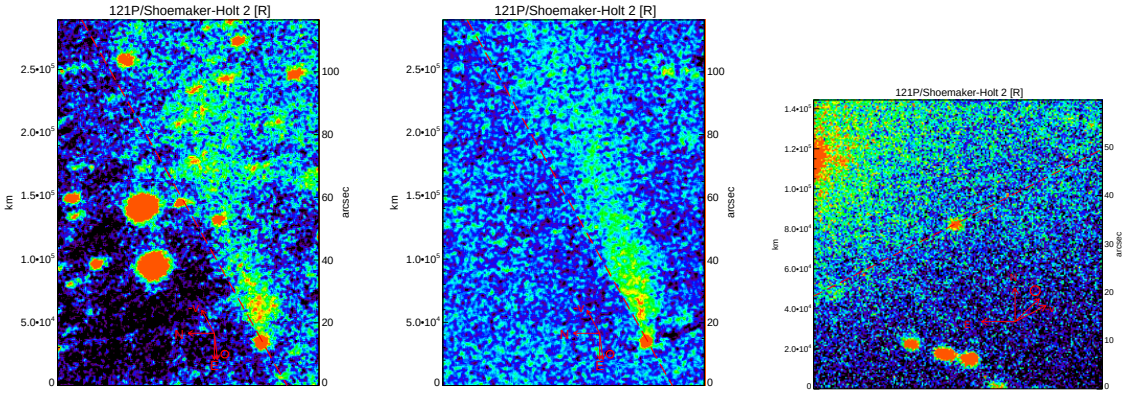

(a) (b) (c)

Figure 5.33: Wider field co-added images of 121P, using false colour to highlight the faint tail. (a) shows the first night's data, during which the seeing was poor and exposure times were doubled, and there were too few images to generate a background image without the comet to subtract. This image is therefore a direct sum of the 4 r'-band images (equivalent exposure time $t_e = 27$ minutes), and contains stars. (b) was produced from the 18 r'-band frames ($t_e = 65$ minutes) taken on the 2nd of March 2006, and has had background objects removed. (c) shows the data obtained with the FTN in May 2006, and shows no tail, although it is not such a deep image (14 minutes).

their result. This further suggests that there is some activity present in the INT frames; the axial-ratio required to explain the difference as due to Lowry et al. observing an r_N = 3.35 km body at a light-curve minimum is a/b = 6.3, which is unrealistic. However, the brightness of the comet does show variations which may be periodic and could be interpreted as being due to the rotating nucleus: the periodogram and best fit folded differential light-curve are shown in fig. 5.34 and fig. 5.35. With only 4 frames taken on the first night and 19 on the second, there is ambiguity in the determined period. A number of periods give visually acceptable light-curves; Figure 5.35 shows 4 that illustrate the range seen in the periodogram. Note that the deepest minima have $\chi^2/\nu < 0.68 (\equiv -1\sigma)$, implying that the error bars on the photometry are over estimated (*i.e.* the brightness measurements are more accurate than the conservative estimates on the uncertainties). The null hypothesis of constant brightness is rejected, at only $\chi^2/\nu = 47.4/21 = 2.2 \equiv 3.8\sigma$, although this would be rejected at a higher confidence level if the error bars on individual points were reduced. The total variation is $\Delta m = 0.15 \pm 0.03$ mag., implying a minimum $a/b \geq 1.1$ and a fairly spherical shape or near pole-on orientation, although (following the discussion on 36P in section 5.4.1) if there is near

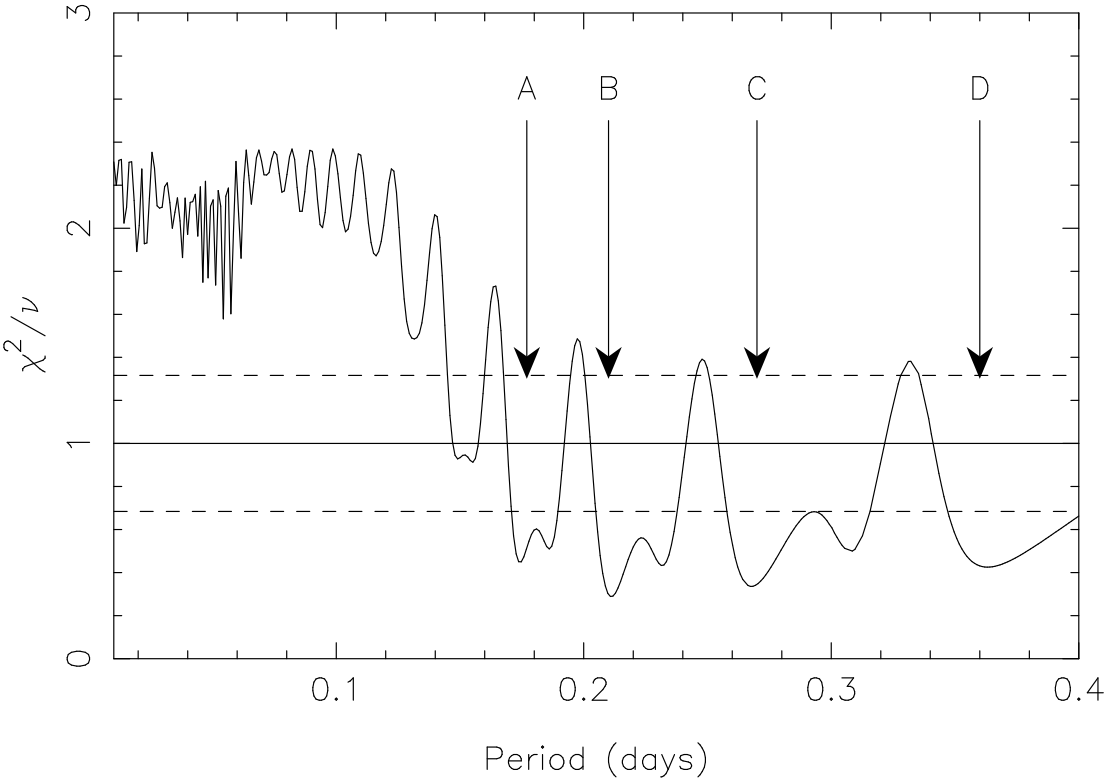

Figure 5.34: Reduced χ^2 periodogram for 121P.

nucleus unresolved coma then the true axial-ratio will be larger.

To determine whether or not 121P was still active, and in particular to investigate the interpretation that it had just ceased outgassing in March, the comet was observed again on the 31st of May 2006, using one hour on the FTN. Based on the radius measured using the INT, the predicted magnitude at this time was $m_R = 20.69$; actually brighter than during the INT observations due to the lower phase angle, and theoretically well within the capabilities of the 2.0m FTN. 14 *R*-band frames were taken over the course of the hour, along with 3 *V*-band and suitable standard star observations for calibration. As the FTN does not have an auto-guider, exposure times were limited to 60 s to minimise trailing of the images due to the telescope's movement. Combining all frames gave a detection of the comet, which was very close to the predicted brightness, with $m_R = 20.63 \pm 0.10$. The profile of this combined image indicated that the comet was inactive ($m_c(3.1'') \geq 24.2$, implying a flux contribution of $\leq 4 \pm 7\%$), and no tail was detected to a 3σ limiting surface brightness of $\Sigma_R \gtrsim 25$. Unfortunately this does not rule out a tail, as the surface brightness in the centre of the tail in the INT data is beyond these

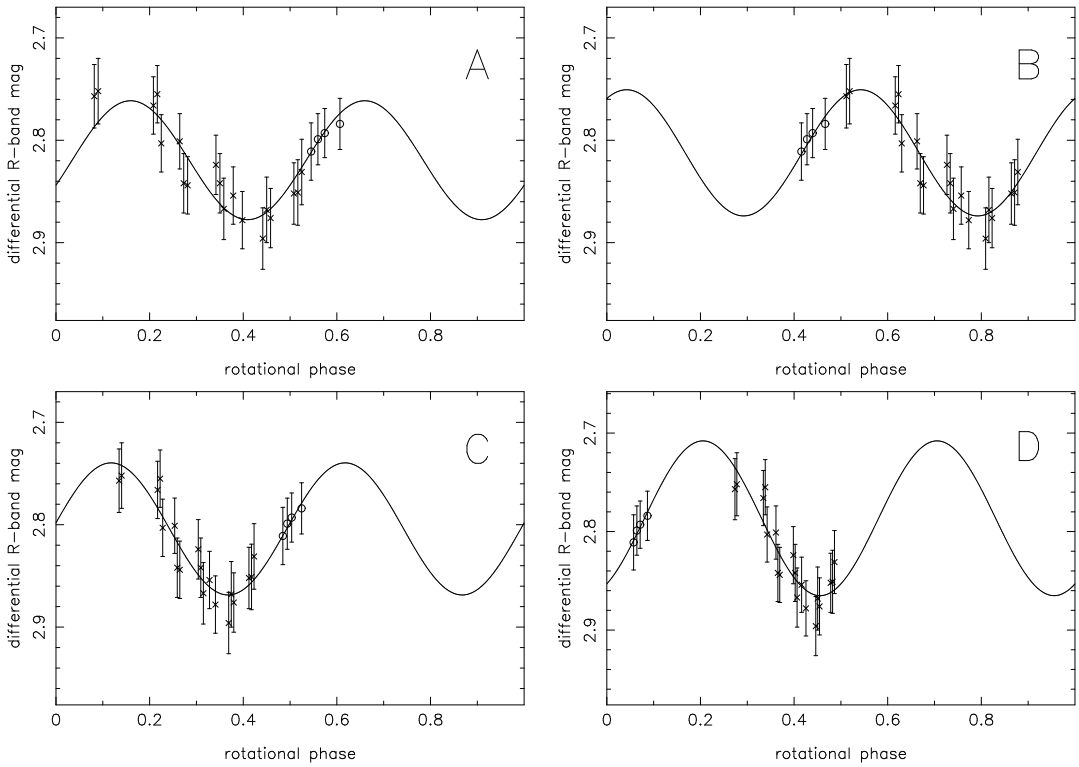

Figure 5.35: Folded differential light-curves for 121P, periods A = 8.4, B = 10.1, C = 12.8 and D = 17.4 hours.

detection limits at $\Sigma_R \approx 25.5$. The FTN observations were therefore unable to constrain the evolution / dissipation of the tail, although the star-like profile suggesting inactivity adds support to the idea that both sets of observations were of a bare nucleus which had recently ceased out-gassing.

If this is the case then a measurement of the phase function can be made. As the measured FTN brightness was close to the predicted value, then β must be close to the canonical 0.035; in fact a fit to these two points gives $\beta = 0.047 \pm 0.020$, and $m_R(1,1,0) = 14.494 \pm 0.006$, implying $r_{\rm N} = 3.61 \pm 0.01$ km. These results are still inconsistent with those of Lowry et al. (2003), and a non-standard phase law does little to improve matters. Including their result gives a phase law with $\beta = 0.036 \pm 0.006$, and an implied $m_R(1,1,0) = 14.65$ and $r_{\rm N}$ = 3.36, but still does not fit their magnitude well. The colours measured for 121P were $(V-R) = 0.53 \pm 0.03$ and $(R-I) = 0.44 \pm 0.03$, from the INT data, and $(V-R) = 0.29 \pm 0.20$ in the FTN data, where the extreme faintness in the few short V-band exposures gives large error bars.

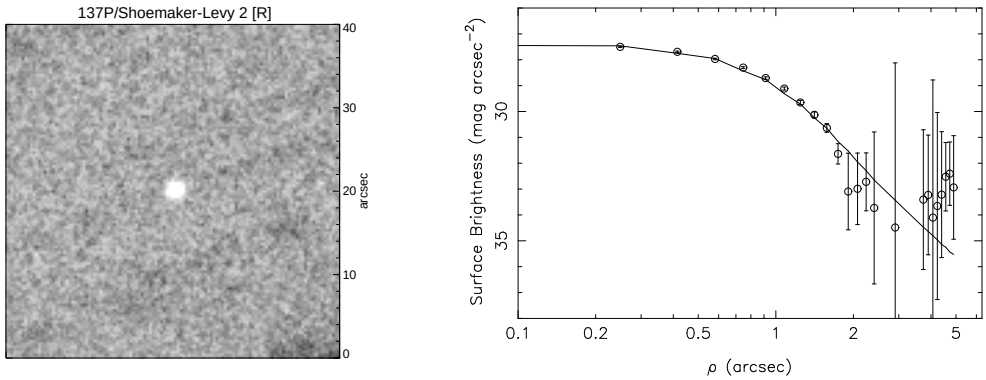

(a) (b)

Figure 5.36: Image showing 137P, created from 22×140 second exposures taken on the second night of the 2005 NTT run. The stellar profile matches the comet, implying that the comet was inactive.

5.10 137P/Shoemaker-Levy 2

137P/Shoemaker-Levy 2 was a secondary target during the March 2005 NTT run, as its extremely large distance (7.0 AU, inbound) gave it a predicted brightness of $m_R = 23.0$, making it a challenging target even with the 3.6m NTT. However, a snap-shot was taken on the second night of observations at a point when all the primary targets were either below the horizon or too close to field stars. The comet was detected at a similar brightness to 17P, so was added to the light-curve target list. An image produced by shifting and adding all *R*-band data and the corresponding profile (fig. 5.36) show that the comet was inactive, as expected as it was close to aphelion. The limit on any coma contribution within a $5''$ aperture was formally found to be $m_c \geq 22.9$, which corresponds to up to 82% of the flux, although at $\rho = 5''$ sky noise entirely dominates. Although most of the background sky is removed by the process that gives fig. 5.36, the comet profile can not be measured accurately beyond $\Sigma = 32$ mag arcsec^{-2}. The profile is clearly stellar in the inner part; measuring the surface brightness at $\rho = 2''$ gives $m_c \geq 25.0$, corresponding to $\leq 14 \pm 10\%$ of the flux.

22 *R*-band images were taken of 137P, but the loss of the 3rd night of the run to bad weather meant that these data covered only 3 hours (table A.8). There is no statistically significant variation within these data, and therefore no constraint on the rotation

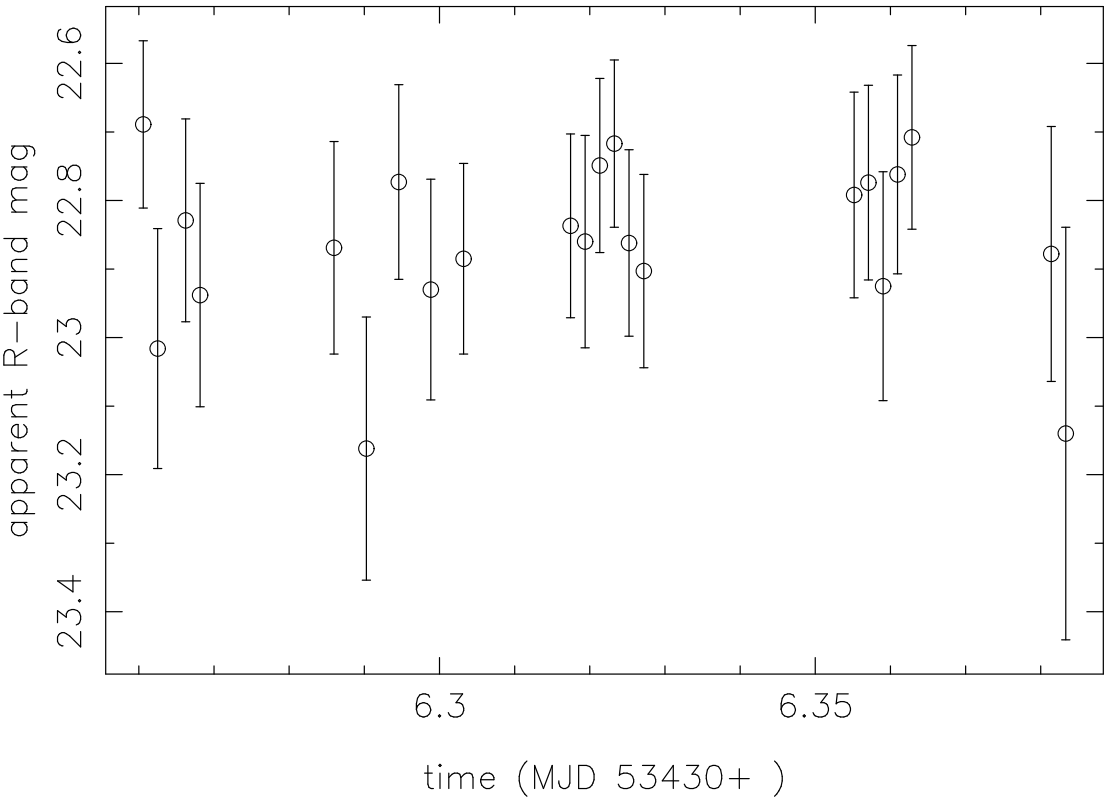

Figure 5.37: Photometric data for 137P. There is no statistically significant variation within the data; in the one night of data there is no evidence for rotation.

period, other than to say that 137P does not rotate unusually quickly, has a shape very close to spherical or was observed pole on. The data are shown un-folded in fig. 5.37. The mean magnitude is $m_R = 22.86 \pm 0.03$, and therefore $r_{\rm N} = 3.58 \pm 0.05$ km, which is close to the limit of $r_{\rm N} \leq 3.7$ km measured by Lowry et al. (2003). The colour indices for this nucleus are $(V-R) = 0.71 \pm 0.18$ and $(R-I) = 0.54 \pm 0.15$, which places 137P at the red end of the distribution of measured nuclei colours, admittedly with relatively large error bars due to its faintness.

5.11 P/2004 H2 (Larsen)

P/2004 H2 (Larsen) [hereafter H2] was observed in July 2005 at only its second opposition since discovery in April 2004. Consequently little was known about the comet prior to the INT run, and an initial snap-shot was performed to try and recover it, and

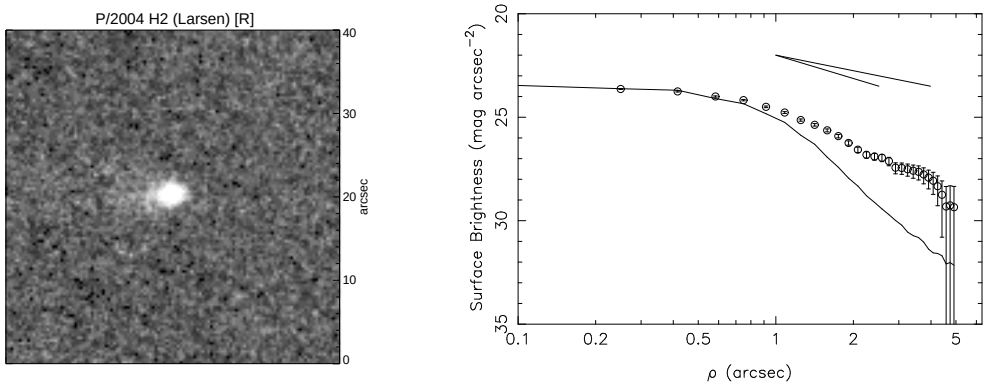

(a) (b)

Figure 5.38: Image showing P/2004 H2, in which a faint tail can be seen to the West (left in this image) of the nucleus. The profile also shows that the comet was weakly active, although the flux from the nucleus dominates in the photometry.

possibly measure a nucleus size. It was detected in the snap-shot and was seen to be bright enough, with a stellar appearance, to encourage continued observation, and was subsequently observed on all 7 nights of the run. A total of 98 r'-band frames were taken; the combined image shown in fig. 5.38 (a) is made up of the 16 taken on the 4th night. It can be seen in this image that the comet was weakly active, with a small tail extending in a Westerly direction from the nucleus. The profile also shows the comet to be active, with $m_c = 23.85$ measured within $\rho = 5''$. The comet flux is dominated by the nucleus though, as this corresponds to only $13 \pm 11\%$ of the total flux, under the assumption of steady state coma. This assumption is only an approximation in this case, as the slope of the profile is slightly steeper than $m = -1.5$. The level of activity is quantified by $Af\rho = 6.0 \pm 0.1$ cm, within $\rho = 11,000$ km, in agreement with the assessment that this comet was only very weakly active at the time of observation.

H2 was moving relatively slowly on the sky at the time of observation, allowing for both long exposure times (210 s) and the use of common stars to generate entirely differential light-curves over three night time-spans. These were searched for periodicities, and also combined by comparing the brightness of the comparison stars in the overlapping nights (3 & 5) to give a full 7 night differential light-curve relative to the stars in the middle nights, although the difference in error bars between the differential and calibrated light-curves was found to be negligible. Therefore the calibrated light-

curve, adjusted to take into account the changing observational geometry by reducing the photometry to absolute values, was used. No convincing periodicity was identified.

As the comet is active, I find a lower limit to the absolute magnitude and an upper limit to the radius. The light-curve does give an accurate measurement of $m_R = 21.590 \pm 0.007$, which reduces to an absolute magnitude of $m_R(1,1,0) \geq 15.875$ and therefore a mean effective radius of $r_{\rm N} \leq 1.91 \pm 0.01$ km. The mean measured colours of this comet are $(V-R) = 0.49 \pm 0.02$ and $(R-I) = 0.28 \pm 0.04$, although the individual measurements have considerable scatter around these means, possibly due to variations in the near nucleus coma.

Table 5.1: Derived physical parameters and colours from time-series photometry on JFCs.

Comet	m_R	m_c[a]	$m_R(1,1,0)$	r_N [km]	P_{rot} [hr]	a/b[b]	D_N[b] [g cm^{-3}]	$(V-R)$	$(R-I)$
7P	22.465±0.016	≥25.3	15.532±0.016	2.24±0.02	$7.9^{+1.6}_{-1.1}$	1.3±0.1	0.22±0.08	0.40±0.05	0.41±0.06
14P	22.281±0.007	≥25.5	14.787±0.007	3.15±0.01	7.53±0.10	1.7±0.1	0.32±0.02	0.57±0.07	0.51±0.06
17P	22.864±0.020	≥24.6	16.241±0.020	1.61±0.01	7.2—12.8	1.3±0.1	0.20±0.02	0.41±0.07	0.44±0.08
36P[c d]	21.370±0.016	≥22.4	15.272±0.016	2.52±0.02	3.56±0.02	1.4±0.1	1.24±0.07	0.46±0.05	0.52±0.04
36P[e]	21.570±0.008	≥24.5 (3.3″)	15.247±0.008	2.55±0.01	40.6±0.6	1.9±0.1	0.01±0.01	0.48±0.03	0.56±0.03
40P[d]	22.08±0.02	≥22.2	≥ 15.72	≤ 2.05	n/a	n/a	n/a	0.37±0.10	0.65±0.11
47P[c]	21.680±0.007	≥27.4	14.638±0.007	3.37±0.01	11.2—44.0	1.5±0.1	0.04±0.01	0.45±0.03	0.38±0.03
47P[e d]	22.01±0.04	≥22.9	14.93±0.04	2.96±0.05	n/a	1.4±0.1	n/a	0.29±0.06	0.79±0.07
92P	21.938±0.007	≥24.6	15.700±0.007	2.07±0.01	6.22±0.05	1.7±0.1	0.49±0.06	0.54±0.04	0.54±0.04
94P[d]	20.974±0.015	≥22.1 (3.0″)	≥ 15.19	≤ 2.62	n/a	n/a	n/a	0.62±0.05	0.44±0.06
121P[e]	20.775±0.006	≥25.0	14.660±0.006	3.35±0.01	10^{+8}_{-2}	1.15±0.03	0.12±0.04	0.53±0.03	0.44±0.03
121P[f]	20.63±0.10	≥24.2 (3.1″)	14.60±0.10	3.44±0.16	n/a	n/a	n/a	0.29±0.20	n/a
137P	22.86±0.03	≥25.0 (2.0″)	14.51±0.03	3.58±0.05	n/a	n/a	n/a	0.71±0.18	0.54±0.15
H2[d]	21.590±0.007	≥23.9	≥ 15.88	≤ 1.91	n/a	n/a	n/a	0.49±0.03	0.28±0.04

[a]Limiting coma magnitude measured within 5″, unless stated.

[b]Lower limits as the orientation of the rotation axis is unknown.

[c]Results from 2005 NTT run. For each of the comets with multi-run data the individual results are presented here; the conclusions based on the combined data, including phase curves, are given in the text.

[d]Faint coma present. Note that these results do not include any correction for the presence of faint near-nucleus coma.

[e]Results from 2006 INT run.

[f]Results from 2006 FTN observations.

Chapter 6

Ensemble properties of JFC nuclei

Here I take the results presented in the last two chapters, and consider how they influence the understanding of JFCs in general. Although there are differences in the properties measured for individual comets, these data allow constraints to be placed on the properties of the population. Specifically, I consider the size distribution of the ecliptic comets, the range in spin-rates and shapes and therefore densities, and also trends in surface colours of these objects.

6.1 Size distribution

The size distribution of any population of bodies is of critical importance in constraining their formation and subsequent collisional evolution. Happily, it is also one of the more straight forward characteristics of the population to measure, as at least reasonable estimates of the size of bodies can be made with snap-shot observations. Time-series data allow better measurements of their sizes, as this removes uncertainties due to their rotational light-curve. Converting the measured magnitude to the size of an object depends on its albedo and phase function; there are only 5 JFCs for which both of these are independently well measured (2P/Encke, 9P/Temple 1, 10P/Temple 2, 19P/Borrelly and 28P/Neujmin 1; two of which have a size measurement from resolved imaging by space-craft), although a few more comets have measurements of one or the other. The uncertainty due to the unknown albedo can be overcome by considering a distribution of absolute magnitudes instead of sizes, although this makes little practical difference for comets as one has to assume a standard albedo, making the distributions equivalent. Where the albedo of a particular nucleus is known it is used in the following discussion; the fact that most measured albedos are close to the canonical 4% value means that they can be compared with the sizes from assumed albedos without introducing any bias. Previous measurements of the size distribution of JFCs have followed a similar assumption.

The distribution is generally plotted as a cumulative size distribution (CSD), ex-

pressed in terms

$$N_{\rm S}(> r_{\rm N}) \propto r_{\rm N}^{-q_{\rm S}} \tag{6.1}$$

or

$$N_{\rm L}(< m_R(1,1,0)) \propto 10^{q_{\rm L} m_R(1,1,0)} \tag{6.2}$$

for a cumulative luminosity (brightness) distribution. As discussed above, these are entirely equivalent if the albedo of all the nuclei is the same, and for this case Irwin et al. (1995) showed that $q_{\rm S} = 5q_{\rm L}$. Hereafter I therefore only refer to the size distribution, and drop the subscript when referring to $q \equiv q_{\rm S}$. A number of measurements of these distribution co-efficients have been made, generally based on snap-shot observations of a large number of nuclei. Lowry et al. (2003) measured $q = 1.6 \pm 0.1$ based on a sample of 33 comets, and Weissman & Lowry (2003) updated this to $q = 1.59 \pm 0.03$, based on 41 JFCs with $r_{\rm N} \geq 1.4$ km. They chose to fit the size distribution to only those nuclei with $r_{\rm N} \geq 1.4$ km as the slope of the CSD is approximately constant above this radius, while below it there is a sharp cut-off. This is generally assumed to be due to observational bias due to the difficulty in detecting faint nuclei, although could also be a product of mass loss or disruption of small nuclei (Lamy et al. 2004). The latest size distribution from these authors has $q = 1.73 \pm 0.06$ (Weissman & Lowry 2006). Another estimate comes from Fernández et al. (1999), who use selected data in quality classes 1-3 (uncertainties on $m_V(1,1,0)$ up to ± 1 mag.) from the catalogue presented by Tancredi et al. (2000), with cut-offs in both absolute magnitude and perihelion distance. The discrepancy between Fernández et al.'s estimate of $q = 2.65 \pm 0.25$ and those of Lowry et al. can be explained by these cut-offs (leaving only 12 comets) and the large uncertainties on magnitudes in Tancredi et al.'s catalogue. Tancredi et al. (2006) present an updated catalogue and find $q = 2.7 \pm 0.3$ for $r_{\rm N} \geq 1.5$ km. Meech et al. (2004) measure $q = 1.45 \pm 0.05$ over the range $1 \leq r_{\rm N} \leq 10$ km, and a steeper $q = 1.91 \pm 0.06$ in the range $2 \leq r_{\rm N} \leq 5$ km, showing the large dependence on the choice of size range. They also apply a monte-carlo method to their snap-shot data to correct for observational bias and find that the JFC CSD is consistent with a model distribution

with $q = 2.5$ and real cut-off at small radii (0.3-2.0 km). Hicks et al. (2006) measure $q = 1.50 \pm 0.08$ from Near Earth Asteroid Tracking (NEAT) survey data, although this makes use of observations of active comets and a coma subtraction technique. Finally, Lamy et al. (2004) collates the data from most of these catalogues, together with their own unpublished results, those from Licandro et al. (2000b) and also from other papers on individual comets, to calculate $q = 1.9 \pm 0.3$ for JFC nuclei with $r_N \geq 1.6$ km.

The results presented in chapters 4 and 5 add four new and 12 improved radii measurements (these do not include the upper limits for the weakly active comets). As previously described, I assume $p_R = 0.04$ and $\beta = 0.035$ mag. deg^{-1} (the uncertainties introduced by these assumptions are discussed later in this section). A measurement of the CSD can be made by combining my data with the Lamy et al. (2004) catalogue (and also including other size measurements published since 2004: Lowry & Fitzsimmons 2005; Fernández et al. 2006). To allow direct comparison between my results and those in the Lamy et al. catalogue, all radii with unknown phase function were scaled to $\beta = 0.04$ mag. deg^{-1} using

$$r_2 = r_1 10^{0.2\alpha(\beta_2 - \beta_1)} \tag{6.3}$$

giving a total of 69 JFC nuclei with reliable radii based on the same assumed albedo and phase function.

The best fit to the CSD for all 69 nuclei (fig. 6.1) has $q = 1.74 \pm 0.01$, for a weighted fit to all the data. Note that this error bar does not give a true reflection of the uncertainty, as such a fitting procedure assumes independent data points and this is not the case for a cumulative distribution, and it does not take into account the uncertainties due to albedo and phase function. The true uncertainty on q is considered below. Fitting to *only* the $r_N \geq 1.6$ km comets gives $q = 1.91$. For radii smaller than this, the CSD levels off, again most likely due to observational incompleteness. While it is clearly better to fit only the approximately linear part of the CSD below the 'knee' at r_N = 1.6 km, the weighted fit to all 69 comets matches the linear part of the curve, as the

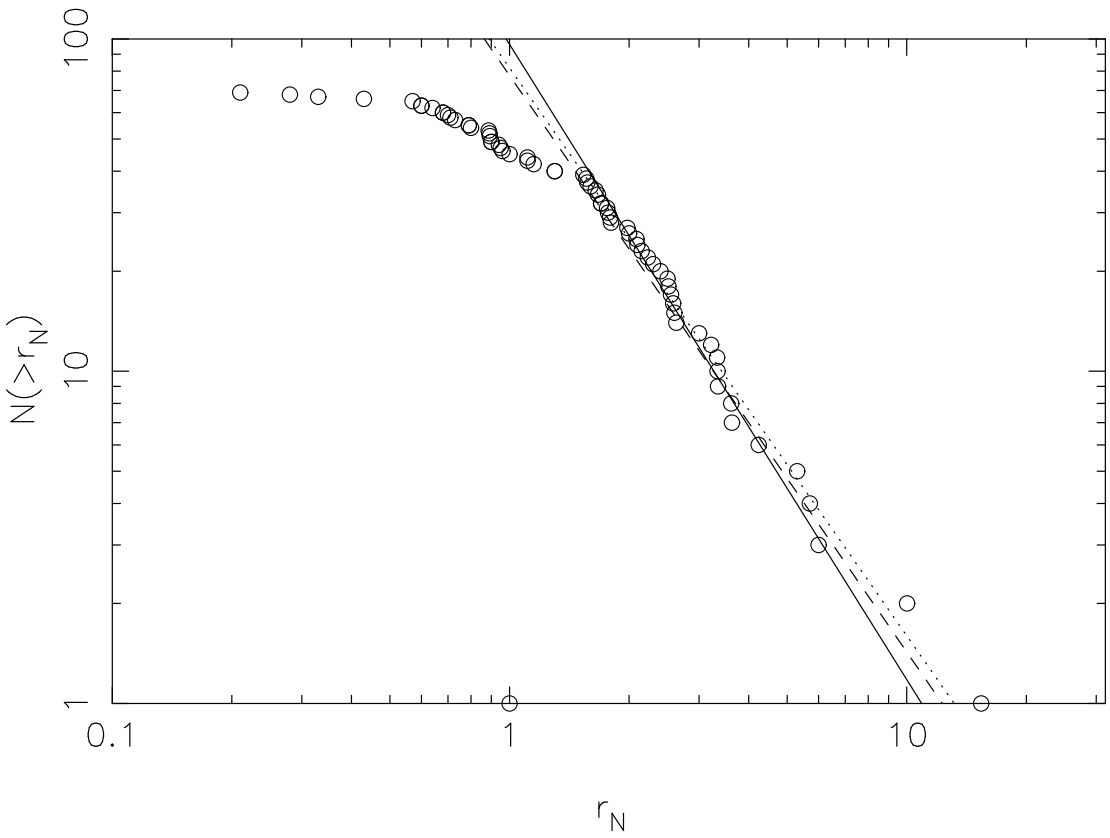

Figure 6.1: Cumulative size distribution for all JFCs, including radii from the compilation by Lamy et al. (2004), this thesis, and other recent papers (see text). The best fit straight line to the linear region with $r_N \geq 1.6$ km has $q = 1.91$ (solid line), while a weighted fit to all the data provides a reasonable approximation with $q = 1.74$ (dashed line). Using a different technique which weights the points on $\sqrt{N}$, and again fitting only to the linear regime, gives the dotted line with $q = 1.7$, similar to the other solutions.

CSD is dominated by the larger nuclei. A test was made fitting the data using a second technique, which weights the points as $\sqrt{N}$, which gave $q = 1.7 \pm 0.3$. Considering the uncertainties discussed below, this a similar result. The first technique is used here.

The uncertainty on these fits is dominated by the difference caused by inclusion or exclusion of the largest nuclei from the sample. The largest JFC is 29P/Schwassmann-Wachmann 1, which can justifiably be rejected on the grounds that it can alternatively be classified as a Centaur, as it orbits entirely beyond Jupiter's orbit with orbital semi-major axis $a = 6.0$ AU. Removing this from the list gives a best fit to the remaining 68 nuclei with $q = 1.80$. Removing the next largest comet, 28P/Neujmin 1, further increases the gradient of the CSD to $q = 1.86$. Fitting to only the $r_N \geq 1.6$ km region

gives an even greater increase in the gradient when the largest nuclei are removed, with $q = 2.06$ and 2.19 after removal of 29P and 28P respectively. The effect that inclusion or exclusion of these two comets on the CSD was also noted by Lamy et al. (2004), who used a different fitting method, so this is not a procedural problem. It is clear that the CSD is dominated by the largest comets, which makes the inclusion of the new result of Fernández et al. (2006) of importance, as they report 162P/Siding Spring to have $r_N = 6.0 \pm 0.8$, making this the next largest JFC after 29P and 28P. This not only influences the size distribution (although its presence or absence does not affect the fit to the same magnitude that the larger two nuclei do), but it also shows that even at the large end of the distribution there are still more comets being discovered; 162P was only found in 2004, most likely escaping earlier detection due to its low levels of activity.

Changing the assumed phase function will alter the observed CSD. The phase function for JFCs is an interesting parameter in its own right, as it is related to the surface properties (roughness), and could also be related to the albedo if the empirical correlation seen in asteroids (Belskaya & Shevchenko 2000) applies to comets. Lamy et al. (2004) collate measurements of β for 7 JFCs with a range of $0.025 \leq \beta \leq 0.06$ mag. deg^{-1}, and in addition Sekanina (1991) gives $\beta = 0.037$ mag. deg^{-1} for 10P/Temple 2. Adding the steep value of $\beta = 0.083$ mag. deg^{-1} reported for 47P in chapter 5 gives a range of $\sim$0.06 mag. deg^{-1} in measurements, which for a typical observation at $\alpha = 10^\circ$ gives a $\sim$30% change in the radius. These data also suggest that the normally assumed values of β are slightly low; the average is at $\beta = 0.05$ mag. deg^{-1}, although this is based on only 9 measurements. It is possible that the recent detection of steeper phase functions is due to an inverse correlation between size and β, with earlier measurements necessarily concentrating on the largest comets and improved technology allowing the study of smaller, more phase darkened nuclei; again, the small number of measurements means that such a relationship lacks statistical significance.

To investigate the effect that changing the assumed value of β has on the CSD, the

subset of the full database for which the phase of observation was reported (41 comets) was varied using equation 6.3 for a range of values of β. This subset has $q = 2.29$ for $\beta = 0.04$, and contains neither 29P (for which α at the time of observation was not reported) nor 28P (as comets with known phase function were omitted from the list). As from above that there is little difference between fitting q to the whole data set and fitting to only the linear part, for this investigation the fitting was carried out over the full range, which greatly simplified the process due to the change of the position of the 'knee' with β. It should be noted that a large number of the comets which are excluded from this list due to the non-reporting of α are from Lamy et al.'s *HST* work, and therefore more likely to have been observed at large phase angle and be susceptible to a large alteration in measured radius with a change in β. The variation in the fitted CSD was investigated for $0 \leq \beta \leq 0.1$, in steps of 0.005, covering the full range discussed above and more extreme values to either side of the distribution. Generally, as the assumed value of β increases the size of individual comets increases, but the variation in α at the time of observation means that the change in size varies between comets, obviously being largest for comets observed at large phase angle. This means that both the gradient and the shape of the CSD varies as nuclei change their relative sizes. The steepness of the distribution increases with increasing β, with the 'knee' in the distribution becoming more pronounced and moving to larger r_{N}. The change of q with β (fig. 6.2 (a)) is not a smooth function, as the discrete radii and their changes relative to each other cause the best fit to jump between values of q. Figure 6.3 shows example CSDs for phase functions at opposite ends of the observed distribution. The large change between $q(0.025) = 1.76$ and $q(0.085) = 2.47$ demonstrates that the assumed phase function is a source of a large uncertainty in the CSD.

The same method was also repeated with the inclusion of the 9 fixed radii, for comets with known β, included in the CSD. These acted to anchor the distribution as the radii of the other comets varied around them, and meant that $q(\beta)$ varied more smoothly, with smaller jumps between fits, and over a smaller range in q (fig. 6.2 (b)). The fact that 28P is included in this distribution as a large fixed radius nucleus at the end

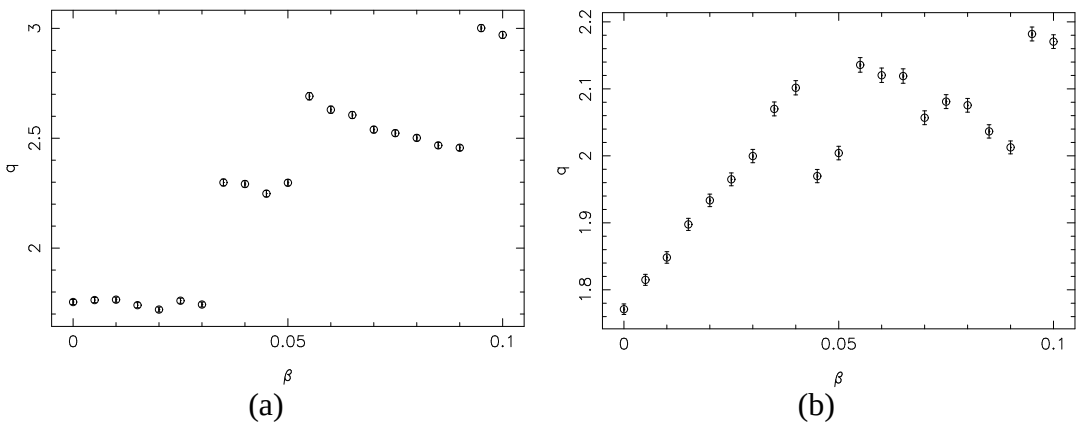

(a) (b)

Figure 6.2: Cumulative size distribution gradient q against assumed phase function β, for (a) 41 JFCs with unknown β but reported α and for (b) also including 9 JFCs with fixed radii due to having known β.

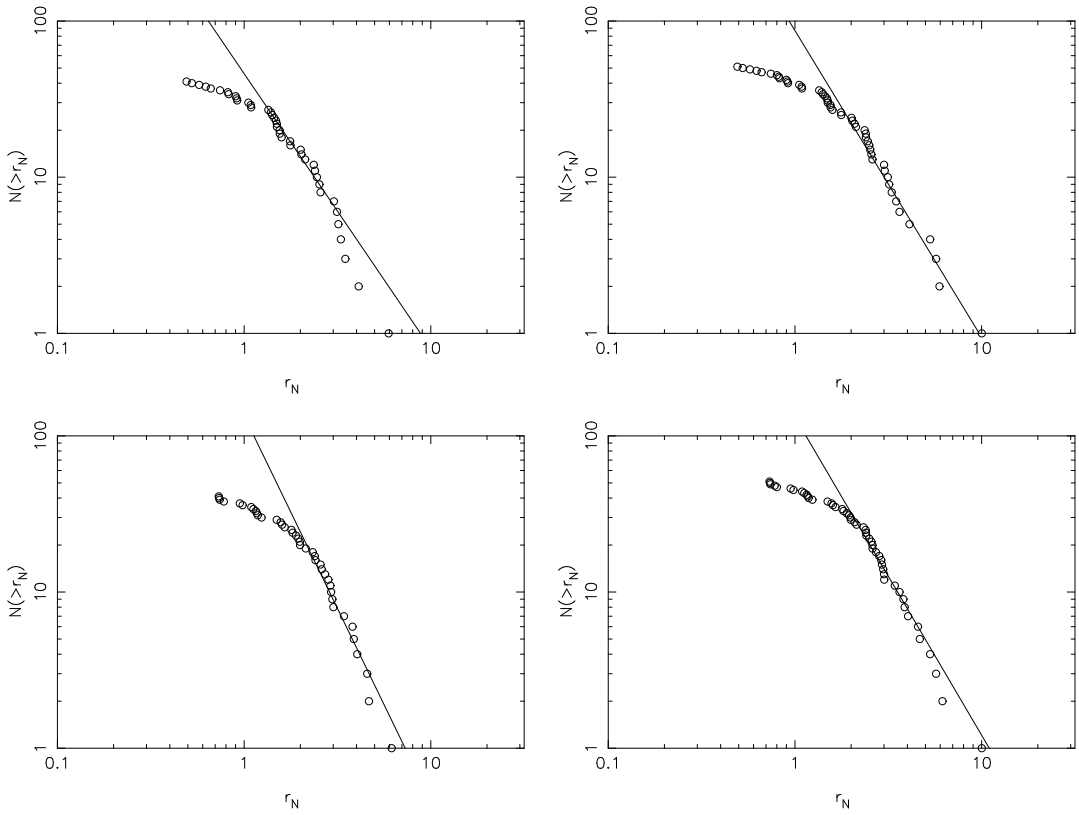

Figure 6.3: Cumulative size distributions for $\beta = 0.025$ and 0.085; without the 9 fixed nuclei on the left, and including them on the right.

of the distribution no doubt plays a large part in this. The range observed in this case was between $q(0.025) = 1.96$ and $q(0.085) = 2.04 \pm 0.01$, with a peak at $q(0.055) = 2.14 \pm 0.01$.

I choose to report the best fit CSD as the one including all 69 nuclei, as this is the most complete catalogue yet assembled. This necessarily has $\beta = 0.04$, which, lacking further data, seems a reasonable value to take in the centre of the distribution. The best fit is then that shown in fig. 6.1, although I expand the error bars on the fit to include the uncertainties due to both the choice of inclusion/exclusion of 29P and the assumed phase function, giving $q = 1.9^{+0.3}_{-0.2}$, for JFCs with $r_N \geq 1.6$ km.

This is lower than the theoretical $q = 2.5$ distribution derived by Dohnanyi (1969) for a collisionally relaxed population of self-similar bodies, with the same strength per unit mass, but is similar to the distribution for a collisional population of gravity controlled (strengthless) bodies, $q = 2.04$ found by O'Brien & Greenberg (2003). With the reasonably large uncertainty on the size distribution due to the small number of JFCs observed it can only be said that the CSD is consistent with this theoretical result. It is also important to note that this theoretical distribution does not give a constant slope, but is 'wavy'. While the JFC CSD does vary around the best fit straight line, this is more likely an artefact of the small numbers than a truly wavy distribution. For other Solar System minor body populations with better statistics, such as the NEOs and main belt asteroids, such waves in the CSD are seen (O'Brien & Greenberg 2005).

A comparison between the JFC CSD and the size distributions of other populations is of interest. The supposed parent population of the JFCS, the KBOs, have considerably steeper CSDs, although these are measured at larger sizes as the size ranges at which comets and KBOs have been observed are different. The values of $q = 3.20 \pm 0.10$ (Larsen et al. 2001) and 3.0 ± 0.5 (Trujillo et al. 2001) are for $r > 20$ km. It is therefore difficult to compare this steep distribution with the shallower JFC distribution, as it does not necessarily continue to the JFC nuclei size regime. It has been suggested that the KBO CSD has two parts, with the larger objects being pri-

mordial but the smaller ones collisional remnants, and therefore possibly with a CSD similar to the JFCs (*e.g.* Davis & Farinella 1997). However, recent results from X-ray occultation data (Chang et al. 2006) suggest that an extrapolation of Trujillo et al. (2001)'s size distribution holds true down to 100m scales, suggesting a large difference between KBO and JFC size distributions. Such a difference has yet to be explained. Weissman & Lowry (2003) collate CSD measurements and estimates for other minor bodies: For the other JFC related population, the Centaurs, there are insufficient data to give a good measurement of the CSD, although estimates put it at $q \approx 3$. As discussed above, asteroids and NEOs have wavy distributions, but the slopes of their CSDs fall closer to the JFC value at $q \approx 2$ than the KBOs. Taken together, and bearing in mind the above caveats regarding the lack of observations at similar scales, these various measurements tend to imply that CSDs are larger for outer Solar System bodies, implying a greater excess of small objects at large $R_{\rm h}$. If this is the case, then this implies that factors such as cometary activity may strongly modify the CSD of JFCs.

6.2 Rotational properties

Figure 6.4 shows histograms of spin rates for JFCs, KBOs, Centaurs and asteroids. The rotation rate distribution of JFCs provides another test to determine whether they are a collisionally relaxed population, or whether torques due to out-gassing substantially alter this distribution. For a collisionally relaxed population, these distributions should show a Maxwellian shape, as seen in large ($r > 20$ km) asteroids (Pravec et al. 2002 – their fig. 3 is recreated in fig 6.4(D) for comparison). Following Pravec et al., I plot the rotation frequency $f = 1/P_{\rm rot}$ normalised using the geometric mean $\langle f \rangle$ of each sample, which accounts for different sized bodies.

The histograms for JFCs, KBOs and Centaurs are not obviously Maxwellian in nature. Naïvely, it is expected that torques due to out-gassing from nuclei will act to flatten the comet distribution from an initial Maxwellian, as the torques will speed up

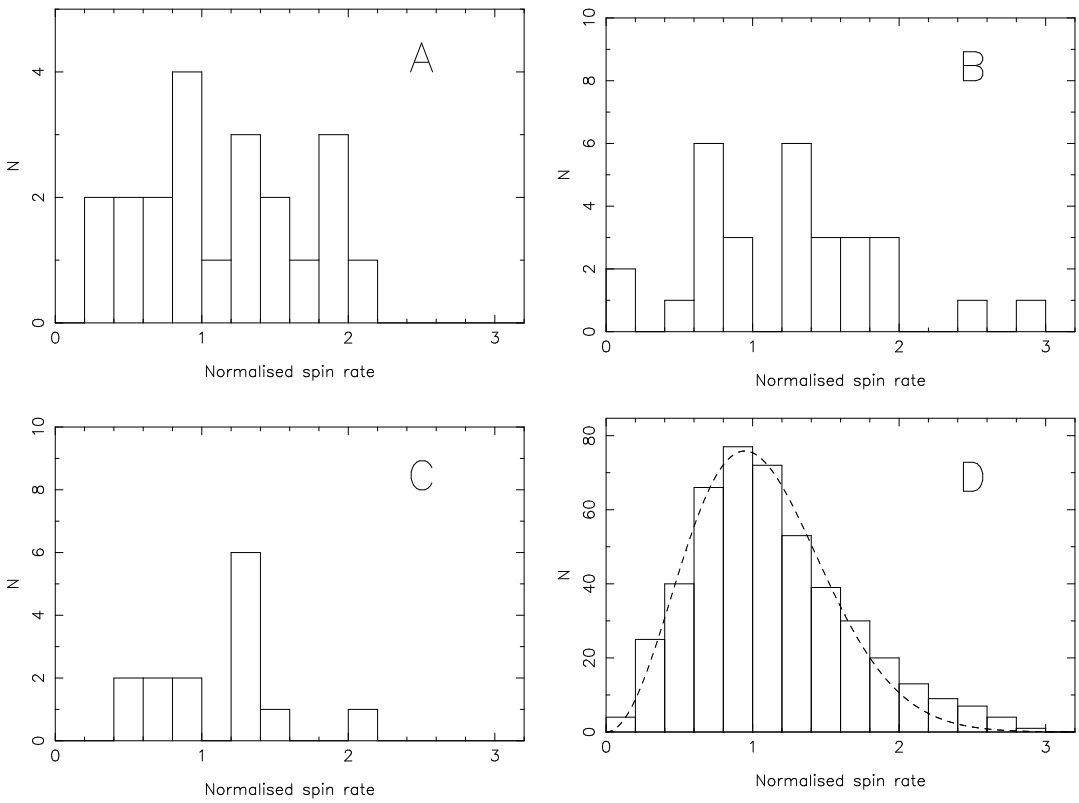

Figure 6.4: Histogram of normalised spin rates ($f/\langle f \rangle$, where $f = 1/P_{\rm rot}$) rates for (A) JFCs, (B) KBOs, (C) Centaurs and (D) asteroids. The asteroidal data is reproduced from Pravec et al. (2002), and shows the Maxwellian distribution in spin rates expected for a collisionally evolved system.

or slow down the rotation, although detailed numerical modelling is required to give the theoretical distribution for a cometary population. The JFC distribution appears relatively flat, with a slight excess at low spin rate / long rotation period, possibly due to the enhanced survival of spun down nuclei compared with those spun up towards the critical rate for remaining gravitationally bound. In fact the comet distribution is very well matched by a flat distribution; a Kolmogorov-Smirnov test comparing the normalised frequency distribution in fig. 6.4 (A) with a flat distribution with the same mean and standard deviation gives a D statistic of 0.07, implying that the distribution is entirely consistent with being flat (probability of $P = 1.00$). Given the small sample size, it is pointless to fit either a Maxwellian or any other complex theoretical distribution to the JFC data at present.

While there is an apparent contradiction between the CSD suggesting that the JFCs

are consistent with a population of collisional fragments, and the non-Maxwellian spin rate distribution, this is not the case. The CSD suggests an initial population that is made up from collisional fragments (presumably the remains of large KBOs), while the spin rate distribution indicates that the population no longer maintains the rotational velocities imparted by these collisions. The spin rate of the nucleus can be modified; most obviously by out-gassing, but also by (for example) the YORP effect (Rubincam 2000) or tidal torques due to close approaches to a planet. The timescales for these effects are considered by Samarasinha et al. (2004); out-gassing changes to spin states are dominant and can occur on timescales comparable to the orbital period of the comet. It is therefore not surprising to find that the spin rate distribution does not reflect a collisional population, even if the CSD does. The timescale for mass loss to significantly alter the size of the nucleus is very much longer, with only a few hundred metres lost from the surface over the dynamical lifetime of the comet (Weissman & Lowry 2003).

In rotation period, the distributions observed in KBOs and JFCs are similar; a Kolmogorov-Smirnov test gives a D statistic of 0.14, implying a probability of $P = 0.97$ that the two samples have the same distribution. Both populations lack the very fast ($P_{\rm rot} < 1$ hour) rotators seen in small asteroids, and also both are affected by the same observational bias; very slow rotators are less likely to be detected in any of these populations due to the length of observations, and therefore large amounts of telescope time, required to search for rotation periods of a few days or more. The KBO spin rate distribution shown in fig. 6.4 (D) is consistent with a flat distribution (K-S test gives D=0.13 and therefore P=0.71); the limited data does not appear to have a Maxwellian distribution. While KBOs may not be a collisional population (as evidenced by their steep size distribution), they would also not be expected to have the same flattened distribution as active comets. More spin rate data is clearly required on both comets and KBOs, and especially Centaurs, which are plotted in fig. 6.4 (C).

The rotation period of the nucleus can further be used to constrain its mechanical properties by plotting $P_{\rm rot}$ against $r_{\rm N}$. Toth & Lisse (2006) apply the theory of Davids-

son (1999) to divide the $P_{\rm rot}$–$r_{\rm N}$ plane into three regions; the allowed, damaged and forbidden regions. The precise location of these regions depends on the choice of tensile strength and density of the nucleus; nuclei in the allowed region are small enough or slow rotating enough that they are not disrupted, those in the damaged region are fractured due to shear forces but are gravitationally bound, while any object in the forbidden region would have spun apart. For all possible material properties considered Toth & Lisse found that nuclei fell into the allowed region, including very low strength and density models. The comets presented here also fall into this region.

6.3 Elongations and bulk densities

Using equation 3.19 I calculate the minimum bulk density $D_{\rm N}$ of each nucleus using the light-curve derived parameters a/b and $P_{\rm rot}$. This gives only the minimum density for two reasons; firstly, because the axial-ratios measured from light-curves are only minimum values due to the unknown orientation of the rotation axis, and secondly because the limit is calculated for the point where gravitational forces just balance centripetal forces, and there is no reason why the comet needs to be spinning at its fastest possible rate. Therefore it is not the individual density limits measured for comets that are of interest (these are listed in table 5.1), but the limiting behaviour of the population. Figure 6.5 shows $\log(P_{\rm rot})$ against a/b for all of the comets described in chapter 5, and also JFCs from previous works.

Firstly, looking at the distribution of axial-ratios, it can be seen that JFCs have generally been found to have small projected axial ratios, implying that they are not very extended bodies. The exceptions to this are 19P/Borrelly and the Centaur/JFC 29P, which are the two comets with $a/b \approx 2.5$. While these comets show that nuclei can be very elongated, they typically have $a/b \sim 1.5$. Although these projected axial ratios only put minimum limits on the actual a/b, the rotation axes of observed comets are expected to be randomly orientated; even with only 21 data points in fig. 6.5 it is

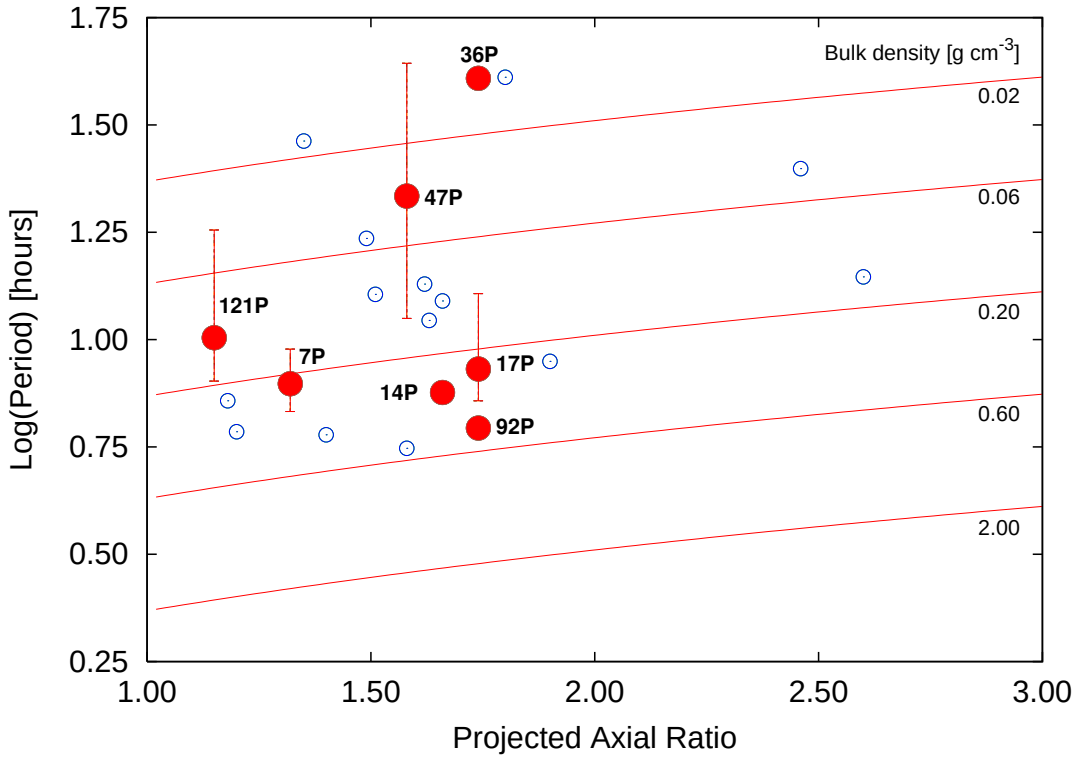

Figure 6.5: Rotation period against projected axial ratio for all JFC nuclei. The error bars on 7P, 17P and 47P cover the full range of possible periods discussed in the text, with the point at the strongest period according to the periodogram. Where error bars are not visible it is because the uncertainty in the best fit period is smaller than the point size. The open circles show the data from previous works; see fig. 3.3 for identification of each comet and references. The solid lines show where a strengthless body would lie on these axes for a variety of densities. There appears to be a cut-off in densities at ~ 0.6 g cm^{-3}.

likely that the clustering towards low a/b indicates a real trend towards low elongation shapes.

The reasonably flat distribution in spin rate discussed in the previous section is also apparent in the even distribution of rotation periods in fig. 6.5, and it is also clear that there is a fairly sharp cut off at short $P_{\rm rot}$. This corresponds to a cut-off in minimum densities at ~ 0.6 g cm^{-3}. In asteroids, there is a clear cut-off for bodies with $r > 80$ m at ~ 3 g cm^{-3} (Pravec et al. 2002), and it has been suggested (Lowry & Weissman 2003; Weissman et al. 2004) that a 0.6 g cm^{-3} cut-off for comets is equivalent to this. The lower value implies that comets are under-dense when compared to asteroids, due to their larger volatile content and/or more porous structure. The implication of this is that the true average density of nuclei is ~ 0.6 g cm^{-3}, as minimum densities would

be measured below the true value due to the limitations of the light-curve method described above, but none would be observed to be above it. For a large enough sample of a population with randomly inclined rotation axes and a rotation distribution including some comets spinning near to their break up rate, then the observed cut-off will give the true density of the bodies (under the assumption that nuclei have a similar average D_{N}). A limit around D_{N} = 0.6 g cm^{-3} agrees with the results from the *Deep Impact* mission, which found comet 9P/Temple 1 to have a low $D_{\mathrm{N}} = 0.4 \pm 0.3$ g cm^{-3} (Richardson & Melosh 2006), and the result of Asphaug & Benz (1996) who obtained $D_{\mathrm{N}} = 0.6$ g cm^{-3} for D/Shoemaker-Levy 9 based on its tidal disruption within Jupiter's Roche limit. To further examine the distribution of measured minimum densities, a histogram of these $N(D_{\mathrm{N}})$ against D_{N} is shown in fig. 6.6: There is an excess at low minimum density due to nuclei with long rotation periods, which are presumably spinning at well below their critical rate. $N(D_{\mathrm{N}})$ then decreases until the cut-off at 0.6 g cm^{-3}, where the distribution stops. This shape is similar to that seen in the better populated histogram of asteroid densities, although with the asteroid cut-off at a larger value.

While the low apparent density of comets when compared with asteroids is attributed to higher porosity and/or volatile content, the relative proportions of ice and rock within a body and the porosity cannot be found independently. However it is possible to express the fraction of a nucleus, by mass, made up of ice in terms of D_{N} and the porosity Ψ, which is the fraction of void space within the total volume:

$$\frac{M_{\mathrm{ice}}}{M_{\mathrm{N}}} = \frac{1-(1-\Psi)D_{\mathrm{rock}}/D_{\mathrm{N}}}{1-D_{\mathrm{rock}}/D_{\mathrm{ice}}}, \tag{6.4}$$

where D_{ice} and D_{rock} refer to the densities of the volatile ices ($\sim$ 1 g cm^{-3}) and dust ($\sim$ 3 g cm^{-3} for silicates) respectively. Using this equation for a range of assumed values of Ψ allows calculation of the corresponding proportions of ice and rock that would be required to give a density of 0.6 g cm^{-3}. Inserting this value for D_{N} into equation 6.4 gives the mass fraction of ice of $M_{\mathrm{ice}}/M_{\mathrm{N}} = 2 - 2.5\Psi$, and thus a minimum value for the porosity of $\Psi = 40\%$ for an entirely ice nucleus. This is considerably higher than

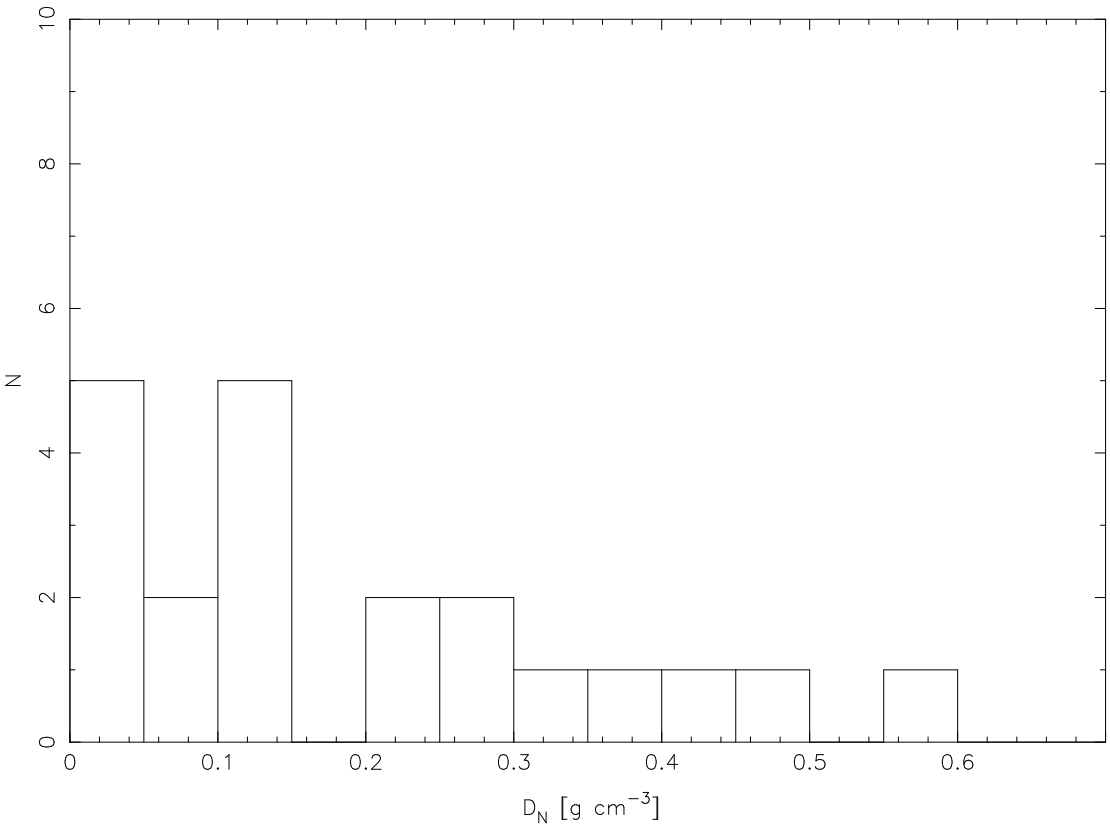

Figure 6.6: Histogram of measured minimum densities. Again, there appears to be a cut-off in densities at ~ 0.6 g cm^{-3}, and a large number of nuclei with only weak constraints on the density.

the values found through lab-based studies of meteorites, which have an average micro-porosity around 10%, with the most porous having $\Psi_\mu \approx 30\%$ (Britt & Consolmagno 2003) Therefore this suggests considerable macro-porosity or voids within nuclei. A value of $\Psi = 50\%$ requires that the nucleus is 75% ice to give $D_{\rm N}$ = 0.6 g cm^{-3}, while a nucleus with this density and a porosity of $\Psi \geq 60\%$ must be silicate dominated (less than half of its mass as ice). In the limiting case of a comet almost entirely depleted in volatiles ($M_{\rm ice} \rightarrow 0$), an $\sim 100\%$ silicate nucleus must have $\Psi \approx 80\%$ to give the low observed density. Figure 6.7 shows how $M_{\rm ice}/M_{\rm N}$ varies with porosity for a variety of densities: Higher densities imply that the porosity and ice fraction must be lower, while for low densities the porosity must be very large, with void space dominating over solid matter to such a degree that the fraction of the mass as volatiles makes little difference.

For a known composition and density, equation 6.4 can be used to find the porosity. A good example is the *Deep Impact* mission, which found 9P to be an 'icy dirt-ball' (*i.e.*

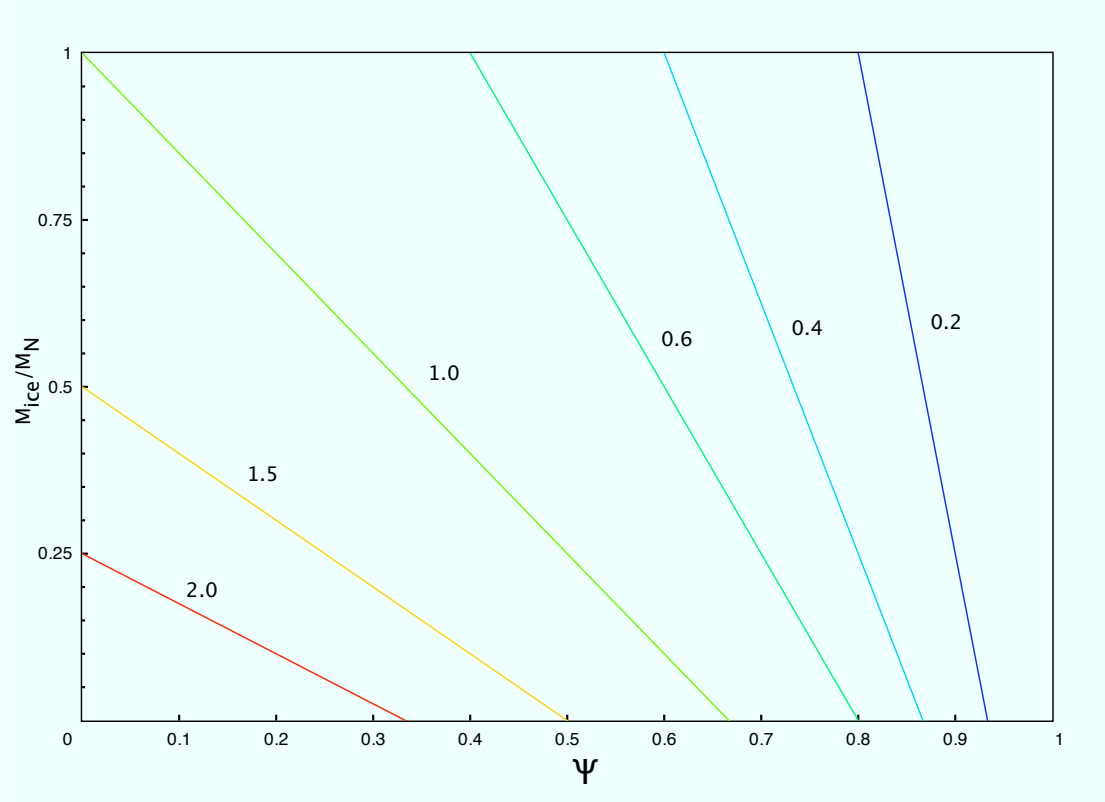

Figure 6.7: The composition (fraction of mass as volatiles) against porosity for various values of D_N. The lines are labelled with the value of D_N they correspond to. A value of D_N = 0.6 g cm^{-3} is implied from light-curves.

silicate dominated) due to the large amount of dust in the cratering experiment ejecta compared with gas from ices. A dust to volatile ratio of $\sim$ 2:1 (by volume) and density of 0.4 g cm^{-3} (Richardson & Melosh 2006) give $M_{ice}/M_N = 0.15$ and $\Psi = 0.83$. I do not attempt to find nucleus composition information from coma dust:gas ratios for other comets, as the assumption that the proportions of material in the coma are the same as those in the nucleus can not be made; ground based observations found that the *Deep Impact* crater ejecta had a considerably higher dust:gas ratio than the pre-impact coma (Meech et al. 2005). Both this *Deep Impact* result and the implied low density from the light-curves presented above suggest that JFCs are in general very porous bodies, with their volume containing more empty space than solid matter.

In fig. 6.8 I compare the position of JFC nuclei with the results from similar studies on their supposed parent population, the KBOs, using the recently published compilations of all KBO light-curve data by Lacerda & Luu (2006) and Trilling & Bernstein

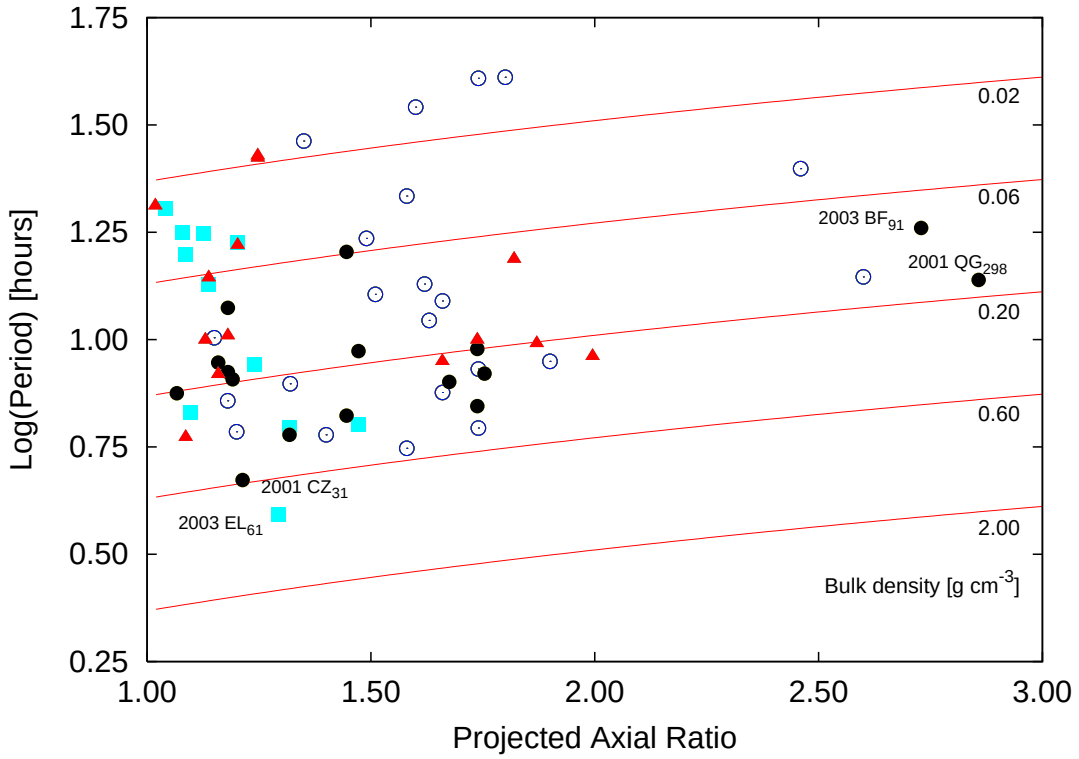

Figure 6.8: Same as fig. 6.5, but including data on KBOs (filled circles) and Centaurs (triangles) from Lacerda & Luu (2006), Trilling & Bernstein (2006), Ortiz et al. (2006) and Rabinowitz et al. (2006). The KBOs tend to have lower axial ratios, most likely due to the larger size of known KBOs - the largest KBOs ($r \geq 200$ km) are plotted as filled squares, and cluster towards the spherical side of the plot. The KBO data also falls above the 0.6 g cm^{-3} density line, and taken together with the JFC data support the hypothesis of a cut-off at this density. The labelled objects are referred to in the text.

(2006) [see these papers for references to results for individual objects], and also the new results of Ortiz et al. (2006) and Rabinowitz et al. (2006). Figure 6.8 shows the position of the 29 KBOs (filled circles) and 14 Centaurs & Scattered disk objects (triangles) with measured light-curves from these papers together with the JFC nuclei from fig. 6.5. The rotation periods plotted are for double-peaked light-curves, following the assumption that the changes in brightness are due to the changing observed cross-section of a rotating elongated body.

It is clear from fig. 6.8 that the comets and the outer Solar System bodies have similar minimum bulk densities, supporting the theory that JFCs come from the Kuiper Belt. I note that the KBOs also have minimum bulk densities below the postulated JFC cut-off of 0.6 g cm^{-3}, with the single exception of 2003 EL$_{61}$. This object is truly

exceptional in many ways; it is Pluto-sized, yet appears to rotate in 3.9 hours, is bluer than other KBOs and has a high albedo (see Rabinowitz et al. 2006). Accordingly, I regard 2003 EL_{61} as an outlier when discussing the general properties of KBOs. Other than 2003 EL_{61}, the fastest rotating KBO known is 2001 CZ_{31}, which has a rotation period of $P_{\rm rot}$ = 4.7 hours (Lacerda & Luu 2006), and therefore a density of $D_{\rm N} \geq 0.6$ g cm^{-3}. This agrees with the theory that KBOs and comets are rubble piles and underdense compared with asteroids, again suggesting a higher proportion of volatile ices and higher porosity.

In KBOs, the observed distribution in a/b tends towards 1, implying that these objects are generally more spherical than the nuclei. However this is likely an observational bias as the known KBOs are much larger due to the practical difficulties presented in observing distant KBOs with $r < 50$ km, and therefore more likely to be shaped under self-gravity. Lacerda & Luu (2006) note that only the 'smaller' of KBOs ($r < 200$ km) are particularly extended, and even these have minimum axial ratios $a/b < 2$. The exceptions are 2003 BF_{91} and 2001 QG_{298}, which have $a/b \geq 2.73$ and 2.86 respectively. 2003 BF_{91} is one of the smallest KBOs known, with an absolute visual magnitude of $H_V = 11.7$, corresponding to a radius of 9 km assuming a 10% albedo (Trilling & Bernstein 2006), or $r = 15$ km assuming a comet-like 4% albedo. This small size and large axial ratio suggests that there could be more elongated objects among the smaller KBOs, which have not been detected due to their extreme faintness. 2001 QG_{298} also shows a large photometric variation, which would correspond to a very large elongation for a single $r \approx 120$ km body, however this object is thought to be a contact binary due to the shape of its light-curve (Sheppard & Jewitt 2004).

6.4 Surface colours

Figure 6.9 shows all the available broad-band colours $(R-I)$ against $(V-R)$ for JFCs. Broadband colours of cometary nuclei are reasonable probes of surface properties (*e.g.*

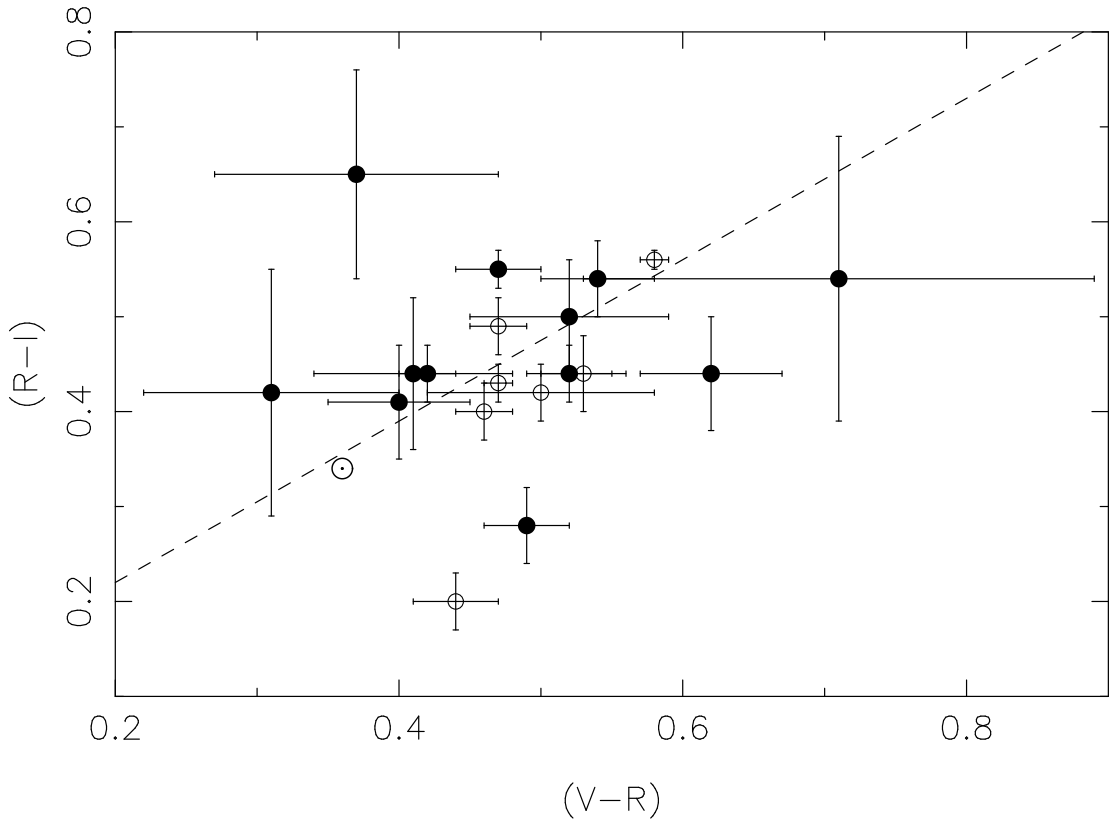

Figure 6.9: $(R-I)$ against $(V-R)$ for all JFCs with known colours. Filled circles – this work; open circles – comets with colours previously determined using the same multi-filter photometry method used here. The position of the Sun on these axes is marked using the symbol $\odot$. Data from: 2P/Encke: Jewitt 2002; 6P/d'Arrest: Jewitt 2002; Lowry & Weissman 2003; 22P/Kopff: Lamy et al. 2002; 28P/Neujmin 1: Delahodde et al. 2001; 45P/Honda-Mrkos-Pajdusakova: Lamy et al. 1999; 49P/Arend-Rigaux: Millis et al. 1988; Lowry et al. 2003; 143P/Kowal-Mrkos: Jewitt et al. 2003. Where more than one reference is given, weighted averages of the values were taken.

Davidsson & Skorov 2002), and due to the featureless nature of nuclei spectra provide equally good information while being easier to perform than spectroscopy. Colours are also instructive in that they allow comparison between comets and other solar system bodies. For example, while short period cometary nuclei are found to be redder than the Sun[1], they are less red than Kuiper-belt objects, the population from which they are thought to originate.

Prior to this work there were relatively few JFC nuclei with both $(V-R)$ and $(R-I)$ colours. While my data has not altered the mean values measured, they have shown

[1]The Solar colours quoted in various papers in the comet literature vary; I take $(V-R)_{\odot} = 0.35$ and $(R-I)_{\odot} = 0.33$ from the recent study by Holmberg et al. (2006), who use Sun-like stars to give precise Solar colours in a number of common filter systems.

that there is a larger range in colours than previously recorded, although the large uncertainties for the nuclei with extreme colours mean that they could be consistent with the range previously observed. Although the snap-shot colours on 44P give it the bluest $(V-R)$ ($=0.31\pm0.09$) in fig. 6.9, the range in $(V-R)$ extends slightly bluer, with the comet-asteroid transition object 107P/Wilson-Harrington having $(V-R)=0.20\pm0.04$ (Lowry & Weissman 2003) (not shown as there is no $(R-I)$ colour for this object). At the other end of the $(V-R)$ scale is 137P, which is considerably more red than most comets, although with relatively large error bars which bring it into line with the others.

In the paper I published on comets 7P, 14P and 92P (Snodgrass et al. 2005b) I described an increase in $(R-I)$ with increasing $(V-R)$ indicative of a steadily increasing spectra through these bands, as seen in primitive asteroids and the few cometary nuclei which have been observed spectroscopically (Luu 1993). This trend was also supported by the second NTT data set. Although the trend is not as visually obvious with the inclusion of the INT data, a weighted best fit to all the data still gives a straight line consistent with the earlier result at a 2σ level:

$$(R-I)_{\rm nuc} = m(V-R)_{\rm nuc} + c \begin{cases} m = 0.74 \pm 0.12 \\ c = 0.12 \pm 0.01 \end{cases} \tag{6.5}$$

While comets 45P/Honda-Mrkos-Pajdusakova, H2 and 40P are not very close to this line (the first two well below the line in the lower centre of the figure, 40P above the trend in the upper left) they all showed some activity during the observations. In the case of both 40P and H2 the coma was very weak, while 45P was observed by Lamy et al. (1999) using the HST when the comet was active and at large phase angle ($\alpha \approx 90^\circ$), but with a coma subtraction method. In all of these cases, the activity is not sufficient to reject the colour data as weak activity at large $R_{\rm h}$ should be dust dominated and therefore of similar optical properties to the nucleus, but also means that their difference from the rest of the data should not be over-interpreted.

Figure 6.10 is a colour-colour plot showing the data on KBOs (filled circles) and

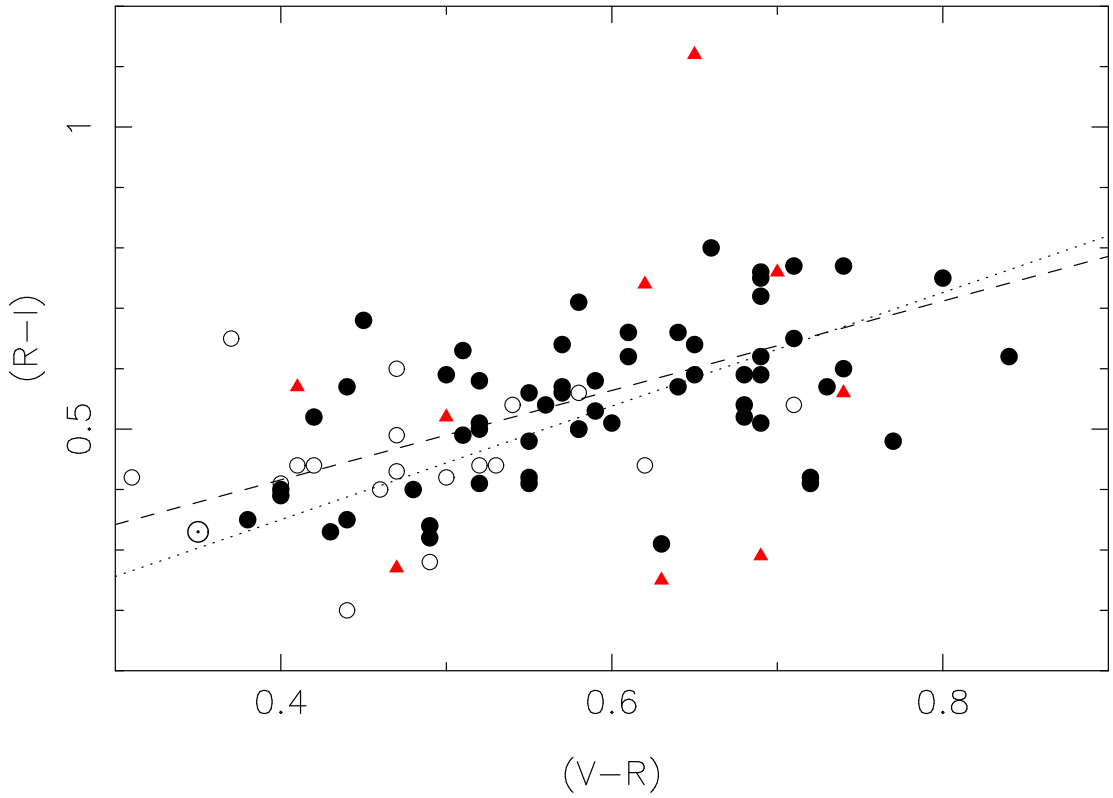

Figure 6.10: $(R-I)$ against $(V-R)$ for all JFCs, KBOs and Centaurs with known colours. Open circles – JFCs; filled circles – KBOs; triangles – Centaurs. The position of the Sun on these axes is marked using the symbol $\odot$. The dashed line shows the best fit to the comet data, the dotted line is the fit to the KBOs. KBO and Centaur data from Jewitt & Luu (2001); Peixinho et al. (2004).

that of JFCs (open circles), with the same trend line over-plotted (KBO data from Jewitt & Luu 2001; Peixinho et al. 2004). It is clear that this line provides a reasonable fit to the data, although there is considerable scatter in the KBO results, which is confirmed by a fit to the KBO data which is consistent (at a 2σ level) with that for JFCs:

$$(R-I)_{\rm KBO} = m(V-R)_{\rm KBO} + c \begin{cases} m = 0.94 \pm 0.06 \\ c = -0.03 \pm 0.01 \end{cases} \tag{6.6}$$

This is plotted as a dotted line in fig. 6.10. However, while both populations follow approximately the same trend in colours, it is clear that the KBOs are generally redder than the comet nuclei. The mean colour of JFC nuclei is $\overline{(V-R)}_{\rm nuc} = 0.45 \pm 0.11$ (N = 31), compared with $\overline{(V-R)}_{\rm KBO} = 0.59 \pm 0.08$ (N = 62) for the KBO population. It has been suggested that 'space weathering' produces the very red surfaces seen in KBOs

and that cometary activity resurfaces nuclei to give them more neutral colours (Jewitt 2002). These data support this hypothesis; the similar $(V-R)$–$(R-I)$ relations suggesting similar spectra and therefore a common source, while the JFCs tend towards the blue side of the distribution and lack the 'ultra-red matter' of KBOs. Under this paradigm, the very red colour measured for 137P may indicate that it is a relatively young comet which has undergone little resurfacing, although I remain cautious of inferring too much from the colour in light of its large uncertainty. Note that the Centaurs (triangles in fig. 6.10, data also from Jewitt & Luu 2001; Peixinho et al. 2004) have a similar spread in $(V-R)$ to the KBOs, but do not appear to show the same trend as the JFCs and KBOs, and exhibit a very large variation in $(R-I)$. This is somewhat surprising, as Centaurs are thought to be the intermediate dynamical population through which KBOs pass to become JFCs, but there are only nine Centaurs in fig. 6.10 and further data may clarify the situation.

To further investigate the idea that the more neutral JFCs are 'resurfaced' KBOs, it is desirable to use a one dimensional parameter to describe the relative redness of these objects. To do this the $(V-R)$ and $(R-I)$ data shown in fig. 6.10 were translated into distance along the best fit line x, which has arbitrary units linearly related to the normal colour indices, with increasing x corresponding to redder colours. The weighted average best fit between the JFC and KBO best fit lines quoted above was used (with $m = 0.90 \pm 0.05$ and $c = 0.09 \pm 0.01$) giving a translation of

$$x = 0.45(V-R) + 0.67(R-I) - 0.06 \tag{6.7}$$

Histograms of the number of objects $N(x)$ per bin ($\mathrm{d}x = 0.05$) are shown in fig. 6.11. It can be seen that the JFC distribution does indeed appear to be consistent with the KBO distribution, but lacking in 'ultra-red' matter. The two populations are a good match at the bluer end. The KBO colours appear to be approximately normally distributed (the fitted distribution has mean $\overline{x}_{\mathrm{KBO}} = 0.75$ and standard deviation $\sigma_{\mathrm{KBO}} = 0.14$), as do the JFCs, despite the relatively poor statistics ($\overline{x}_{\mathrm{JFC}} = 0.61$, $\sigma_{\mathrm{JFC}} = 0.10$). The model

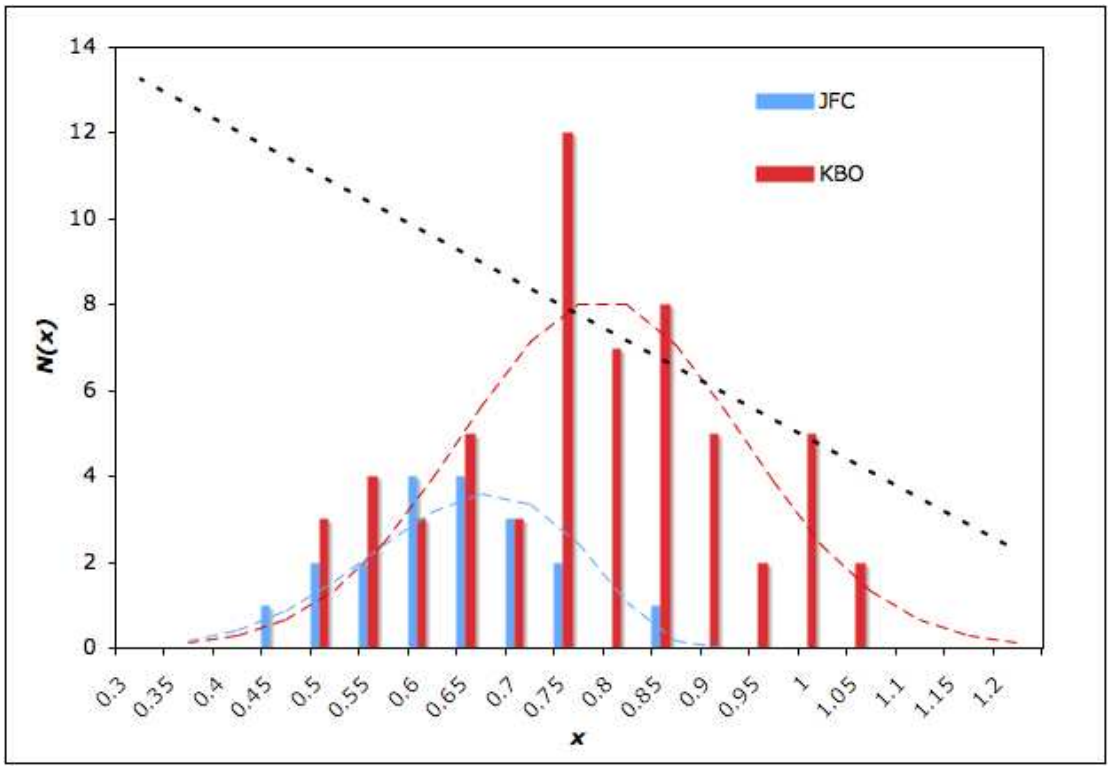

Figure 6.11: The $(R-I)$ against $(V-R)$ data was reduced onto distance x along the best fit (see text). This plot shows the histograms of $N(x)$ against x for JFCs and KBOs. The KBOs (red) are reasonably well matched by a normal distribution (red dashed line). The JFCs (blue) appear to have a truncated distribution; the model JFC population (blue dashed line) was created by convolving the KBO model with a 'de-reddening' term that is $\propto -x$ (dotted black line - arbitrary units).

distribution plotted for the JFCs (blue dashed line) however is not the best fit normal distribution, but one generated by convolving the fitted KBO distribution with a 'de-reddening' term: $N(x)_{\mathrm{JFC}} = N(x)_{\mathrm{KBO}} \otimes f(x)$, where the fraction of objects remaining $f(x) \propto -x$. Thus the 'de-reddening' depends on the colour, with the most red KBOs being most depleted, with more neutrally coloured objects remaining. A least squares fit gave $f(x) = 2.8 - 3.5x$ (again, in non-physical units) and gave a good reproduction of the observed JFC distribution. This de-reddening function means that 100% of the KBO surfaces remain at $x = 0.5$ and they are entirely depleted beyond $x = 0.8$. Clearly this model is very approximate in its treatment of distributions, but it serves to demonstrate a possible transformation route between the KBO and JFC distributions. A more thorough approach would be to treat a large number of test particles, with a starting distribution like that observed in KBO colours, and then test the effect of different the-

oretical 'de-reddening' models on the resultant JFC colours by computing the change in colour for individual comets. While an interesting problem, such calculations are beyond the scope of this thesis.

Although a linear decrease in the number of surviving KBO surfaces with colour can be invoked to explain the observed JFC colours, a physical interpretation of this effect is required. A plausible solution is to assume that the observed variation in KBO colour is associated with the ages of their surfaces, and that space weathering reddens the surfaces in an approximately linear fashion with time. Under this paradigm the objects in very red tail of the distribution are very old, while the bluer ones have under gone some 'resetting' of their surfaces (*e.g.* due to a collision[2]) more recently. When a KBO is perturbed into the inner Solar System, the onset of cometary activity acts to resurface the nucleus. For younger KBOs, whose surfaces are not very different to their sub-surfaces as they have not been weathered for long, this has little effect, but for the very ancient and red surfaces, the difference is important. One interesting aspect of this interpretation is that it suggests that nuclei surfaces, being younger, are a closer match to their interiors, and thus may provide a better view of 'primordial' material than the ancient weathered surfaces of KBOs.

Remaining questions include: To what degree is the distribution seen in both populations due to different surface ages / processing, versus the effect of any underlying intrinsic variation in surface materials? Also, does cometary activity act as a 'reset' switch, with an essentially instant effect on the surface, or is it a more gradual process? The latter could also explain the above model of linear loss of KBO surfaces in the process of creating comets; in this case we would expect to see dynamically new ecliptic comets having more red colours, and that the colour of nuclei would become bluer with time. It is therefore important to search for observational signatures of continued sur-

[2]Modelling by Jewitt & Luu (2001) suggests that collisions between KBOs are actually unlikely to be responsible for the observed range in KBO colours. Here I still assume that the distribution is related to the age of the surface, as it is difficult to explain why the alternatives (that the range is either intrinsic or that different bodies undergo different reddening processes) should follow the de-reddening model described to produce the JFC distribution.

face evolution within the JFC population. If reddening of surface material occurs on a time-scale shorter than that for significant orbital change of a JFC, then one might see a correlation with orbital parameters. However, plots of $(V-R)$ against both semi-major axis a and the fraction of orbital period spent at $R_h \leq 3$ AU showed no correlation. Therefore the nucleus colour does not depend on the orbital parameters of the JFC.

A remaining possibility is that the timescale for significant reddening of the surface is shorter than the orbital period. 28P/Neujmin 1 has a large amount of extant photometry (collated by Delahodde et al. 2001 and Lamy et al. 2004) and is well known as a comet that is essentially dormant throughout much of its orbit, only showing a small amount of activity near perihelion. Taking these colours and plotting them against position in the orbit shows no correlation, it appears that the surface colour of 28P is constant throughout its orbital cycle. Therefore I conclude that significant reddening does not occur on time-scales of less than 20 years and the colours measured for individual comets are not dependant on their orbital position at the time of observation.

Chapter 7

Concluding remarks and future work

This thesis presents the results of observations of 29 ecliptic comets; 18 based on snap-shot observations and time-series obtained on a further 11. Multi-epoch data were obtained for five of these comets. These were observed in four runs, two using the 3.6m NTT and two using the 2.5m INT, and additionally one hour of time on the 2m FTN. All comets were observed at $R_{\rm h} \geq 3$ AU, where comets are expected to show relatively little activity due to a drop in the theoretical H_2O sublimation rate at this distance. However 10 of the 24 observations where the comet was detected at sufficient S/N to look for coma showed activity, with variation between the highly active 103P (which was visibly active on two occasions, including when beyond 5 AU) and those with very weak activity which was only detected in surface brightness profiles from deep co-added images. The fraction of comets active beyond $R_{\rm h}$ = 3 AU is then $f(R_{\rm h} \geq 3) \approx$ 40%. Beyond 4 and 5 AU, the observed active fractions are $f(R_{\rm h} \geq 4) = \frac{5}{16} \approx 30\%$ and $f(R_{\rm h} \geq 5) = \frac{2}{7} \approx 30\%$. It is obvious that a significant fraction of JFCs show activity at large distances; it is likely that these comets retain some weak coma throughout their orbits, which must be remembered when considering reports of apparently inactive nuclei at large $R_{\rm h}$.

For those observations of comets which were shown to be *effectively* inactive based on a star-like surface brightness profile (12 comets), measurements of nuclear properties were made. These results were combined with other data from the literature to constrain various properties of the population. The cumulative size distribution of JFCs was shown to be well represented by a $N(> r_{\rm N}) \propto r_{\rm N}^{-q}$ relation where $q = 1.9^{+0.3}_{-0.2}$. The uncertainties on q were found to be dominated by the largest nuclei, and the choice of the assumed phase function used to find the radius. This CSD is consistent with theoretical models for a population of strengthless collisional fragments.

Time-series observations on 11 comets gave constraints on the shape (minimum axial-ratios) and rotation period. The distribution of spin rates for JFCs was found to be inconsistent with a collisional population, being well represented by a flat distribution instead of the Maxwellian seen in asteroids. This implies that torques from out-gassing

act to alter the spin states of comets, as expected. The axial-ratios of JFCs tend to be modest, typically around $a/b = 1.5$ with none observed at $a/b > 3$. Assuming strengthless nuclei, these rotation periods and axial-ratios are combined to put limits on the bulk density. There is a cut-off in minimum densities at ~ 0.6 g cm^{-3}, implying that the true density of nuclei is near this value. This implies that they are remarkably porous, with $\Psi \gtrsim 70\%$ for nuclei with similar proportions of dust and ice to that found for 9P/Temple 1 by *Deep Impact*.

The surfaces of nuclei have red colours, and a trend of increasing $(R-I)$ with $(V-R)$ is found, implying a continually rising spectrum and a consistent reddening agent across these wavelengths. The colours are not found to be dependant on the orbit of the comet or its position along the orbit at the time of observation. The colours of JFCs are shown to be consistent with an initial population matching the KBO colours that has been modified by a de-reddening function that depends on the colour, with very red objects depleted more than neutral ones.

Further comparison between JFCs and KBOs shows that their size distributions appear to be inconsistent, with a steep CSD for KBOs implying that they are not a collisional population, at least at large sizes. This may extend down to the cometary size regime, in which case it is difficult to explain the shallower distribution seen in comets unless a large proportion of comets are very short lived. The rotational properties and densities of the two populations appear to be similar, although the known KBOs are observed to be less elongated due to an observational bias towards large bodies. While it makes sense that the bulk densities of the JFCs are similar to their parent population, the similarity in rotation rate is unexpected as the rotation rates of comets show signs of modification by cometary activity. This is based on a relatively small sample size though; there is ample opportunity to add to to the understanding of these distributions with further light-curve studies.

Other useful future directions for this work include measuring the phase function for more comets, as the distribution of this parameter is poorly understood. Such work

requires multiple observations over an extended period to get a range in α, and also sufficient light-curve coverage at each epoch to account for rotational phase effects. Not only would this allow further interpretation of the surface properties (roughness, single particle albedo), but it would give an improved measure of the mean value of β and reduce a major contribution to the uncertainty on the size distribution. It would be interesting to see whether or not there is any relation between size and phase function, based on a weak correlation of increasing β with decreasing size seen in the current small data set.

There is scope for more detailed modelling of the surface colour change between KBOs and JFCs, as the treatment of distributions presented here is simplistic but does imply that a de-reddening function can be used to describe the alteration of surfaces. Further observations of both populations will also be useful, to fill in the distributions. Linking these observations with an independent measure of the dynamical age of the comet would also be an interesting exercise.

Finally, while this thesis has dealt with the ecliptic or Jupiter Family comets, it would be of interest to extend similar observations and analysis into the other cometary regimes in the solar system, to test whether different classes of comet (from different source regions in the proto-Solar nebula) have different physical properties. This is a more challenging prospect for long period or dynamically new comets, as they show greater levels of activity to larger heliocentric distance, and therefore require 8m class telescopes to observe them when effectively inactive at very large distance. Study of dynamically new comets before they become active would allow investigation of an exceptionally 'un-altered' primordial body, but such work is hampered by the fact that these comets are generally only discovered once they become active in the inner Solar System. Hopefully, the new Pan-STARRS telescopes will detect candidates for such studies, as this survey will detect moving objects down to $m_R \approx 24$ (Kaiser & Pan-STARRS Team 2005). Easier populations of comets to study, due to their very low activity at low $R_{\rm h}$, are the NEO and Main Belt comet populations. The study of NEO

comets is the study of one of the potential end states of a JFC, where the nuclei have lost volatiles or built up a thick crust so show little out-gassing, and thus helps in the understanding of their evolution. The MBCs are possibly a distinct group which formed roughly where they are now, and therefore provide another probe of a different region of the Solar nebula. With both of these populations, the primary problem is identifying low activity comets among the asteroids, as the definitive test for being a comet is the presence of coma.

The work in this thesis and by other investigators is giving us an understanding of the physical properties of JFCs and how these are related to their parent bodies. An improved measurement of the size distribution is in agreement with the population being collisionally relaxed, while an important and previously unconsidered source of uncertainty on this measurement is identified. The large number of light-curves presented allows a first investigation of the distribution of rotation rates, which is found to be consistent with a flat distribution, most likely a result of torques due to out-gassing. The densities of nuclei and KBOs are found to be low and consistent with very high porosity. Finally, the surface colours of JFCs are shown to be consistent with being a sub-set of the KBO population depleted in very red bodies according to a linear relation.

References

A'Hearn, M. F., Belton, M. J. S., Delamere, W. A., et al. 2005, *Deep Impact: Excavating Comet Tempel 1*, Science, **310**, 258

A'Hearn, M. F., Campins, H., Schleicher, D. G., & Millis, R. L. 1989, *The nucleus of Comet P/Tempel 2*, ApJ, **347**, 1155

A'Hearn, M. F., Millis, R. L., Schleicher, D. G., Osip, D. J., & Birch, P. V. 1995, *The ensemble properties of comets: Results from narrowband photometry of 85 comets, 1976-1992*, Icarus, **118**, 223

A'Hearn, M. F., Schleicher, D. G., Millis, R. L., Feldman, P. D., & Thompson, D. T. 1984, *Comet Bowell 1980b*, AJ, **89**, 579

Asphaug, E. & Benz, W. 1996, *Size, Density, and Structure of Comet Shoemaker-Levy 9 Inferred from the Physics of Tidal Breakup*, Icarus, **121**, 225

Bar-Nun, A., Herman, G., Laufer, D., & Rappaport, M. L. 1985, *Trapping and release of gases by water ice and implications for icy bodies*, Icarus, **63**, 317

Belskaya, I. N. & Shevchenko, V. G. 2000, *Opposition Effect of Asteroids*, Icarus, **147**, 94

Bernstein, G. M., Trilling, D. E., Allen, R. L., et al. 2004, *The Size Distribution of Trans-Neptunian Bodies*, AJ, **128**, 1364

Bessel, F. W. 1836a, *Bemerkungen über mögliche Unzulänglichkeit der die Anziehungen allein berücksichtigenden Theorie der Kometen. Von Herrn Geheimen-Rath u Ritter Bessel*, Astronomische Nachrichten, **13**, 345

Bessel, F. W. 1836b, *Beobachtungen uber die physische Beschaffenheit des Halley's schen Kometen und dadurch veranlasste Bemerkungen*, Astronomische Nachrichten, **13**, 185

Boehnhardt, H. 2004, *Split comets*, in Comets II, ed. M. C. Festou, H. U. Keller, & H. A. Weaver (University of Arizona Press), 301–316

Boehnhardt, H., Delahodde, C., Sekiguchi, T., et al. 2002, *VLT observations of comet 46P/Wirtanen*, A&A, **387**, 1107

Bottke, W. F., Cellino, A., Paolicchi, P., & Binzel, R. P. (Eds), 2002, *Asteroids III* (University of Arizona Press)

Brahe, T. 1578, *Tychonis Brahe Dani de mundi: aetherei recentioribus phaenomenis liber secundus qui est de illustri stella caudata ab elapso fere triente Nouembris anni 1577, usg: in finem ianuarij sequentis conspecta* (Uraniborg)

Brandt, J. C. & Chapman, R. 2004, *Introduction to Comets* (Cambridge Univeristy Press)

Britt, D. T. & Consolmagno, G. J. 2003, *Stony meteorite porosities and densities: A review of the data through 2001*, Meteoritics and Planetary Science, **38**, 1161

Britt, D. T., Yeomans, D. K., Housen, K., & Consolmagno, G. J. 2002, *Asteroids Density, Porosity, and Structure*, in Asteroids III, ed. W. F. Bottke, A. Cellino, P. Paolicchi, & R. P. Binzel (University of Arizona Press), 485–500

Brownlee, D. E., Horz, F., Newburn, R. L., et al. 2004, *Surface of Young Jupiter Family Comet 81P/Wild 2: View from the Stardust Spacecraft*, Science, **304**, 1764

Chandrasekhar, S. 1969, *Ellipsoidal figures of equilibrium* (The Silliman Foundation Lectures, New Haven: Yale University Press)

Chang, H.-K., King, S.-K., Liang, J.-S., et al. 2006, *Occultation of X-rays from Scorpius X-1 by small trans-neptunian objects*, Nature, **442**, 660

Chapman, C. R., Williams, J. G., & Hartmann, W. K. 1978, *The asteroids*, ARA&A, **16**, 33

Christian, D. J., Pollacco, D. L., Skillen, I., et al. 2006, *The SuperWASP wide-field exoplanetary transit survey: Candidates from Fields 23hr $<$ RA $<$ 03hr*, MNRAS, **372**, 1117

Cowan, J. J. & A'Hearn, M. F. 1979, *Vaporization of comet nuclei - Light curves and life times*, Moon and Planets, **21**, 155

Davidsson, B. J. R. 1999, *Tidal Splitting and Rotational Breakup of Solid Spheres*, Icarus, **142**, 525

Davidsson, B. J. R. & Gutiérrez, P. J. 2004, *Estimating the nucleus density of Comet 19P/Borrelly*, Icarus, **168**, 392

Davidsson, B. J. R. & Gutiérrez, P. J. 2005, *Nucleus properties of Comet 67P/Churyumov Gerasimenko estimated from non-gravitational force modeling*, Icarus, **176**, 453

Davidsson, B. J. R. & Gutiérrez, P. J. 2006, *Non-gravitational force modeling of Comet 81P/Wild 2*, Icarus, **180**, 224

Davidsson, B. J. R. & Skorov, Y. V. 2002, *On the Light-Absorbing Surface Layer of Cometary Nuclei. I. Radiative Transfer*, Icarus, **156**, 223

Davis, D. R., Durda, D. D., Marzari, F., Campo Bagatin, A., & Gil-Hutton, R. 2002, *Collisional Evolution of Small-Body Populations*, in Asteroids III, ed. W. F. Bottke, A. Cellino, P. Paolicchi, & R. P. Binzel (University of Arizona Press), 545–558

Davis, D. R. & Farinella, P. 1997, *Collisional Evolution of Edgeworth-Kuiper Belt Objects*, Icarus, **125**, 50

Davis, L. E. 1999, *Stellar Photometry Tools in IRAF*, in ASP Conf. Ser. 189: Precision CCD Photometry, 35

Delahodde, C. E., Meech, K. J., Hainaut, O. R., & Dotto, E. 2001, *Detailed phase function of comet 28P/Neujmin 1*, A&A, **376**, 672

Delsemme, A. H. & Miller, D. C. 1970, *Physico-chemical phenomena in comets-II. Gas adsorption in the snows of the nucleus*, Planet. Space Sci., **18**, 717

Dohnanyi, J. W. 1969, *Collisional models of asteroids and their debris*, J. Geophys. Res., **74**, 2531

Dones, L., Weissman, P. R., Levison, H. F., & Duncan, M. J. 2004, *Oort cloud formation and dynamics*, in Comets II, ed. M. C. Festou, H. U. Keller, & H. A. Weaver (University of Arizona Press), 153–174

Donn, B., Daniels, P. A., & Hughes, D. W. 1985, *On the Structure of the Cometary Nucleus*, BAAS, **17**, 520

Duncan, M., Levison, H., & Dones, L. 2004, *Dynamical evolution of ecliptic comets*, in Comets II, ed. M. C. Festou, H. U. Keller, & H. A. Weaver (University of Arizona Press), 193–204

Edgeworth, K. E. 1949, *The origin and evolution of the Solar System*, MNRAS, **109**, 600

Encke, J. F. 1836, *Über die Wiederkehr des Pons'schen (Enckeschen) Cometen im Jahre 1835 und die Hypothese des widerstehenden Mittels. Von Herrn Professor u. Ritter Encke (Beschluß.)*, Astronomische Nachrichten, **13**, 265

Fernández, J. A. 1980, *On the existence of a comet belt beyond Neptune*, MNRAS, **192**, 481

Fernández, J. A., Tancredi, G., Rickman, H., & Licandro, J. 1999, *The population, magnitudes, and sizes of Jupiter family comets*, A&A, **352**, 327

Fernández, Y. R., Campins, H., Kassis, M., et al. 2006, *Comet 162P/Siding Spring: A Surprisingly Large Nucleus*, AJ, **132**, 1354

Fernández, Y. R., Lisse, C. M., Ulrich Käufl, H., et al. 2000, *Physical Properties of the Nucleus of Comet 2P/Encke*, Icarus, **147**, 145

Fernández, Y. R., Lowry, S. C., Weissman, P. R., et al. 2005, *New near-aphelion light curves of Comet 2P/Encke*, Icarus, **175**, 194

Festou, M. C., Keller, H. U., & Weaver, H. A. 2004, *A brief conceptual history of cometary science*, in Comets II, ed. M. C. Festou, H. U. Keller, & H. A. Weaver (University of Arizona Press), 3–16

Fitzsimmons, A., Snodgrass, C., & Hainaut, O. 2004, *Comet P/2003 SQ_{215} (NEAT-Loneos)*, IAU Circ., **8274**

Fujiwara, A., Kawaguchi, J., Yeomans, D. K., et al. 2006, *The Rubble-Pile Asteroid Itokawa as Observed by Hayabusa*, Science, **312**, 1330

Gombosi, T. I. & Houpis, H. L. F. 1986, *An icy-glue model of cometary nuclei*, Nature, **324**, 43

Greenberg, J. M. 1998, *Making a comet nucleus*, A&A, **330**, 375

Groussin, O., Lamy, P., Jorda, L., & Toth, I. 2004, *The nuclei of comets 126P/IRAS and 103P/Hartley 2*, A&A, **419**, 375

Hainaut, O. 2001, *La Silla Telescope Views Comet Hale-Bopp at 2 Billion Kilometres*, ESO Press Photos, 07a

Hainaut, O. 2003, *ESO La Silla SciOps Technical Report: LSO-TRE-ESO-40200-1061/1.0*, Tech. rep., ESO

Halley, E. 1705, *A synopsis of the Astronomy of Comets* (London)

Harris, A. W. 2002, *On the Slow Rotation of Asteroids*, Icarus, **156**, 184

Hicks, M. D., Bamberry, R. J., Lawrence, K. J., & Kollipara, P. 2006, *Near-Nucleus Photometry of Comets Using Archived NEAT Data*, Icarus, in press

Hirao, K. & Itoh, T. 1987, *The Sakigake / Suisei Encounter with Comet P/Halley*, A&A, **187**, 39

Ho, P. Y. 1962, *Ancient and mediaeval observations of comets and novae in Chinese sources*, Vistas in Astronomy, **5**, 127

Holmberg, J., Flynn, C., & Portinari, L. 2006, *The colours of the Sun*, MNRAS, **367**, 449

Holsapple, K. A. 2001, *Equilibrium Configurations of Solid Cohesionless Bodies*, Icarus, **154**, 432

Holsapple, K. A. 2004, *Equilibrium figures of spinning bodies with self-gravity*, Icarus, **172**, 272

Howell, S. B. 1989, *Two-dimensional aperture photometry - Signal-to-noise ratio of point-source observations and optimal data-extraction techniques*, PASP, **101**, 616

Hsieh, H. H. & Jewitt, D. C. 2006, *A population of comets in the main asteroid belt*, Science, **312**, 561

Hsieh, H. H., Jewitt, D. C., & Fernández, Y. R. 2004, *The Strange Case of 133P/Elst-Pizarro: A Comet among the Asteroids*, AJ, **127**, 2997

Irwin, M., Tremaine, S., & Zytkow, A. N. 1995, *A Search for Slow-Moving Objects and the Luminosity Function of the Kuiper Belt*, AJ, **110**, 3082

Jewitt, D. C. 2002, *From Kuiper Belt Object to Cometary Nucleus: The Missing Ultrared Matter*, AJ, **123**, 1039

Jewitt, D. C. & Danielson, G. E. 1984, *Charge-coupled device photometry of Comet P/Halley*, Icarus, **60**, 435

Jewitt, D. C. & Luu, J. X. 1993, *Discovery of the candidate Kuiper belt object 1992 QB1*, Nature, **362**, 730

Jewitt, D. C. & Luu, J. X. 2001, *Colors and Spectra of Kuiper Belt Objects*, AJ, **122**, 2099

Jewitt, D. C. & Meech, K. J. 1986, *Cometary grain scattering versus wavelength, or 'What color is comet dust'?*, ApJ, **310**, 937

Jewitt, D. C. & Meech, K. J. 1987, *Surface brightness profiles of 10 comets*, ApJ, **317**, 992

Jewitt, D. C. & Sheppard, S. 2004, *The Nucleus of Comet 48P/Johnson*, AJ, **127**, 1784

Jewitt, D. C., Sheppard, S., & Fernández, Y. 2003, *143P/Kowal-Mrkos and the Shapes of Cometary Nuclei*, AJ, **125**, 3366

Johnson, R. E., Cooper, J. F., Lanzerotti, L. J., & Strazzulla, G. 1987, *Radiation Formation of a Non-Volatile Comet Crust*, A&A, **187**, 889

Kaasalainen, M., Mottola, S., & Fulchignoni, M. 2002, *Asteroid Models from Disk-integrated Data*, in Asteroids III, ed. W. F. Bottke, A. Cellino, P. Paolicchi, & R. P. Binzel (University of Arizona Press), 139–150

Kaiser, N. & Pan-STARRS Team. 2005, *The Pan-STARRS Survey Telescope Project*, Bulletin of the American Astronomical Society, **37**, 1409

Keller, H. U., Arpigny, C., Barbieri, C., et al. 1986, *First Halley multicolour camera imaging results from Giotto*, Nature, **321**, 320

Kern, S. D. & Elliot, J. L. 2006, *The Frequency of Binary Kuiper Belt Objects*, ApJ, **643**, L57

Kuiper, G. P. 1951, *On the Origin of the Solar System*, in Proceedings of a topical symposium, commemorating the 50th anniversary of the Yerkes Observatory and half a century of progress in astrophysics, ed. J. A. Hynek (New York: McGraw-Hill), 357

Lacerda, P. & Luu, J. X. 2006, *Analysis of the rotational properties of Kuiper Belt Objects*, AJ, **131**, 2314

Lamy, P. L., Toth, I., A'Hearn, M. F., & Weaver, H. A. 1999, *Hubble Space Telescope Observations of the Nucleus of Comet 45P/Honda-Mrkos-Pajdusakova and Its Inner Coma*, Icarus, **140**, 424

Lamy, P. L., Toth, I., Fernandez, Y. R., & Weaver, H. A. 2004, *The sizes, shapes, albedos, and colors of cometary nuclei*, in Comets II, ed. M. C. Festou, H. U. Keller, & H. A. Weaver (University of Arizona Press), 223–264

Lamy, P. L., Toth, I., Jorda, L., et al. 2002, *The Nucleus of Comet 22P/Kopff and Its Inner Coma*, Icarus, **156**, 442

Lamy, P. L., Toth, I., Jorda, L., Weaver, H. A., & A'Hearn, M. 1998a, *The nucleus and inner coma of Comet 46P/Wirtanen*, A&A, **335**, L25

Lamy, P. L., Toth, I., & Weaver, H. A. 1998b, *Hubble Space Telescope observations of the nucleus and inner coma of comet 19P/1904 Y2 (Borrelly)*, A&A, **337**, 945

Lamy, P. L., Toth, I., Weaver, H. A., et al. 2000, *The nucleus of 13 short-period comets*, Bulletin of the American Astronomical Society, **32**, 1061

Landolt, A. U. 1992, *UBVRI photometric standard stars in the magnitude range 11.5-16.0 around the celestial equator*, AJ, **104**, 340

Larsen, J. A., Gleason, A. E., Danzl, N. M., et al. 2001, *The Spacewatch Wide-Area Survey for Bright Centaurs and Trans-Neptunian Objects*, AJ, **121**, 562

Lebofsky, L. A. & Spencer, J. R. 1989, *Radiometry and a thermal modeling of asteroids*, in Asteroids II, ed. R. P. Binzel, T. Gehrels, & M. S. Matthews (University of Arizona Press), 128–147

Levison, H. F. 1996, *Comet Taxonomy*, in ASP Conf. Ser. 107: Completing the Inventory of the Solar System, 173–191

Licandro, J., Serra-Ricart, M., Oscoz, A., Casas, R., & Osip, D. 2000a, *The Effect of Seeing Variations in Time-Series CCD Inner Coma Photometry of Comets: A New Correction Method*, AJ, **119**, 3133

Licandro, J., Tancredi, G., Lindgren, M., Rickman, H., & Hutton, R. G. 2000b, *CCD Photometry of Cometary Nuclei, I: Observations from 1990-1995*, Icarus, **147**, 161

Lomb, N. R. 1976, *Least-squares frequency analysis of unequally spaced data*, Ap&SS, **39**, 447

Lowry, S. C., Coates, A. J., Fitzsimmons, A., Jones, G. H., & Lisse, C. M. 2005, *Deep Impact Observing at the Isaac Newton Telescope*, The Newsletter of the Isaac Newton Group of Telescopes, **10**, 6

Lowry, S. C. & Fitzsimmons, A. 2001, *CCD photometry of distant comets II*, A&A, **365**, 204

Lowry, S. C. & Fitzsimmons, A. 2005, *William Herschel Telescope observations of distant comets*, MNRAS, **358**, 641

Lowry, S. C., Fitzsimmons, A., Cartwright, I. M., & Williams, I. P. 1999, *CCD photometry of distant comets*, A&A, **349**, 649

Lowry, S. C., Fitzsimmons, A., & Collander-Brown, S. 2003, *CCD photometry of distant comets. III. Ensemble properties of Jupiter-family comets*, A&A, **397**, 329

Lowry, S. C., Fitzsimmons, A., Hicks, M., Lawrence, K., & Forti, G. 2006, *Comet P/2006 HR*$_{30}$ *(Siding Spring)*, IAU Circ., **8735**

Lowry, S. C. & Weissman, P. R. 2003, *CCD observations of distant comets from Palomar and Steward Observatories*, Icarus, **164**, 492

Luu, J. X. 1993, *Spectral diversity among the nuclei of comets*, Icarus, **104**, 138

Luu, J. X. & Jewitt, D. C. 1992, *Near-aphelion CCD photometry of Comet P/S Schwassmann-Wachmann 2*, AJ, **104**, 2243

Lyttleton, R. A. 1948, *On the Origin of Comets*, MNRAS, **108**, 465

Marsden, B. G., Sekanina, Z., & Everhart, E. 1978, *New osculating orbits for 110 comets and analysis of original orbits for 200 comets*, AJ, **83**, 64

McBride, N., Green, S. F., Chantal Levasseur-Regourd, A., Goidet-Devel, B., & Renard, J.-B. 1997, *The inner dust coma of Comet 26P/Grigg-Skjellerup: multiple jets and nucleus fragments?*, MNRAS, **289**, 535

McBride, N., Green, S. F., Davies, J. K., et al. 2003, *Visible and infrared photometry of Kuiper Belt objects: searching for evidence of trends*, Icarus, **161**, 501

McCafferty, P. & Baillie, M. 2005, *The Celtic Gods: Comets in Irish Mythology* (Tempus)

Meech, K. J., Ageorges, N., A'Hearn, M. F., et al. 2005, *Deep Impact: Observations from a Worldwide Earth-Based Campaign*, Science, **310**, 265

Meech, K. J., Belton, M. J. S., Mueller, B. E. A., Dicksion, M. W., & Li, H. R. 1993, *Nucleus properties of P/Schwassmann-Wachmann 1*, AJ, **106**, 1222

Meech, K. J., Hainaut, O. R., & Marsden, B. G. 2004, *Comet nucleus size distributions from HST and Keck telescopes*, Icarus, **170**, 463

Merline, W. J., Weidenschilling, S. J., Durda, D. D., et al. 2002, *Asteroids Do Have Satellites*, in Asteroids III, ed. W. F. Bottke, A. Cellino, P. Paolicchi, & R. P. Binzel (University of Arizona Press), 289–312

Millis, R. L., A'Hearn, M. F., & Campins, H. 1988, *An investigation of the nucleus and coma of Comet P/Arend-Rigaux*, ApJ, **324**, 1194

Morbidelli, A. & Brown, M. E. 2004, *The Kuiper belt and the primordial evolution of the Solar System*, in Comets II, ed. M. C. Festou, H. U. Keller, & H. A. Weaver (University of Arizona Press), 175–191

Newton, I. 1726, *Proposition XLI, Problem XXI: To determine the trajectory of a comet moving in a parabola, from three given observations*, in The Principia: mathematical principles of natural philosophy. A new translation and guide (1999), ed. I. B. Cohen & A. Whitman (University of California Press), 901–929

Noll, K. S., Levison, H. F., Grundy, W. M., & Stephens, D. C. 2006, *Discovery of a Binary Centaur*, Icarus, **184**, 611

O'Brien, D. P. & Greenberg, R. 2003, *Steady-state size distributions for collisional populations: Analytical solution with size-dependent strength*, Icarus, **164**, 334

O'Brien, D. P. & Greenberg, R. 2005, *The collisional and dynamical evolution of the main-belt and NEA size distributions*, Icarus, **178**, 179

Oort, J. H. 1950, *The structure of the cloud of comets surrounding the Solar System and a hypothesis concerning its origin*, Bull. Astron. Inst. Netherlands, **11**, 91

Ortiz, J. L., Gutiérrez, P. J., Santos-Sanz, P., Casanova, V., & Sota, A. 2006, *Short-term rotational variability of eight KBOs from Sierra Nevada Observatory*, A&A, **447**, 1131

Osip, D., Campins, H., & Schleicher, D. G. 1995, *The rotation state of 4015 Wilson-Harrington: Revisiting origins for the near-Earth asteroids*, Icarus, **114**, 423

Peixinho, N., Boehnhardt, H., Belskaya, I., et al. 2004, *ESO large program on Centaurs and TNOs: visible colors-final results*, Icarus, **170**, 153

Pravec, P. & Harris, A. W. 2000, *Fast and Slow Rotation of Asteroids*, Icarus, **148**, 12

Pravec, P., Harris, A. W., & Michałowski, T. 2002, *Asteroid Rotations*, in Asteroids III, ed. W. F. Bottke, A. Cellino, P. Paolicchi, & R. P. Binzel (University of Arizona Press), 113–122

Pravec, P., Scheirich, P., Kušnirák, P., et al. 2006, *Photometric survey of binary near-Earth asteroids*, Icarus, **181**, 63

Prialnik, D., Benkhoff, J., & Podolak, M. 2004, *Modeling the structure and activity of comet nuclei*, in Comets II, ed. M. C. Festou, H. U. Keller, & H. A. Weaver (University of Arizona Press), 359–387

Rabinowitz, D. L., Barkume, K., Brown, M. E., et al. 2006, *Photometric observations constraining the size, shape, and albedo of 2003 EL61, a rapidly rotating, Pluto-sized object in the Kuiper Belt*, ApJ, **639**, 1238

Richardson, D. C., Elankumaran, P., & Sanderson, R. E. 2005, *Numerical experiments with rubble piles: equilibrium shapes and spins*, Icarus, **173**, 349

Richardson, J. E. & Melosh, H. J. 2006, *Modeling the Ballistic Behavior of Solid Ejecta from the Deep Impact Cratering Event*, in 37th Annual Lunar and Planetary Science Conference, ed. S. Mackwell & E. Stansbery, 1836

Rickman, H. 1986, *Masses and densities of Comets Halley and Kopf*, in ESA SP-249: Comet Nucleus Sample Return Mission, ed. O. Melita, 195–205

Rickman, H. 1989, *The nucleus of Comet Halley - Surface structure, mean density, gas and dust production*, Advances in Space Research, **9**, 59

Rickman, H. 2004, *Current questions in cometary dynamics*, in Comets II, ed. M. C. Festou, H. U. Keller, & H. A. Weaver (University of Arizona Press), 205–208

Rodgers, S. D., Charnley, S. B., Huebner, W. F., & Boice, D. C. 2004, *Physical Processes and Chemical Reactions in Cometary Comae*, in Comets II, ed. M. C. Festou, H. U. Keller, & H. A. Weaver (University of Arizona Press), 505–522

Rubincam, D. P. 2000, *Radiative Spin-up and Spin-down of Small Asteroids*, Icarus, **148**, 2

Russell, H. N. 1916, *On the Albedo of the Planets and Their Satellites*, ApJ, **43**, 173

Sagdeev, R. Z., Szabo, F., Avanesov, G. A., et al. 1986, *Television observations of comet Halley from VEGA spacecraft*, Nature, **321**, 262

Samarasinha, N. H., Mueller, B. E. A., Belton, M. J. S., & Jorda, L. 2004, *Rotation of cometary nuclei*, in Comets II, ed. M. C. Festou, H. U. Keller, & H. A. Weaver (University of Arizona Press), 281–299

Schwehm, G. & Schulz, R. 1998, *The International Rosetta mission*, in ASSL Vol: 236: Laboratory astrophysics and space research, 537

Sekanina, Z. 1991, *Comprehensive model for the nucleus of Periodic Comet Tempel 2 and its activity*, AJ, **102**, 350

Sekanina, Z. 1997, *Detection of a Satellite Orbiting The Nucleus of Comet Hale-Bopp (C/1995 O1)*, Earth Moon and Planets, **77**, 155

Sheppard, S. S. & Jewitt, D. 2004, *Extreme Kuiper Belt Object 2001 QG_{298} and the Fraction of Contact Binaries*, AJ, **127**, 3023

Snodgrass, C., Fitzsimmons, A., & Lowry, S. C. 2005a, *Physical properties of seven cometary nuclei* IAU Symposium 229. Asteroids, Comets, Meteors: ACM 2005, 7th-12th August 2005, Búzios, Rio de Janeiro, Brazil, P5.11

Snodgrass, C., Fitzsimmons, A., & Lowry, S. C. 2005b, *The nuclei of comets 7P/Pons-Winnecke, 14P/Wolf and 92P/Sanguin*, A&A, **444**, 287

Snodgrass, C., Lowry, S. C., Fitzsimmons, A., Larson, S., & Skiff, B. 2005c, *Comet P/2005 JQ_5 (Catalina)*, IAU Circ., **8531**

Soderblom, L. A., Becker, T. L., Bennett, G., et al. 2002, *Observations of Comet 19P/Borrelly by the Miniature Integrated Camera and Spectrometer Aboard Deep Space 1*, Science, **296**, 1087

Sosa, A. & Fernández, J. A. 2005, *Cometary masses derived from nongravitational forces* IAU Symposium 229. Asteroids, Comets, Meteors: ACM 2005, 7th-12th August 2005, Búzios, Rio de Janeiro, Brazil, P14.30

Stern, S. A. 1995, *Collisional Time Scales in the Kuiper Disk and Their Implications*, AJ, **110**, 856

Stern, S. A. 1996, *On the Collisional Environment, Accretion Time Scales, and Architecture of the Massive, Primordial Kuiper Belt.*, AJ, **112**, 1203

Swings, P., McKellar, A., & Minkowski, R. 1943, *Cometary Emission Spectra in the Visual Region.*, ApJ, **98**, 142

Szutowicz, S. 2000, *Active regions on the surface of Comet 43P/Wolf-Harrington determined from its nongravitational effects*, A&A, **363**, 323

Tancredi, G., Fernández, J. A., Rickman, H., & Licandro, J. 2000, *A catalog of observed nuclear magnitudes of Jupiter family comets*, A&AS, **146**, 73

Tancredi, G., Fernández, J. A., Rickman, H., & Licandro, J. 2006, *Nuclear magnitudes and the size distribution of Jupiter family comets*, Icarus, **182**, 527

Tholen, D. J. 1984, *Asteroid taxonomy from cluster analysis of Photometry*, PhD thesis, University of Arizona

Tody, D. 1986, *The IRAF Data Reduction and Analysis System*, in Instrumentation in astronomy VI; Proceedings of the Meeting, Tucson, AZ, Mar. 4-8, 1986. Part 2 (Bellingham, WA: Society of Photo-Optical Instrumentation Engineers), 733

Tody, D. 1993, *IRAF in the Nineties*, in ASP Conf. Ser. 52: Astronomical Data Analysis Software and Systems II, 173

Toth, I. 2006, *Search for comet-like activity in asteroid 7968 Elst-Pizarro and limitation of its rotational pole orientation*, A&A, **446**, 333

Toth, I. & Lisse, C. M. 2006, *On the rotational breakup of cometary nuclei and centaurs*, Icarus, **181**, 162

Trilling, D. E. & Bernstein, G. M. 2006, *Light curves of 20-100 km Kuiper Belt Objects using the Hubble Space Telescope*, AJ, **131**, 1149

Trujillo, C. A., Jewitt, D. C., & Luu, J. X. 2001, *Properties of the Trans-Neptunian Belt: Statistics from the Canada-France-Hawaii Telescope Survey*, AJ, **122**, 457

Wallis, M. K. & Wickramasinghe, N. C. 1985, *Halley's comet - Its size and decay rate*, MNRAS, **216**, 453

Weissman, P. R. 1986, *Are cometary nuclei primordial rubble piles?*, Nature, **320**, 242

Weissman, P. R., Asphaug, E., & Lowry, S. C. 2004, *Structure and density of cometary nuclei*, in Comets II, ed. M. C. Festou, H. U. Keller, & H. A. Weaver (University of Arizona Press), 337–357

Weissman, P. R. & Lowry, S. C. 2003, *The Size Distribution of Jupiter-Family Cometary Nuclei*, in Lunar and Planetary Institute Conference Abstracts, 2003

Weissman, P. R. & Lowry, S. C. 2006, *Size Distribution, Structure and Density of Cometary Nuclei*, in LPI Workshop: Asteroid and Comet Interiors. Abstracts, 3025

Whipple, F. L. 1950, *A comet model. I. The acceleration of Comet Encke*, ApJ, **111**, 375

Whipple, F. L. 1951, *A Comet Model. II. Physical Relations for Comets and Meteors.*, ApJ, **113**, 464

Whipple, F. L. 1955, *A Comet Model. III. The Zodiacal Light.*, ApJ, **121**, 750

Whipple, F. L. 1984, *Comet P/Holmes, 1892III - A case of duplicity?*, Icarus, **60**, 522

Whipple, F. L. 1999, *Note on the structure of comet nuclei*, Planet. Space Sci., **47**, 301

Williams, I. P., Fitzsimmons, A., & O'Ceallaigh, D. 1993, *1993 SB and 1993 SC*, IAU Circ., **5869**

Yeomans, D. K. 1991, *Comets: A chronological history of observation, science, myth and folklore* (Wiley)

Zeilik, M., Gregory, S. A., & Smith, E. v. P. 1973, *Introductory Astronomy & Astrophysics* (Saunders HBJ, Orlando)

Appendix A

Photometric Data Tables

In this appendix I present the photometric data for each comet on which time-series data was taken. Each table contains columns giving the UT date at the time of observation, the airmass of the comet at that time, and the *R*-band magnitude of the comet with its associated uncertainty.

Table A.1: Apparent *R*-band magnitudes for comet 7P.

Date (Jan. 2004)	Airmass	m_R
21.0420	1.235	22.530±0.096
21.0438	1.238	22.594±0.099
21.0455	1.242	22.486±0.118
21.0473	1.247	22.670±0.108
21.0491	1.251	22.737±0.113
21.0508	1.255	22.364±0.112
21.0526	1.260	22.436±0.116
21.0772	1.348	22.629±0.095
21.0790	1.357	22.591±0.096
21.0808	1.365	22.646±0.099
21.0826	1.374	22.501±0.089
21.0844	1.383	22.494±0.089
21.0862	1.393	22.677±0.103
21.0879	1.402	22.505±0.090
21.1270	1.718	22.623±0.101
21.1287	1.738	22.507±0.095
21.1304	1.759	22.355±0.104
21.1322	1.782	22.189±0.096
21.1340	1.804	22.148±0.092
21.1358	1.828	22.295±0.103
21.1375	1.853	22.271±0.104
21.1399	1.886	22.412±0.119
21.1417	1.913	22.371±0.134
21.1434	1.941	22.355±0.133
21.1452	1.970	22.327±0.124
21.1469	1.999	22.200±0.099
21.1487	2.030	22.265±0.106
21.1505	2.062	22.332±0.114
22.1021	1.513	22.633±0.109
22.1038	1.527	22.288±0.087
22.1055	1.540	22.354±0.089
22.1072	1.555	22.389±0.093
22.1090	1.569	22.509±0.099
22.1108	1.585	22.389±0.092
22.1125	1.601	22.519±0.102
22.1379	1.901	22.409±0.098
22.1397	1.928	22.319±0.091
22.1415	1.957	22.467±0.104
22.1432	1.986	22.344±0.102
22.1450	2.017	22.226±0.093
22.1468	2.049	22.480±0.104
22.1486	2.082	22.445±0.102

Table A.2: Apparent *R*-band magnitudes for comet 14P.

Date (Jan. 2004)	Airmass	m_R
21.1734	1.817	22.818±0.120
21.1763	1.774	22.635±0.105
21.1792	1.734	22.704±0.104
21.1821	1.696	22.665±0.104
21.1850	1.660	22.604±0.099
21.2244	1.318	22.419±0.069
21.2273	1.300	22.333±0.066
21.2302	1.284	22.395±0.067
21.2331	1.268	22.367±0.072
21.2360	1.253	22.316±0.065
21.2542	1.173	22.212±0.063
21.2571	1.163	22.197±0.063
21.2600	1.152	22.252±0.064
21.2629	1.143	22.208±0.061
21.2659	1.133	22.204±0.061
21.2853	1.083	22.213±0.060
21.2882	1.077	22.266±0.059
21.2912	1.071	22.187±0.060
21.2941	1.066	22.197±0.059
21.2970	1.061	22.207±0.060
21.3150	1.039	22.329±0.060
21.3179	1.036	22.273±0.060
21.3208	1.034	22.333±0.062
21.3237	1.032	22.389±0.061
21.3266	1.030	22.316±0.062
21.3299	1.029	22.398±0.062
21.3328	1.028	22.410±0.062
21.3361	1.027	22.540±0.065
21.3390	1.027	22.507±0.066
22.1868	1.606	22.193±0.059
22.1897	1.575	22.239±0.054
22.1973	1.500	22.113±0.048
22.2002	1.474	22.109±0.053
22.2277	1.282	22.098±0.052
22.2306	1.266	22.189±0.053
22.2335	1.251	22.103±0.050
22.2363	1.237	22.094±0.050
22.2392	1.224	22.165±0.052
22.2586	1.147	22.279±0.052
22.2614	1.138	22.243±0.048
22.2643	1.129	22.409±0.053
22.2672	1.121	22.299±0.049

Table A.3: Apparent *R*-band magnitudes for comet 17P.

Date (March 2005)	Airmass	m_R
6.2004	1.162	22.920±0.100
6.2019	1.157	23.058±0.106
6.2243	1.088	23.190±0.118
6.2258	1.084	22.915±0.091
6.2273	1.080	23.122±0.109
6.2289	1.077	23.054±0.103
6.2304	1.073	22.961±0.094
6.2318	1.070	22.910±0.088
6.2334	1.066	23.044±0.103
6.2553	1.028	22.924±0.095
6.2588	1.024	23.040±0.102
6.2622	1.020	22.928±0.094
6.2655	1.016	22.863±0.091
6.2690	1.013	22.972±0.102
7.1940	1.175	22.446±0.108
7.1955	1.169	22.736±0.131
7.1970	1.163	22.932±0.162
7.1985	1.158	22.839±0.147
7.2000	1.153	22.729±0.132
7.2015	1.147	22.820±0.142
7.2030	1.142	22.901±0.151
7.2411	1.045	22.703±0.309
7.2458	1.038	22.956±0.163
7.2472	1.035	22.627±0.147
7.2487	1.033	22.635±0.123
7.2501	1.031	22.828±0.146
7.2516	1.029	23.053±0.197
7.2531	1.027	22.806±0.150
7.2546	1.025	22.836±0.170
7.3301	1.019	22.813±0.145
7.3317	1.021	22.901±0.177
7.3352	1.025	22.635±0.136
7.3385	1.029	23.011±0.194
7.3419	1.034	22.780±0.159
7.3656	1.080	22.868±0.154
7.3690	1.089	22.829±0.148
7.3724	1.098	22.768±0.142
7.3758	1.107	22.876±0.180
7.3793	1.118	22.758±0.139

Table A.2: Apparent *R*-band magnitudes for comet 14P, continued.

Date (Jan. 2004)	Airmass	m_R
22.2701	1.113	22.419±0.063
22.2885	1.071	22.407±0.052
22.2913	1.066	22.419±0.053
22.2942	1.061	22.265±0.048
22.2971	1.057	22.418±0.052
22.3000	1.053	22.349±0.049
22.3080	1.043	22.334±0.049
22.3108	1.040	22.346±0.047
22.3137	1.037	22.421±0.054
22.3166	1.035	22.385±0.048
22.3195	1.033	22.285±0.045
22.3296	1.028	22.245±0.045
22.3325	1.027	22.267±0.046
22.3354	1.027	22.213±0.044
22.3383	1.027	22.255±0.046
22.3411	1.027	22.206±0.044

Table A.4: Apparent *R*-band magnitudes for comet 36P.

Date (March 2005)	Airmass	m_R
6.1583	1.667	21.268±0.075
6.1609	1.690	21.299±0.075
6.1723	1.806	21.199±0.077
6.1757	1.847	21.208±0.081
6.1792	1.891	21.250±0.081
7.0755	1.327	21.393±0.068
7.0781	1.330	21.447±0.066
7.0807	1.334	21.424±0.066
7.0834	1.338	21.419±0.066
7.0861	1.343	21.454±0.070
7.1043	1.385	21.365±0.088
7.1077	1.396	21.390±0.077
7.1112	1.408	21.361±0.080
7.1648	1.758	21.619±0.070
7.1675	1.786	21.557±0.073
7.1701	1.816	21.595±0.070
7.1729	1.849	21.567±0.073
7.1755	1.882	21.563±0.070
7.1812	1.961	21.406±0.075
7.1838	2.001	21.324±0.074
7.1865	2.042	21.340±0.075
7.1891	2.087	21.412±0.082
Date (March 2006)	Airmass	m_R
1.9714	1.261	21.153±0.081
1.9735	1.252	21.461±0.126
1.9767	1.240	21.407±0.121
1.9807	1.225	21.433±0.139
1.9828	1.217	21.412±0.135
1.9850	1.210	21.604±0.173
1.9872	1.203	21.540±0.146
1.9893	1.197	21.015±0.200
1.9928	1.187	21.546±0.224

Table A.4: Apparent *R*-band magnitudes for comet 36P, continued.

Date (March 2006)	Airmass	m_R
1.9950	1.181	21.628±0.144
1.9971	1.175	21.464±0.112
1.9993	1.169	21.652±0.117
2.0015	1.164	21.572±0.098
2.0048	1.157	21.611±0.090
2.0070	1.152	21.410±0.081
2.0092	1.148	21.462±0.078
2.0114	1.144	21.516±0.078
2.0135	1.140	21.530±0.091
2.0169	1.135	21.678±0.117
2.0191	1.131	21.400±0.085
2.0212	1.128	21.456±0.082
2.0234	1.125	21.564±0.095
2.0256	1.123	21.515±0.082
2.0412	1.110	21.623±0.088
2.0433	1.110	21.820±0.121
2.0455	1.109	21.612±0.108
2.0477	1.108	21.440±0.084
2.0498	1.108	21.555±0.084
2.0657	1.112	21.482±0.079
2.0679	1.114	21.520±0.080
2.0700	1.115	21.643±0.084
2.0722	1.117	21.623±0.084
2.0744	1.119	21.603±0.085
2.0855	1.133	21.570±0.085
2.0876	1.136	21.743±0.096
2.0898	1.140	21.658±0.090
2.0920	1.143	21.650±0.092
2.0941	1.147	21.650±0.092
2.0976	1.154	21.692±0.084
2.0998	1.159	21.584±0.078
2.1019	1.164	21.566±0.076
2.1041	1.169	21.604±0.078
2.1063	1.175	21.605±0.080
2.1256	1.235	21.702±0.096
2.1278	1.244	21.633±0.086
2.1300	1.252	21.653±0.092
2.1321	1.261	21.708±0.096
2.1343	1.271	21.830±0.105
2.1497	1.349	21.783±0.105
2.1518	1.362	22.249±0.154
2.1540	1.375	21.455±0.081
2.1562	1.389	21.824±0.114
2.1583	1.403	21.751±0.110
2.1739	1.524	21.794±0.109
2.1761	1.544	21.767±0.111
2.1783	1.564	21.595±0.091
2.1805	1.586	21.690±0.098
2.1826	1.608	21.553±0.086
2.1862	1.647	21.704±0.100
2.1884	1.672	21.628±0.098
2.1906	1.698	21.804±0.120
2.1927	1.725	21.603±0.111
2.1949	1.753	22.191±0.228

Table A.4: Apparent *R*-band magnitudes for comet 36P, continued.

Date (March 2006)	Airmass	m_R
2.9127	1.667	21.490±0.088
2.9140	1.652	21.362±0.079
2.9153	1.637	21.387±0.081
2.9166	1.623	21.411±0.089
2.9179	1.609	21.464±0.095
2.9582	1.309	21.460±0.067
2.9595	1.302	21.614±0.072
2.9608	1.296	21.511±0.068
2.9621	1.290	21.404±0.064
2.9634	1.284	21.378±0.064
2.9809	1.214	21.455±0.068
2.9822	1.210	21.567±0.079
2.9835	1.205	21.507±0.075
2.9848	1.201	21.426±0.067
2.9861	1.197	21.573±0.075
3.0005	1.159	21.514±0.069
3.0018	1.156	21.381±0.061
3.0031	1.154	21.431±0.061
3.0044	1.151	21.545±0.069
3.0057	1.148	21.645±0.070
3.0152	1.132	21.457±0.064
3.0165	1.130	21.533±0.062
3.0179	1.128	21.624±0.069
3.0191	1.127	21.575±0.069
3.0204	1.125	21.637±0.073
3.0303	1.115	21.496±0.065
3.0316	1.114	21.585±0.069
3.0329	1.113	21.586±0.068
3.0342	1.112	21.524±0.061
3.0355	1.111	21.561±0.064
3.0699	1.117	21.538±0.076
3.0712	1.118	21.496±0.077
3.0725	1.119	21.568±0.075
3.0738	1.121	21.626±0.080
3.0751	1.122	21.768±0.093
3.0973	1.159	21.714±0.079
3.0986	1.162	21.736±0.081
3.0999	1.165	21.923±0.105
3.1012	1.168	21.793±0.092
3.1025	1.171	21.717±0.097
3.1611	1.441	21.823±0.117
3.1624	1.450	21.762±0.109
3.1637	1.460	21.526±0.097
3.1650	1.471	21.972±0.156
3.1809	1.617	21.912±0.144
3.1822	1.631	21.571±0.101
3.1835	1.645	22.136±0.164
3.1848	1.660	21.596±0.112
3.1861	1.675	21.716±0.126
3.1879	1.697	21.781±0.135
3.1892	1.713	21.945±0.152
3.1905	1.729	22.150±0.187
3.1918	1.746	21.939±0.165
3.1931	1.764	22.133±0.219

Table A.5: Apparent *R*-band magnitudes for comet 40P.

Date (July 2005)	Airmass	m_R
2.1710	1.396	21.985±0.116
2.1761	1.405	21.752±0.109
2.1775	1.408	21.833±0.109
2.1802	1.413	21.857±0.115
2.1816	1.416	21.814±0.110
2.1846	1.424	21.774±0.102
2.1861	1.427	21.684±0.091
3.1155	1.407	22.139±0.209
3.1170	1.404	22.140±0.174
3.1185	1.401	22.102±0.200
3.1209	1.397	22.310±0.253
3.1224	1.395	22.210±0.200
3.1239	1.393	22.188±0.214
3.1254	1.391	22.507±0.313
3.1923	1.453	22.248±0.235
3.1937	1.458	22.173±0.199
3.1953	1.463	22.094±0.209
3.2049	1.501	21.882±0.186
3.2063	1.508	22.501±0.297
3.2086	1.519	22.015±0.211
4.0976	1.445	21.954±0.226
4.0991	1.441	21.792±0.210
4.1043	1.427	21.491±0.202
4.1292	1.386	21.650±0.248
4.1307	1.385	21.675±0.221
4.1322	1.384	22.158±0.308
4.1337	1.383	21.551±0.233
5.0132	2.108	22.393±0.204
5.0147	2.083	22.640±0.248
5.0162	2.060	22.599±0.247
5.0177	2.037	22.438±0.258
5.0351	1.815	22.375±0.209
5.0366	1.799	22.960±0.326
5.0381	1.784	23.024±0.354
5.0396	1.769	22.241±0.169
5.1228	1.390	22.558±0.165
5.1243	1.389	22.121±0.117
5.1310	1.415	22.070±0.110
5.1697	1.415	22.540±0.203
5.1712	1.419	22.174±0.129
5.1727	1.422	22.793±0.225
5.1742	1.425	22.193±0.128
5.2025	1.527	21.701±0.106
5.2040	1.535	21.816±0.111
5.2055	1.542	22.087±0.136
5.2070	1.550	22.296±0.164
6.0326	1.811	22.879±0.452
6.0341	1.795	22.569±0.335
6.0356	1.780	22.189±0.249

Table A.5: Apparent *R*-band magnitudes for comet 40P, continued.

Date (July 2005)	Airmass	m_R
6.0423	1.718	22.243±0.253
6.1179	1.394	22.247±0.232
6.1194	1.392	22.005±0.164
6.1209	1.391	22.206±0.202
6.1224	1.389	22.012±0.171
6.1651	1.414	22.178±0.223
6.1667	1.417	22.215±0.239
6.1681	1.420	22.665±0.355
6.1696	1.423	22.056±0.218
6.2012	1.538	22.004±0.185
6.2027	1.545	22.161±0.237
6.2042	1.553	22.049±0.203
6.9964	2.315	22.689±0.323
6.9979	2.282	22.322±0.227
6.9994	2.251	22.539±0.294
7.0047	2.153	22.196±0.179
7.0212	1.907	21.903±0.221
7.0227	1.888	22.136±0.262
7.0243	1.871	22.401±0.352
7.0258	1.853	22.563±0.333
7.0938	1.434	22.032±0.215
7.0953	1.430	22.222±0.206
7.0968	1.426	22.290±0.207
7.1020	1.415	22.287±0.213
7.1400	1.387	22.204±0.191
7.1415	1.388	22.000±0.141
7.1430	1.389	22.779±0.295
7.1445	1.390	22.082±0.147
7.1806	1.465	21.917±0.171
7.1821	1.470	22.023±0.174
7.1836	1.476	22.117±0.188
7.1851	1.481	22.189±0.201
7.9984	2.214	22.216±0.211
7.9999	2.186	22.143±0.176
8.0014	2.159	22.129±0.186
8.0066	2.072	22.337±0.223
8.0236	1.845	22.001±0.150
8.0251	1.829	22.331±0.186
8.0266	1.813	21.929±0.144
8.1115	1.396	21.985±0.156
8.1130	1.395	22.335±0.194
8.1182	1.390	22.335±0.190
8.1583	1.415	22.396±0.214
8.1598	1.418	22.357±0.212
8.1612	1.421	22.508±0.227
8.1628	1.423	22.986±0.365
8.1999	1.567	22.996±0.464
8.2014	1.576	22.421±0.233
8.2029	1.585	22.189±0.193

Table A.6: Apparent *R*-band magnitudes for comet 47P.

Date (March 2005)	Airmass	m_R
6.1818	1.234	21.785±0.052
6.1832	1.229	21.713±0.057
6.1889	1.210	21.747±0.058
6.1902	1.206	21.689±0.057
6.1915	1.202	21.693±0.055
6.1928	1.198	21.679±0.055
6.1942	1.195	21.639±0.055
6.1955	1.191	21.727±0.049
6.1968	1.187	21.672±0.052
6.1981	1.184	21.719±0.054
6.2361	1.123	21.623±0.044
6.2393	1.121	21.581±0.043
6.2426	1.120	21.582±0.044
6.2457	1.119	21.562±0.043
6.2489	1.118	21.590±0.044
6.2731	1.127	21.590±0.045
6.2744	1.128	21.546±0.043
6.2757	1.130	21.602±0.045
6.2770	1.131	21.520±0.043
7.1171	1.638	21.643±0.075
7.1183	1.625	21.624±0.081
7.1196	1.611	21.645±0.083
7.1209	1.598	21.732±0.082
7.1222	1.585	21.681±0.080
7.1235	1.572	21.623±0.081
7.2091	1.154	21.443±0.052
7.2104	1.151	21.491±0.053
7.2117	1.149	21.650±0.055
7.2130	1.147	21.448±0.051
7.2143	1.145	21.497±0.049
7.2156	1.143	21.425±0.051
7.2200	1.137	21.400±0.051
7.2214	1.135	21.492±0.054
7.2716	1.129	21.479±0.061
7.2747	1.132	21.482±0.058
7.2778	1.136	21.525±0.061
7.2839	1.144	21.504±0.061
7.3060	1.192	21.600±0.065
7.3073	1.195	21.665±0.066
7.3086	1.199	21.624±0.067
7.3099	1.203	21.567±0.066
7.3111	1.206	21.604±0.066
7.3125	1.210	21.644±0.064
7.3137	1.214	21.462±0.062
7.3150	1.219	21.640±0.063
7.3440	1.345	21.897±0.142
7.3453	1.352	21.897±0.134
7.3466	1.359	21.861±0.111
7.3492	1.375	21.912±0.114
7.3505	1.383	21.934±0.135
7.3518	1.391	21.730±0.098
7.3531	1.399	21.773±0.105

Table A.7: Apparent *R*-band magnitudes for comet 121P.

Date (March 2006)	Airmass	m_R
2.2226	1.139	20.837±0.031
2.2277	1.135	20.825±0.028
2.2327	1.132	20.819±0.027
2.2440	1.130	20.810±0.028
3.1062	1.701	20.693±0.030
3.1091	1.667	20.687±0.031
3.1502	1.341	20.702±0.028
3.1531	1.326	20.691±0.028
3.1560	1.311	20.738±0.028
3.1698	1.252	20.737±0.027
3.1727	1.242	20.778±0.028
3.1756	1.232	20.780±0.028
3.1967	1.174	20.760±0.028
3.1996	1.169	20.778±0.028
3.2026	1.163	20.803±0.029
3.2096	1.152	20.790±0.028
3.2163	1.143	20.814±0.028
3.2315	1.131	20.832±0.029
3.2345	1.130	20.804±0.031
3.2374	1.129	20.812±0.028
3.2547	1.133	20.788±0.029
3.2576	1.135	20.787±0.031
3.2605	1.137	20.767±0.032

Table A.8: Apparent *R*-band magnitudes for comet 137P.

Date (March 2005)	Airmass	m_R
7.2606	1.078	22.689±0.122
7.2625	1.075	23.016±0.175
7.2662	1.069	22.829±0.148
7.2681	1.066	22.938±0.163
7.2860	1.048	22.869±0.155
7.2903	1.045	23.162±0.192
7.2946	1.043	22.773±0.142
7.2988	1.041	22.930±0.161
7.3032	1.041	22.885±0.139
7.3174	1.043	22.837±0.134
7.3194	1.044	22.860±0.155
7.3213	1.045	22.749±0.127
7.3233	1.047	22.717±0.122
7.3252	1.048	22.862±0.136
7.3272	1.050	22.903±0.141
7.3552	1.088	22.792±0.150
7.3571	1.092	22.774±0.142
7.3590	1.096	22.925±0.167
7.3609	1.100	22.762±0.145
7.3629	1.104	22.708±0.134
7.3814	1.156	22.878±0.186
7.3833	1.162	23.140±0.301

Table A.9: Apparent *R*-band magnitudes for comet 92P.

Date (Jan. 2004)	Airmass	m_R
21.0629	1.304	21.924±0.079
21.0642	1.298	21.868±0.075
21.0654	1.293	21.892±0.080
21.0667	1.288	21.871±0.065
21.0679	1.283	21.771±0.057
21.0692	1.278	21.860±0.064
21.0704	1.273	21.813±0.060
21.0717	1.268	21.856±0.063
21.0730	1.263	21.796±0.059
21.0742	1.258	21.752±0.070
21.0991	1.189	21.758±0.056
21.1004	1.186	21.772±0.056
21.1017	1.184	21.827±0.058
21.1029	1.181	21.777±0.056
21.1041	1.179	21.816±0.057
21.1054	1.177	21.785±0.057
21.1067	1.175	21.879±0.062
21.1079	1.173	21.913±0.078
21.1092	1.171	21.797±0.057
21.1105	1.169	21.893±0.075
21.1610	1.154	22.343±0.096
21.1622	1.155	22.171±0.076
21.1634	1.156	22.163±0.077
21.1647	1.158	22.168±0.077
21.1659	1.159	22.442±0.095
21.1672	1.160	22.242±0.080
21.1684	1.162	22.249±0.083
21.1696	1.163	22.371±0.096
21.1709	1.165	22.403±0.101
21.2104	1.261	21.911±0.068
21.2116	1.265	22.028±0.077
21.2128	1.270	21.989±0.083
21.2141	1.275	22.011±0.077
21.2154	1.280	21.841±0.075
21.2166	1.285	21.892±0.077
21.2179	1.290	21.881±0.065
21.2192	1.296	21.818±0.064
21.2205	1.301	21.966±0.072
21.2217	1.307	21.920±0.069
21.2403	1.406	21.860±0.066
21.2416	1.414	21.873±0.068
21.2428	1.423	21.908±0.070
21.2441	1.431	21.938±0.072
21.2453	1.440	22.006±0.077
21.2466	1.448	21.909±0.081
21.2478	1.457	22.200±0.107
21.2491	1.466	21.876±0.071
21.2503	1.476	21.997±0.088
21.2516	1.485	21.958±0.073
21.2701	1.655	22.107±0.099
21.2713	1.669	22.029±0.093
21.2726	1.683	22.103±0.095
21.3012	2.125	22.120±0.129
21.3025	2.152	22.522±0.193
21.3038	2.180	22.457±0.172

Table A.9: Apparent *R*-band magnitudes for comet 92P, continued.

Date (Jan. 2004)	Airmass	m_R
21.3050	2.208	22.408±0.168
21.3063	2.237	22.091±0.117
21.3075	2.267	22.422±0.174
21.3088	2.298	22.288±0.140
21.3100	2.329	22.081±0.126
21.3113	2.362	22.447±0.181
21.3125	2.395	22.556±0.199
22.1241	1.151	21.631±0.075
22.1253	1.151	21.570±0.071
22.1265	1.150	21.525±0.068
22.1277	1.149	21.705±0.092
22.1289	1.149	21.520±0.066
22.1302	1.148	21.707±0.092
22.1315	1.148	21.581±0.081
22.1327	1.147	21.671±0.088
22.1340	1.147	21.629±0.085
22.1352	1.147	21.733±0.094
22.1600	1.157	21.734±0.058
22.1624	1.159	21.827±0.063
22.1636	1.161	21.881±0.068
22.1648	1.162	21.749±0.070
22.1661	1.164	21.975±0.071
22.1672	1.165	21.840±0.064
22.1685	1.167	21.872±0.064
22.1697	1.168	21.983±0.070
22.1709	1.170	21.930±0.069
22.2048	1.253	22.041±0.094
22.2060	1.257	22.023±0.096
22.2072	1.262	21.936±0.090
22.2084	1.266	21.896±0.095
22.2097	1.271	22.070±0.098
22.2109	1.275	22.029±0.111
22.2121	1.280	21.926±0.099
22.2133	1.285	21.806±0.075
22.2145	1.290	21.868±0.091
22.2157	1.295	21.847±0.091
22.2451	1.461	21.611±0.076
22.2463	1.470	21.572±0.072
22.2475	1.479	21.738±0.076
22.2487	1.488	21.600±0.079
22.2499	1.498	21.645±0.083
22.2511	1.507	21.761±0.094
22.2523	1.517	21.556±0.079
22.2535	1.527	21.611±0.082
22.2547	1.538	21.727±0.108
22.2560	1.549	21.673±0.091
22.2742	1.741	21.820±0.105
22.2754	1.757	21.850±0.107
22.2766	1.772	21.927±0.114
22.2778	1.788	21.840±0.109
22.2791	1.805	21.855±0.106
22.2803	1.822	21.777±0.098
22.2815	1.839	21.870±0.109
22.2827	1.857	21.804±0.102
22.2839	1.874	21.832±0.108
22.2851	1.893	21.712±0.094

Table A.10: Apparent *R*-band magnitudes for comet 94P.

Date (July 2005)	Airmass	m_R
5.1091	1.691	20.905±0.072
5.1111	1.688	21.038±0.076
5.1147	1.685	21.110±0.082
5.1161	1.684	21.204±0.088
5.1174	1.683	21.012±0.080
5.1188	1.682	21.432±0.103
5.1570	1.732	21.289±0.103
5.1584	1.737	21.223±0.095
5.1598	1.742	21.054±0.084
5.1647	1.759	21.312±0.103
5.1951	1.939	21.118±0.107
5.1964	1.951	21.197±0.103
5.1978	1.962	21.196±0.103
5.1992	1.974	21.284±0.112
6.0203	2.266	21.774±0.315
6.0217	2.245	21.770±0.313
6.0230	2.225	21.534±0.283
6.0279	2.160	21.458±0.271
6.1049	1.694	21.124±0.250
6.1063	1.693	21.026±0.241
6.1077	1.691	21.042±0.241
6.1091	1.689	20.898±0.238
6.1139	1.686	20.734±0.233
6.1512	1.727	20.872±0.247
6.1526	1.731	20.722±0.234
6.1539	1.735	20.874±0.237
6.1553	1.740	21.018±0.241
6.1601	1.757	20.876±0.239
6.1925	1.948	20.376±0.229
6.1939	1.959	20.587±0.231
6.1953	1.971	20.757±0.235
6.2070	2.088	20.721±0.263
6.2084	2.104	20.487±0.241
6.2098	2.121	20.976±0.268
6.2112	2.138	20.573±0.245
7.0089	2.404	20.635±0.153
7.0103	2.380	20.507±0.140
7.0117	2.355	20.557±0.147
7.0131	2.331	20.511±0.140
7.0180	2.256	20.266±0.140
7.0289	2.110	20.198±0.129

Table A.10: Apparent *R*-band magnitudes for comet 94P, continued.

Date (July 2005)	Airmass	m_R
7.0303	2.095	20.163±0.126
7.0643	1.819	20.129±0.124
7.0657	1.812	20.353±0.128
7.0671	1.805	20.428±0.127
7.0685	1.798	20.440±0.129
7.1060	1.691	20.949±0.160
7.1074	1.690	20.807±0.138
7.1088	1.689	20.960±0.152
7.1102	1.688	20.924±0.153
7.1150	1.686	21.037±0.160
7.1487	1.731	21.274±0.190
7.1501	1.736	20.781±0.135
7.1515	1.740	20.997±0.148
7.1529	1.745	21.060±0.148
7.1959	2.009	21.344±0.165
7.1973	2.023	21.148±0.144
7.1987	2.037	21.320±0.155
7.2001	2.051	21.247±0.153
8.0117	2.307	21.931±0.276
8.0131	2.285	21.438±0.158
8.0145	2.264	21.599±0.173
8.0194	2.195	21.605±0.183
8.0339	2.026	21.560±0.178
8.0353	2.013	21.103±0.111
8.0367	1.999	21.134±0.122
8.0763	1.755	21.516±0.145
8.0776	1.750	21.395±0.126
8.0790	1.745	20.778±0.097
8.0805	1.733	20.964±0.103
8.1223	1.691	20.942±0.121
8.1237	1.693	21.121±0.117
8.1251	1.694	21.206±0.121
8.1299	1.700	21.586±0.141
8.1724	1.854	21.371±0.155
8.1738	1.863	21.262±0.128
8.1751	1.872	21.187±0.121
8.1766	1.873	21.064±0.107
8.2069	2.171	20.899±0.130
8.2083	2.190	20.894±0.117
8.2097	2.208	21.117±0.136
8.2111	2.217	20.961±0.118

Table A.11: Apparent *R*-band magnitudes for comet P/2004 H2.

Date (July 2005)	Airmass	m_R
2.1403	1.512	21.779±0.066
2.1432	1.496	21.815±0.071
2.1474	1.473	21.884±0.066
2.1502	1.459	21.803±0.057
2.1552	1.436	21.816±0.057
2.1581	1.424	21.887±0.059
2.1622	1.408	21.838±0.059
2.1650	1.397	21.758±0.055
2.1905	1.331	21.857±0.055
2.1934	1.326	21.765±0.060
2.1963	1.322	21.778±0.065
2.1992	1.319	21.830±0.060
2.2033	1.314	21.925±0.072
2.2061	1.312	21.776±0.061
3.0817	2.130	21.624±0.239
3.0846	2.078	21.724±0.245
3.0876	2.028	21.387±0.172
3.0905	1.982	21.417±0.163
3.0959	1.905	21.467±0.158
3.0988	1.866	21.579±0.172
3.1018	1.830	21.349±0.137
3.1047	1.795	21.421±0.175
3.1550	1.431	21.616±0.078
3.1580	1.418	21.574±0.074
3.1609	1.407	21.649±0.079
3.1639	1.396	21.664±0.078
3.1762	1.359	21.599±0.078
3.1792	1.352	21.599±0.076
3.1821	1.345	21.732±0.082
3.1851	1.339	21.620±0.078
3.2126	1.308	21.630±0.087
3.2167	1.308	21.431±0.103
3.2201	1.308	21.483±0.123
4.0667	2.386	21.361±0.112
4.0697	2.317	21.365±0.130
4.0726	2.252	21.499±0.135
4.0755	2.192	21.441±0.124
4.0798	2.111	21.558±0.131
4.0827	2.060	21.495±0.118
4.1081	1.729	21.474±0.080
4.1111	1.700	21.494±0.079
4.1140	1.673	21.528±0.080
4.1170	1.647	21.463±0.082
4.1216	1.611	21.532±0.066
4.1245	1.589	21.464±0.077
4.1375	1.505	21.306±0.077
4.1404	1.488	21.425±0.077
5.0795	2.070	21.744±0.088
5.0825	2.022	21.636±0.076

Table A.11: Apparent *R*-band magnitudes for comet P/2004 H2, continued

Date (July 2005)	Airmass	m_R
5.0886	1.930	21.578±0.067
5.0915	1.890	21.471±0.064
5.0945	1.852	21.649±0.070
5.0974	1.817	21.581±0.061
5.1398	1.478	21.637±0.067
5.1427	1.464	21.464±0.057
5.1804	1.341	21.604±0.058
5.1833	1.335	21.497±0.051
5.1863	1.331	21.695±0.056
5.1892	1.326	21.661±0.054
5.2105	1.312	21.496±0.062
5.2134	1.312	21.704±0.073
5.2164	1.312	21.938±0.099
5.2193	1.314	21.628±0.092
6.0792	2.032	21.254±0.076
6.0822	1.986	21.450±0.090
6.0851	1.942	21.308±0.078
6.0881	1.901	21.300±0.075
6.1263	1.541	21.267±0.058
6.1293	1.523	21.313±0.063
6.1322	1.506	21.466±0.069
6.1351	1.490	21.337±0.065
6.1745	1.348	21.323±0.063
6.1775	1.342	21.265±0.062
6.1804	1.337	21.395±0.065
6.1834	1.332	21.482±0.065
6.2172	1.315	21.225±0.085
6.2202	1.317	21.212±0.100
7.0742	2.070	21.432±0.091
7.0772	2.021	20.970±0.083
7.1196	1.569	21.679±0.071
7.1225	1.549	21.608±0.069
7.1254	1.531	21.598±0.066
7.1284	1.513	21.667±0.068
7.1600	1.378	21.700±0.072
7.1629	1.370	21.615±0.063
7.2094	1.314	21.750±0.073
7.2123	1.315	21.669±0.066
8.0857	1.864	21.735±0.062
8.0886	1.828	21.632±0.065
8.0926	1.783	21.432±0.061
8.1372	1.454	21.654±0.069
8.1402	1.441	21.578±0.060
8.1431	1.429	21.591±0.064
8.1888	1.321	21.589±0.069
8.1918	1.319	21.621±0.069
8.1947	1.317	21.646±0.069
8.2161	1.320	21.681±0.092
8.2190	1.323	21.721±0.125